# Search for physics beyond the standard electroweak model with the WITCH experiment

**Simon Van Gorp**

Promotor:
Prof. Dr. Nathal Severijns

Proefschrift voorgedragen
tot het behalen van de
graad van Doctor in de
Wetenschappen

March 2012

**Instituut voor**
**Kern- en Stralingsfysica**
Departement natuurkunde en sterrenkunde
Faculteit Wetenschappen

KATHOLIEKE UNIVERSITEIT
LEUVEN

1425

# Search for physics beyond the standard electroweak model with the WITCH experiment

**Simon Van Gorp**

Jury:
Prof. Dr. Nathal Severijns, promotor
Prof. Dr. Marc Huyse, president
Prof. Dr. Gerda Neyens
Prof. Dr. Piet Van Duppen
Prof. Dr. Valeri Afansiev
Dr. Xavier Fléchard
  (Université de Caen, France)
Dr. Alexander Herlert
  (FAIR, Darmstadt, Germany)

Dissertation presented in partial
fulfilment of the requirements for
the degree of Doctor
in Science

March 2011

*Every computer program has at least one bug and can be shortened by at least one instruction - from which, by induction, one can deduce that every program can be reduced to one instruction which doesn't work.*
*(Programmers Wisdom)*

*This can easily be extended to any thesis: Each thesis has at least one misspelling and can be shortened by at least one word...*

# Dankwoord

Het voelt goed om terug te kijken naar de voorbije 4.5 jaar en ook daarbij te denken aan de verschillende mensen die me hebben bijgestaan om mijn doctoraat te voltooien.

Allereerst natuurlijk de mensen die deze thesis mogelijk hebben gemaakt en dan denk ik in het bijzonder aan Prof. Dr. N. Severijns. Nathal overtuigde me om een doctoraat in zijn groep te maken, een beslissing waar ik absoluut geen spijt van heb. Hij gaf mij de vrijheid om me volledig te ontplooien in de dingen die ik graag doe én hij gaf ook het vertrouwen aan Michael en mij om vrij zelfstandig aan de WITCH-opstelling te kunnen werken. Had ik vragen dan was hij steeds bereid om zijn drukke agenda even opzij te schuiven. Hij was, denk ik, voor mij de bijna perfecte promotor waar ik veel van bijleerde. Ik herinner me zeker nog de laatste vlucht die we samen terugnamen van Geneve toen mijn contract ten einde liep.

I would also like to acknowledge the other WITCH colleagues (Sam, Valentin, Martin, Tomica, Peter, Dalibor, Marcus, Alex) for the creation of a nice and productive atmosphere and collaboration. Directe collega Michael verdient een speciaal woordje. Twee jaar lang waren we vaste collega's. We deden praktisch alles samen: naar CERN gaan, werken in Leuven, snowboarden, ... Ik denk dat we samen bijna het ideale team vormden en we met weinig woorden elkaar begrepen. Zonder hem zou mijn thesis en mijn werkomgeving helemaal anders geweest zijn, bedankt daarvoor.

I would also like to thank the other members of the examination committee, Prof. Dr. Marc Huyse, Prof. Dr. Gerda Neyens, Prof. Dr. Valeri Afanasiev, Prof. Dr. Piet Van Duppen, Dr. Xavier Fléchard and Dr. Alexander Herlert for carefully reading my thesis and having an exciting discussion on the results.

Hiernaast zorgde *nonkel Piet* ervoor dat ik de switch maakte van informatica naar fysica. Daar ben ik hem nog altijd dankbaar voor (ook al zorgde deze switch ervoor dat ik een drukke maand augustus tegemoet ging).

Natuurlijk moet ik ook de rest van het IKS bedanken, o.a. de ICT'ers Bert en Luc. Het was Luc die meteen open stond voor het inbouwen van grafische

kaarten in de cluster. Zonder hem had mijn thesis nooit kunnen zijn wat hij nu is. En was het niet voor zijn ICT- ondersteuning dan zocht ik hem op voor zijn mening over onderwerpen zoals het beveiligen van zijn cluster tot bergbeklimmen, kunstschaatsen en hippies. Naast de ICT-deur heb ik ook de deur van Willy platgelopen met ideeën en aanvragen over veranderingen aan onze opstelling, waarna hij telkens met een beter idee op de proppen kwam. Natuurlijk zijn er ook de secretaressen (Isabelle, Sally, Fabienne en Katja) en vanzelfsprekend ook Nancy die mijn bureau piekfijn in orde hield. Bedankt aan allen.

Voorts zijn er de collega's die voor de positieve sfeer in het IKS zorgden. Hieruit vloeide verscheidene sportieve activiteiten voort. De *bike en run* op mijn voetbalschoenen met Dieter of met music-maniac Thomas. De voetbalploeg *nIKS* (Jeroen, Bert, Dieter, Pieter, Kristof, Steffie); verruit de betere voetbalploeg van de Celestijnenlaan en superieur in derbies tegen VSM. Ook het voetballen elke vrijdagmiddag en het 's middags lopen zullen worden gemist. Hetzelfde geldt voor de club van pokeraars, tafelvoetballers alsook voor de voetballers van F.C. Rekencentrum. Bedankt voor de ontspanning naast het dagelijkse werk.

Een belangrijk woord van dank gaat uit naar de meest belangrijke mensen in mijn leven, namelijk mijn familie. Mijn vader Kris, van wie ik in de vooravond van mijn studies afscheid moest nemen, is en zal altijd mijn drijfveer blijven. Dankzij hem vind ik motivatie in wat ik doe. Hij was het die me leerde om -net zoals hem- nooit op te geven, om toch altijd dat lichtpuntje te vinden waaruit hoop ontstaat. Ook genieten van het leven en de belangrijkheid van vrienden zijn slechts enkele van de vele waarden die ik van hem heb meegekregen. Mijn moeder Rit bedank ik omdat ze altijd voor mij klaarstaat met een luisterend oor en een helpende hand. Ik bewonder haar uitgekiend organisatietalent, haar eeuwige opgewektheid en haar onvermijdelijk optimisme. Vervolgens dank ik mijn broer en zussen. Allen hebben op hun eigen manier bijgedragen aan het welslagen van mijn studie. Mijn broer Daan bedank ik voor zijn opgewekte en geïnteresseerde aanwezigheid en om me nog altijd te laten winnen in onderlinge gevechten. Mijn zus Celien voor het resultaat van haar cake-en-taart-bakaanvallen. En mijn zus Jolijn bedank ik voor haar toegewijde bezorgdheid en om mij rust te leren appreciëren.
Voorts wil ik graag mijn vier grootouders bedanken. Ik heb het voorrecht genoten om hen alle vier goed te kennen of te hebben gekend. Zij hebben nooit getwijfeld om mij een stevig hart onder de riem te steken. Vooral oma en opa dank ik voor hun warme hart dat ze mij toedragen. Hun deur stond altijd open voor mij.

Tot slot dank ik iedereen die nog niet vernoemd is en die op een of andere manier heeft bijgedragen tot mijn thesis. Ik denk hierbij aan vrienden en kennissen met een speciaal woordje van dank voor Stephane Boogaerts.

Het laatste woord is gericht aan Liesje. Ik dank haar voor haar opgewektheid en spontaniteit. Ook bedank ik haar voor het geduld tijdens mijn afwezigheden naar Genève alsook voor haar liefdevolle zorgen tijdens het schrijven van mijn thesis.

Bedankt aan allen, zonder jullie had deze thesis nooit geschreven geweest.

Simon Van Gorp
16 maart 2012

# Preface

A physicist tries to understand what happens around him or her by comparing experimental observations to an underlying model. Such underlying models are sometimes difficult to grasp, while others excel in beauty and simplicity. To each of those models, however, there is a limit. Upon reaching this boundary one has to dig deeper to generalize the model, so as to find an even more fundamental description. Eventually the dream of physicists is to grasp everything, from a falling leaf to the birth of a star, in one fundamental (hopefully) beautiful formulation.
This is the aim of the Standard Model, which tries to unify all four forces and all known particles. The Standard Model does a very good job in describing all of our surroundings, but has not been fully put to the test, yet. In this thesis I will show how the WITCH experiment can be used to probe the Standard Model (SM), or more specific, one of its forces: the weak force.

Due to the weak force a radioactive nucleus undergoes $\beta$ decay, i.e. the conversion of a neutron into a proton, or vica versa. In such a decay a neutrino ($\nu$), a tiny nearly massless particle without charge, and a $\beta$ particle are emitted as well and the energy released in the $\beta$ decay process is distributed among the emitted neutrino, the $\beta$ particle and the newly made proton or neutron. This energy distribution is highly sensitive on a parameter called the *beta neutrino angular correlation coefficient a*, the value of which is predicted by the SM. Any discrepancy between the experimentally measured energy distribution and the one predicted by the Standard Model could reveal new, as yet unknown physics. In this work I will discuss the first determination of $a$ with the WITCH experiment, thereby also describing the major tools required to do so, as e.g. the experimental setup and the Penning trap simulation program, *Simbuca*.

In October 2007, one month after my PhD started, a first measurement was performed on $^{35}$Ar, the best current candidate to determine $a$ with the WITCH experiment at ISOLDE, CERN. During this experiment it was noticed that the charge exchange of argon was too fast to allow a successful experiment ($\tau = 8$ ms), while also an unexpected ionization of rest gas particles in the setup showed up. Together with Michael Tandecki –a fellow PhD student– these issues were tackled

in a 2 year campaign during which version 2.0 of the WITCH experiment was constructed. The efforts of both of us to solve the unwanted ionization and the charge exchange issues were discussed already in depth in Michael's thesis, and are therefore not reflected in this thesis. Over the years, the system gradually improved leading to a first determination of $a$ with the setup in June 2011 albeit still with very limited precision as will be discussed in detail in this thesis.

The *Simbuca* Penning trap simulation program came together after trying a numerous amount of methods to speed up the calculation of the Coulomb interaction between ions. Finally, what led to the break-trough, was a simulation library that calculates the gravitational interaction between stars, used in the field of astrophysics. Since the gravitational force and Coulomb force equations have the same structure, that library was modified to calculate the Coulomb interaction between trapped ions. Due to the usage of a graphics card (GPU) the program speeds up the calculation time tremendously. Aside from aiding the analysis for the WITCH experiment, Simbuca was also used to investigate the parameters that influence in-trap-decay efficiency. In a joint collaboration with Dr. Alexander Herlert, a publication is written about this (see Appendix). Further, *Simbuca* was released under the GPL license, such that other users are now using *Simbuca* freely as well.

The *Simbuca* Penning trap simulation package was used together with the ion tracking simulation program (SimWITCH) to reconstruct the recoil energy spectrum measured in June 2011. Many challenges had to be overcome in this experiment, e.g. the setup has been opened multiple times in the week prior to the experiment and the experiment yielded only a low amount of statistics with high background. After careful analysis, however, a first determination value for the $\beta$-$\nu$ angular correlation coefficient with the WITCH experiment could be obtained. Albeit with limited statistical precision, this result clearly showed the feasibility of the WITCH experiment to contribute to weak interaction studies.
With many of the technical difficulties solved, much more statistics could be collected in the run in October 2011 and even more so in the November 2011 run. Now the statistical precision of the available data set is below 5%, thereby opening a new era for WITCH, i.e. a detailed investigation of possible systematic effects.

Finally, when around $1 \times 10^4$ or more ions are stored in a Penning trap, the motion of an ion changes significantly, i.e. the ions will cluster together in an ion cloud, comparable with the image of a rotating galaxy, and will move around in the ion trap as if they would be a single ion. This thesis gives an outlook of the presence of non-neutral plasmas in the WITCH setup, which was never looked into before. Typical plasma parameters and methods to influence the plasma behaviour will be discussed in the last chapter of this thesis. This information will help to interpret the recently collected as well as the future datasets to be acquired with the WITCH setup.

# Abstract

A measurement of the beta-neutrino angular correlation coefficient $a$ yields information on possible exotic couplings in the weak interaction. To this end the energy distribution of the recoiling daughter nucleus after $\beta$ decay, which depends on $a$, is measured precisely. Any deviation of the measured distribution with the one expected from the Standard Model can reveal new physics. If no deviation is found stringent limits can be set on the possible presence of different types of new physics beyond the Standard Model. The WITCH experiment, located at ISOLDE, CERN aims to determine $a$ with a final precision below 1%.

Ion bunches are created with REXTRAP and injected in the WITCH setup. The energy of these ion bunches is pulsed down in the Pulsed Drift Tube section, prior to the capture of the ions in the first of two Penning traps. The motion of the radioactive ions is cooled before the transfer to a second Penning trap, the decay trap, which acts as the scattering-free source of the experiment. The ions can decay in this trap while being stored for a couple of seconds. When an ion undergoes $\beta$ decay, it can escape the trap and the energy of the recoiling daughter nucleus is measured with a retardation spectrometer and an MCP detector. By varying the electric potential barrier in the retardation spectrometer, the recoil energy spectrum is obtained.

The expected recoil energy spectrum is reconstructed with an ion tracking simulation program, called *SimWITCH*, and a Penning trap simulation program, called *Simbuca*. This versatile simulation package was developed to investigate the behaviour of multiple ions in a Penning trap. Due to its novel approach of using a graphics card (GPU) instead of a conventional CPU, the Coulomb interaction between the ions can be calculated much faster. Furthermore *Simbuca* incorporates three realistic buffer gas models, the possibility of importing realistic electric and magnetic field maps and different order integrators with adaptive step size and error control.

The simulation package was used to analyse the first acquired retardation spectrum with WITCH, taken in an experiment in June 2011. Even though the statistics gathered is low, a first determination of $a$ with the WITCH experiment was

possible. The analysis method for a typical WITCH experiment will be explained and it will be shown that a statistical precision below 1% can indeed be reached with the WITCH experiment. An outlook is given about the follow up experiments in October and November 2011, in which enough statistics were obtained to reach a statistical precision of around 4%. The WITCH experiment is now in a phase where systematic effects will have to be looked into and a preliminary result can be obtained even before a final dataset for a high precision result can be collected.

The development of *Simbuca* made it possible to look at the behaviour of multiple ($10^6$ to $10^7$) ions in a Penning trap, a regime that is currently being reached by the setup. Due to the mutual Coulomb interaction between the ions, they will cluster together to form an ion plasma which rotates around its own center of mass. The influence of this behaviour on the resonant quadrupole eigenfrequency will be discussed. An estimate for the range of the plasma parameters is extracted from simulations as well. Finally, an outlook is given on how to influence and/or determine these parameters. This will analyse the already available as well as future high statistics datasets of WITCH.

# Contents

# Chapter 1

# Weak Interaction Theory

## 1.1 $\beta$ decay theory

### 1.1.1 Fermi's formalism for $\beta$ decay

Radioactivity was discovered by accident in 1896 by Henri Becquerel. Three years later Ernest Rutherford separated two types of radioactive decay: $\alpha$ decay and $\beta^-$ decay [Rutherford, 1899]. In 1934, $\beta^+$ decay was observed for the first time in the decay of $^{30}P^+$ by Frédéric and Irène Joliot-Curie [Joliot & Curie, 1934], and Luis Alvarez discovered Electron Capture (EC) in $^{48}V^+$ [Alvarez, 1937]. A radioactive particle undergoes $\beta$ decay when a proton is converted to a neutron or vice versa. These processes take place inside the nucleus of an atom and can be summarized as:

- $\beta^-$ decay: $n \rightarrow p + e^- + \bar{\nu}_e$
- $\beta^+$ decay: $p \rightarrow n + e^+ + \nu_e$
- EC decay: $p + e^- \rightarrow n + \nu_e$

where $n$ represents a neutron, $p$ a proton, $e^-$ an electron, $e^+$ a positron and $\nu_e(\bar{\nu}_e)$ the (anti) neutrino. Also in 1934 Enrico Fermi developed the first quantum mechanical description of nuclear $\beta$ decay [Fermi, 1934]. He wrote down a $\beta$ decay Hamiltonian in analogy to the classical electromagnetic interaction Hamiltonian:

$$H_{e.m.} = -e\frac{\bar{p}}{mc} \cdot \bar{A}(\bar{r}) \tag{1.1}$$

with $\bar{p}$ the momentum and $\bar{A}(\bar{r})$ the vector potential of the particle. This Hamiltonian describes the time-dependent interaction between a radiation system (e.g. an atom) and the surrounding electromagnetic field, which leads to an exchange of energy between the system and this field. To describe $\beta$ decay, Fermi replaced three parameters in the electromagnetic interaction Hamiltonian [Fermi, 1934]:

- the electromagnetic interaction strength $e$ (electric charge) by $g$, the coupling constant for the weak interaction. Unlike $e$, $g$ is not a fundamental constant but it is proportional to $m_w^2$, with $m_w$ the mass of the $W$ boson which mediates the decay in question.

- the differential operator $-\frac{\bar{p}}{mc}$ by $\tau^+$ that changes a neutron (charge 0) into a proton (charge 1).

- the vector field $\bar{A}(\bar{r}) = \psi_\gamma^*(\bar{r})$ by $\psi_e^*(\bar{r})\psi_\nu^*(\bar{r})$

The total Hamiltonian for $\beta$ decay can then be written as:

$$H_\beta = g\left(\psi_{e-}^*(\bar{r})\psi_{\bar{\nu}}(\bar{r})\tau^+ + \psi_{e+}^*(\bar{r})\psi_\nu(\bar{r})\tau^-\right) \tag{1.2}$$

with the first term for $\beta^-$ decay and the second term for $\beta^+$ decay. The Hamiltonian density can now be defined as

$$\mathcal{H}_\beta = \psi_p^\dagger H_\beta \psi_n \tag{1.3}$$

$$= g\left[\psi_p^\dagger \tau^+ \psi_n \psi_{e-}^\dagger \psi_{\bar{\nu}} + h.c.\right] \tag{1.4}$$

with h.c. the hermitian conjugate, representing $\beta^+$ decay.

Pauli (1933) had previously shown that the Hamiltonian could have only five different forms to be be relativistically invariant: these are S, the scalar interaction; P, pseudoscalar; V, vector; A, axial vector; and T, tensor. Fermi knew this but chose, as shown above, to use only the vector interaction. Despite the fact that this theory is old it is still useful today for the phenomenological description of low energy decay processes, because the $W$ bosons are very heavy ($m_w$=80 GeV) and the momentum transfer in $\beta$ decay is rather small.

## 1.1.2   V-A theory for the $\beta$ decay

Later on, in 1936, Fermi's approach was extended by Gamow and Teller to all possible Lorentz invariant current-current interactions (S,V,T,A and P), so not only restricting to vector currents (V) [Gamow & Teller, 1936].

| | Selection rules | Operators |
|---|---|---|
| Fermi | $\Delta I = 0$ <br> $\Delta T = 0$ <br> $\Delta \pi = 0$ | S/V |
| Gamow Teller | $\Delta I = 0, \pm 1 \ (0 \nrightarrow 0)$ <br> $\Delta T = 0, \pm 1 \ (0 \nrightarrow 0)$ <br> $\Delta \pi = 0$ | T/A |

Table 1.1: Fermi and Gamow-Teller selection rules and operators.

Fermi's theory originally required no difference between the mother and daughter ion of nuclear spin ($\Delta I$), isospin ($\Delta T$) and parity ($\Delta \pi$), and therefore did not include any effects due to nuclear spin. Gamow and Teller included nuclear spin and obtained selection rules, see Table 1.1. The types of decays covered by both the Fermi and the Gamow Teller selection rules are called the *allowed* transitions. *Forbidden* transitions, for example with $\Delta I > 1$, also occur but are not of interest for weak interaction studies, due to their theoretical complication. The Gamow-Teller modification requires either an Axial Vector or a Tensor form of the interaction, while the Fermi selection rules require a Vector or Scalar interaction.

The work of Fierz in 1937 helped to restrict the allowed forms of the interaction [Fierz, 1937]: he showed that if both Scalar and Vector or both Axial Vector and Tensor interactions are present in $\beta$ decay, there would be an interference term in the beta-decay-spectrum, the size of which depends on the electron energy. The failure to observe these interference terms showed that the decay interaction did not contain both S and V, or both A and T.

Experiments showing the presence of Gamow-Teller selections rules and others studying unique forbidden transitions, had shown that either A or T must be present [Langer & Price, 1949]. In addition, a study of the decay of $^{14}$O to $^{14}$N$^*$ had demonstrated that either Scalar or Vector must also be present [Sherr et al., 1949]. This restricted the forms of the interaction to STP, SAP, VTP, or VAP or doublets taken from these combinations. The absence of interference terms in the first-forbidden spectra eliminated the VT, SA, and AP combinations. VP was eliminated because it did not allow Gamow-Teller transitions. This left only the STP triplet or the VA doublet as the possible interactions.

This dilemma was resolved by experimental results obtained, especially by the experiment on $^6$He by Rustad and Ruby in 1953 [Rustad & Ruby, 1953, 1955]. These angular correlation experiments (see 1.2) excluded the STP triplet and assigned a V-A structure to the $\beta$ decay. This V-A (Vector and Axial Vector) structure is the theoretical base of the weak interaction in the Standard Model (SM). In the SM, Scalar, Tensor and Pseudo scalar currents are excluded.

### 1.1.3  Standard Model theory for the $\beta$ decay and Coupling Constants

In it's most general form, the $\beta$ decay Hamiltonian density in Eq.(1.4) is:

$$
\begin{aligned}
\mathcal{H}_\beta \;=\; & (\bar{\psi}_p \psi_n)(C_S \bar{\psi}_{e^-} \psi_{\bar{\nu}} + C_S' \bar{\psi}_{e^-} \gamma_5 \psi_{\bar{\nu}}) \\
& + (\bar{\psi}_p \gamma_\mu \psi_n)(C_V \bar{\psi}_{e^-} \gamma^\mu \psi_{\bar{\nu}} + C_V' \bar{\psi}_{e^-} \gamma^\mu \gamma_5 \psi_{\bar{\nu}}) \\
& + \frac{1}{2}(\bar{\psi}_p \sigma_{\lambda\mu} \psi_n)(C_T \bar{\psi}_{e^-} \sigma^{\lambda\mu} \psi_{\bar{\nu}} + C_T' \bar{\psi}_{e^-} \sigma^{\lambda\mu} \gamma_5 \psi_{\bar{\nu}}) \\
& + (\bar{\psi}_p \gamma_\mu \gamma_5 \psi_n)(C_A \bar{\psi}_{e^-} \gamma^\mu \gamma_5 \psi_{\bar{\nu}} + C_A' \bar{\psi}_{e^-} \gamma^\mu \psi_{\bar{\nu}}) \\
& + (\bar{\psi}_p \gamma_5 \psi_n)(C_P \bar{\psi}_{e^-} \gamma_5 \psi_{\bar{\nu}} + C_P' \bar{\psi}_{e^-} \psi_{\bar{\nu}}) \\
& + h.c. \quad\quad\quad\quad\quad\quad\quad\quad\quad\quad\quad\quad\quad\quad\quad\quad (1.5)
\end{aligned}
$$

with $\gamma_i$ the Dirac matrices, $\sigma_{\lambda\mu}$ the tensor operator equal to $-\frac{1}{2}i(\gamma_\lambda \gamma_\mu - \gamma_\mu \gamma_\lambda)$, $\psi^\dagger = \bar{\psi}\gamma_4$ and $C_i(')$ the coupling constants (i=S,V,T,A,P). As shown in the previous section, the Standard Model allows only Vector and Axial Vector type interactions, hence $C_{S,T,P}^{(')} = 0$. Furthermore in 1956 Lee and Yang proposed a measurement to check parity conservation for the weak interaction [Lee & Yang, 1956]. The experiment was performed by Wu et al. in 1957 and led to the discovery of maximum parity violation in the weak interaction [Wu et al., 1957]. A discovery for which, Lee, Yang and Wu received the Nobel Price of Physics. Maximum violation of parity means $C_i = C_i'$. The Pseudoscalar contribution, if non-zero, would give negligible contributions in $\beta$ decay, since the nucleons can be treated non-relativistically.

The Standard Model assumes the following values for the coupling constants:

$$
\begin{aligned}
C_V &= C_V' = 1 \\
C_A &= C_A' \approx -1.27 \\
C_S &= C_S' = 0 \\
C_T &= C_T' = 0 \\
C_P &= C_P' = 0. \quad\quad\quad\quad\quad\quad\quad\quad\quad\quad\quad\quad (1.6)
\end{aligned}
$$

The exact value of $C_A = C_A'$ is to be obtained from neutron decay [Severijns et al., 2006]. Without making any assumptions except that the coupling constants are

real (no violation of time reversal symmetry) one can deduce experimental limits on the above Scalar, Tensor and Pseudoscalar coupling constants. A least-square fit to relevant experimental data from nuclear $\beta$ decay and neutron decay [Severijns et al., 2006] yielded (90% C.L.)

$$-1.40 < \quad C_A/C_V \quad < -1.17$$
$$-0.065 < \quad C_S/C_V \quad < 0.070$$
$$-0.076 < \quad C_T/C_A \quad < 0.090.$$

from which it is clear that there is still significant room for improving on these limits. Currently, all available experimental data are consistent with the pure V-A Standard Model interaction.

### 1.1.4 From coupling constants to correlation coefficients

It is possible to determine the $C_i'$-coefficients directly from experiments. Therefore, Jackson, Treimann and Wyld calculated for the weak interaction Hamiltonian in Eq. (1.5) the $\beta$ decay transition probability as a function of the observable *correlation coefficients* [Jackson et al., 1957]. For an ensemble of non-oriented nuclei, the distribution function in the neutrino, electron and electron polarization direction ($\boldsymbol{\sigma}$) is given by:

$$\omega(\boldsymbol{\sigma}|E_\beta, \Omega_\beta, \Omega_\nu)dE_\beta d\Omega_\beta d\Omega_\nu =$$

$$\frac{F(\pm Z, E_\beta)}{(2\pi)^5} p_\beta E_\beta (E_0 - E_\beta)^2 dE_\beta d\Omega_e d\Omega_\nu \frac{\xi}{2}$$

$$\left\{ 1 + a\frac{\mathbf{p}_\beta \cdot \mathbf{p}_\nu}{E_\beta E_\nu} + b\frac{m_\beta}{E_\beta} \right.$$

$$\left. + \boldsymbol{\sigma} \cdot \left[ G\frac{\mathbf{p}_\beta}{E_\beta} + H\frac{\mathbf{p}_\nu}{E_\nu} + K\frac{\mathbf{p}_\beta}{E_\beta + m_\beta}\left( \frac{\mathbf{p}_\beta \cdot \mathbf{p}_\nu}{E_\beta E_\nu} \right) + L\frac{\mathbf{p}_\beta \times \mathbf{p}_\nu}{E_\beta E_\nu} \right] \right\}. \quad (1.7)$$

Here, $E_{\beta,\nu}$, $\mathbf{p}_{\beta,\nu}$ and $\Omega_{\beta,\nu}$ refer to the total energy, momentum and emission angle of the $\beta$ particle and the neutrino, respectively, and $E_0$ is the total energy available in the decay. The vector $\boldsymbol{\sigma}$ is the direction in which the polarization of the $\beta$ particle is measured. The upper sign refers to $\beta^-$ decay whereas the lower sign refers to $\beta^+$ decay. $F(\pm Z, E_\beta)$ is the Fermi function that takes into account the Coulomb interaction between the $\beta$ particle and the daughter nucleus with charge Z. $\xi$ is a normalization factor proportional to the decay rate and contains

the nuclear beta decay matrix elements $M_F$ and $M_{GT}$:

$$\begin{aligned} \xi \;\; = \;\; & |M_F|^2 \left( |C_S|^2 + |C'_S|^2 + |C_V|^2 + |C'_V|^2 \right) \\ & + |M_{GT}|^2 \left( |C_A|^2 + |C'_A|^2 + |C_T|^2 + |C'_T|^2 \right). \end{aligned} \qquad (1.8)$$

The coefficients $a$, $b$, $G$, $H$, $K$ and $L$ represent the strength of the different correlations and are called correlation coefficients. In the case of a pure Gamow-Teller (GT) or Fermi (F) decay, these coefficients depend solely on the coupling constants $C_i$ and $C'_i$, i.e. on the structure of the weak interaction. If the decay is a mixed F/GT transition, the correlation coefficients also depend on the F/GT mixing ratio $\rho = C_A M_{GT} / C_V M_F$.

The $G$, $H$, $K$ and $L$ correlations in Eq.(1.7) are experimentally hard to measure since one has to know the polarization of the $\beta$ particle with quite high precision. More sensitive to non-Standard Model Physics are the $\beta$-$\nu$ angular correlation, $a$, and the Fierz interference term, $b$.

The Fierz interference term is an important parameter because it doesn't depend on any observable vector quantity and is thus present in all correlation measurements. It depends on the coupling constants via:

$$b\xi = \pm 2\Gamma Re \left[ |M_F|^2 \left( C_S C^*_V + C'_S C'^*_V \right) + |M_GT|^2 \left( C_T C^*_A + C'_T C'^*_A \right) \right], \quad (1.9)$$

with $\Gamma$ given by:

$$\Gamma = \sqrt{1 - \alpha^2 Z^2}, \qquad (1.10)$$

with $\alpha$ the fine-structure constant. The Standard Model predicts the Fierz interference term to be zero.

## 1.2  The $\beta$-$\nu$ angular correlation, $a$

The $\beta$-$\nu$ angular correlation coefficient $a$ is sensitive to all types of coupling constants and as such it was used in the past to determine experimentally the V-A structure of the weak interaction (see section 1.1.2). Currently it is still one of the best observables to search for physics beyond the standard model in $\beta$ decay.

| Interaction | $a$ |
|:-----------:|:---:|
| V | 1 |
| A | -1/3 |
| S | -1 |
| T | 1/3 |

Table 1.2: The $\beta$-$\nu$ angular correlation coefficient $a$ for pure forms of the weak interaction.

## 1.2.1 Theoretical expression

Including the first order Coulomb corrections (i.e. up to order $\alpha Z$ [Vogel & Werner, 1983]), $a$ is given by:

$$a\xi = |M_F|^2 \left[ |C_V|^2 + |C'_V|^2 - |C_S|^2 - |C'_S|^2 \mp \frac{\alpha Z m_e}{p_\beta} 2Im\left(C_S C_V^* + C'_S C'^*_V\right) \right]$$

$$+ \frac{|M_{GT}|^2}{3} \left[ |C_T|^2 + |C'_T|^2 - |C_A|^2 - |C'_A|^2 \pm \frac{\alpha Z m_e}{p_\beta} 2Im\left(C_T C_A^* + C'_T C'^*_A\right) \right].$$

$$(1.11)$$

For a pure Fermi transition and assuming time reversal invariance this can be approximated as:

$$a \approx 1 - \frac{|C_S|^2 + |C'_S|^2}{|C_V|^2}. \tag{1.12}$$

Since the Fierz interference term influences any correlation measurement, the observable that is actually determined in a $\beta$-$\nu$-angular correlation measurement is

$$\tilde{a} = \frac{a}{1 + \left\langle \frac{m_e}{E_\beta} \right\rangle b}. \tag{1.13}$$

Note that according to the Standard Model $\tilde{a} = a$ (since $b = 0$).

The values of $a$ for pure Vector and Axial Vector (Standard Model) and Scalar and Tensor (non Standard Model) interactions are shown in table 1.2. Any admixture of, for instance, a Scalar type interaction into the Standard Model Vector interaction in a pure Fermi decay will yield an $a$ parameter that differs from the Standard Model value.

It should also be noted that both the equations for $a$ and $b$ as given in [Jackson et al., 1957] do not include so-called induced currents or recoil order corrections, which play a role at the sub-percent level only [De Leebeeck, 2011].
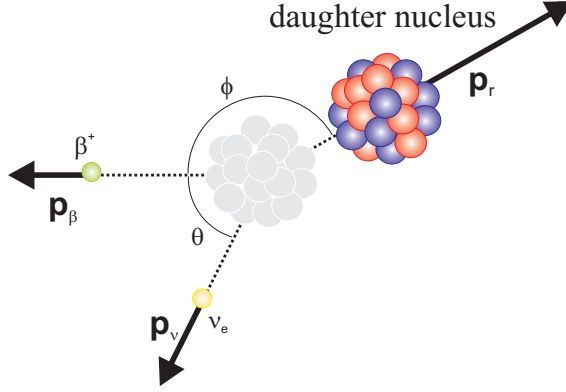
Figure 1.1: Schematic view of the kinematics in nuclear $\beta$ decay

The formulation of the correlation coefficients (Eq. 1.7) can be rewritten as an angular distribution function $W(\theta)$

$$W(\theta) = 1 + \tilde{a}\frac{p_\beta p_\nu}{E_\beta E_\nu}cos(\theta) \tag{1.14}$$

with $\theta$ the angle between the two propagation directions of the emitted leptons, see Figure 1.1.

If one can measure this angular distribution function, the $\beta$-$\nu$ angular correlation coefficient $a$ can be determined. From the measurement of $a$, one can then calculate the coupling constants (Eq. 1.11) and extract information on possible Scalar or Tensor currents or put more stringent limits on them (1.7).

**An example : $0^+ \rightarrow 0^+$ decay**

The expression

$$h \equiv \frac{\boldsymbol{\sigma} \cdot \boldsymbol{p}}{|\boldsymbol{p}|} \tag{1.15}$$

is called the helicity, of a particle, which is a good quantum number for a massless particle (like the neutrino). If $h = +1$ it is said to be positive. In a similar way, a negative helicity means $h = -1$.

Since the $\beta$ particle has a non-zero mass it can be proven that its helicity is not invariant under a Lorentz transformation, which makes it a poor quantum number for a $\beta$ particle. For $\beta$ particles, $\frac{\boldsymbol{\sigma} \cdot \boldsymbol{p}}{|\boldsymbol{p}|} = \pm v/c$ and is called the (longitudinal) polarization of the $\beta$ particle ($-v/c$ for electrons and $+v/c$ for positrons).

By applying the anti-commutation relations of the $\gamma_i$-matrices it can be shown that the helicities of both leptons (emitted in $\beta$ decay) should be opposite in order to have a non-vanishing interaction in the case of Axial Vector and Vector contributions, while the helicities should be equal in the case of Pseudoscalar, Scalar and Tensor interactions.

Lets now consider a pure $0^+ \rightarrow 0^+$ $\beta^+$ transition, i.e. a pure Fermi decay. According to the Standard Model, this decay proceeds via a pure Vector interaction. However, as was shown in reference [Severijns et al., 2006] and in the corresponding equation (1.7), Scalar interactions are not ruled out experimentally.

In a $0^+ \rightarrow 0^+$ decay the leptons should have opposite spin since they do not carry away angular momentum. For a pure Vector interaction this means that the leptons are emitted parallel (since their helicities must be opposite). For a pure Scalar decay, the helicities must be the same, thus neutrino and $\beta$ particle will be emitted in opposite directions.
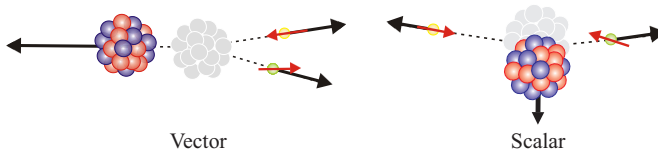


Vector                    Scalar

Figure 1.2: The propagation directions for the $\beta^+$ particle, neutrino and daughter nucleus after a $0^+ \rightarrow 0^+$, $\beta^+$ decay driven by a pure Vector and pure Scalar interaction. Thick, black arrows indicate momentum vectors, thin vectors indicate spin vectors. Via conservation of momentum and energy the angular distribution $W(\theta)$ can be written as the recoil nucleus energy distribution [Kofoed-Hansen, 1954].

Since the momentum of the recoil nucleus is the vector sum of the neutrino and $\beta$ particle momenta, the Vector interaction will, on average, result in a higher recoil energies than the Scalar interaction. Note that this is consistent with equation 1.14. For a pure Vector interaction, $a = 1$, thus $W(\theta)$ will be larger than for a scalar interaction, for which $a = -1$.

## 1.2.2 Methods to measure $a$

To characterize the decay and determine $a$, one has access to five parameters since the decay process takes place in a two dimensional plane. Figure 1.1, shows these 5 parameters: three momenta $p_\nu, p_\beta, p_{recoil}$ and two angles $\theta$ and $\phi$. Due to conservation of momentum and energy only two parameters are necessary to reconstruct the complete kinematics of the decay. Since it is difficult to detect neutrinos, a possible experiment is restricted to 3 observables: the momentum (or

energy) of both the $\beta$ particle and the recoiling nucleus and the angle between the ejected $\beta$ particle and the nucleus.

The most common technique involves detecting the $\beta$ particle and the recoil nucleus in coincidence to reconstruct the kinematics of the decay. In general the $\beta$ particle is used as a start trigger for the TOF measurement of the recoil ions, needed to determine $p_{recoil}$. Together with the measured energy of the $\beta$ particle the full event can be reconstructed and $a$ can be extracted. A different approach, adopted by the WITCH experiment, is to measure the recoil energy distribution of the daughter nucleus after the decay. These methods often use a combination of electromagnetic fields, i.e. a spectrometer, to guide the recoiling ions after their decay to a detector.

In general the main difficulty in the determination of the $\beta$-$\nu$ angular correlation, is the observation of the recoil nucleus and the precise determination of its kinetic energy after decay due to its low energy of typically up to only a few 100 eV. The classical approach to implant radioactive ions in a foil is thus not possible, since the recoil nucleus would scatter so much that all kinematic information is lost. To circumvent this obstacle a wide range of traps have recently been developed to store radioactive atoms or ions in a scattering-free environment. An overview will be given in Sec 1.4.

## 1.3   Measuring $a$ via the recoil energy distribution

The energy distribution of the recoiling nucleus after $\beta$ decay can be constructed from the Jackson-Treimann formula (Eq (1.7)), as is shown in Ref. [Kofoed-Hansen, 1954]. Integrating Eq.(1.7) over all possible $\beta$ particle polarizations $\sigma$ and transforming the angles $\Omega_{\beta,\nu}$ to the kinetic energy of the recoil nucleus ($E_R$) results in:

$$P(E_\beta, E_r)dE_\beta dE_r = \frac{M}{2}F(Z, E_\beta)\left[ep_\nu + bp_\nu + \frac{a}{2}\left(2ME_r - p_\beta^2 - p_\nu^2\right)\right]dE_\beta dE_r,$$

$$(1.16)$$

with $F(Z, E_\beta)$ the Fermi function that includes Coulomb corrections. The integration of $P(E_\beta, E_r)$ over the total $\beta$ energy, $E_\beta$, is numerically solvable and yields the energy distribution of the daughter nucleus after $\beta$ decay.

The recoil energy of the daughter nucleus after the $\beta$ decay $_Z^A X \rightarrow _{Z\pm1}^A X$ can be calculated using conservation of energy and momentum and with $p_\nu = 0$:

$$0 = p_{recoil} + p_\beta \tag{1.17}$$

$$Q = E_{rec,kin} + E_{\beta,rec}, \tag{1.18}$$

with Q the mass difference between the parent and daughter nucleus, i.e. the decay energy, and the relativistic equations:

$$E_{tot} = E_{kin} + mc^2 \tag{1.19}$$

$$E_{rec,kin} = p^2 c^2 + m^2 c^4, \tag{1.20}$$

yielding the maximum recoil energy, $E_{rec}^{max}$, for the daughter nucleus after the decay as

$$E_{rec}^{max} = \frac{Q^2 \pm 2Qm_\beta c^2}{2(M_{at}(_Z^A X)c^2 + Q - m_\beta c^2)} \tag{1.21}$$

$$\approx \frac{Q^2 \pm 2Qm_\beta c^2}{2M_{at}(_{Z\pm1}^A X)c^2} \tag{1.22}$$

where $M_{at}$ represents the atomic mass of the particle, and the upper (lower) sign correspond to $\beta^-$ ($\beta^+$) decay.

For example for the decay of $^{35}$Ar the maximum recoil energy is 452 eV. The dependence of the recoil energy distribution on the value of $a$ in the case of V, A, S and T type $\beta$ decay is shown in Fig. 1.3.

Due to the operating principle of the WITCH setup, with its retardation spectrometer, only recoil energies above a certain threshold voltage are detected. Therefore, not the differential spectrum is measured but the integral spectrum. Figure 1.4 shows the dependence of such a spectrum on the different possible values for $a$.

Finally the aim of the WITCH setup is to measure this distribution very precisely and search for tiny deviations from the Standard Model expected value (i.e. assuming only Vector and Axial Vector type decays). From this one can then probe the existence of scalar (and tensor) currents or put limits on their existence.
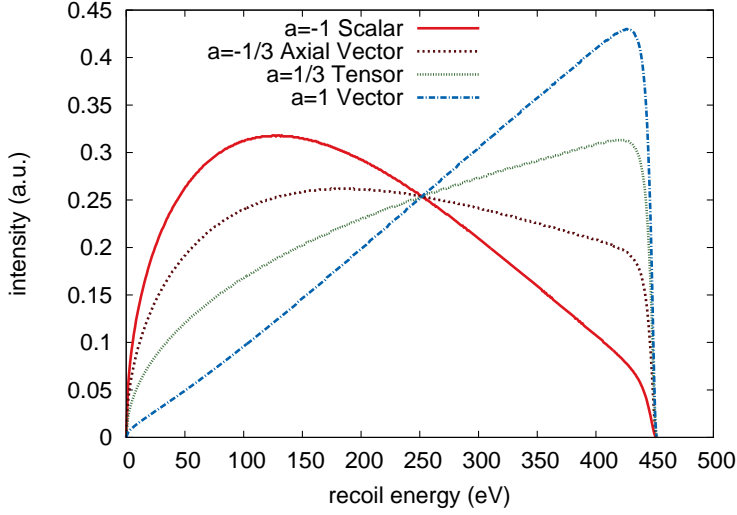
Figure 1.3: Differential recoil energy distribution of the $^{35}$Cl daughter nucleus after $\beta^+$ decay of $^{35}$Ar for different $\beta$-$\nu$ angular correlation coefficients $a$ with $F(Z, E_\beta)$ = 1 and $b = 0$.
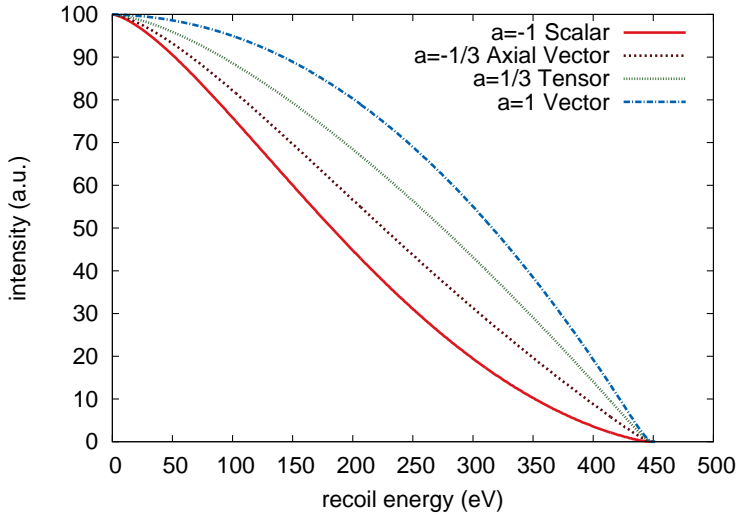


Figure 1.4: Integral recoil energy distribution of the $^{35}$Cl daughter nucleus after $\beta^+$ decay of $^{35}$Ar for different $\beta$-$\nu$ angular correlation coefficients $a$ with $F(Z, E_\beta)$ = 1 and $b = 0$. In general a larger value for $a$ results in a higher chance to observe daughter nuclei with a higher recoil energy.

$^{35}$Ar ε Decay    1980Wi13

Decay Scheme

Intensities: Iγ per 100 parent decays

3/2+    0.0    1.775 s
$^{35}_{18}$Ar$_{17}$

%ε+%B+=100
Q⁺=5965.3⁸

| | IΒ⁺ | Iε | Log *ft* |
|---|---|---|---|
| 3967.5 | 0.0071 | 7.2 | 4.81 |
| 3918.48 | 0.0073 | 6.3 | 4.88 |
| 3002.74 | 0.089 | 0.00106 | 4.975 |
| 2693.6 | 0.162 | 0.00123 | 5.001 |
| 1763.15 | 0.265 | 7.1 | 5.453 |
| 1219.44 | 1.23 | 0.00206 | 5.100 |
| 0.0 | 98.02 | 0.0707 | 3.761 |

1/2+  3967.5
3/2+  3918.48
5/2+  3002.74
3/2+  2693.6
5/2+  1763.15
1/2+  1219.44
3/2+  0.0    stable

$^{35}_{17}$Cl$_{18}$
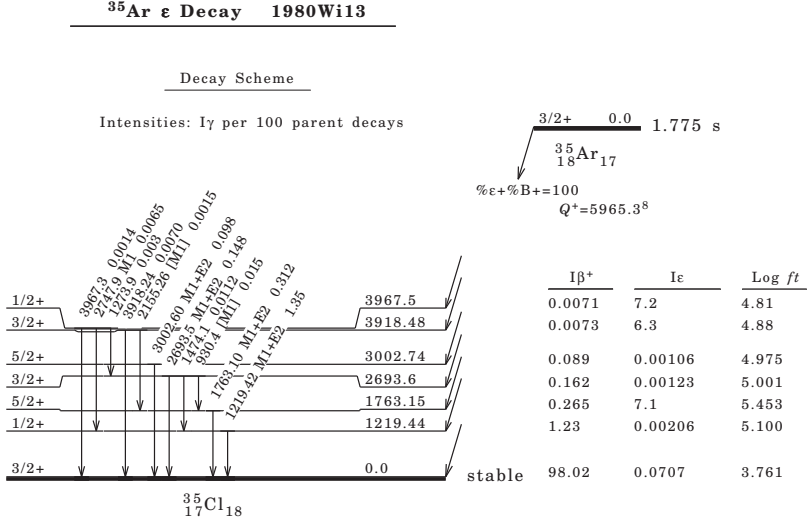
Figure 1.5: Decay scheme of $^{35}$Ar, taken from [NUDAT 2.5, 2011]

## 1.3.1 Gamma recoil correction

Not only the emission of a $\beta$ particle or neutrino but also the emission of a $\gamma$ ray causes the nucleus to recoil. We assume that the $\gamma$ decay happens instantaneously after the $\beta$ decay. This is a valid assumption since the maximum half-life of an exited state is of the order of nanoseconds while, according to simulations, a decayed ion has to travel at least 3 microseconds before it hits the wall of the Penning trap and is lost there. Considering that the decay of an excited state happens several orders of magnitude faster we can assume the decay happens instantaneously.

The recoil energy of a $\gamma$-transition of energy $E$ for a nucleus of mass $m$ is given by

$$E_{rec,\gamma} = \frac{E_\gamma^2}{2mc^2}. \tag{1.23}$$

If the $\gamma$ ray follows the $\beta$ decay, a significant effect on the shape of the recoil spectrum is seen. For an angle $\theta$ between the direction of recoil caused by the $\beta$ decay (energy $E_{rec,\beta}$) and the direction of recoil caused by the $\gamma$ decay (energy

$E_{rec,\gamma}$) the total recoil energy is given by

$$
\begin{aligned}
E_{rec,tot} &= \frac{p_{E_{tot}}^2}{2M} = \frac{p_{E_{rec,\beta}}^2 + p_{E_{rec,\gamma}}^2 - 2p_{E_{rec,\beta}}p_{E_{rec,\gamma}}\cos(\theta)}{2M} \\
&= E_{rec,\beta} + E_{rec,\gamma} - \frac{\cos(\theta)p_{E_{rec,\beta}}p_{E_{rec,\gamma}}}{M} \\
&= E_{rec,\beta} + E_{rec,\gamma} - 2\cos(\theta)\sqrt{E_{rec,\beta}E_{rec,\gamma}} \\
&= E_{rec,\beta} + \frac{E_\gamma^2}{2mc^2} - 2\cos(\theta)\sqrt{E_{rec,\beta}\frac{E_\gamma^2}{2mc^2}}.
\end{aligned}
\tag{1.24}
$$

As the direction of emission of the $\gamma$-ray is arbitrary, the angle $\theta$ is picked randomly from the interval $[0, 2\pi]$. If the $\gamma$ is emitted in the direction of the moving daughter nucleon ($\theta = 0$) the kinetic energy is reduced, while a $\gamma$ emitted in opposite direction of the ion movement ($\theta = \pi$) yields a maximum recoil energy for the daughter nucleus (i.e. $E_{rec,\beta}$).

If several $\gamma$-rays follow each other sequentially, all the different recoil energies have to be combined. This will very much complicate the shape of the recoil spectrum, especially if the different branching ratios are not very well known.

In the specific case of $^{35}$Ar, 98.0% of the decays proceed to the ground state, see Figure 1.6. About 1.2 %, however, $\beta$ decays to the excited 1.219 MeV level in $^{35}$Cl followed by a $\gamma$ decay to the ground state. The maximum recoil energy of the nucleus from the $\beta$ decay to the excited state is 271 eV. The energy kick the daughter nucleus gets due to the $\gamma$ decay is 22.8 eV. This energy is thus randomly distributed in all $\theta$ directions. Note that although the angle $\theta$ is randomly distributed $cos(\theta)$ is not since it is not a linear function. The $cos(\theta)$ distribution has a higher density at its minimum and maximum (-1 and 1). Due to this the recoil energy distribution is not linearly distributed but has a S-shape like distribution.

Overall the effect due to the $\gamma$ decay will slightly alter the shape of the recoil spectrum of the $^{35}$Cl daughter nuclei as can be seen in Figure 1.6. Note that the recoil due to $\gamma$ decay mimics the existence of scalar currents (i.e. causes less counts to be observed in the high-energy part of the recoil spectrum and more in the low-energy part).
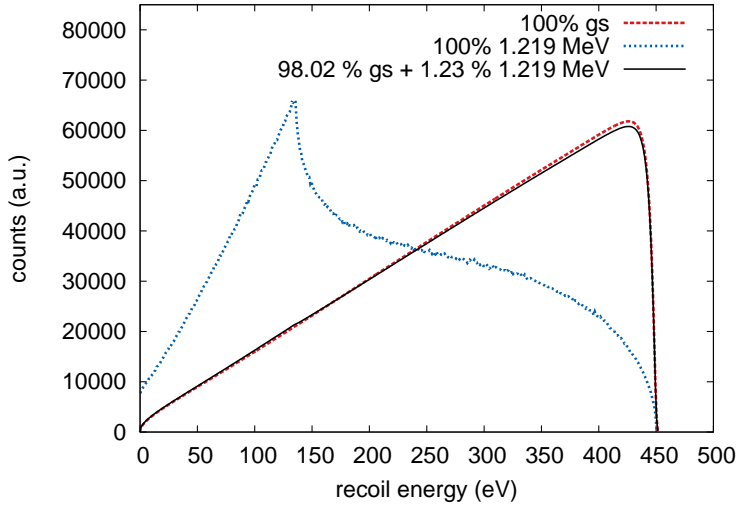
Figure 1.6: Due to the 1.23 % $\beta$-branching to the 1.219 MeV excited state in the $^{35}$Cl daughter nucleus, of $^{35}$Ar $\beta$ decay (Fig. 1.5), the shape of the recoil energy spectrum is slightly modified. For didactic purposes also the branch for 100 % decay to the $\gamma$ state is shown. In the latter case the nucleus first $\beta$ decays to the excited state with a maximum recoil energy of 271 eV, hereafter it undergoes $\gamma$ decay with an energy of 22.8 eV in a random direction.

## 1.4 Other beta neutrino measurements

The $\beta$-$\nu$ angular correlation has been addressed already by various experiments. There still is a high interest in such measurements to date. A handful of experiments are in the data taking phase and new experiments are being proposed. Table 1.3 lists an overview of the current state of the art measurements of $a$. Modern experiments almost all use ion traps (both Paul- and Penning traps) or atom traps (Magneto Optical Traps; MOT). The main difference between both types of traps is that ion traps can trap any charged particle, while MOT traps rely on the availability and technical feasibility of excitation schemes for the trapped atoms. Both particle traps, however, have become a standard tool to measure, among other correlations, the $\beta$-$\nu$ angular correlation.

### 1.4.1 Past experiments

The determination of $a$ in the pure Gamow-Teller decay of $^{6}$He [Johnson et al., 1963] probably still stands as one of the most successful experiments in the field.

In this experiment the radioactive $^6$He nuclei where taken from a reactor, using the reaction $^9$Be(n,$\alpha$)$^6$He. Subsequently, the recoil energy was measured by an electromagnetic $\frac{m}{q}$ analyzer. Even today, almost 50 years later, their result $a$=-0.3308(30) puts the most stringed limits on the Tensor coupling constants.

Another interesting technique is measuring the energy Doppler broadening of the energy of a delayed proton or $\gamma$ after $\beta$ decay, which depends on the kinetic energy of the recoiling nucleus. Such measurement was performed at ISOLDE for the superallowed $0^+ \rightarrow 0^+$ decay of $^{32}$Ar, implanted in a carbon foil. By measuring the broadening of the energy of the proton, the $\beta$-$\nu$ angular correlation coefficient was determined to be $a$=0.9989(65) [Adelberger et al., 1999]. Due to an improvement in the measurement of the Q-value for the $^{32}$Ar decay this value was later changed to $a$=1.0050(52) [Blaum et al., 2003].

## 1.4.2 Current experiments other than WITCH

With the development of particle traps a series of new experiments entered the field. One of these is the MOT trap experiment at Berkeley. This group first published a result of $a$=0.5243(91), in the $\beta$ decay of $^{21}$Na [Scielzo et al., 2004], a result that is three standard deviations off the Standard Model value of $a = 0.5587(27)$ [Severijns et al., 2008]. The reason for this turned out to be the formation of molecular sodium in the MOT trap, which influences the recoil energy distribution. After this effect was investigated thoroughly a new measurement yielded $a$=0.5502(60), in good agreement with the Standard Model value [Vetter et al., 2008]. The decay of $^{21}$Na is a mixed Fermi and Gamow-Teller decay, dominated by the Fermi contribution, so that this results provides mainly limits on a possible Scalar type weak interaction.

However, the best limit on Scalar currents to date stems from a measurement on $^{38m}$K with the TRINAT MOT trap at TRIUMF, yielding $\tilde{a} = 0.9981(30)^{(32)}_{(37)}$ [Gorelov et al., 2005]. Here the recoil ions, and their TOF, were detected in coincidence with the $\beta$ particles, which allows a reconstruction of each event.

Such a coincidence measurement is also used by the LPC trap experiment at GANIL, CAEN [Rodríguez et al., 2006]. The main difference is the use of a Paul trap as scattering-free source of the ions, making it the first experiment that uses an ion trap to determine the beta-neutrino angular correlation [Fléchard et al., 2008]. Recently the result of a measurement on the pure Gamow-Teller $\beta$ decay of $^6$He has been published, yielding in $a = -0.3335(73)$ [Fléchard et al., 2011], i.e. in good agreement with the SM value. A new campaign has started in collaboration with the WITCH team, to perform a measurement on $a$ in the $\beta^+$ decay of $^{35}$Ar with the LPC trap setup. A first experiment on this nucleus, in June 2011, yielded

enough data for a statistical precision on $a$ below 2% [Couratin, 2012]. Due to the TOF technique it was also possible to separate the different charge states after the decay and thus obtain the charge state distribution of the $^{35}$Cl daughter ions after the $\beta$ decay. This distribution is imperative for a precise determination of the $\beta$-$\nu$ angular correlation with the WITCH experiment at ISOLDE and is being used in the data analysis there (see Chapter 5).

The aSPECT setup [Glück et al., 2005] uses cold neutrons produced at ILL, Grenoble, to measure the $\beta$-$\nu$ correlation in free-neutron decay. Similar to the WITCH setup a retardation spectrometer is used to probe the energy of the recoiling protons, see section 2.4. The first published result of the aSPECT collaboration yields $a = -0.1151(40)$, with the error being purely statistical [Baeßler et al., 2008]. Systematic errors are currently being investigated in detail. The largest contribution to this being the half-life of the neutron, which thus limits the accuracy on $a$.

Almost all of the above experiments are planning more precise measurements. For example with the TRINAT setup a new measurement is planned on $^{38m}$K aiming at improving the previous result by a factor of 2 to 3 which would reduce the uncertainty on $a$ from 0.4% to 0.18%. Similarly the LPC trap group has already obtained data from the $\beta$ decay of $^6$He with about 20 times more statistics, allowing a final error below 1%. Also, a more precise determination of $a$ on $^{35}$Ar with LCP trap is proposed.

Table 1.3: List of most relevant $a$-parameter measurements for Scalar and Tensor current searches. The quoted errors are 68%CL.

| isotope | S or T | $a_{exp}$ | source | measurement technique | reference |
|---|---|---|---|---|---|
| $^6$He | T | $-0.3308(30)$ | gas | recoil energy spectrum | [Johnson et al., 1963] |
| $^6$He | T | $-0.3335(73)$ | Paul | $\beta$-recoil coincidences | [Fléchard et al., 2011] |
| $n$ | S/T | $-0.1151(40)$ | $n$-beam | recoil energy spectrum | [Baeßler et al., 2008] |
| $^{38m}$K | S | $0.9981(30)^{(32)}_{(37)}$ | MOT | $\beta^+$ delayed $\gamma$ shift | [Gorelov et al., 2005] |
| $^{21}$Na | S | $0.5502(60)$ | MOT | $\beta$-recoil coincidences | [Vetter et al., 2008] |
| $^{32}$Ar | S | $1.0050(52)$ | C-foil | $\beta^+$ delayed $p$ broadening | [Blaum et al., 2003] |
| $^{35}$Ar | S | $1.12(33)$ | Penning | recoil energy spectrum | see Chapter 5 |

# Chapter 2

# The WITCH Setup

Since the WITCH experiment is a precision experiment all parts of the setup have to be well understood and fine-tuned with respect to each other. Since radioactive beam time is precious, an off-line source was installed to get a better handle and feel of the experiment. This surface ionization ion-source works in combination with a small ( $\approx$ 10 cm long) **R**adio **F**requency **Q**uadrupole (RFQ), to extract a pulsed beam for testing purposes. For a detailed discussion of this off line ion-source and RFQ, see Ref [Tandecki, 2011; Traykov et al., 2011].

When an online experiment is performed, the 30 keV continuous beam from ISOLDE is first being captured and transformed into bunches by the REXTRAP setup, a buffer gas filled Penning Trap, that is typically operated with a frequency of around 1 Hz[1]. This bunched beam is then delivered to the **H**orizontal **B**eamline (HBL) of WITCH, which guides the ions to the **V**ertical **B**eamline (VBL). There the ions are being pulsed down from 30keV to ground potential in the **P**ulsed **D**rift **T**ube (PDT) section, which overcomes the use of High Voltage platforms. Next, the ion bunches are injected into and prepared (i.e. mass-separated and cooled via buffer-gas collisions) in the first Penning trap or Cooler Trap. Thereafter, the ions are transferred into the Decay Trap (also a Penning Trap), which acts as a scattering-free source for WITCH. The ions can decay in there and their recoil energy is then probed with a combination of the spectrometer electrodes and a **M**icro **C**hannel **P**late detector (MCP). By varying the applied voltage barrier on the spectrometer electrodes and counting the amount of ions which pass the barrier, an (integral) recoil energy spectrum can be obtained. This is the basic operation of the WITCH experiment.

---

[1]REXTRAP is also used to deliver beams to other experiments like Miniball. In these experiments the operation frequency is of the order of 50 Hz.

## 2.1 Creating and delivering a radioactive beam to WITCH

### 2.1.1 CERN

In 1954, twelve Western European countries united to build a place for nuclear research; CERN or 'Conseil European pour la Recherche Nuclaire'. CERN was and still is the biggest laboratory for nuclear and particle physics research in Europe and has made major contributions to Science and Computer Science over the years. For example the discovery of $W^+$, $W^-$ and $Z^0$ bosons in the UA1 and UA2 experiments in 1983 [Rubbia, 1984], for which C. Rubbia and S. Van Der Meer received the Nobel Prize in Physics. Another major contribution from CERN in a different field was the Word Wide Web. Initially based on hypertext and developed to make it easier for researchers to share knowledge, WWW was made available to the public in 1993, and has grown ever since. Recently CERN is also the major leader in *grid computing*, which combines computer resources worldwide to reach a common goal.
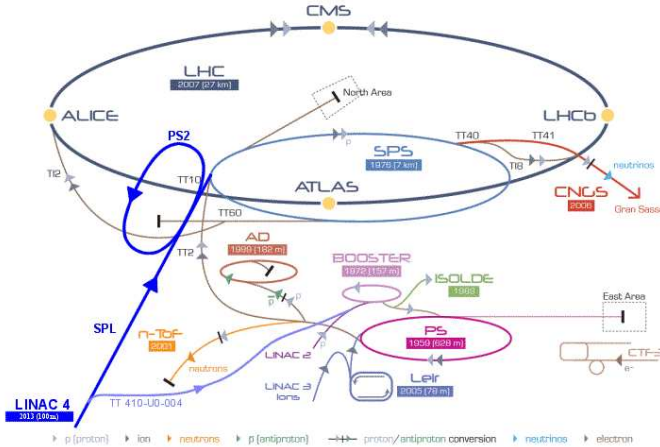


Figure 2.1: An overview of the CERN accelerators and main experimental facilities.

However, the main goal of CERN has always been nuclear and particle physics research. For this, CERN combines multiple accelerators and experimental halls, see figure 2.1. Protons (or heavy ions) are first created in a **LIN**ear **AC**celerator (LINAC) with an energy of 50 MeV and then transferred to the PS Booster accelerator (PSB). The PSB increases the energy of the protons from the LINAC to 1.4 GeV before they are transferred towards the ISOLDE experimental hall, or

to the next accelerator, the Proton Synchrotron (PS). Each next accelerator will increase the particle energy further.

Protons accelerated to 28 GeV from the PS are, e.g., shot onto a target in the AD hall to create an antiproton beam. This beam is used by various experiments like ALPHA, ASACUSA, ATRAP and AEGIS which all try to make antihydrogen and study its properties. Recently, in May 2011, antihydrogen atoms where trapped for up to 1000 seconds by the ALPHA collaboration, thereby opening up the possibility for performing precision atomic spectroscopy on antihydrogen atoms [Reich, 2010].

Aside from transferring the beam to the AD, the PS can also deliver the beam to the Super Proton Synchrotron (SPS). This accelerates the beam to 450 GeV and can transfer it to the CNGS experimental hall. In the CNGS hall, a neutrino beam is created and shot under the Alps towards the Gran Sasso laboratory, Italy, where the neutrinos are detected and one tries to observe neutrino oscillations fractions [Elsener et al., 1998].

The SPS can also inject the beam in two directions in the **L**arge **H**adron **C**ollider or LHC, which is worldwide the largest collider to date with 27 km circumference. It is CERN's and worlds most famous collider and represents a large-scale, worldwide scientific cooperation project. The LHC smashes the counter-rotating protons, each with 3.5 TeV energy, onto each other to create 7 TeV events[2]. Due to this high energy the protons will break up and reveal their *building blocks*. These collisions are happening inside the ATLAS, CMS, LHCb and ALICE detectors and are used to probe various predictions of the Standard Model and extensions of it, including the existence of the highly anticipated Higgs Boson [Higgs, 1966].

## 2.1.2   ISOLDE

The ISOLDE (**I**otope **S**eparator **O**n**L**ine **DE**vice [Kugler, 2000]) facility, see Figure 2.2, receives protons with a time separation of 1.2 s from the PSB with a 1.4 GeV energy and an average intensity up to 2 $\mu$A. These protons impinge on a thick target to create a mixture of elements via spallation, fission, or fragmentation reactions [Hoff, 1993]. A radioactive beam is extracted from the target by ionizing the nuclides in this mixture via surface ionization, electron impact in a plasma, or laser ionization [Fedosseev et al., 2008]. Over the years ISOLDE has developed many different target-ion-source combinations, allowing the users to study radioisotopes from more than 60 different elements, ranging from $^{6}_{2}$He to $^{232}_{88}$Ra and with intensities ranging up to $10^{11}$ atoms per $\mu$A proton beam.

---

[2]In 2013, the whole accelerator will be stopped for 20 months for maintenance and an energy upgrade aiming for 14TeV collisions.
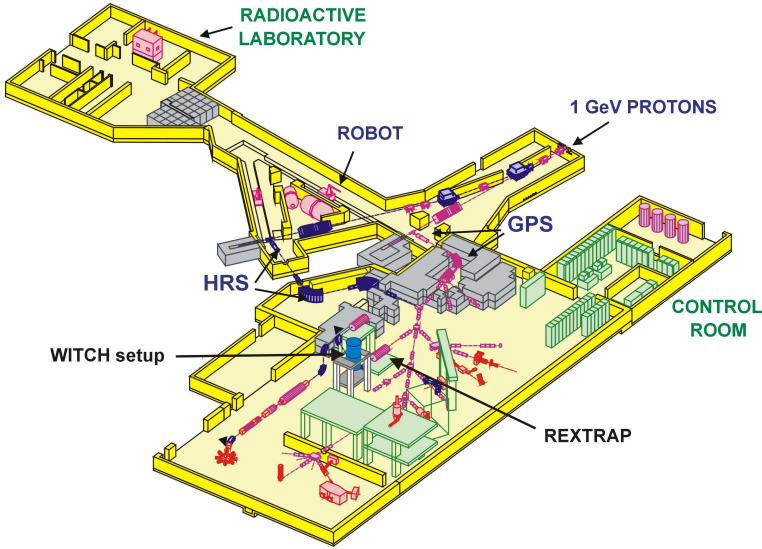
Figure 2.2: Overview of the ISOLDE experimental hall. Shown are the two separators (GPS and HRS) and the WITCH setup, which is coupled to REXTRAP.

These radioactive beams are then transferred at 30 kV or up to 60 kV from the target area to the user experiments through use of two mass separators, the High Resolution Separator (HRS), or the General Purpose Separator (GPS). The GPS has a mass selectivity $\Delta m/m \approx 1000$ and can deliver beam to three experiments simultaneously, while the HRS has $\Delta m/m = 5000$ but can serve only one user at a time. An experiment scheduled on the HRS can opt to use the ISCOOL, which is an RFQ cooler and buncher that reduces the emittance of the beam from $30\pi \cdot mm \cdot mrad$ to $3\pi \cdot mm \cdot mrad$ [Mane et al., 2009]. For masses with A=40, 25% is lost in transmission through this RFQ [Frånberg et al., 2008][3]. Furthermore, a noble gas ion can be neutralized due to charge exchange on the gas in the RFQ, which is not ideal in the case of $^{35}$Ar, the prime physics candidate for WITCH. Thus if the high mass selectivity and improved emittance are not needed, the use of GPS is preferred for an experiment on $^{35}$Ar with the WITCH setup.

After the separators, the beam is sent to the users. REXTRAP (see following section) is used by WITCH or by experiments using the REX post-accelerator to transform the continuous ISOLDE beam into bunches.

_____

[3]If the buffer gas is turned off in the RFQ, the transmission is only 30 % due to the narrow injection and ejection bore of the RFQ and the divergent beam from the ion source [Herlert, 2010].
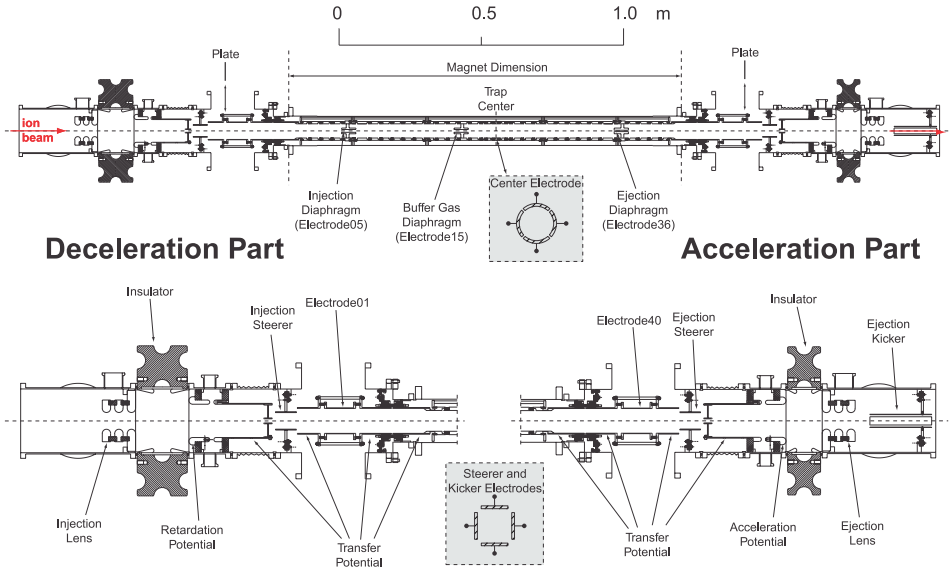
Figure 2.3: Overview of the mechanical structure of the REXTRAP electrodes and beamline.

## 2.1.3 REXTRAP

REXTRAP is a large Penning trap, used for radioactive isotope beam manipulation [Ames et al., 2005]. It is the first element of beam preparation for WITCH and the REX-ISOLDE post-acceleration section. It accepts the continuous ISOLDE beam and cools the ions via buffer gas collisions while they travel through it.

The REXTRAP setup combines a 2.975 T superconducting magnet with a 1.3 m long electrode structure to trap the ions, which is shown in Figure 2.3. Both the deceleration and the acceleration part are symmetric with respect to the centre of the trap. They consist mainly of lenses and steering elements to manipulate the injection and ejection of the ion beam. Except for the kicker and steerer elements all electrodes are cylindrically shaped. The trap structure itself consists of about 30 electrodes with an inner diameter of 40 mm. The central ring electrode is split into eight parts to be able to apply different excitations.

By applying different voltages to the different trap electrodes, a guiding trap potential in the axial direction can be realized, see Figure 2.4. The ions can be ejected from the trap by switching the potential barrier at the exit of the trap. Between the Electrode01 and the transfer potential as well as between Electrode40 and the transfer potential, plates (injection plate and ejection plate, respectively) can be inserted via pneumatic feedthroughs (see Fig. 2.3). These plates allow one

| Name | $^{35}$Ar run (June 2011)(V) | $^{35}$Ar (November 2011)(V) |
|---|---|---|
| XBTS.HT-EINZEL | N/A | 18200 |
| XBTS.KI10A | N/A | 44 |
| XRA0.QP20 | 860 | 1031 |
| XRA0.QP30 | 1510 | 1574 |
| XRA0.QS40 (X,Y) | 1300(-30,0) | 1336 (20,-21) |
| XTRAP.KI-INJ (X,Y) | 430 (0,-10) | 422 (20,36) |
| XTRAP.LENS-INJ | -700 | -700 |
| XTRAP.RET-POT | -4300 | -4400 |
| XTRAP.ST-INJ (H,V) | -1200 (0,-15) | -1364 (41,0) |
| XTRAP.TRANS-POT | -1200 | -1250 |
| XTRAP.ELEC01 | -110/100 | -100/100 |
| XTRAP.ELEC02 | -1650 | -1650 |
| XTRAP.ELEC03 | -500 | -500 |
| XTRAP.ELEC05A-B | 175/0 | 160/0 |
| XTRAP.ELEC16 | 80 | 80 |
| XTRAP.ELEC17 | 42 / 42 | 42 /42 |
| XTRAP.ELEC18 | 14/24 | 1 |
| XTRAP.ELEC24 | 14/-14 | 14/-14 |
| XTRAP.ELEC26 | 42/-30 | 42/-30 |
| XTRAP.ELEC27 | 80/-50 | 80/-50 |
| XTRAP.ELEC28 | 90/-70 | 90/-70 |
| XTRAP.ELEC29 | 100/-90 | 100/-90 |
| XTRAP.ELEC32 | 125/-135 | 125/-135 |
| XTRAP.ELEC33 | 195/-170 | 195/-170 |
| XTRAP.ELEC36 | 230/-220 | 230/-220 |
| XTRAP.ELEC37 | -500 | -500 |
| XTRAP.ELEC38 | -950 | -950 |
| XTRAP.ELEC39 | -1900 | -1900 |
| XTRAP.ELEC40 | -4300 | -4300 |
| XTRAP.ST-EJC. (X,Y) | -1400 (0,0) | -1371 (-17,-6) |
| XTRAP.ACC-POT | -6000 | -6000 |
| XTRAP.ACC-POT | 100 | 100 |
| XTRAP.LENS-EJC (X,Y) | -610 (-40,60) | 0(0,23) |

Table 2.1: Overview of all beam components of REXTRAP. Settings are given for the WITCH experiments in June 2011 (110618_0540_36Ar_Kl10A_52V.cvs) and in November 2011 (111109_0725_GPS_35Ar_retuned_Fred). A few trap electrodes change values for injection and ejection, their value is given as $injection(V)/ejection(V)$. For steerers the bias voltage is given together with (in brackets) the offset in both directions.

## Electrode Structure
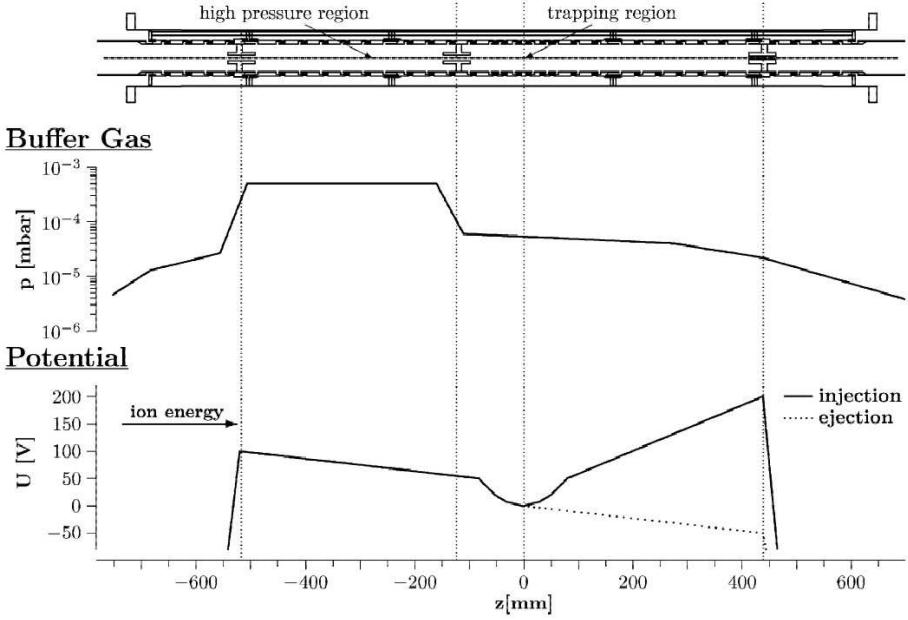


Figure 2.4: REXTRAP set-up: the trap electrode structure, buffer gas distribution and potential along the trap axis are shown (from [Ames et al., 2005]).

to measure the beam current in the corresponding regions of REXTRAP.

The first section of REXTRAP has a high neon buffer gas pressure of $10^{-3}$ mbar which causes ions to lose enough energy via collisions to be trapped in the potential minimum in the second part of the trap, Figure 2.4. In this section of the trap, with a buffer gas pressure of $3.2 \cdot 10^{-4}$ mbar, *rotating wall* or *sideband excitation* (see section 3.4) can be applied [Ames et al., 2005]. A more recent investigation of mass separation and space-charge effects in REXTRAP is described in Ref. [Gustafsson et al., 2011]. Table 2.2 shows the characteristic REXTRAP parameter values that can be compared with the WITCH Penning trap parameters as given in Table 3.1.

After the ions are cooled down, REXTRAP either sends bunches to REX-ISOLDE at 50 Hz, or to the WITCH experiment, with a 1 Hz frequency. The injection voltages were optimized to match the WITCH PDT acceptance [Coeck, 2007].

For beam testing of REX-ISOLDE or WITCH an off-line surface ion source is installed in front of REXTRAP. This ion source can deliver beams consisting of $^{39}$K, $^{41}$K, $^{133}$Cs, $^{85}$Rb or $^{87}$Rb ions.

| Parameter | Value | Unit |
|-----------|-------|------|
| B | 2.975 | T |
| $D = \frac{U_0}{d^2}$ | $3.5 \cdot 10^4$ | $\frac{V}{m^2}$ |
| $P_{buffergas}$ | $3.2 \cdot 10^{-4}$ | mbar |
| Buffer gas | Argon of Neon | |
| Total length | 0.9 | m |
| Capacity | $< 10^8$ | ions [Ames et al., 2005] |
| Efficiency | $> 40$ | % |

Table 2.2: REXTRAP Penning Trap characteristic parameters.

| Abbreviation | Function |
|--------------|----------|
| HB | Horizontal beamline |
| VB | Vertical beamline |
| KICK | Kickers |
| BEND | Benders |
| STEE | Steerers |
| EINZ | Einzellens |
| RETA | Retardation electrode |
| PDT | Pulsed drift tube |
| DRIF | Drift electrode |
| MCPD | MCP detector |
| FCUP | Faraday cup detector |
| DIAP | Diaphragm |
| IONS | Off-line ion source |

Table 2.3: Beam electrodes and diagnostics naming conventions, as used in figures 2.5 and 2.6.

## 2.2   Beamline

The purpose of the WITCH beamline is solely to transport the ion bunches from REXTRAP into the first WITCH Penning trap. To this end the beamline is divided into two sections, the horizontal beamline (HBL) and the vertical beamline (VBL). It is further possible to insert a bender in the middle of the HBL to take ions from the WITCH ion source and RFQ combination instead of ions coming from REXTRAP [Tandecki, 2011]. The WITCH setup has in total: 6 sets of steerer electrodes, 2 kickers (and benders), 15 electrodes and 3 einzel-lenses. Table 2.3 shows the abbreviations of the electrode names.
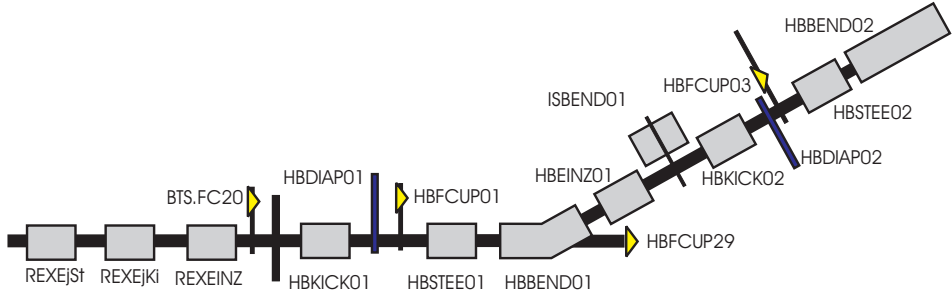
Figure 2.5: Overview of the electrode layout in the horizontal beamline using the naming conventions of table 2.3. The REXTRAP Ejection Steerers/Kickers (REXEjSt and REXEjKi), Einzellens (REXEINZ) and last Faraday cup (BTS.FC20) are also shown.

## 2.2.1  HBL

After the beam is cooled down and transformed into bunches by REXTRAP it is guided to the horizontal beamline (HBL) of WITCH. The HBL transports the beam without noticeable losses to the VBL. Figure 2.5, gives an overview of the HBL electrode system and table 2.4 summarizes the applied voltages on these electrodes. The main challenge is to steer the beam efficiently trough the 29° and 90° kicker-bender electrodes. To this end steerer plates are used to correct the beam and an einzellens was installed to be able to better focus the beam before it enters the 90° bender.

A surface ionization source (a copy of the one used at REXTRAP), in combination with a small RFQ [Traykov et al., 2011] are fixed on top of the horizontal beamline This allows the creation and use of ion bunches in WITCH without the necessity to use REXTRAP. The ions from the RFQ are guided into the horizontal beamline by inserting an additional 90° bender (ISBEND01) in the system.
The first 29° kicker in the beamline is used as beamgate for WITCH. The entire HBL is one single vacuum section, and is typically at a pressure of $2 \cdot 10^{-8}$mbar.

## 2.2.2  VBL

Figure 2.6 gives an overview of the electrodes in the vertical beamline (VBL) of WITCH, while table 2.5 displays typical voltages used on these electrodes. The VBL contains mainly cylindrical electrodes[4] and steerers and can roughly be divided into two sections.

---

[4]Diameter=59.5 mm

| Name | Simulated Voltages ([Coeck, 2007]) (V) | $^{35}$Ar run (June 2011)(V) | $^{35}$Ar run (Nov. 2011)(V) |
|---|---|---|---|
| HBKICK01L | -1220 | -1240 | -1130 |
| HBKICK01R | 1220 | 1240 | 1130 |
| HBSTEE01U | 0 | 0 | 0 |
| HBSTEE01D | 0 | 0 | 0 |
| HBBEND01L | -2090 | -2090 | -2105 |
| HBBEND01R | 2090 | -2090 | 2105 |
| HBEINZ01 | 12900 | 10000 | 11200 |
| HBKICK02U | -1260 | -1150 | -1300 |
| HBKICK02D | 1260 | 1150 | 1300 |
| HBSTEE02L | 0 | 20 | -100 |
| HBSTEE02R | 0 | -20 | 100 |
| HBBEND02U | -2185 | -2186 | -2185 |
| HBBEND02D | 2185 | 2186 | 2185 |

Table 2.4: Overview of all beam components of the horizontal beamline. The first column shows the simulated values, while the second and third column list the values used during the June 2011 run (110620_0700_settings_last_hours.set) and November 2011 run (2011-11-10_2010.set), respectively. Note that during the November 2011 run the beam transport efficiency was improved by a factor 6, from 5% to around 30 %.

The Pulsed Drift Tube (PDT) is installed in the first section. This electrode shifts the potential energy of the ions down from 30kV to ground potential. The second part of the VBL consists of twelve drift electrodes to guide the ion bunch into the magnetic field.

## PDT

The *Pulsed Drift Tube* or PDT in the VBL lowers the energy of the arriving 30 keV ion bunches from REXTRAP to ground potential to make capture of these ions in the cooler Penning trap possible. While the ion cloud is traversing the PDT electrode (with a length of 69.3 cm and a typical time acceptance of 2.8 $\mu s$), the electrical potential of the electrode is switched down from 21 kV to -9 kV, leaving the ions with 9 keV kinetic energy. Further slowing down of the ions to an energy below 200 eV, is achieved by moving the ions over a slowly increasing electrical potential created by the retardation and drift electrodes (see Table 2.5 for typical values of these electrodes). Figure 2.7 illustrates the operation of the PDT.

For a detailed description of the working principle of the PDT, see Ref. [Coeck et al., 2007]. Recent improvements to the pulsed drift tube resistances (see
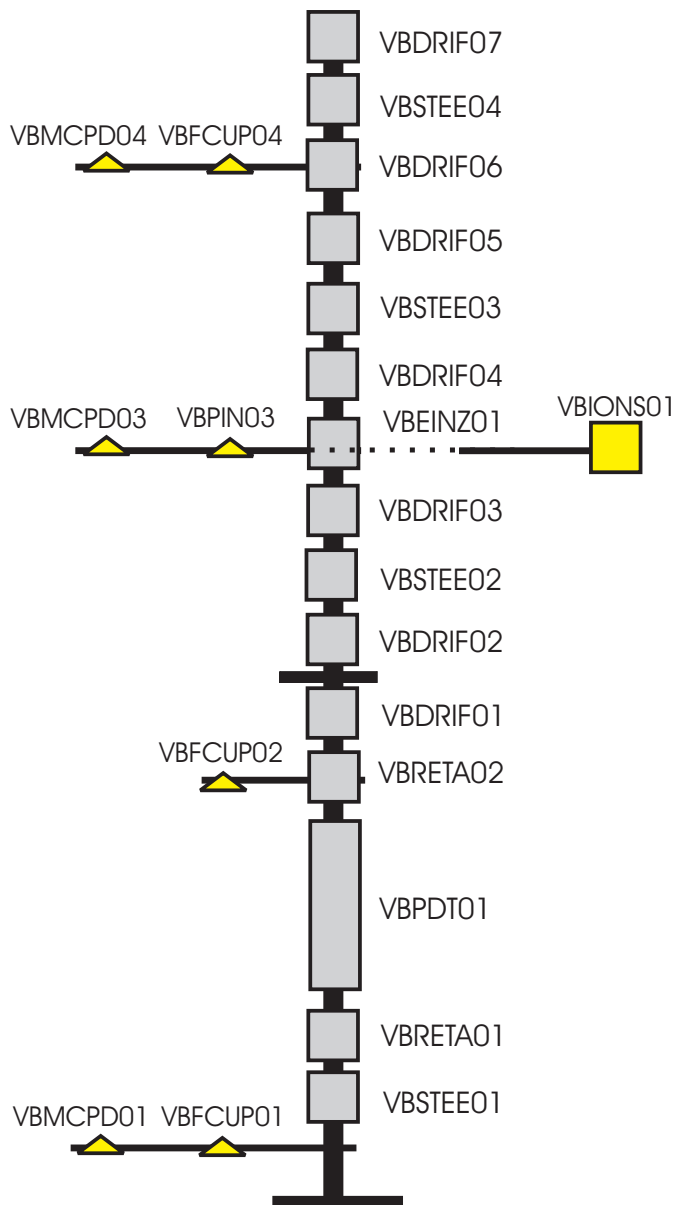
Figure 2.6: General overview of the electrodes and diagnostics in the vertical beamline following the naming conventions of table 2.3.

| Name | Simulated Voltages ([Coeck, 2007]) (V) | $^{35}$Ar run (June 2011)(V) | $^{35}$Ar run (Nov. 2011)(V) |
|---|---|---|---|
| VBSTEE01D | 0 | -35 | -150 |
| VBSTEE01U | 0 | -175 | 150 |
| VBSTEE01L | 0 | -250 | -300 |
| VBSTEE01R | 0 | 250 | 300 |
| VBRETA01 | 0 | 0 | 0 |
| VBPDT01P | 21000 | 21000 | 21000 |
| VBPDT01N | -9150 | -9000 | -9000 |
| VBRETA02 | -4200 | -4800 | -4800 |
| VBDRIF01 | -3900 | -4000 | -4000 |
| VBDRIF02 | -1900 | -2000 | -2000 |
| VBSTEE02D | -1900 | -1790 | -1765 |
| VBSTEE02U | -1900 | -1810 | -1835 |
| VBSTEE02L | -1900 | -1830 | -1830 |
| VBSTEE02R | -1890 | -1770 | -1770 |
| VBDRIF03 | -1900 | -1600 | -1800 |
| VBEINZ01 | -1200 | -1800 | -950 |
| VBDRIF04 | -1400 | -1400 | -1400 |
| VBSTEE03D | -1560 | -1200 | -1240 |
| VBSTEE03U | -1560 | -1200 | -1160 |
| VBSTEE03L | -1500 | -1210 | -1210 |
| VBSTEE03R | -1480 | -1190 | -1200 |
| VBDRIF05 | -1700 | -1000 | -1000 |
| VBDRIF06 | -1300 | -800 | -200 |
| VBSTEE04D | -380 | -815 | -390 |
| VBSTEE04U | -380 | -785 | -410 |
| VBSTEE04L | -380 | -805 | -380 |
| VBSTEE04R | -380 | -795 | -420 |
| VBDRIF07 | -300 | -600 | -400 |
| VBDRIF08-11 | -200 | -400 | -250 |
| VBDRIF12 | -0 | -250 | -250 |

Table 2.5: Overview of all beam components of the vertical beamline. The first column shows the simulated values, while in the second and third columns the values used during the June 2011 run (110620_0700_settings_last_hours.set) and November 2011 run (2011-11-10_2010.set), respectively, are listed. Note that during the November run the beam tuning was improved by a factor 6, from 5% to around 30 %.
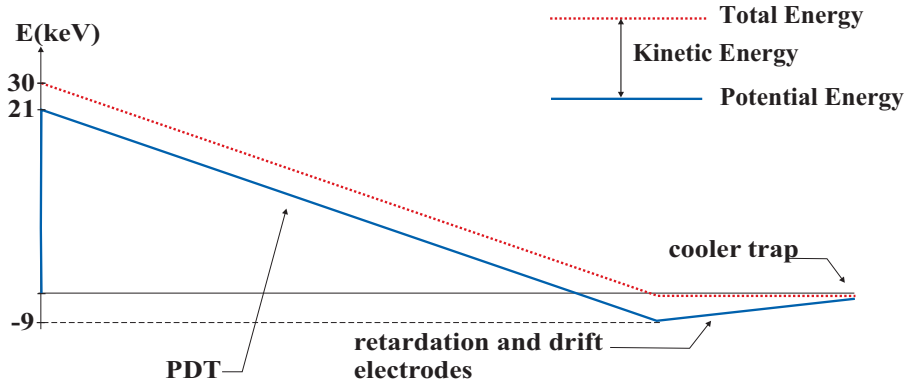
Figure 2.7: Influence of the PDT on the kinetic and potential energy of the ions. First the Pulsed Drift Tube is switched from 21 kv to - 9 kV, leaving the ions with a kinetic energy of 9 keV instead of 30 keV. The ions then move towards the cooler trap over an increasingly steeper electrical potential created by the retardation and drift electrodes (see Table 2.5 for typical values of these electrodes). Overall the ions have a typical energy between 0 and 200 eV when being captured in the cooler trap.

Ref. [Tandecki, 2011]) have enabled the operation of the PDT with a frequency of up to 10 Hz.

## 2.3   Traps

The WITCH setup contains two ion Penning traps. The first trap, or cooler trap, cools the ion bunches with helium buffer gas. If needed, separation of contaminating ion masses and centering of the beam is also possible in the cooler trap. The cooled ion cloud is then transferred to the second Penning trap, or decay trap. It is this trap that acts as the scattering-free source for the experiment. The radioactive ions are stored in here with a trapping potential up to a few volts until they undergo $\beta$ decay and can escape the trap. Since this section is the heart of the experiment I will elaborate on the Penning traps extensively in a separate section (Sec. 3).

## 2.4   Spectrometer

Unfortunately, a detector to directly measure the kinetic energy of (recoiling) ions with energies of up to a few 100 eV only does not exist. Therefore, the energy
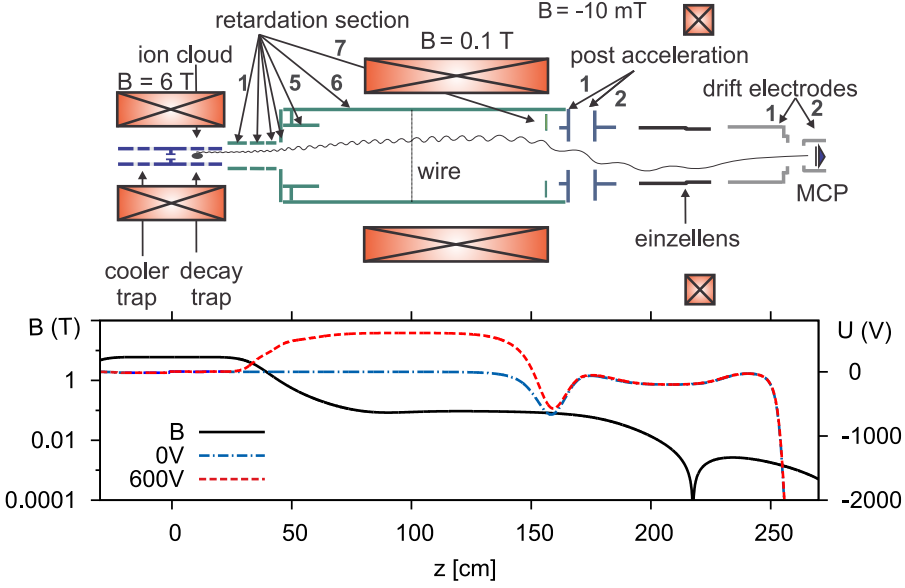
Figure 2.8: Schematic overview of the WITCH Penning traps, the spectrometer, the MCP detector and the magnetic and electrical fields. The change in electrical potential along the symmetry axis is shown for the cases without retardation voltage (dash-dotted line) and with 600 V retardation (dotted line). The different electrodes in the spectrometer, i.e. in the retardation section, acceleration section and drift section, are indicated by numbers. Typical values for the voltages applied on the spectrometer electrode are listed in Table 2.6
.

of the ions is probed with a special type of spectrometer, the so-called MAC-E filter [Lobashev & Spivak, 1985], see figure 2.8. A MAC-E filter consists of two (superconducting) solenoids, which are producing a magnetic guiding field. A recoiling ion escaping the decay trap after $\beta$ decay is guided on its cyclotron motion around the magnetic field lines into the spectrometer. On their way from the high magnetic field region in the decay trap $(B_1)$ to the low magnetic field in the center of the spectrometer $(B_2)$, the magnetic gradient force transforms most of the cyclotron energy into longitudinal motion. Due to the slow varying magnetic field $B$ the momentum transforms adiabatically, and therefore the magnetic moment $\mu$ stays constant

$$\mu = \frac{E_\perp}{B} = constant, \tag{2.1}$$

and thus:

$$\frac{B_1}{B_2} = \frac{E_{1\perp}}{E_{2\perp}} \tag{2.2}$$

When the recoil ions arrive in the so-called analysis plane, in the middle of the spectrometer, almost all radial motion has been converted into longitudinal motion, i.e. the longitudinal energy equals to good approximation the total energy of the recoiling ion. In this analysis plane an electric potential $U_0$ on the main electrode will then block all ions with charge $q$ with

$$E_{rec} - E_{2\perp} < qU_0 \tag{2.3}$$

and allow all other ions to pass on. Since the longitudinal fraction of the energy is limited to $E_2 \frac{B_1}{B_2}$ an ion can still overcome the potential barrier if

$$qU_0 \leq E_{rec} \leq qU_0 \left(1 + \frac{B_2}{B_1}\right). \tag{2.4}$$

The resolving power, $\Delta E$, of the spectrometer is thus given by

$$\frac{\Delta E}{E_{rec}} = \frac{B_2}{B_1} = 0.016. \tag{2.5}$$

For a strictly monochromatic energy line the spectrometer response function will show a step, the edge of which is smeared by an amount equal to spectrometer energy resolution $\Delta E$. The WITCH spectrometer is typically operated at 6 T and 0.1 T and thus has a resolution of $\Delta E = 7.5$ eV for a recoil energy of 452 eV (case of $^{35}$Ar).

Behind the retardation plane the recoil ions are pulled off the magnetic field lines by applying a high negative voltage, up to -8 kV in the so-called re-acceleration section. The ions are then focused onto the MCP detector by means of an einzel lens electrode and two drift electrodes.

## 2.4.1 Unwanted ionization

The combination of magnetic and electrical fields can also lead to unwanted trapping of positive and/or negatively charged particles in the system, which is an inherent challenge for MAC-E type spectrometers [Kraus et al., 2005; Baeßler et al., 2008]. These 'secondary' charges can stem from field emission of electrodes or from a high background pressure in the system. These charged particles can be accelerated towards an electrode and ionize rest gas on their path. This ionized gas can again be accelerated towards an electrode, thus triggering an avalanche effect of creation of charges. To circumvent this, the vacuum system, insulators,

| Name | Simulated Voltages ([Delauré, 1997]) (V) | $^{35}$Ar run (June 2011) (V) | $^{35}$Ar run (Oct. & Nov. 2011)(V) |
|---|---|---|---|
| SPDRIF01 | 0% | 0% | 0 % |
| SPDRIF02 | 30% | 40 % | 0 % |
| SPDRIF03 | 60% | 49 % | 0 % |
| SPDRIF04 | 80% | 82 % | 0 % |
| SPDRIF05 | 80% | 82 % | 0 % |
| SPDRIF06 | 100% | 100 % | 100 % |
| SPDRIF07 | 100% | 100 % | 100 % |
| SPACC01 | -2000 | 0 | -2000 |
| SPACC02 | -9000 | -1000 | -6000 |
| SPEINZ | -600 | -200 | -500 |
| SPDRIF01 | -9000 | 0 | -5000 |
| SPDRIF02 | -9000 | -6400 | -3230 |
| MCP | -9000 | -6400 | -3230 |

Table 2.6:    Overview of all electrodes in the spectrometer retardation section (SPRETA01-07), post acceleration section (SPACC01-2), einzel lens (SPEINZ) section, drift section (SPDRIF01-2) and the MCP detector. The first column shows the simulated, design, values, while in the second and third columns the values used during the June 2011 run and November 2011 run, respectively, are listed. Note that the voltages in the retardation section are given in percentage of the applied retardation barrier voltage. Positions of the different electrode sections are indicated in Fig. 2.8.

and electrodes of WITCH were modified and improved (i.e. sharp edges were removed and rounded and all electrodes were electropolished to obtain a more smooth surfaces) as is explained in detail in Ref. [Tandecki, 2011].

However, even in a high vacuum environment a charged particle can still be trapped along a magnetic field line and in an electric potential well, as is illustrated in Fig 2.9. Due to the endless moving back and forth of the particle along the magnetic field lines rest gas that is present in the setup can still be ionized. In the WITCH setup this was the case in the retardation section inside the spectrometer, and in the einzellens section.

Electrons can be stored in the spectrometer since a retardation potential for ions is a potential well for electrons. The stored electrons can ionize the helium buffer gas that is leaking trough from the cooler trap to the decay trap and these helium ions can end up on the detector to be counted as if they where recoil ions. Note that this is an energy dependent effect; when a higher retardation potential is applied, more electrons are trapped causing more helium atoms to be ionized leading to a higher count rate on the detector. An effective way to empty this trap was by
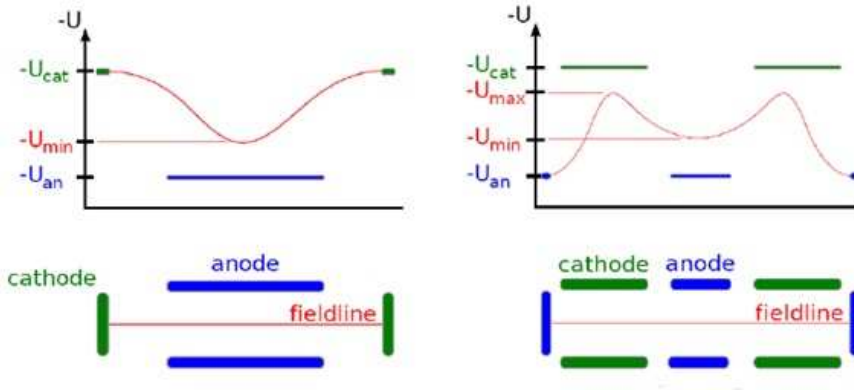
Figure 2.9: Possible configurations for the (unwanted) trapping of electrons. On the left a cathode-to-cathode trap, on, the right a vacuum-to-vacuum trap. The combination of the magnetic field line and an electric potential acts as a magnetic bottle effect, trapping the electron. Due to this infinite trapping the chance that the electron will ionize rest-gas molecules is finite even though a very low background pressure is present.

installing a wire in the analysis plane that picks up any electron that hits the wire. The wire was installed in the beginning of 2011 and proved to be a solid solution.

The second unwanted (Penning) trap, this time in the einzel lens section of the setup, was removed by installing a compensation magnet, with a field of $B=$-10 mT , in the einzel lens region. Without this compensation magnet it is impossible to reach the design voltages of 10kV on the neighboring electrodes of the einzellens (i.e. SPACC02 and SPRIF010. At -3 to 4 -kV the SPDRIF01 power supply trips when ramping up the electrodes. The reason for this is that SPACCE02, SPEINZ01 and SPDRIF01, along with the magnetic field in that region, form a Penning-like trap for electrons. Electrons thus spiral around the magnetic field-lines while bouncing back and forth between the high negative potentials on the MCP and in the post-acceleration section. These electrons can be created by field emission from the electrodes, and have a high probability to ionize rest gas in the system since they are trapped around the magnetic field lines, see ref [Tandecki, 2012, 2011] for more details. When combining the compensation magnet, which has a field of -10 mT in its center, with the magnetic fields of the 6 T and 0.1 T magnets, the magnetic field strength in the einzel lens region is reduced from $10\,\mathrm{mT}$ to $1 \cdot 10^{-5}$ T, thereby effectively emptying the unwanted Penning Trap.

## 2.5 MCP detector and Data Acquisition

Since WITCH has to detect low energy ions with high efficiency at high count-rate a Micro Channel Plate (MCP) detector was chosen for ion detection. This type of detector has an efficiency of around 50% for ions and can handle count rates of the order of 1 MHz. The whole MCP has $6 \cdot 10^6$ channels of which each has a deadtime of $\tau_c = R \cdot C = 32 \cdot 10^6 (\Omega) \cdot 213 \cdot 10^{-12} (F) = 6.8$ ms. The position information of the impinging particles can also be extracted from more advanced MCP designs. Although this is in principle not needed for the WITCH experiment valuable information can be extracted from this (see below).

A Roentdek DLD80 position sensitive MCP with an active diameter of 83 mm was chosen, similar as the one described in detail in [Liénard & et al., 2005]. This MCP consists of a 2000 Å thick conductive layer on top of bulk glass. The conductive layer is coated with a $SiO_2$ layer with 210 Å thickness.

The MCP has an open area ratio, and thus efficiency, of around 52.3(3)% [Liénard & et al., 2005]. In principle the efficiency also depends on the incident angle and energy, but due to the negative bias of -7 kV on the MCP, which causes impinging particles to accelerate and to be focused towards the MCP, these effects can be neglected. The theoretical position resolution that can be obtained with this detector is 110(26) $\mu$m [Liénard & et al., 2005]. However this still has to be studied in more detail for the WITCH detector.

Signals can be extracted from the MCP in two parallel branches as is explained in more detail in Ref. [Kozlov et al., 2008]. The fast branch counts the main MCP signal, used for counting, while the slower branch is used to extract the position and pulse height information. The pulse height distribution yields additional information of the incident particles since it is different for both ions and $\beta$'s (or dark counts which have a similar pulse height distribution as $\beta$ particles). The slow branch has a relatively high dead-time and should therefore not be used for precise analysis of the recoil energy spectrum. The main advantage of the slow branch is that it allows one to make cuts in time bin, position and pulse height, making it a valuable tool to better understand the setup. Also, this allows one to cross check for systematic effects (e.g. misalignment) and to compare the resulting position distribution at the MCP with the tracking simulations.

## 2.6 Experimental Cycle and timings

The timings for operating the WITCH setup can basically be cut in three parts, as is shown schematically in Figure 2.10. A first part deals with the beam transport, i.e. the beam gate and the PDT timings, guiding ions from REXTRAP into the WITCH Penning traps. A second part is dealing with the preparation of the
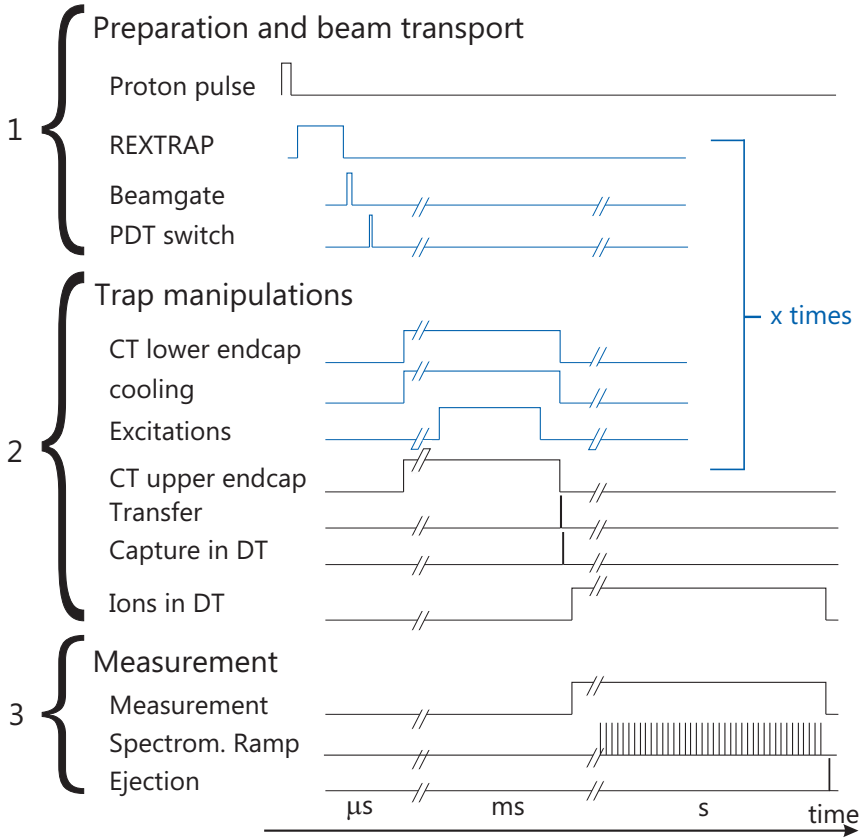
Figure 2.10: Overview of the experimental timing cycle of the WITCH setup. CT and DT represent the cooler- and decay-trap respectively. Stacking is possible by loading the cooler trap multiple times with bunches from REXTRAP.

ions in the cooler trap and their transfer to the decay trap. This step requires different timings due to the necessary cooling in a quadrupole potential and possibly excitations to center the ions. Finally, when the radioactive ions are stored and decay in the decay trap, the recoil energy distribution is probed by changing the voltage in the spectrometer at different times. When the measurement cycle is finished the ions are shot down from the decay trap and a new cycle is started. Note that due to the high repetition rate of the PDT, multiple loading (or *stacking*) of the cooler trap in one measurement cycle is possible, see following section.

Figure 2.11 shows the typical timings for different ion species in the WITCH beam line after the REXTRAP trigger. If the time $(t_1)$ for one ion species $(m_1)$ is known,
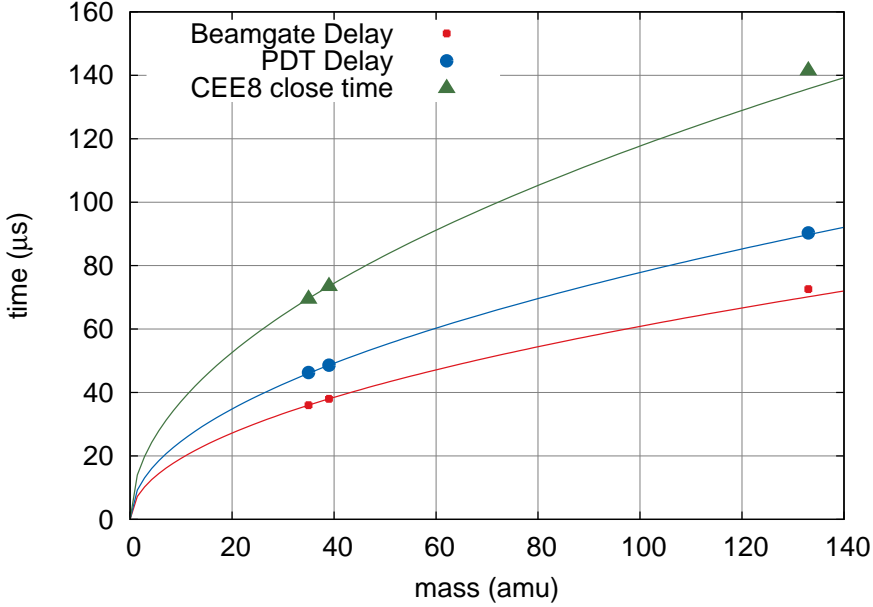
Figure 2.11: Experimentally determined timings for the beamgate delay, PDT delay and the rise time of the cooler trap upper endcap (CEE8) after the REXTRAP trigger. Timings were determined with $^{35}$Ar,$^{39}$K and $^{133}$Cs. Once a timing is known for a certain mass it is possible to estimate the timings for another mass with Eq 2.6 as is shown.

the timing ($t$) for another ion species ($m$) can be estimated from:

$$t = \sqrt{\frac{m}{m_1}} t_1.$$
(2.6)

## 2.7 Stacking

Stacking means multiple loading and subsequent cooling of ion bunches in the cooler trap before transferring the ions to the decay trap [Hasse et al., 1994]. This technique allows to increase the amount of ions in the trap in one measurement cycle by a factor 2 to 3.

Prior to using the stacking method, REXTRAP created one bunch of ions for WITCH from each PSB proton pulse on the target. In this scenario useful argon-ions are *thrown away*. The release curve of $^{35}$Ar from the target has a decay time

of 400 ms[5] while the charge exchange half-life in REXTRAP is of the order of 100 ms. Taking more ions from the target in REXTRAP would lead to large losses due to charge exchange. On the other hand, when a short cycle in REXTRAP is used, the majority of produced $^{35}$Ar ions is thrown away due to the long release time of the target; i.e. only a small fraction of the argon ions is captured.

The implemented stacking solution allows WITCH to fetch multiple argon-ion bunches from REXTRAP after each proton pulse impact on the target. Cooling of the ions in REXTRAP can be done in 100 ms, allowing for example for four 100 ms bunches to be extracted from REXTRAP for each proton pulse impinging on the target. In principle even more bunches can be extracted but at some point this is less efficient since the half-life of $^{35}$Ar is rather short (1.77 seconds). Also one has to keep in mind e.g. that time used for preparing the ions cannot be used to get statistics for the recoil energy spectrum, and that the typical cooling time in WITCH before the ions can be transfered to the decay trap is 200 to 300 ms.

The conditions of the experiment in November 2011 were mimicked with $^{39}$K from the REXTRAP surface ion source to test this stacking method. Results are shown in Figure 2.12. One can see that with more accumulations a higher intensity is indeed reached but also that the signal strength became more unstable and that sudden jumps in intensity occur more frequently. About four accumulations in one stacking period seems to be an optimal number to limit these instabilities.

## 2.8   Isotope selection

The choice of an isotope for an experiment is often a compromise between an interesting physics case and the technical limits imposed by the experiment and by ISOLDE.

Below follows a list of constraints on the isotope selection for WITCH:

- The production **yield** at ISOLDE should be sufficiently high. Since the WITCH experiment is looking for a tiny deviation in the recoil energy spectrum, more statistics translate directly into a higher chance to observe such a deviation (or to impose stringent limits on it). Preferably the production yield should be of the order of $10^{7-8}$ particles/s or higher.

- The **half-life** of the isotope should be between 0.5 and 3 seconds. If the half-life is too short, the majority of the ions would already decay during the preparation time in REXTRAP and in the cooler trap, which is in total

---

[5]This statement is valid for the new ISOLDE targets with a smaller grain-size as was used for the first time in the WITCH experiment in November 2011. Targets that were used earlier typically have a four times faster release time.
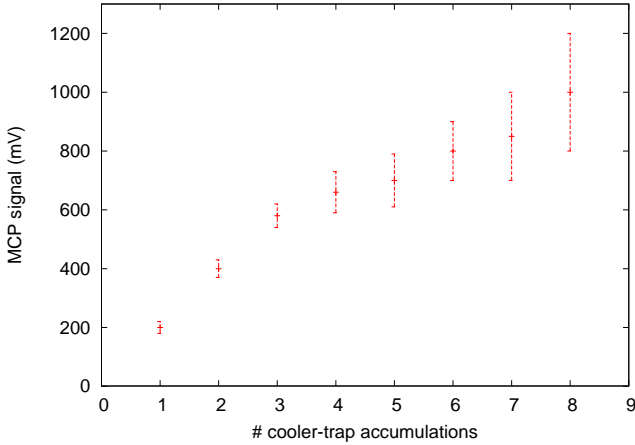
Figure 2.12: Resulting signal on the spectrometer MCP as a function of the number of accumulated bunches in the cooler trap. The error bars represent the maximum deviation of the observed signal intensity. During this measurement the MCP was set at -1900 V.

around 300 ms. A too long half-life on the other hand causes too few decays and thus a low amount of observed recoil ions.

- The isobaric and isomeric **contamination** in the ISOLDE beam should be minimal. In principle isobaric purification is possible either in REXTRAP or in the cooler trap. However, when more than about 1000 ions are present in a Penning trap Coulomb effects start to play a role and it is believed that this makes separation of different masses difficult as will be discussed later in section 6.4.1. Long-lived contaminants should be avoided since these can contaminate the system for a long time with their radioactivity.

- The **ionization potential** should preferentially be low, otherwise the ions can be neutralized very quickly in REXTRAP. For example, for argon the half-life in REXTRAP due to charge exchange is 72 ms [Tandecki, 2011]. Therefore noble gases should be avoided.

- A **stable daughter isotope** is strongly preferred. Otherwise, radioactive daughter isotopes will be implanted on the MCP detector and will create a false signal once they decay there.

- The **decay scheme** of the isotope should be very well known. Especially the branching ratios and the energy of levels de-exiting via $\gamma$ emission have to be known precisely, since these influence the shape of the recoil energy spectrum, see section 1.3.1.

- Preferably, the isotope should decay partly via **electron capture** (EC). The recoil energy distribution for EC decay is mono-energetic and at a higher energy compared to the recoil from $\beta$ decay. Measuring the energy resolution of the peak of the mono-energetic recoil ions from EC decay is a direct measurement of the response function of the spectrometer. However, such isotopes are not common since only isotopes with a low Q-value favor a large fraction of EC decays. In addition to a low Q-value, the half-live is in general also longer.

- Finally, the **decay mode** of the isotope should preferentially be via $\beta^-$ decay. After $\beta^-$ decay a $1^+$ ion becomes a $2^+$ ion, while after $\beta^+$ decay the $1^+$ ions become neutral and will thus be undetectable. Luckily some electrons are shaken off after $\beta$ decay because of the sudden change of charge in the nucleus, thereby producing $1^+$ and higher charge states. Still, in general about 60 to 80 % of the daughter nuclei will be neutral after $\beta^+$ decay.

From a physics point of view it is more favorable to look for scalar currents, since the equation for $a$ has an extra factor of $\frac{1}{3}$ in front for tensor currents, see Equation 1.11. In this respect, $0^+ \rightarrow 0^+$ super-allowed transitions are favorable since they undergo pure Fermi decay and have the right half-life for a measurement [Hardy & Towner, 2005]. Another interesting category of isotopes are the mirror transitions, in which the amount of protons and neutrons is mirrored in mother and daughter nuclei. These are mixed transitions, but their properties are well known and most mirror nuclei decay primarily via Fermi decay [Severijns et al., 2008]. A non-exhaustive list of possible isotope candidates is given in Table 2.8. In this list only $0^+ \rightarrow 0^+$ super-allowed transitions and mirror nuclei that have a high Fermi contribution in their $\beta$ decay ($|\rho|^2 < 0.1$) an for which 0.2 s$< t_{1/2} < 10$ s are shown.

From this list $^{35}$Ar has been selected as the prime candidate for the WITCH experiment to measure the $\beta$-$\nu$-angular correlation coefficient $a$, mostly due to its high production yield at ISOLDE, its well known and simple decay scheme and the fact that the Fermi/Gamow-Teller ratio for its $\beta$ decay is precisely known.

## 2.8.1 $^{35}$Ar

The shape of the recoil energy spectrum for $^{35}$Ar as well as the effect of decay to an excited state and a following gamma recoil was already discussed in section 1.3. Here we will deal with the CaO target to produce $^{35}$Ar at ISOLDE and with the charge state distribution of the $^{35}$Cl recoil ions resulting from the $\beta$ decay of $^{35}$Ar.

| M | state | $t_{1/2}$ (s) | yield (ions/$\mu C$) | D | state | $t_{1/2}$ (s) | $\Delta E$ (MeV) | $T_{R,max}$ (eV) | $P_{EC}$ % | BR % | $a_{SM}$ |
|---|---|---|---|---|---|---|---|---|---|---|---|
| $^{26}$Al | isom | 6.345 | $6.8 \cdot 10^4$ | $^{26}$Mg | gs | stable | 4.23255(17) | 280.7 | 0.082 | $> 99.997$ | 1 |
| | gs | $7.4\ 10^5$y | * | | exc | 476 fs | 2.20 | 53.2 | | 97.3 | |
| $^{34}$Cl | gs | 1.527 | $1.3 \cdot 10^3$ | $^{34}$S | gs | stable | 5.49178(20) | 387.9 | 0.080 | $> 99.988$ | 1 |
| | isom | 1920 | $2.2 \cdot 10^5$ | | exc | 325 fs | 3.511 | 138 | | 28.5 | |
| $^{38}$K | isom | 0.924 | $6.3 \cdot 10^6$ | $^{38}$Ar | gs | stable | 6.044440(11) | 429.1 | 0.085 | $> 99.998$ | 1 |
| | gs | 458 | $7.9 \cdot 10^7$ | | exc | 470 fs | 3.7456 | 144.2 | | 99.8 | |
| | | | | | gs | stable | 5.9131 | 408.9 | | $<0.6$ | |
| $^{42}$Sc | gs | 0.681 | * | $^{42}$Ca | gs | stable | 6.42563(38) | 444.2 | 0.099 | 99.9941(14) | 1 |
| | excit | 61.7 | $1.5 \cdot 10^3$ | | exc | 250 fs | 3.8528 | 139.5 | | 100 | |
| $^{46}$V | gs | 0.423 | 0 | $^{46}$Ti | gs | stable | 7.05071(89) | 496.6 | 0.101 | $99.9848^{+0.0013}_{-0.0042}$ | 1 |
| $^{50}$Mn | gs | 0.283 | $7.6 \cdot 10^5$ | $^{50}$Cr | gs | $1.8\ 10^{17}$y | 7.63243(23) | 542.3 | 0.107 | 99.9423(30) | 1 |
| | isom | 105 | * | | exc | 1.25 ps | 4.6983 | 185.6 | | 8.0 | |
| $^{33}$Cl | gs | 2.511 | $1.4 \cdot 10^2$ | $^{33}$S | gs | stable | 5.5826(4) | 414.5 | 0.074 | 98.45(14) | 0.887(3) |
| | | | | | exc | 1.17 ps | 4.742 | 287.1 | | 0.48 | |
| $^{35}$Ar | gs | 1.775 | $2.0 \cdot 10^8$ | $^{35}$Cl | gs | stable | 5.9661(7) | 452.6 | 0.072 | 98.36(7) | 0.9004(16) |
| | | | | | exc | 150 fs | 4.7458 | 271.3 | | 1.23 | |

Table 2.7: Table of interesting isotopes for a $\beta$-$\nu$-angular correlation coefficient measurement with the WITCH experiment as listed in [Coeck, 2007]. M and D represents respectively the mother and daughter nuclei. Only $0^+ \rightarrow 0^+$ super-allowed transitions [Hardy & Towner, 2005] and mirror nuclei [Severijns et al., 2008] that have a high Fermi contribution in their $\beta$ decay ($|\rho|^2 < 0.1$) and with $0.2s < t_{1/2} < 10s$ are included.
*No information available.

**Target and production yield**

Calcium oxide powder targets have successfully been used at ISOLDE to produce argon isotopes. Such targets outperform other targets, like MgO sintered powder or $TiO_x$ fibers. It was noted however that some CaO target units showed a low absolute yield from the beginning or a rapid decrease over time when irradiated with protons [Ravn et al., 1997]. Recently, it was found that the performance of the ISOLDE targets was related to their structure at nanometer scale [Stora, 2010; Fernandes, 2010]. The fast degradation and following drop of yield was found to be caused by sintering of the material due to the exposure to high temperatures and/or high proton intensities impinging on the target. Systematic studies of the synthesis conditions, the kinematics and the air-reactivity of the nanometric powder were performed to investigate the target nanostructural properties. From this it was concluded that a target with a smaller grain size and with a porosity of 47% (compared to 33% for the previously used CaO targets) would be beneficial. The new target was tested during the WITCH run in November 2011 and no sign of degradation was observed during its operation [Ramos, 2012; Ramos et al., 2011]. Furthermore the target showed an improved yield of around an order of magnitude to $2 \cdot 10^8$ ions/$\mu$C.
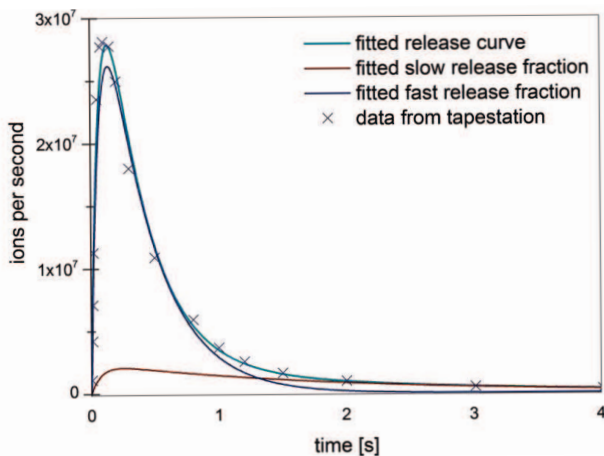


Figure 2.13: Release curve of $^{35}$Ar from the improved (nanostructured) CaO target. 95.4 % of the argon ions are released in the fast release curve which has a fitted time constant of 360 ms. Figure taken from [Gottberg, 2011].

| charge state | contribution (%) |
|:---|:---:|
| $1^+$ | 74.6(1.0) |
| $2^+$ | 17.3(4) |
| $3^+$ | 5.7(2) |
| $4^+$ | 1.7(2) |
| $5^+$ | $< 1$ |

Table 2.8: Charge state distribution of $^{35}$Cl daughter ions after the $^{35}$Ar decay. These charge states constitute together about 28(10)% of all recoils, the remainder being neutral. From [Couratin, 2012].

Figure 2.13 shows the release curve for the $^{35}$Ar$^+$ ions from the improved (nanostructured) CaO target. The release time follows the equation:

$$p(t) = \frac{1}{N} \cdot \left(1 - e^{-t/t_r}\right) \left(\alpha e^{-t/t_{\tau_1}} + (1 - \alpha) e^{-t/t_{\tau_2}}\right) \tag{2.7}$$

with $t_r$ the rise time (81 ms), $t_{\tau_1}$ the fast release time (360 ms) and $t_{\tau_2}$ the slow release time (1.8 s). In the case of this target the fast release yields $1.9 \cdot 10^8$ ions/$\mu$C (95.4 %) argon ions and the slow release $9.6 \cdot 10^6$ ions/$\mu$C (4.6 %) argon ions. The fast release time of 360 ms for this newer type of targets is slower than with the old targets (100 ms). Since the cooling in REXTRAP typically takes around 100 ms, use of the stacking technique is thus preferred with the new targets in order to increase the amount of collected statistics.

**Charge state distribution**

$^{35}$Ar$^+$ has the drawback that it is a $\beta^+$-emitter. After $\beta^+$ decay 72(10)% of the $^{35}$Cl daughter ions are neutral and are thus lost, while the remaining 28(10)% undergo electron shake-off thus providing charge states from $1^+$ up to $5^+$ [Couratin, 2012]. The exact charge state distribution and the ratio of neutral and charged particles after the $\beta^+$ of $^{35}$Ar was determined in a measurement performed with the LPC trap setup at GANIL [Couratin, 2012], as discussed in Section 1.4.2. The charge state distribution obtained is shown in Figure 2.14 and summarized in Table 2.8.
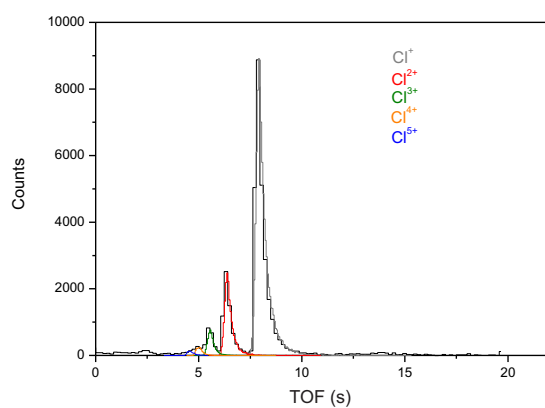
Figure 2.14: Charge state distribution of the daughter $^{35}$Cl ions after $\beta^+$ decay of $^{35}$Ar. Figure taken from [Couratin, 2011].

# Chapter 3

# Penning Traps

The WITCH decay Penning trap acts as the scattering-free source where the ions decay and are as such the heart of the experiment. In this chapter the general principle and the equations of motion of an ion in a Penning Trap will be described. Deviations from the single ion motion via imperfections in $B$- and $E$- field will be discussed as well as the influence of image charges. The influence of Coulomb interaction will be discussed in Chapter 6. Finally, an overview of possible excititation of the ion motion in a Penning Trap will be given at the end of this chapter.

## 3.1 Operating Principle

A Penning Trap is a three dimensional device to trap charged particles. To do so an electrostatic quadrupole potential $U$ confines the particles in axial direction while a strong static axial magnetic field confines them in radial direction. The corresponding magnetic and electric fields are:

$$\mathbf{B} = B \cdot \hat{\mathbf{e}}_z \tag{3.1}$$

$$\mathbf{E} = -\nabla U$$

$$= -\nabla \left( \frac{U_0}{d^2}(x^2 + y^2 - 2z^2) \right) = \frac{U_0}{d^2}(r^2 - 2z^2)$$

$$= -\frac{U_0}{2d^2}(x\hat{\mathbf{e}}_x + y\hat{\mathbf{e}}_y + z\hat{\mathbf{e}}_z), \tag{3.2}$$

| Parameter | Value |
|---|---|
| B | 6 T |
| length cooler trap | 25 cm |
| length decap trap | 20 cm |
| $dz_0$ | 4 cm |
| $r_0$ | 2 cm |
| $d$ | 3 cm |
| $D = \frac{U_0}{d^2}$ | $1.8 \cdot 10^4 \; \frac{V}{m^2}$ |
| $P_{buffergas}$ | $1 \cdot 10^{-4} - 1 \cdot 10^{-5}$ mbar |
| Buffer-gas | Helium |
| Capacity | $1 \cdot 10^{-7} - 1 \cdot 10^{-8}$ ions |
| Efficiency | $> 80 \; \%$ |

Table 3.1: Characteristic parameters of the WITCH Penning traps. Buffer gas is only present in the cooler trap.
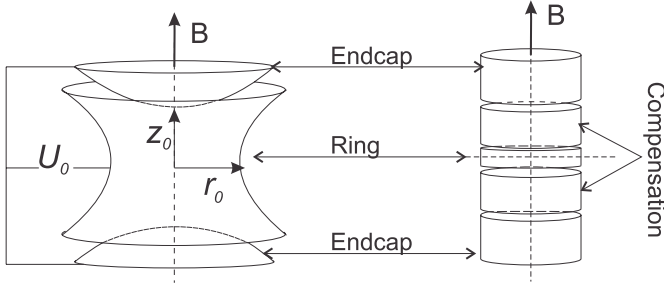


Figure 3.1: Hyperbolic trap (left) and a corresponding cylindrical trap (right). Correction electrodes are necessary for a cylindrical trap in order to obtain a quadrupole potential in the trap centre. Figure taken from [Mukherjee et al., 2008a].

with $U_0$ the potential between the ring- and endcap-electrodes of the trap and $d$ a characteristic Penning trap parameter

$$d = \sqrt{\frac{(z_0^2 + \frac{r_0^2}{2})}{2}}, \tag{3.3}$$

with $z_0$ the distance from the trap center to the end of the correction electrodes and $r_0$ the distance from the trap center to the side electrodes (see Fig. 3.1).

Since the quadrupole potential has a hyperbolic equipotential surface, the most natural way to make a Penning trap is by using hyperbolic electrodes (see Fig. 3.1 and Ref. [Gabrielse et al., 1989]). However, the quadrupole potential can also be

constructed from a set of cylindrical electrodes (see Fig. 3.1). In this case, however, the $d$ parameter does not have a useful meaning any more as being a characteristic parameter. For this type of Penning Traps $U_0/d^2$ is then used to characterize the potential well depth. Since any electrical field mismatch will result in a shift of the eigenmotion (see Section 3.2.2), a hyperbolic trap is used in very sensitive experiments, like e.g. for mass measurements [Mukherjee et al., 2008b]. For other applications cylindrical traps are usually used. These are easier to construct, allow easy access to the centre of the trap and the trapping potential can further be changed while particles are inside the trap. The voltages on a cylindrical Penning Trap can be tuned such that a quadrupole potential is approximated [Raimbault-Hartmann et al., 1997; Brown & Gabrielse, 1986].

## 3.2   A single particle in a Penning Trap

### 3.2.1   Motion of a single ion in a Penning Trap

If a particle with mass $m$, charge $q$ and velocity $\mathbf{v} = (v_x, v_y, v_z)$ moves in the Penning Trap, it will experience a force due to the electric and magnetic fields:

$$\mathbf{F} = q\mathbf{E} + q(\mathbf{v} \times \mathbf{B}) \tag{3.4}$$

With $\mathbf{F} = m\mathbf{a}$, the equations of motions can be written as

$$\ddot{\mathbf{r}} = \frac{q}{m}(\dot{\mathbf{r}} \times \mathbf{B} + \mathbf{E}). \tag{3.5}$$

Substituting equations 3.2 this results in

$$\begin{pmatrix} \ddot{x} \\ \ddot{y} \\ \ddot{z} \end{pmatrix} - \omega_c \begin{pmatrix} \dot{y} \\ -\dot{x} \\ 0 \end{pmatrix} - \frac{\omega_z^2}{2} \begin{pmatrix} x \\ y \\ -2z \end{pmatrix} = 0. \tag{3.6}$$

with the cyclotron frequency

$$\omega_c = \frac{qB}{m} \tag{3.7}$$

and the axial frequency

$$\omega_z = \sqrt{\frac{qU_0}{md^2}}. \tag{3.8}$$

Since the magnetic field is along the z-axis the z-component of the motion is a pure electrostatic motion, that does not depend on the magnetic field. Thus for the axial motion, equation 3.6 reduces to

$$\ddot{z} + \omega_z^2 z = 0 \Leftrightarrow z(t) = A_z cos(\omega_z t + \phi_z), \tag{3.9}$$

which is nothing more than a harmonic oscillation along the magnetic field axis. The x- and y-components of the motion are a combination of a dominant restraining force due to the magnetic field and a repulsive electrostatic force that tries to push the particle out of the trap in radial direction. The radial vector $\boldsymbol{\rho}$,

$$\boldsymbol{\rho} = \begin{pmatrix} x \\ y \\ 0 \end{pmatrix} \qquad (3.10)$$

is introduced to reduce equation 3.6 to

$$\ddot{\boldsymbol{\rho}} = \omega_c \dot{\boldsymbol{\rho}} \times \hat{\mathbf{e}}_z + \frac{1}{2}\omega_z^2 \boldsymbol{\rho}. \qquad (3.11)$$

For $\omega_z \to 0$, equation 3.11 reduces to a uniform circular motion around the magnetic field with frequency $\omega_c$. The extra term $\frac{1}{2}\omega_z^2\boldsymbol{\rho}$ comes from the repulsive electrostatic potential and introduces an extra centrifugal force that reduces the cyclotron motion frequency $\omega_c$ to $\omega_+$. The interplay of the magnetic field with the repulsive potential gives, in addition, rise to a much slower circular magnetron motion with frequency $\omega_-$. This magnetron motion is a slow orbital drift motion around the top of the radial potential hill.

To solve the radial part of the Penning trap equations of motions the variable

$$u = x + iy \qquad (3.12)$$

is introduced. Using $u$, Equation 3.6 can be transformed to

$$\ddot{u} + (i\omega_c)\dot{u} - 2\omega_z^2 u = 0, \qquad (3.13)$$

The general solution of this equation is given by

$$u(t) = R_+ e^{-i(\omega_+ t + \phi_+)} + R_- e^{-i(\omega_- t + \phi_-)}, \qquad (3.14)$$

with $\omega_-$ the magnetron and $\omega_+$ the reduced cyclotron frequency, defined as:

$$\omega_- = \frac{1}{2}\left(\omega_c - \sqrt{\omega_c^2 - 2\omega_z^2}\right). \qquad (3.15)$$

$$\omega_+ = \frac{1}{2}\left(\omega_c + \sqrt{\omega_c^2 - 2\omega_z^2}\right), \qquad (3.16)$$

and $R_{+(-)}$, $\phi_{+(-)}$ the radii and phases of the cyclotron (magnetron) motion, determined by the initial conditions[1]

───────────────

[1]The radial motion is often solved differently by introducing new variables which depend on $\rho \times \hat{\mathbf{e}}_z$. See Refs. [Brown & Gabrielse, 1986; Coeck, 2007] for details.

Transforming Equation (3.14) gives for x and y in Cartesian coordinates:

$$
\begin{aligned}
x(t) &= r_+ \cdot sin(\omega_+ t + \phi_+) - r_- \cdot sin(\omega_- t + \phi_-) \\
y(t) &= r_+ \cdot cos(\omega_+ t + \phi_+) - r_- \cdot cos(\omega_- t + \phi_-).
\end{aligned} \tag{3.17}
$$

which is the equation of an *epicycloid*. It describes a trajectory on a radius $r_-$ around the trap center, with the radius $r_+$ superimposed on $r_-$. The particle thus moves within a circular strip between the inner radius $|r_- - r_+|$ and the outer radius $r_- + r_+$.

The total radial motion of the particle thus consists of two independent motions: the magnetron motion with frequency $\omega_-$ and the cyclotron motion with frequency $\omega_+$. These motions are shown in Fig. 3.2, together with the harmonically oscillating axial motion.
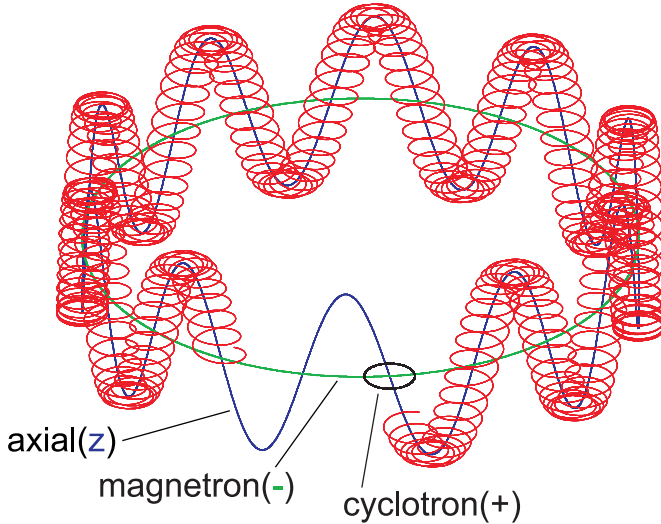


Figure 3.2: The ion motion in a Penning trap can be decoupled into three independent eigenmotions. The fast cyclotron motion ($\omega_+$), the slow magnetron motion ($\omega_-$) and the axial motion, which is an harmonic oscillation with frequency $\omega_z$.

The energy in the axial direction is continuously converting between kinetic and potential energy. While the cyclotron motion has almost solely kinetic energy and the magnetron motion almost only potential energy. Reducing the energy in these motions reduces their amplitude, except for the magnetron motion. Any dissipative process (e.g. buffer-gas collisions) that removes energy from the

| | $^{35}$Ar | $^{39}$K | $^{133}$Cs |
|---|---|---|---|
| $\nu_c$ (Hz) | $3.95151 \cdot 10^6$ | $3.54702 \cdot 10^6$ | $1.03988 \cdot 10^6$ |
| $\nu_+$ (Hz) | $3.95135 \cdot 10^6$ | $3.54686 \cdot 10^6$ | $1.03972 \cdot 10^6$ |
| $\nu_z$ (Hz) | $3.54655 \cdot 10^4$ | $3.36014 \cdot 10^4$ | $1.81935 \cdot 10^4$ |
| $\nu_-$ (Hz) | $1.59161 \cdot 10^2$ | $1.59162 \cdot 10^2$ | $1.59179 \cdot 10^2$ |

Table 3.2: Typical Penning Trap frequencies for $^{35}$Ar, $^{39}$K and $^{133}$Cs for the WITCH Penning trap characteristics as given in Table 3.1

magnetron motion increases the magnetron radius until the particle hits the electrode walls and is lost. Luckily this typically takes quite long, see Sec.3.3. In the case of the WITCH Penning traps with typical Penning trap parameters as given in Table 3.1 a centered $^{35}$Ar ion will be lost only after 8 minutes. More details about this time estimate can be found in section 3.3.

The following relations between the three characteristic frequencies in an ideal Penning trap can be deduced from equation 3.15:

$$\omega_+ + \omega_- = \omega_c \tag{3.18}$$

$$\omega_-^2 + \omega_+^2 + \omega_z^2 = \omega_c^2 \tag{3.19}$$

$$2 \cdot \omega_- \cdot \omega_+ = \omega_z^2. \tag{3.20}$$

With Eq.( 3.19) called the invarience theorem [Brown & Gabrielse, 1986]. The frequencies further obey the following relation

$$\omega_+ \gg \omega_z \gg \omega_-. \tag{3.21}$$

In first order the magnetron motion is independent of the mass of the particle

$$\omega_- \approx \frac{U_0}{2Bd^2}, \tag{3.22}$$

and

$$\omega_+ \approx \omega_c.$$

Typical WITCH Penning trap frequencies for $^{35}$Ar, $^{39}$K and $^{133}$Cs ions are listed in Table 3.2, given the parameters of the traps (as listed in Table 3.1). The $\nu_c$ and $\nu_+$ frequencies are of the order of MHz while $\nu_-$ is only a couple 100 Hz. The axial frequency $\nu_z$ has a value in between these frequencies and is typically of the order of 10 kHz.

Note that one can influence the axial length of an ion cloud by changing the trapping depth $U_0/d^2$. The axial cloud size can be made smaller by increasing the potential difference between the ring electrode and the endcap electrode, causing the trapped ions to move in a steeper potential and thus over a shorter distance. The radial length can be changed by varying the magnetic fields since the centrifugal force equals the force exerted by the magnetic field for these ions:

$$r = \frac{mv}{eB} \tag{3.23}$$

with $m$ the mass of the ion, $v$ its velocity, $e$ the electric charge and $r$ the radius. One can conclude that a higher magnetic field thus shrinks the ion cloud.

### 3.2.2 Deviations from the ideal motion

In this section deviations from the ideal motion of an ion in the WITCH Penning traps will be discussed. For one ion stored in a Penning trap the largest deviations from the ideal motion stem from mechanical imperfections. Image charges are not of importance for the WITCH experiment due to the low charge and small radii of the trapped ions. When multiple ions are stored in a Penning trap the single ion picture changes significantly and will therefore be discussed separately, see section 6.

**Electric field imperfections**

Ref. [Bollen et al., 1990] discusses in depth the effects of imperfections in the electrical field created by hyperbolic Penning trap electrodes. Analogously it is possible to define the electric field imperfections in the WITCH cylindrical Penning traps.

The electric field constructed by the a set of Penning trap electrodes can be expressed in spherical coordinates, $r, \theta, \varphi$,

$$\phi = \sum a_m \phi_{ln_{lm}} \tag{3.24}$$

with

$$\phi_{lm} = r^l P_l^m(cos\theta)cos(m\varphi) \tag{3.25}$$

and

$$a_m = \frac{U_0}{2z_0^m}C_m \tag{3.26}$$

where $P_l^m(cos\theta)$ is a Legendre polynome, $U_0$ the potential difference between ring- and endcap electrode, and $z_0$ the half axial length of the trap. Odd terms of $C_m$

do not contribute due to the cylindrical symmetry of a Penning trap. Furthermore for a cylindrical Penning trap the C coefficients can be calculated analytically as given in Eq. (9.27) in Ref. [Brown & Gabrielse, 1986]. These coefficients depend on the radius ($r_0$) and half axial length ($z_0$) of the trap, as well as on the length of the correction electrodes ($\Delta z_c$). For the WITCH Penning traps, with the typical parameters listed in Table 3.1, this results in:

$$C_2 = -1 \quad C_4 = 0.0028 \quad C_6 = 0.00042 \tag{3.27}$$

The quadrupole term is represented by $C_2$. Electrical imperfections stem from the octupole term ($C_4$) and result in a shift in all eigenfrequencies [Bollen et al., 1990]:

$$\Delta\omega_\pm = \pm \frac{3}{4} \frac{C_4}{z_0^2} \frac{\omega_z^2}{(\omega_+ - \omega_-)} (r_\pm^2 + 2r_\mp^2 - 2z^2), \tag{3.28}$$

$$\Delta\omega_z = \frac{3}{4} \frac{C_4}{z_0^2} \omega_z^2 (z^2 - 2r_+^2 + 2r_-^2), \tag{3.29}$$

$$\Delta\omega_c = \frac{3}{4} \frac{C_4}{z_0^2} \frac{\omega_z^2}{(\omega_+ - \omega_-)} (r_+^2 - r_-^2). \tag{3.30}$$

The cyclotron excitation frequency for a centered ion cloud with a half axial length $z_0$=2 mm, a magnetron radius of 1 mm and a cyclotron radius of 0.1 mm will shift -56 Hz due to electric field imperfections. The axial frequency of this cloud will shift only 0.08(or 0.4) Hz when the difference between the ring and endcap electrode voltages is 20(450) V.

Note that frequency shifts due to electric field imperfections grow quadratically with the distance from the ion to the trap centre ($z$ and $r_-$). For example, the same ion cloud but with a half axial length $z_0$=4 cm yields a shift of +64 Hz in axial frequency. Analogously, when the ion cloud is moving on a magnetron radius of 2 mm instead of 1 mm, the shift in the cyclotron frequency rises from -3 Hz to -12 Hz. For the WITCH setup, the exact value of the excitation frequencies is not of importance since the frequencies are tuned experimentally, thereby taken into account experimental imperfections that can shift the excitation frequencies.

Note that higher order dodecapole ($C_8$) imperfections do not significantly shift the frequencies in a cylindrical Penning trap (which is not true for a hyperbolic Penning trap [Bollen et al., 1990]). Finally, the open endcaps also perturb the electrical field by changing the value of $C_4$ by approximately 5% [Brown & Gabrielse, 1986].

**Magnetic field inhomogeneity**

The magnetic field, $B_0$, is not constant in the trap region but has a certain homogeneity which causes a shift in the cyclotron frequency $\omega_c$. Mass measurement

experiments measure precisely the cyclotron frequency to determine the mass of the species and thus require a high homogeneity. At WITCH this is not of such importance. The shift of the cyclotron frequency $\omega_c$ is given by

$$\frac{\Delta\omega_c}{\omega_c} = \beta_2(z^2 - r_-^2) \tag{3.31}$$

with $\beta_2$ the relative strength of the hexapole component of the magnetic field.

**Magnetic field tilt**

A tilt of the magnetic field axis with an angle $\theta$ with respect to the symmetry axis of the Penning trap will result in a shift of all three ion eigenfrequencies. The shift for the cyclotronfrequency [Brown & Gabrielse, 1986] is given as:

$$\Delta\omega_c \approx \frac{9}{4}\omega_- sin^2\theta. \tag{3.32}$$

For example for a misalignment angle of $\theta = 0.5°$ and a voltage difference of 5 V between ring- and endcap electrode, $\Delta\omega_c = 0.16$ Hz which is negligible. Note that even for large unrealistic misalignment angles of 10% this does not distort the normal operation of the WITCH Penning Traps [Van Gorp, 2007].

Although a tilt in the magnetic field does not jeopardize standard operation of the Penning traps, it will strongly influence a measurement on the beta neutrino angular correlation coefficient [Tandecki, 2011]. Indeed, e.g. the process of conversion of radial energy (of the daughter ion after $\beta$ decay) into axial energy that takes place in the spectrometer (Sec. 2.4) will be influenced by any magnetic field misalignment.

**Image charges**

An ion that circulates in the Penning trap will induce image charges in the trap electrodes that surround it. These image charges create an electric field that reacts on the stored ion and shifts its motional frequencies. Image charges become the dominant distortion in the eigenfrequencies when ions are stored on a large radius in the trap i.e. when they are close to the Penning trap electrodes, and when the trapped ions have a high charge state. Therefore image charges are the main systematic effect in FT-ICR measurements and are well described in the literature (e.g. [Winters et al., 2006]). However, for typical experimental conditions such as at WITCH, image charges can be neglected due to both the low radii and the low charge of the stored ions.

## 3.3   Buffer-gas cooling

When ions are injected in a Penning trap they often have too much kinetic energy[2]. This energy is then gradually lost or *cooled* by multiple collisions with the present *buffer-gas*. In good approximation these buffer-gas collisions are elastic, i.e. the total kinetic energy is conserved in the collision. The energy of a particle after an elastic collision with a buffer-gas atom follows from the conservation laws of kinetic energy and momentum. In one dimension, the speed of the particle after the collision is:

$$v_{p,f} = \frac{v_{p,i}(m_p - m_g) + 2m_g v_{g,i}}{m_g + m_p} \tag{3.33}$$

with the subscript $p$ and $g$ representing the particle and buffer-gas atom, respectively and $i$ and $f$ respectively, the initial and final value of the particle's velocity. From Eq. (3.33) one can see that the ion will be slowed down most if the masses are approximately the same, while hitting a much lighter gas atom doesn't change the velocity much. Hitting a much heavier buffer-gas atom causes the fast particle to bounce back with high speed.

Although gas collisions are in reality a discrete process, it can in first order be described as a continuous drag force acting on the ions

$$\mathbf{F}_D = -\delta m \dot{\mathbf{r}}, \tag{3.34}$$

with $\delta$ the damping coefficient defined as

$$\delta = \frac{q}{m} \frac{1}{K_{mob}} \frac{p/p_N}{T/T_N}, \tag{3.35}$$

with the buffer-gas pressure(temperature) $p(T)$ relative to the normal pressure(temperature) $p_N = 1.013 \cdot 10^5 (T_N = 273.15)$, and with $K_{mob}$ the ion-mobility. The ion-mobility describes the drag of a particle through a gas and thus depends on both the mass of the ion and the mass of the buffer-gas. For example for $^{39}\mathrm{K}^+ (^{35}\mathrm{Ar}^+)$ in Helium buffer-gas, the ion mobility equals $21.2 \cdot 10^{-4} (20.8 \cdot 10^{-4}) \frac{m^2}{V \cdot s}$. More tabulated values can be found in [Viehland & Mason, 1995].

One can now insert Eq. (3.34) for the drag force in the equation of motions for a particle in a Penning trap (Eq. 3.6) to obtain the total motion of a particle in the Penning trap

$$\begin{pmatrix} \ddot{x} \\ \ddot{y} \\ \ddot{z} \end{pmatrix} - \omega_c \begin{pmatrix} \dot{y} \\ -\dot{x} \\ 0 \end{pmatrix} - \frac{\omega_z^2}{2} \begin{pmatrix} x \\ y \\ -2z \end{pmatrix} - \delta \begin{pmatrix} \dot{x} \\ \dot{y} \\ \dot{z} \end{pmatrix} = 0. \tag{3.36}$$

_____

[2]For WITCH, the ions enter the cooler trap with an energy between $50\,\mathrm{eV}$ and $100\,\mathrm{eV}$.

The axial motion is still decoupled from the radial motion and can thus be solved separately

$$\ddot{z} + \delta\dot{z} + \omega_z^2 z = 0 \Leftrightarrow z(t) = A_z e^{-(\delta/2)t} cos(\omega_z t + \phi_z). \tag{3.37}$$

which is a damped harmonic oscillator with an exponentially decreasing amplitude (time constant $\delta/2$).

Analogously to solving the equations of motion without buffer-gas, Eq. (3.36) can be transformed into

$$\ddot{u} = -(i\omega_c + \delta)\dot{u} + \frac{\omega_z^2}{2}u, \tag{3.38}$$

by introducing

$$u(t) = x(t) + i \cdot y(t). \tag{3.39}$$

The solution of Equation (3.38) is

$$u(t) = \quad u_-(0) \cdot e^{(-\frac{i\omega_c}{2} - \frac{\delta}{2} + \frac{i}{2}\sqrt{(\omega_c - i\delta)^2 - 2\omega_z^2})t}$$

$$+ \quad u_+(0) \cdot e^{(-\frac{i\omega_c}{2} - \frac{\delta}{2} - \frac{i}{2}\sqrt{(\omega_c - i\delta)^2 - 2\omega_z^2})t} \tag{3.40}$$

which, after transformation into normal Cartesian coordinates, results in

$$\begin{pmatrix} x(t) \\ y(t) \end{pmatrix} = r_-(0)e^{-\alpha_- t} \begin{pmatrix} cos(\omega'_- t) \\ -sin(\omega'_- t) \end{pmatrix} + r_+(0)e^{-\alpha_+ t} \begin{pmatrix} cos(\omega'_+ t) \\ -sin(\omega'_+ t) \end{pmatrix}. \tag{3.41}$$

The new frequencies $\omega'_\pm$ are defined as

$$\omega'_\pm = \omega_\pm \pm \Delta\omega$$

$$\Delta\omega = \frac{\delta^2}{16} \cdot \frac{8\omega_z^2 + \delta^2}{(\omega_c^2 - 2\omega_z^2)^{3/2}} \tag{3.42}$$

while the damping coefficients $\alpha_\pm$ are given as

$$\alpha_\pm = -\frac{\delta}{2}\left(1 \pm \left(1 + \frac{\omega_z^2 + (\delta)^2/8}{\omega_c^2 - 2\omega_z^2}\right)\right). \tag{3.43}$$

Under influence of buffer gas the radius of the cyclotron motion thus decreases with a time constant $\alpha_+ \approx \delta$. While the magnetron radius increases many orders of magnitude slower with a time constant $\alpha_- \approx -\frac{\delta}{2}\left(\frac{\omega_z}{\omega_c}\right)^2$ as shown in Figure 3.3.
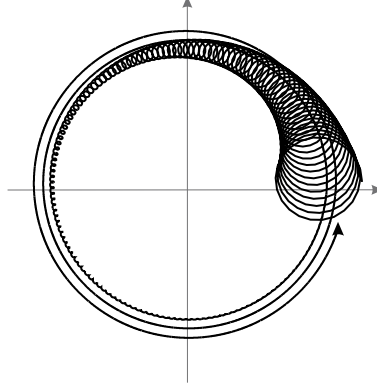
Figure 3.3: Influence of buffer gas on the radial motion of an ion in the x-y plane of a Penning trap. A fast damping of the cyclotron motion and a slow increase of the radius of the magnetron motion is observed.

Note that the Stokes model described here is only an approximation, since it continuously cools down the ion and does not take into account *buffer gas heating*. This is the process when a cooled trapped ion collides with a buffer gas atom such that energy is transferred from the buffer gas atom to the ion. More advanced buffer gas models can take these realistic gas collisions into a account. E.g. the $K_0$ model and the polarizability model, as will be discussed in Section 4.5.3, or the *IonCool* buffer-gas model [Schwarz, 2006].

The maximum energy due to buffer-gas heating can be calculated using Equation 3.33, with $v_g = \sqrt{2k_bT/m_g}$ and $v_p = \sqrt{2k_bT/m_p}$:

$$E_{max} = k_b T m_p \left[ \frac{\sqrt{m_p} - \frac{m_g}{\sqrt{m_p}} + 2\sqrt{m_g}}{m_g + m_p} \right]^2 , \qquad (3.44)$$

yielding a maximum energy of 50 meV at room temperature for $^{35}$Ar (and $^{39}$K) ions due to helium buffer gas heating. Equation 3.33 can also be used to investigate the influence of different parameters on the buffer gas heating. For example cooling of argon ions with helium, neon or argon buffer gas yields a maximum energy of 50 meV, 38 meV and 29 meV respectively. To bring down the effect of the buffer gas heating one can also cool the buffer gas itself prior to bringing it in the Penning traps. Helium buffer gas at liquid nitrogen (77K) or liquid helium (4K) temperature gives a maximum energy of 13 meV and 0.67 meV, respectively, for the stored argon ions.

Figure 3.4 shows the simulated maximum energy due to buffer gas heating with the $K_0$ model. This simulation governs 500 cooled $^{39}$K ions in a Penning trap with helium buffer gas and a simulation lifetime of 50 ms; Coulomb interaction
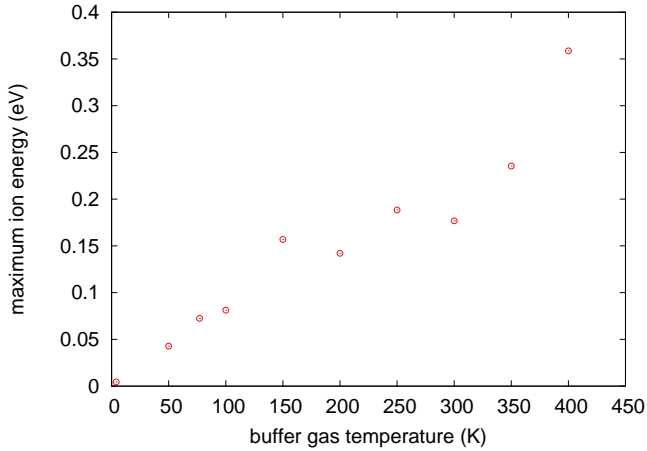
Figure 3.4: Simulated influence of the buffer gas heating effect for different buffer gas temperatures on the radial and the total energy of the ions. The simulation was performed for 500 cooled $^{39}$K ions and helium buffer gas at room temperature. A lower temperature of the buffer gas results in a lower maximum ion energy. The scatter on the data is due to the low amount of simulated ions (500).

between the ions was not taken into account. Buffer gas atoms with a lower temperature cause less heating to the trapped ions. Since the WITCH setup is at room temperature (293 K) and uses helium buffer-gas, this buffer gas can heat the ions to 0.37 eV according to these simulations.

## 3.4   Particle Excitations

When a time-varying electric field is applied on one or more of the Penning trap electrodes, the motion of a charged particle can be influenced. When such a particle excitation is applied with the correct frequency it is then possible to change one, two or three eigenmotions and leave the other(s) independent. Changing electric fields are superimposed in the trap by applying rf-fields with specific frequencies on opposing segments of the eightfold segmented ring electrode (Figure 3.5).

These excitations make it possible to influence the ion motion in the trap and change the ion energy. The most common excitations –also used by the WITCH setup– are the dipole excitation, to bring the ions out of centre, and a quadrupole excitation in combination with buffer gas, to centre ions with a specific mass. In the past few years also the rotating wall excitation has gained interest. This excitation has been applied successfully when up to $10^7$ ions are stored in a Penning trap
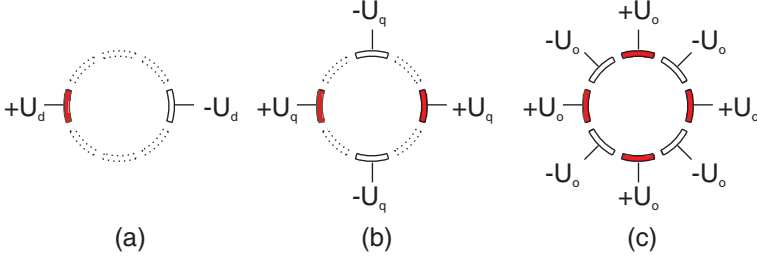
Figure 3.5: The segmented WITCH ring electrode can be used for different excitations. Dipole excitation (a), quadrupole excitation (b) and a octupole excitation (c).

and will be discussed later since this type of excitation only works with a large amount of ions, where the Coulomb interaction has a significant influence on the ion cloud shape and energy distribution (see Chapter 6).

In the following discussion the phases of the excitations will be neglected. Since at WITCH typically a large amount of ions is trapped, the average phase difference between the excitation and the ion cloud will be zero.

### 3.4.1 Dipole excitation

The simplest type of excitation is a dipole excitation, where a time varying electric field is applied on two opposing segments of the ring electrode (see Fig. 3.5(a)),

$$\mathbf{E_d} = \frac{U_d}{r_0} cos(\omega_{rf}t + \phi_{rf})\hat{\mathbf{e}}_x, \tag{3.45}$$

with $U_d, \phi_{rf}$ and $\omega_{rf}$ respectively the excitation amplitude, phase and angular frequency. To simplify the discussion we introduce the constant $k_d$ as

$$k_d = \frac{qU_d}{mr_0}, \tag{3.46}$$

with $r_0$ the distance between the center of the trap and the excitation electrodes. The acceleration exerted by the dipole excitation on a particle thus equals $k_0 cos(\omega_{rf}t + \phi_{rf})$ and can be added to the equations of motions of a particle in a Penning trap (Eq.3.6):

$$\begin{pmatrix} \ddot{x} \\ \ddot{y} \\ \ddot{z} \end{pmatrix} - \omega_c \begin{pmatrix} \dot{y} \\ -\dot{x} \\ 0 \end{pmatrix} - \frac{\omega_z^2}{2} \begin{pmatrix} x \\ y \\ -2z \end{pmatrix} - k_d cos(\omega_{rf}t + \phi_{rf}) \begin{pmatrix} 1 \\ 0 \\ 0 \end{pmatrix} = 0. \tag{3.47}$$

The radial motion is thus still uncoupled from the axial motion. Furthermore, the equation is solvable as shown in Ref. [Coeck, 2007] and has two resonant excitation frequencies $\omega_-$ and $\omega_+$.
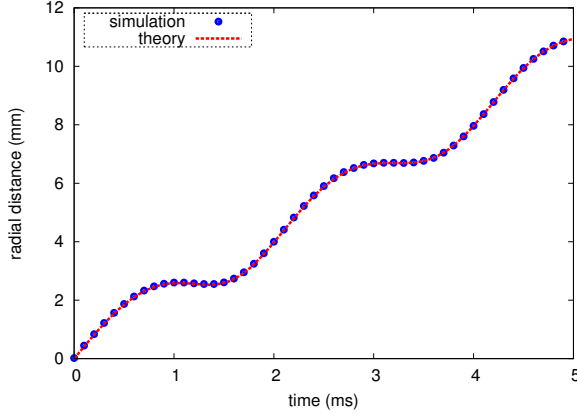


Figure 3.6: Radial distance of a trapped ion from the trap centre as a function of the excitation time. A magnetron dipole excitation at $\omega_-$ moves the ion away from the center of the trap.

**Dipolar rf-excititation of the magnetron motion**

When a dipolar excitation is applied at $\omega_{rf} \approx \omega_-$ the radius of the ion increases linearly with the excitation time. Figure 3.6 shows the radial distance of an ion to the centre of the trap as a function of the excitation time when a dipole excitation at $\nu_- = 1500.15$ Hz is applied. Since the magnetron frequency is in first order independent of the mass, a dipole excitation at this frequency brings all ions to a larger radius, independent of their mass. The slope of this linear increase in radius is given by

$$\frac{k_d}{2(\omega_+ - \omega_-)}, \tag{3.48}$$

and thus depends linearly on the excitation amplitude. Note that the distance to the center of the trap of an excited particle is not exactly linear over time but oscillates with frequency $2\omega_-$.

**Dipolar rf-excititation of the cyclotron motion**

Similar effects occur when the dipolar excitation is applied at $\omega_{rf} \approx \omega_+$. The main difference is that here the cyclotron excitation can be used to decenter ions

with a specific mass, since $\omega_+$ scales inversely with the mass. Another difference is that this excitation will bring the ions to a certain fixed radius independent of the excitation duration, instead of slowly but continuously pushing the ions outwards, as an excitation on the $\omega_-$ frequency does. Due to the continuous addition of kinetic energy of the ion, the ion velocity will increase and collisions with the buffer gas atom will occur more frequently. This process continues to happen until a saturation point is reached, i.e. when the radius of the ion will not increase any further but will stabilize at

$$r = \frac{U_d}{\delta B}.\tag{3.49}$$

With $\delta$ as defined in Eq.(3.35). Because an excitation at the magnetron frequency does not increase the kinetic energy of the ion, it does not give rise to this saturation behaviour.

## 3.4.2 Quadrupolar rf-excitation

An excitation can also be applied by using a oscillating quadrupolar electric field (see Fig 3.5):

$$\mathbf{E}_q = -2\frac{U_q}{r_0^2} \cdot cos(\omega_q t + \phi_q) \cdot (y\hat{\mathbf{e}}_y - x\hat{\mathbf{e}}_x).\tag{3.50}$$

Adding a quadrupole excitation to the basic motion of an ion (Eq.3.6), and solving the equation [Brown & Gabrielse, 1986], shows that $\omega_c$ is the resonant excitation frequency. At this frequency the magnetron and cyclotron radius (i.e. $r_-$ and $r_+$ respectively) evolve as

$$r_\pm = r_\pm(0)cos\left(\frac{\omega_{conv}}{2}t\right) \mp r_\mp(0)sin\left(\frac{\omega_{conv}}{2}t\right)cos(\phi_{rf} - \phi_+ - \phi_-),\tag{3.51}$$

with

$$\omega_{conv} = \frac{k_q}{2(\omega_+ - \omega_-)},\tag{3.52}$$

and $k_q$ defined analogously as for a dipolar excitation

$$k_0 = 2\frac{qU_q}{mr_0^2}.\tag{3.53}$$

$\omega_{conv}$ is the conversion frequency that continuously changes the magnetron motion into pure cyclotron motion and back with a period $T_{conv} = 2\pi/\omega_{conv}$, as is shown in Figure 3.7.

A quadrupole excitation thus couples the magnetron motion to the cyclotron motion and interchanges continuously the two motions into each other. For
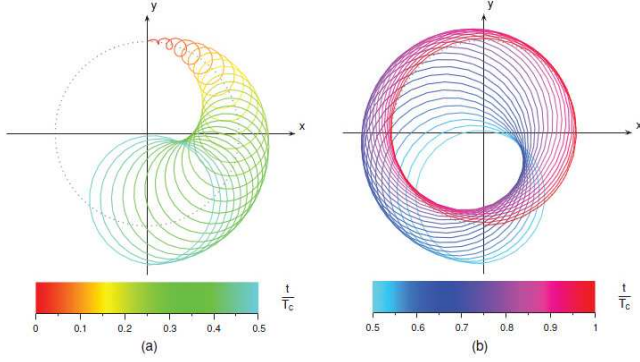
Figure 3.7: Principle of a quadrupole excitation with $\omega_{rf} = \omega_c$. The initially pure magnetron motion (a) is converted into pure cyclotron motion (b). After which there is again a conversion to the pure magnetron motion and the entire conversion process starts again. As long as the quadrupole excitation is applied this conversion continues with a period $T_{conv} = 2\pi/\omega_{conv}$.

example for an $^{35}$Ar ion that is excited in the WITCH Penning trap with an rf-amplitude of 1 V, the conversion between magnetron and cyclotron motion will occur continuously with a period of 7.5 ms.

**Mass selective centering**

The equations of motion for quadrupole excitation in a buffer gas filled Penning trap are solvable [König et al., 1995]. As discussed in detail before (Section 3.3), ions lose their kinetic energy via buffer gas collisions, causing the cyclotron radius to shrink with a time constant $\alpha_+ \approx \delta$, while the magnetron radius increases many orders of magnitude slower with a time constant $\alpha_- \approx -\frac{\delta}{2}\left(\frac{\omega_z}{\omega_c}\right)^2$. Since a quadrupole excitation continuously converts potential energy of the magnetron motion into pure kinetic energy in the cyclotron motion the ion will lose energy due to buffer gas collisions and its orbit will shrink in radius, as is shown in Figure 3.8.

Since $\omega_c = \frac{q}{m}B$ the centring is mass-selective and a Penning trap can be used to separate ion species by mass.

This type of excitation is often also called *sideband cooling*. This method was pioneered by ISOLTRAP [Bollen et al., 1990; Savard et al., 1991] and is now used as a basic principle in many ion traps to cool and centre the ions. Note that the magnetron motion can also be coupled to the axial motion, but this has never been applied at WITCH (nor at REXTRAP and ISOLTRAP). This method is
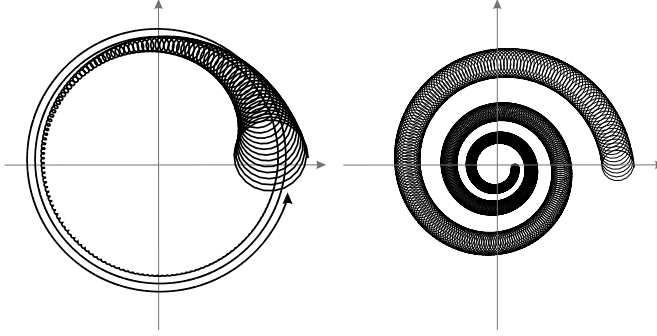
Figure 3.8: Influence of buffer gas on the radial motion of an ion in the x-y plane of a Penning trap is shown on the left. Here, a fast damping of the cyclotron motion and a slow increase of the magnetron motion is observed. When an additional quadrupole excitation is applied (right) the ion is centred in the Penning Trap.

often used to cool very light ions and leptons [Brown & Gabrielse, 1986; Van Dyck et al., 1977].

### 3.4.3 Octupole excitation

An octupole excitation could in principle cool the ions much faster and should thus be beneficial. Such an electric field is given by

$$\mathbf{E}_o = -4\frac{U_o}{r_0^4} \cdot cos(\omega_o t + \phi_o) \cdot \left( (x^3 - 3xy^2)\hat{\mathbf{e}}_x + (y^3 - 3x^2y)\hat{\mathbf{e}}_y \right). \qquad (3.54)$$

Adding this to the equations of motion of an ion in a Penning trap results in analytically unsolvable equations. Octupole excitations have, however, been investigated experimentally [Ringle et al., 2007; Eliseev et al., 2007] and with simulations [Rosenbusch, 2009; Van Gorp, 2007]. This type of excitation can be applied to obtain a faster cooling and centring time of the ions, and a better mass selectivity. However, octupole excitations are highly dependent on the initial phase and position of the ion and are therefore disregarded at this point.

A careful investigation of octupole excitations in the many particle regimes has not been performed yet. This might well be beneficial for WITCH, since the high dependence of the position and phase will likely smear out over all the trapped ions.

# 3.5 The WITCH Penning Traps

## 3.5.1 Mechanical design

A mechanical drawing of the WITCH Penning traps is shown in Figure 3.9. Both traps are of cylindrical type which also allows producing the quadrupole potential required for trapping charged particles [Gabrielse & Mackintosh, 1984; Raimbault-Hartmann et al., 1997]. The cooler trap, which is an exact copy of the ISOLTRAP cooler trap, is separated from the decay trap by a pumping diaphragm with a diameter of 2 mm and a length of 5 cm. This to prevent buffer gas from the cooler trap to diffuse into the decay trap and into the spectrometer section. Both traps are located in a superconducting magnet with a variable magnetic field up to 9 T and a field homogeneity of $\delta B < 10^{-5}$. When 16 V is applied to the endcap electrodes of the Penning trap, the characteristic trap parameter $U_0/d^2$ equals $1.8 \cdot 10^4$ V/m$^2$.
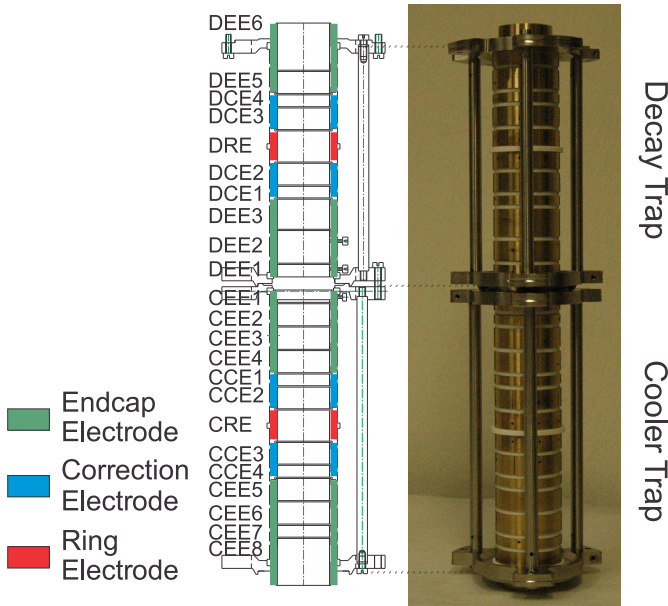


Figure 3.9: Overview of the WITCH Penning traps. The total height is 42.9 cm.

The WITCH Penning trap electrodes are made from high conductivity oxygen-free copper. The electrodes were first plated with a 10-15 $\mu$m layer of nickel and subsequently coated with a gold layer. Normally silver is used instead of nickel, but since silver cannot withstand the baking procedure at WITCH, nickel was preferred. Nickel causes small distortions in the magnetic field which are known

to broaden the mass resolution with a factor $10^{-10}$ of $10^{-8}$ for a large amount of ions. Nevertheless this effect is still less than the effects due to space charges and such high mass selectivity is not of importance for normal WITCH operation. The nickel layer in between the gold and the copper layer prevents the copper layer to diffuse trough the gold layer and to oxidize at the electrode surface. The electrodes are electrically insulated with Macor and (TECA)PEEK insulators. The ring electrode of both Penning traps is eightfold segmented to be able to apply the different excitation schemes discussed in Sec 3.4. It is possible to apply two different dipole excitations and one quadrupole excitation on the ring electrode as is shown in Fig 3.10. The support structure for the electrodes is made from titanium, which is a strong material, is non-magnetic and can withstand the baking procedure. A custom made titanium-zirconium-vanadium NEG foil [Chiggiato & Costa-Pinto, 2005] folded into a cylinder is slided over the Penning trap structure to maximize the pumping capacity in the Penning trap section.
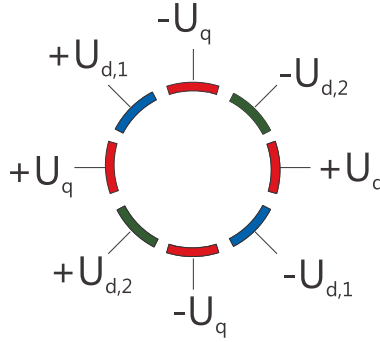


Figure 3.10: The ring electrode is eigthfold segmented to allow the use of a quadrupole excitation and two different dipole excitations.

## 3.5.2 Buffer-gas system

The prime physics candidate for the WITCH experiment is argon, which has a tendency to charge exchange rapidly, like all noble gases. In the past this has troubled normal operation of the WITCH setup, since the charge exchange half-life of argon in the WITCH cooler trap turned out to be only 8 ms [Tandecki, 2011]. To this end the buffer-gas system was upgraded to a much cleaner state containing a minimum amount of impurities. These impurities can come from out-gassing in the buffer gas system and from the buffer gas bottle itself. Typical buffer gas pressures range from $10^{-4}$ to $10^{-5}$ mbar, corresponding to $2.5 \cdot 10^9$ to $2.5 \cdot 10^8$ particles in one $mm^3$. Since gas from a He-57 bottle[3] contains three impurities

_____

[3]He-57 gas is 99.9997 % pure.

in a million helium atoms, typically around 750 to 7500 impurities per cubic mm are flushed with the buffer gas into the Penning traps. Ion clouds in the WITCH Penning traps typically have densities in this range (see Tab. 6.1), so it is not very unlikely that due to the many ion-buffer gas collisions, the probability of charge exchange with impurities in the buffer gas is significant.
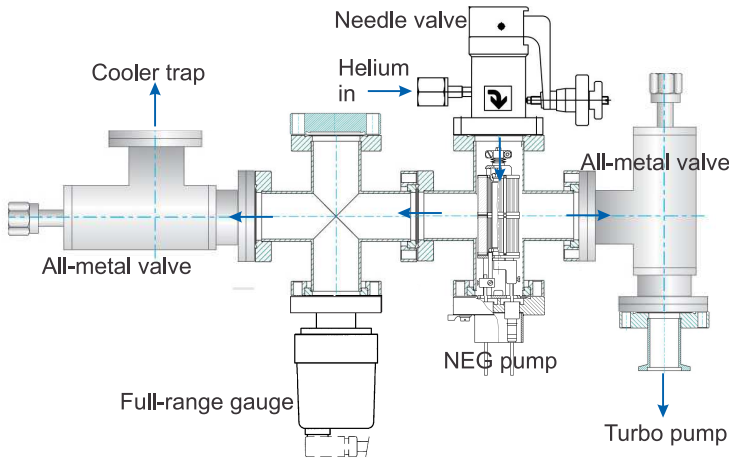


Figure 3.11: Buffer gas cross piece.

In order to prevent this charge exchange to occur, the buffer gas system of WITCH is now made of all-metal parts and no polymers were used anymore so as to minimize the amount of impurities in the system, see figure 3.11. The new buffer gas cross piece has three valves for maximum flexibility and to have the possibility to connect a turbo pump when baking. A NEG pump is also attached to the buffer gas cross piece. This lowers the base pressure and absorbs contaminations from the He-gas bottle but does does not absorb helium atoms. Recent measurements have shown that due to this improved buffer gas system, charge exchange losses were not noticeable anymore when storing ions for up to 10 seconds in the cooler trap.

### 3.5.3   Electronic design

The heart of the WITCH experiment is a PCI-7811R FPGA (Field Programmable Array) unit that handles the timing patterns of WITCH, see figure 3.12. This device has a very high resolution (25 ns) and accuracy, and is therefore used to trigger the two Penning trap electrode voltage power supplies. A separate power supply is used for the endcap voltages since they typically require a higher voltage (limited to -15,450 V) compared to the standard electrodes (limited to -15,15V).

Three RF switch boxes combine the ring electrode voltage with the oscillation frequency for a specific excitation set with a function generator (Standford DS345).
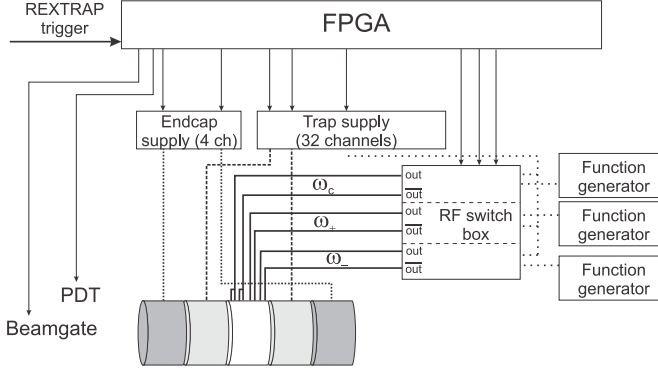


Figure 3.12: Overview of the electronics to control the WITCH Penning traps electrode voltages and timing patterns.

## 3.5.4  Trap cycle

The ion bunches that arrive from REXTRAP typically undergo a six stage trapping cycle which is also shown in Figure 3.13.

1. The voltage of the bottom electrode of the cooler trap (CEE8) is kept low such that ions can enter the cooler trap. Meanwhile the voltage on the upper electrode of the cooler trap (CEE1) is at a sufficiently high potential -typically a few 100 V- to block the path of the ions.

2. When the whole ion bunch fits in the cooler trap the bottom endcap is raised to the same voltage as the upper endcap. The ions are now trapped in the cooler trap and can undergo buffer gas collisions to lose kinetic energy. Meanwhile excitations can also be applied, for example to centre the ions or to remove a specific ion species. At this stage several bunches can be stacked by lowering the lower endcap quickly to accept the following incoming bunch, see section 2.7.

3. When the ions have been stored for 100 to 300 ms in the cooler trap they are cooled to a few eV and the voltage on the upper and lower endcap is lowered to a few volts.

4. The cooled ion cloud is transferred from the cooler trap to the decay trap by changing the potentials on almost all Penning trap electrodes. Note that the electric potentials for this ion transfer have to be optimized, such that
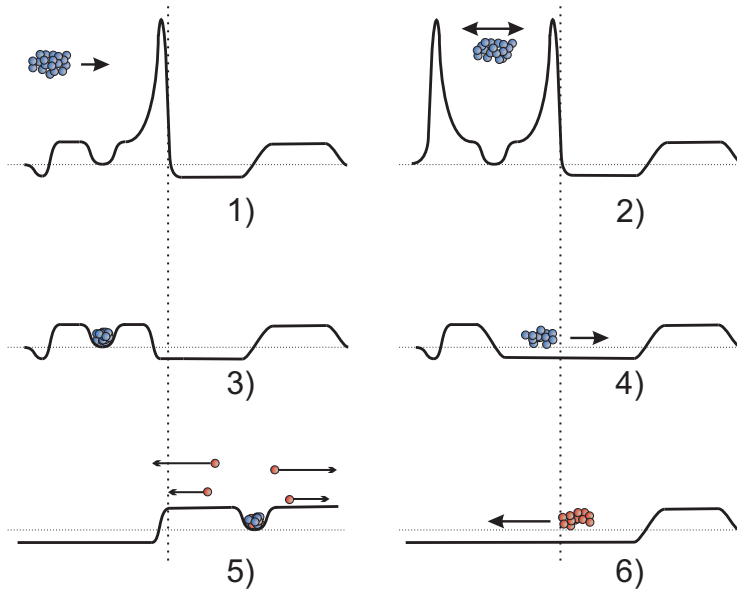
Figure 3.13: Overview of WITCH trapping cycle. The full line represents the applied voltage in the Penning traps at a given moment in time. The dotted line separates the cooler trap on the left from the decay trap on the right. Radioactive ions are represented by blue spheres, while red spheres represent ions that have decayed.

the velocity and position distribution of the ion cloud are not changed. This is realized by applying a Wiley-McLaren type potential [Wiley & McLaren, 1955].

5. The bottom endcap of the decay trap is raised, such that a quadrupole potential is applied wherein the ion cloud is trapped. The now stored ion cloud serves as scattering-free source for the WITCH experiment. Here the radioactive ions will escape the trap when they receive enough kinetic energy from the $\beta$ decay to overcome the trapping potential, which typically is a few eV. In principle the lower endcap can be raised to reflect decayed ions in the spectrometer and as such increase the collected amount of events.

6. When a measurement cycle is finished, the ions are ejected downwards, trough the cooler trap, to prevent any radioactive contamination and start the next measurement with an empty trap system.

# Chapter 4

# Simbuca

In this chapter, the paper entitled *Simbuca, using a graphics card to simulate Coulomb interactions in a Penning trap* is presented. This describes a complete Penning Trap simulation program called *Simbuca*. Simbuca is the first program that utilizes a graphics card (GPU) to speed up the calculation of the Coulomb interaction between charged particles. The development of this code made it possible to analyse the first data on $^{35}$Ar, that was taken with the WITCH experiment in June 2011.

Later in this chapter (Sec.4.9) additional improvements on the simulation code are discussed.

---

*Simbuca, using a graphics card to simulate Coulomb interactions in a Penning trap*

S. Van Gorp[1], M. Beck[2], M. Breitenfeldt[1], V. De Leebeeck[1], P. Friedag[2], A. Herlert[3], T. Iitaka[6], J. Mader[2], V. Kozlov[5], S. Rocia[1], G. Soti[1], M. Tandecki[1], E. Traykov[1], F. Wauters[1], Ch. Weinheimer[2], D. Zákoucký[4], N. Severijns[1]

[1] *K.U.Leuven, Instituut voor Kern- en Stralingsfysica, Celestijnenlaan 200D, B-3001 Leuven, Belgium*

[2] *Universität Münster, Institut für Kernphysik, Wilhelm-Klemm-Strasse 9, D-48149 Münster, Germany*

[3] *CERN, CH-1211 Genève 23, Switzerland*

[4] *Nuclear Physics Institute, ASCR, CZ-250 68 Rež, Czech Republic*

[5] *Karlsruhe Institute of Technology, Institut für Kernphysik, Postfach 3640, D-76021 Karlsruhe, Germany*

[6] *Computational Astrophysics Laboratory, RIKEN, 2-1 Hirosawa, Wako, Saitama 351-0198, Japan*

## 4.1 abstract

In almost all cases, N-body simulations are limited by the computation time available. Coulomb interaction calculations scale with $\mathcal{O}(N^2)$ with $N$ the number of particles. Approximation methods exist already to reduce the computation time to $\mathcal{O}(N\ logN)$, although calculating the interaction still dominates the total simulation time. We present *Simbuca*, a simulation package for thousands of ions moving in a Penning trap which will be applied for the WITCH experiment. *Simbuca* uses the output of the Cunbody-1 library, which calculates the gravitational interaction between entities on a graphics card, and adapts it for Coulomb calculations. Furthermore the program incorporates three realistic buffer–gas models, the possibility of importing realistic electric and magnetic fieldmaps and different order integrators with adaptive step size and error control. The software is released under the GNU General Public License and free for use.

## 4.2 Introduction

In the last decades ion traps have become an indispensable tool for the measurements of a wide range of observables in atomic and nuclear physics [Kluge & Blaum, 2004]. Ion traps have not only pushed the limits for mass measurements [Blaum, 2006] but are also used to prepare beams for post acceleration [Ames et al., 2005], to improve the emittance of ion beams [Herfurth et al., 2001], to assist decay studies [Kowalska et al., 2009], to improve the mass separation at ISOL-facilities [Aliseda et al., 2004] and for low energy weak interaction physics [Kozlov et al., 2008; Rodríguez et al., 2006].

The WITCH experiment [Beck et al., 2003] (see Fig. 4.1), located at CERN/ISOLDE combines two Penning ion traps to measure the $\beta$-$\nu$ angular correlation coefficient $a$, which is sensitive to the weak interaction in nuclear beta decay [Kozlov et al., 2008; Severijns et al., 2006]. Instead of detecting the difficult to observe neutrino, it measures the recoil energy of the daughter ions after $\beta$ decay. The radioactive ions are stored in a Penning trap instead of collecting them in a foil in order to be able to observe the full
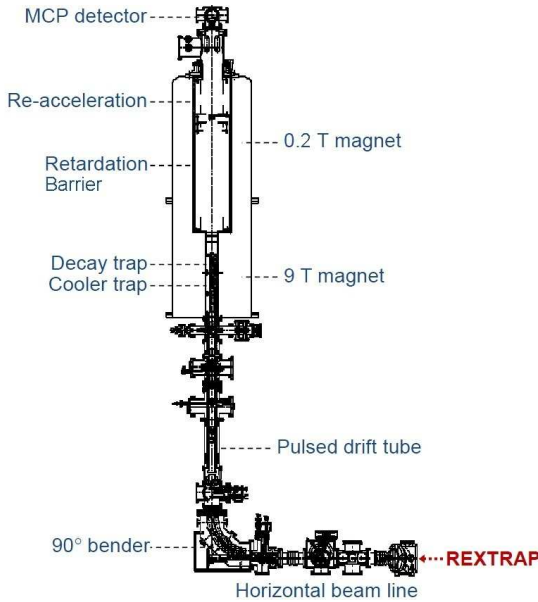
Figure 4.1: Layout of the WITCH setup at ISOLDE.

and unchanged recoil energy when they undergo decay. This recoil energy is typically only a couple of hundreds of eV. The WITCH experiment probes this recoil energy by applying a voltage barrier in the adjacent retardation spectrometer and counting the ions that overcome the barrier and reach the Micro Channel Plate (MCP) ion detector [Coeck et al., 2006].

As WITCH aims to measure $a$ with high accuracy (order of 0.5%), good knowledge and precise control over possible systematic effects is needed. The retardation spectrometer of WITCH (MAC-E filter type [Lobashev & Spivak, 1985; Müller et al., 2003]) consists of a combination of electric fields created by twelve electrodes and magnetic fields from three magnets. To understand the behaviour of ions in this spectrometer a tracking routine for charged particles under the influence of electromagnetic fields was developed by F. Glück [Gluck, 2012]. This routine, however, only gives correct information if one can characterise the source of the particles, i.e. the cloud of ions in the decay trap of WITCH. To this end a Penning trap simulation program, *Simbuca*, was developed.

Furthermore, optimization of the traps is necessary since WITCH needs a well-cooled source of ions. The temperature of the buffer–gas influences the width of the measured recoil energy (see Fig. 4.2) as was simulated in Ref. [Coeck & et al., 2007]. Also other effects such as space-charge effects due to Coulomb interactions, the buffer–gas pressure, electrode potentials and excitations will affect the parameters of the ion cloud. Hence, these effects are also implemented in the simulation program.

The equations of motion of a single particle inside a Penning trap, also in the presence
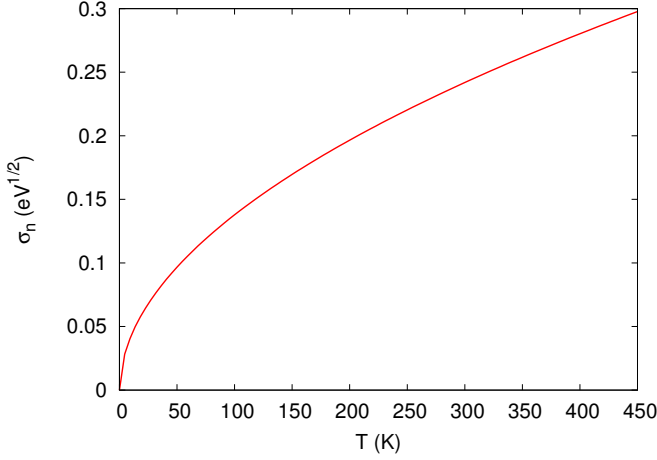
Figure 4.2: Broadening of the response function depending on the temperature of helium buffer–gas atoms.

of a dipolar radiofrequency (rf) excitation field, are well known and can be solved analytically [Schmidt, 2001; Brown & Gabrielse, 1986]. Ion clouds with high densities and low temperatures can be described as non-neutral plasmas and their properties are also well understood [Dubin & O'Neil, 1999]. Such a weakly correlated cloud of charges is considered a plasma when the cloud is large in all its dimensions compared to the Debye length, $\lambda_D = \sqrt{kT/4\pi nq^2}$, with $T$ the temperature of the ions, $n$ the density and $k$ the Boltzmann constant. At the typical densities and temperatures which apply to the WITCH Penning traps or similar Penning trap systems like REXTRAP [Ames et al., 2005], one is far from the one particle picture but also not yet in the plasma regime. Since the equations of motion for a large number of interacting particles that do not form a plasma cannot be solved analytically, one has to use computer simulations to understand the behaviour of such ion clouds.

These effects were investigated for up to 500 particles in Ref. [Coeck & et al., 2007]. Since the calculation of the Coulomb force was done on a normal processor (or CPU) it was impossible to simulate more particles within a reasonable amount of time. With the *Simbuca* code that is presented here, this problem is eliminated by using the Graphical Processing Unit (GPU) to calculate the Coulomb interaction.

# 4.3 Penning Traps

## 4.3.1 Penning Trap Principles

A Penning trap is a three–dimensional device in which charged particles can be stored and manipulated [Brown & Gabrielse, 1986]. An electrostatic field of the form

$$\mathbf{E} = \frac{U_0}{2d^2}(x\hat{\mathbf{e}}_x + y\hat{\mathbf{e}}_y - 2z\hat{\mathbf{e}}_z), \tag{4.1}$$

with $U_0$ the potential difference between the ring and endcap electrodes (see Fig. 4.4), $d = \sqrt{(z_0^2 + r_0^2/2)/2}$ the trap dimension, $r_0$ the radius of the ring electrode and $2z_0$ the axial separation between the endcap electrodes in the case of a hyperbolic trap, confines the charged particles in the axial direction, while a strong axial magnetic field confines the particles in the radial direction.

The combination of these two fields leads to decoupling of the total motion in three independent eigenmotions, each with a specific angular frequency, $\omega_-$, $\omega_+$ and frequency $\omega_z$ (see Fig. 4.3). The following relations between these frequencies hold in an ideal Penning trap:

$$\omega_{\pm} = \frac{1}{2}\left[\omega_c \pm \sqrt{\omega_c^2 - 2\omega_z^2}\right] \tag{4.2}$$

$$\omega_c = \omega_+ + \omega_- \tag{4.3}$$

$$\omega_+ \gg \omega_z \gg \omega_- \tag{4.4}$$

with $\omega_c = \frac{qB}{m}$ the so-called cyclotron frequency.

The three eigenmotions can be described as:

1. The magnetron motion emerges due to the interplay of the magnetic and electric field and causes a drift of the particle around the trap centre in a plane perpendicular to the magnetic field axis. To first order the magnetron frequency (see Eq. (4.2)) is given by the mass independent approximation

$$\omega_- \approx \frac{U_0}{2Bd^2}. \tag{4.5}$$

2. The cyclotron motion describes the fast rotation of the particle around the magnetic field lines, and hence evolves in a plane perpendicular to the magnetic field axis. This motion has the frequency

$$\omega_+ \approx \omega_c = \frac{qB}{m}, \tag{4.6}$$

with $q$ the charge and $m$ the mass of the ion.
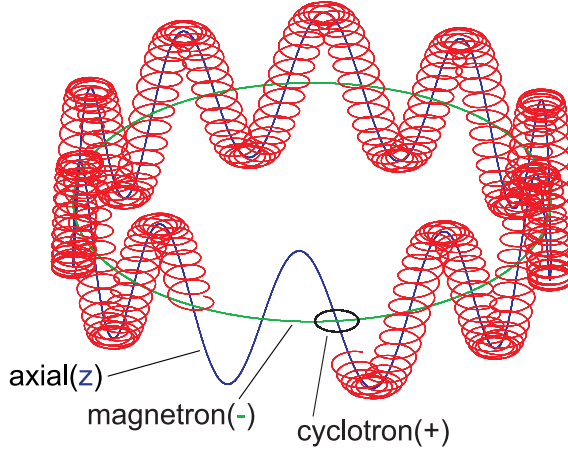
Figure 4.3: The full motion of an ion in a Penning trap can be decoupled into three independent eigenmotions: the cyclotron motion, the magnetron motion and the axial motion.

3. The axial motion is a harmonic oscillation parallel to the magnetic field axis with frequency

$$\omega_z = \sqrt{\frac{qU_0}{md^2}}. \tag{4.7}$$

Buffer–gas in a Penning trap absorbs the kinetic energy of the axial and cyclotron motion, but not of the magnetron motion. In its most simple form buffer–gas cooling can be described by adding a Stokes damping force to the equations of motion, $\boldsymbol{F}_S = -\delta m \frac{d\boldsymbol{r}}{dt}$, with $\delta$ the damping coefficient given by

$$\delta = \frac{q}{m} \frac{1}{K_0} \frac{P/P_N}{T/T_N}, \tag{4.8}$$

with $P$ ($T$) the buffer–gas pressure (temperature) expressed relatively to $P_N = 1.01325 \times 10^5$ Pa ($T_N = 293$ K) the normal pressure (temperature) and $K_0$ the ion mobility. The advantage of a Stokes force is that it allows an analytical solution of the particle motion. In the work presented here a more realistic approach is followed, based on the probability that a neutral buffer–gas atom collides with a particle (see section 4.5.3).

Manipulation of charged particles for centring or mass selection in a Penning trap can be done by applying certain radiofrequency fields, or excitations. In this paper only two common excitations will be briefly discussed, more information can be found in Ref. [Savard et al., 1991].

• An electric dipolar rf excitation at the, to first order, mass independent frequency $\nu_- = \frac{\omega_-}{2\pi}$ (see Eq. (4.5)). This excitation increases the particle's orbit. If an ion cloud is considered, this excitation shifts the entire cloud, as if it was a single

particle, on an orbit with a larger radius. The overall observed effect is a shift of the cloud centre rather than the creation of a torus-like structure [Coeck & et al., 2007].

- Another often used excitation is a quadrupolar rf excitation at the mass dependent frequency $\nu_c = \nu_+ + \nu_- = \frac{\omega_c}{2\pi}$, also referred to as sideband cooling. This excitation couples the magnetron and cyclotron motions such that a conversion between these two radial modes takes place. If the excitation is applied in a buffer–gas filled Penning trap it can be used for mass selective cooling (and centering). Because, in addition, the cyclotron motion is cooled by buffer–gas the overall effect will be that the magnetron radius decreases as well and only ions with the corresponding mass will be centered [Savard et al., 1991]. Note that it was shown that the Coulomb interaction between the ions broadens and shifts the frequency $\nu_c$ [Ames et al., 2005].

## 4.3.2 The WITCH Penning traps
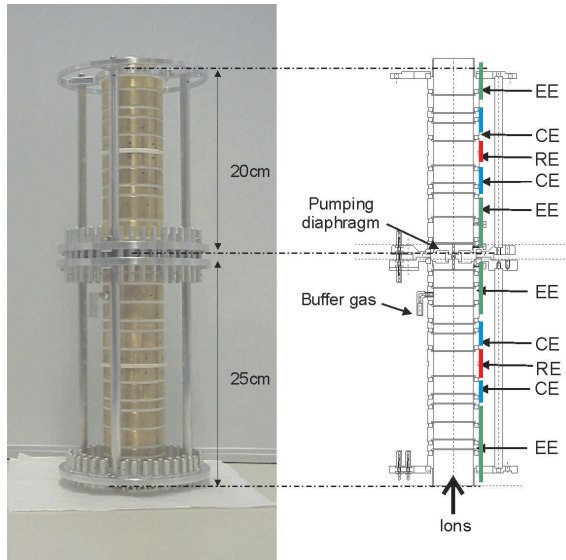


Figure 4.4: The two WITCH Penning traps, below the cooler trap, above the decay trap. RE refers to the central ring electrodes, CE marks the correction electrodes and EE are the endcap electrodes.

The WITCH setup uses two Penning ion traps installed in a 9 T magnetic field. Both traps have a cylindrical shape (see Fig. 4.4) with an inner diameter of 4 cm. The lower one, the cooler trap, handles the capturing, cooling and purification of the incoming ion beam. The well-cooled ions of interest are then transferred to the second trap, the so-called decay trap. The ions in the decay trap act as the radioactive source for the

WITCH experiment and as such, scattering effects should be minimized. To limit the buffer–gas pressure in the decay trap, a pumping diaphragm was installed to minimize leakage of the buffer–gas (typically $10^{-3} - 10^{-5}$ mbar) from the cooler trap .

The central ring electrodes (marked RE) are eightfold segmented while the two inner correction electrodes (CE) are fourfold segmented. This allows the use of various excitation schemes discussed above.

# 4.4 Coulomb interaction between ions

## 4.4.1 Introduction

Since the Coulomb force is a long-range force, the force between all the particles has to be calculated. This means that the simulation cost scales in general with $\mathcal{O}(N^2)$ with $N$ being the number of particles. Methods such as the Barnes-Hut tree [Barnes & Put, 1986] or the FFM algorithm [Carrier et al., 1988] reduce the calculation cost to $\mathcal{O}(N\ logN)$. These methods divide the three–dimensional space into cubic cells, so that only nearby particles are treated individually while particles in distant cells can be grouped to a single particle positioned at their center of mass [Nyland et al., 2008]. Another method that has been successfully applied is the scaled Coulomb force [Beck et al., 2001; Sturm et al., 2009]. All these algorithms help to reduce the calculation cost at the expense of accuracy. Furthermore the calculation of the interaction still dominates the simulation time. Here we present a new method using a graphics card to calculate the Coulomb interactions between particles, without making any approximation. It will be shown that the Coulomb interaction can be calculated much faster using the graphics card rather than using a conventional CPU (see section 4.6.1).

## 4.4.2 The Chamomile Scheme adapted for Coulomb interactions

Recently, an optimized algorithm for N-body simulations was presented [Hamada & Iitaka, 2007]. The basis of this approach is to accelerate the calculation of the N-body gravitational interaction by calculating the exerted force on a Graphics Processing Unit (GPU). Three characteristics of the calculation make it well suited for this approach. First, the calculation of pairwise interaction is relatively simple, because only 20 floating point operations are needed to calculate the Coulomb force between two particles. Second, each particle interacts with all the other particles and hence parallelism is straightforward. Third, in 2006, CUDA, a C like programming language for GPUs, was developed which allows programming without the need for in-depth knowledge of any graphics library [cuda, 2011]. All this renders the GPU very well suited to calculate the Coulomb interaction.

Hamada and Iitaka developed the Chamomile scheme to calculate gravitational N-body interactions on a programmable graphics card and implemented this in the Cunbody-1 library [Hamada & Iitaka, 2007]. This library has the function *cunbody1_force(xj, mj, xi, eps, ai, nmax, nmax)* available for the user. Here, $xj(=xi)$ is a two–dimensional
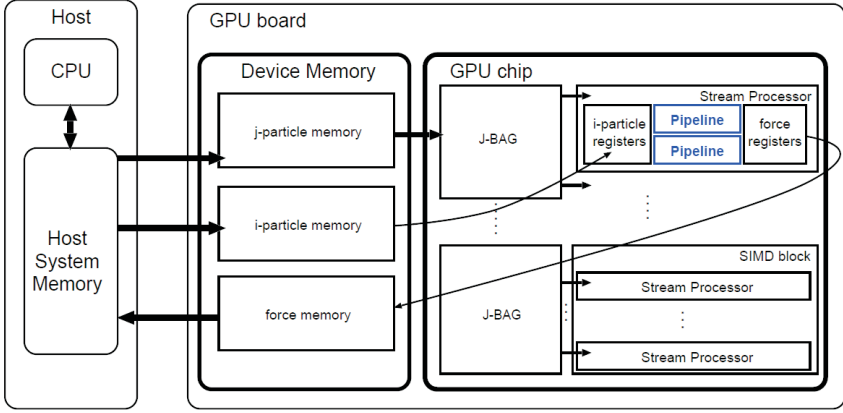
Figure 4.5: The Chamomile scheme applied to the GPU (from Ref. [Hamada & Iitaka, 2007])

.

array with the positions of all particles with mass $mj$, while *eps* is a softening factor to prevent division by zero, $nmax$ is the number of particles, and $ai$ the acceleration due to gravitation as calculated by the library.

The function *cunbody1_force(xj, mj, xi, eps, ai, nmax, nmax)* calculates the acceleration, $\boldsymbol{a}_i = \boldsymbol{F}_i/m_i$ of the nmax particles due to the gravitational interaction among them. The force acting on the $i$-th particle due to the $j$-th particle is

$$\boldsymbol{f}_{i,j} = G\frac{m_i m_j}{|\boldsymbol{r}_{i,j}|^2}\hat{\boldsymbol{r}}_{i,j} \tag{4.9}$$

where $\boldsymbol{r}_{i,j} = \boldsymbol{r}_j - \boldsymbol{r}_i$, $\hat{\boldsymbol{r}}_{i,j} = \boldsymbol{r}_{i,j}/|\boldsymbol{r}_{i,j}|$, G is the gravitational constant, and $m_i$ and $m_j$ are mass of the $i$-th and $j$-th particle, respectively. The total force acting on the $i$-th particle, $\boldsymbol{F}_i$ is given by

$$\boldsymbol{F}_i = \sum_{j=1}^{nmax} \boldsymbol{f}_{i,j}. \tag{4.10}$$

Figure 4.5 illustrates the implementation of the cunbody-1 function on a GPU [Hamada & Iitaka, 2007]. The subroutine allows calculating the force that one group of particles ($j$-particles) exerts on another group ($i$-particles), although in this case both groups of particles are the same. First, the positions of $i$-particles and $j$-particles are copied from the host computer to the device memory of GPU and the force on the $i$-particles is set to zero. The $j$-particles are divided into blocks of particles called J-BAGs with the size of each shared memory and the $i$-particles are divided into blocks of particles called I-POTs with the total number of pipelines. Second, the first J-BAG is broadcasted from the

device memory to the shared memory in each stream processor and the force on the first I-POT is accumulated in parallel. The summation of Eq. (4.10) with the two indices is carried out by repeating this block-wise process with J-BAG as the outer loop and the I-POT as the inner loop. See Ref. [Hamada & Iitaka, 2007] for more details.

The Coulomb force acting on the charge $q_i$ due to the charge $q_j$ is given by

$$\boldsymbol{f}_{i,j}^{Coulomb} = -k_e \frac{q_i q_j e^2}{|\boldsymbol{r}_{i,j}|^2} \hat{\boldsymbol{r}}_{i,j}, \tag{4.11}$$

with $k_e$ the Coulomb constant and $e$ the elementary charge. Since both the Coulomb force (Eq. (4.11)) and the gravitational force (Eq. (4.10)) are described by similar operations, it is possible to scale the output $ai$ so that the force due to Coulomb interaction is obtained.

When calling the *cunbody1_force(xj, mj, xi, eps, ai, nmax, nmax)* function, all $mj[i]$ are set equal to 1 (meaning that all charges are $1^+$), xj[i][3]=xi[i][3] with [3] referring to the particle position (x, y, z), $eps = 1 \cdot 10^{-23}$ and nmax equals the number of particles[1]. The function calculates the acceleration $ai[i]$ due to gravitational interaction. The Coulomb force between the ions can then be obtained by scaling the resulting gravitational acceleration $ai[i]$:

$$a_{Coulomb}[i] = -\frac{e^2 k_e}{mj[i]} \cdot ai[i]. \tag{4.12}$$

The minus sign indicates that equal charges repel each other. This scaling was checked thoroughly and implemented in *Simbuca*.

## 4.5 The Simbuca simulation program

### 4.5.1 Simbuca overview

*Simbuca* is a modular Penning trap simulation program written in C$^{++}$; see Fig. 4.6 for an overview. The program can easily be adapted to be used for Paul traps or RFQs. Thanks to its modularity, different parts of the program can be used for other purposes. For example, one can use the collision methods implemented in *coll.cpp* and compile it with another program to check how helium gas affects ion beam optics in beam tuning. Another example would be to use the first order Gear method in *ode.cpp* as an integrator for a totally different application where particle trajectories are calculated. A Sourceforge site was set up for *Simbuca*[2], where one can download the simulation program for free [Simbuca, 2011]. The different files that make up *Simbuca* will be discussed briefly here. For more detailed information, the reader is referred to their implementation [Simbuca, 2011].

- *mtrand.h* is a function to create random numbers between [0:1].

---

[1] Here $i$ stands for the $i^{th}$ particle in the array.
[2] A subversion repository is set up to allow synchronisation with the latest version of *Simbuca*.
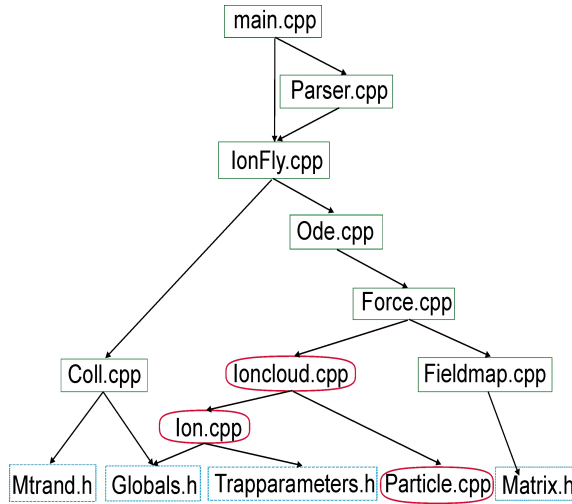
Figure 4.6: Overview of the different C$^{++}$ files in *Simbuca*. The files with dotted lines indicate header files, ovals refer to classes while rectangular boxes refer to implementation files.

- *globals.h* contains all the physical constants used in *Simbuca*.
- *trapparameters.h* contains the Penning trap characteristic parameters such as the trap depth $U_0/d^2$ and the magnetic field $B$.
- *matrix.h* is a C$^{++}$ container of the matrix class.
- *particle.cpp* is a class containing positions and speeds in the three directions x, y and z.
- *ion.cpp* is a class that contains the mass of the ion. This class uses the constants from *Trapparameters.h* to calculate the trap specific frequencies $\omega_+, \omega_-$ and $\omega_c$.
- *coll.cpp* handles the collisions. The speed of the ion is given as input and, if a collision has occurred, the updated speed after the collision is returned. See section 4.5.3 for more information about the buffer–gas collisions.
- *ioncloud.cpp* is a class that contains two arrays (vectors) of the self–defined types ions and particles in *ion.cpp* and *particle.cpp*, respectively. The ioncloud is a static global variable, i.e. there is one ioncloud that is used in all the separate files.
- *fieldmap.cpp* is used to read the fieldmaps of the magnetic and electric fields in both radial and axial direction. The magnetic fieldmap can be obtained from the manufacturer of the magnet. Electric fieldmaps can be constructed with programs like Comsol [comsol, 2011].
- *force.cpp* consists of two files. One for a simulation on the CPU and one for a simulation on the GPU. Depending on the process unit variable *pu* in the Makefile either *force_gpu.cpp* or *force_cpu.cpp* will be copied to *force.cpp* and then compiled. *force.cpp* calculates the Coulomb force, the force due to the electric

and magnetic fields in the Penning trap and, if applied, additional forces from excitations.

- *ode.cpp* is the heart of the program. The ordinary differential integrators are implemented here. See section 4.5.2 for more information about the implementation of these integrators.

- *ionFly.cpp* initialises all the environmental variables when the program starts such as the order of the integrator and what buffer–gas model to use. *ionFly.h* gives an overview of all the functions that can be used in *main.cpp*.

- *parser.cpp* imports data from previous simulations and uses them as starting point for new simulations.

- *logger.cpp* constructs a log file function used by all the other files in the program.

- *main.cpp* is the only file that has to be modified if different simulations are performed. The user can set different environment parameters here like Coulomb interaction, boundary inclusion, order of the integrator, ...

- the *Makefile* compiles *Simbuca* and can create backups of the program. Here, the user can change the compiler (g++ or icpc) and the processing unit (CPU or GPU).

### 4.5.2 Integrator

The integrator is the heart of the routine. It is the numerical method that calculates the discrete trajectory of a particle by integrating the exerted force and thereby the particle's acceleration. There exists a variety of explicit and implicit methods with different integration 'orders'. The 'order' $k$ of an integration method defines the error per time step $\Delta t$ as $\mathcal{O}(\Delta t^{k+1})$ while the total accumulated error is $\mathcal{O}(\Delta t^k)$.

For every interval, the force (and hence the acceleration) is calculated. In a Penning trap, the largest motional frequency involved, i.e. the reduced cyclotron frequency $\omega_+$, is in the range of MHz which implies a large number of time steps being required in the simulation, since the fastest motion has to be resolved.

Three integrators are implemented in *Simbuca* and will be discussed here: a first order Gear method, a fourth order Runge–Kutta method and a fifth order Dormand–Prince method:

The first order Gear method[3] differs from the other methods since it calculates the force only once for each time step. In order to get a good evaluation, this method first predicts the force, then calculates it and updates the predicted value. Finally the method adapts the prediction algorithm for the next time step [Gear, 1971]. This means that the Gear method is of first order and hence is a fast method. However, one should carefully verify that the energy is conserved in the system. The largest time step one can use, while the total energy in the sytem is still conserved, is $5 \cdot 10^{-9}$ s [Rosenbusch, 2009].

The Runge–Kutta fourth order method with adaptive step size and error control is described in Ref. [Vetterling et al., 2003]. Adaptive step size means that the step size

---

[3]Unlike the other implemented methods, the Gear method uses a fixed step size.

will be made smaller till the required accuracy is reached and the step size will be made larger if the accuracy is too high. The error control over the step size is responsible for the value of the step size, i.e. it assures that $\Delta t$ changes smoothly rather than abruptly. A sudden change of $\Delta t$ would cause the integrator to calculate the time step again so that valuable simulation time would be lost.

The Dormand–Prince fifth order method is based on the same principle as the Runge–Kutta integrator but it is more precise and faster. This gain in speed can be explained since a fifth order method takes more precise steps then a fourth order method. Hence, under the same error tolerance, the fifth order Dormand–Prince method can take bigger steps then the fourth order Runge–Kutta method, and thus complete the same simulation faster.

Comparison of the Gear method (with fixed step size) and the Dormand–Prince method (with adaptive step size) showed that the Gear method is twice as fast, if an error tolerance of $1 \cdot 10^{-8}$ is used and a (conservative) step size, $\Delta t = 1 \cdot 10^{-9}$. In the simulations discussed in this paper, the Gear method was chosen as integrator since it is the fastest method that gives reliable results.

### 4.5.3 Buffer–gas collisions

Helium is used as buffer–gas in the WITCH Penning traps to cool the ensemble of ions to an energy below 1 eV. The buffer–gas pressure is in that case crucial since it influences the energy of the ions directly. It is important to know the energy of the ions after the cooling procedure since this, in turn, smears out the recoil energy that WITCH aims to measure very precisely and thereby also broadens the response function of the system (see Fig. 4.2 in section 4.2).

It is of utmost importance that the ion mobility is properly simulated by the collision model. A performant buffer–gas model for Penning traps, $IonCool$, is described in Ref. [Schwarz, 2006]. In the simulation package described in this paper three different, more straightforward, collision models are implented:

1. The Langevin theory (Ref. [Gioumousis & Stevenson, 1958]) defines the probability $P$ of having an ion–buffer–gas collision as:

$$P = 1 - exp\left( -\frac{e}{2\epsilon_0} \sqrt{\frac{\alpha_e}{\mu}} \frac{p}{k_b T} \cdot \Delta t \right) \tag{4.13}$$

   with $e$ the unit of charge, $\epsilon_0$ the vacuum permittivity, $\alpha_e$ the polarizability of the buffer–gas atoms, $\mu$ the reduced mass of ion and buffer–gas atoms, $p$ the pressure of the buffer–gas, $T$ its temperature, $k_b$ the Boltzmann constant and $\Delta t$ the step size in the integration routine which is typically around $10^{-8} - 10^{-9}$ seconds. This is called the polarizability model.

2. The second implemented model, the $K_0$ model (Ref. [Petersson, 2006]), is based on the experimentally measured relation between the ion mobility, $K_0$, and its drift velocity $v_d$ as given in Ref. [Viehland & Mason, 1995]. This relation can be fitted

by a Nelder function as shown in Ref. [Petersson, 2006]:

$$K_0(v_d) = \frac{a + v_d}{b_0 + b_1(a + v_d) + b_2(a + v_d)^2}.$$ (4.14)

For $^{40}Ar^+$ ($^{133}Cs^+$) ions in helium buffer–gas the obtained parameters in this equation are $a = 10720$ (11590), $b_0 = 2.0833 \cdot 10^7$ ($2.084 \cdot 10^7$), $b_1 = -3067.13$ ($-3420$) and $b_2 = 0.151211$ (0.19008). This fit, in turn, is used to calculate the probability for an ion–buffer–gas collision, $P$:

$$P = 1 - exp\left(-\frac{q}{\mu K_0(v_d)} \cdot \Delta t\right)$$ (4.15)

3. The commonly used HS1 model, included in the SIMION package [Appelhans & Dahl, 2002], is a hard sphere, elastic, collision model for ion-neutral collision at typical buffer–gas pressures. This model compares the distance that an ion traveled in the gas (the speed times the timestep) with the mean free path, $\lambda$, of this ion. The chance for a collision is then defined as:

$$P = 1 - exp\left(-\frac{v_{ion} \cdot \Delta t}{\lambda}\right) = 1 - exp\left(-\frac{\sigma \cdot P \cdot v_{rel}}{k_b T} \cdot \Delta t\right),$$ (4.16)

with $v_{ion}$ the speed of the ion, $v_{rel}$ the relative speed of the buffer–gas compared to the ion and $\sigma$ the collision cross–section:

$$\sigma = \pi \left(r_{ion} + r_{gas}\right)^2,$$ (4.17)

with $r_{ion}$ and $r_{gas}$ the radius of the ion and the gas, respectively.

A collision occurs within a certain time interval $\Delta t$ when P is larger than a random number generated between 0 and 1. If a collision has occurred, a gas atom is generated with a velocity randomly picked from the Maxwell–Boltzmann distribution. A hard sphere collision is then calculated to update the new velocity components of the ion.

Before using the routine for simulating collisions between the ions and the buffer–gas, it was first compared to experimental data. To this end, the drift of ions through a gas under the influence of a static electric field **E** has been simulated. After some time the velocities of all ions converged to the drift velocity $v_d$. The ion mobility $K_0$ is then defined as

$$K_0 = \frac{v_d}{E} \frac{P/P_N}{T/T_N}.$$ (4.18)

In Fig. 4.7, the simulated ion mobility $K_0$ is plotted for different drift velocities $v_d$ for $^{40}Ar^+$ in helium buffer–gas at 294 K and at a pressure of $1 \cdot 10^{-3}$ mbar. These simulation results are compared to experimental data from Ref. [Viehland & Mason, 1995]. The $K_0$ model turns out to be slightly better than the Langevin model although overall they both perform well and twice as precise as older models [Coeck & et al., 2007]. The Langevin model gives a good correspondence independent of the mass of the ion while the $K_0$ model has to be adapted for a low or high mass via the Nelder equation (see Eq. (4.14)). If the $K_0$ model is used for other masses it was shown that a maximum deviation of 10
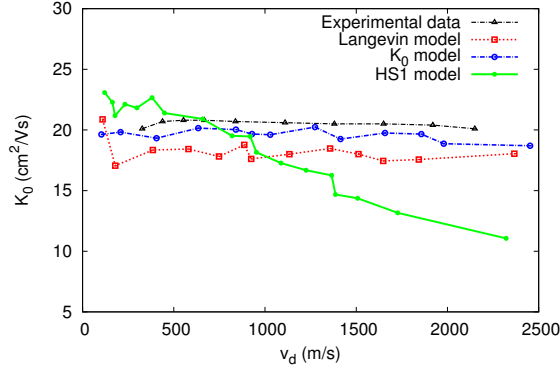
Figure 4.7: The drift velocity $v_d$ versus the ion mobility $K_0$ for $^+$Ar ions in helium gas. Both the Langevin and $K_0$ model are in good agreement with the experimental data from Viehland et al. [Viehland & Mason, 1995] while the HS1 model drifts away from the experimental data for larger drift velocities.

% can occur indicating that the resulting ion mobility is still of the correct order. More information about the deviation of the $K_0$ model for high and low masses can be found in Ref. [Petersson, 2006]. Furthermore, both the Langevin and the $K_0$ model simulate the behaviour of the experimental data better than the HS1 model that is commonly used in SIMION.

# 4.6   Simbuca performance

## 4.6.1   Comparison of CPU and GPU

To evaluate the gain from applying the Chamomile scheme to a GPU, simulations were performed for different numbers of particles with the Coulomb interaction using both a CPU and a GPU. The test system consisted of an Intel i7 @ 3.07 Ghz, 8 GB RAM DDR2[4], a 64-bit SUSE 11.1 operating system and a GPU with a GTX 470 chipset. Initially, also different GPUs were tested. Compared to the GTX 470 graphics card a GeForce 9800 GTX card was found to be 3 times slower while the GTX 480 showed no significant speed difference.

The motion of a specified number of particles moving in a Penning trap without buffer–gas and with a simulation lifetime of 100 ms was simulated with *Simbuca*. The first order Gear integrator with fixed step size ($\Delta t = 5 \cdot 10^{-9}$) was chosen (see section 4.5.2).

Figure 4.8 shows the factor that is gained in time when using a GPU. For a simulation with 500 particles the GPU outperforms the CPU by a factor of 25. As one can see the

---

[4]1 GB RAM is sufficient.
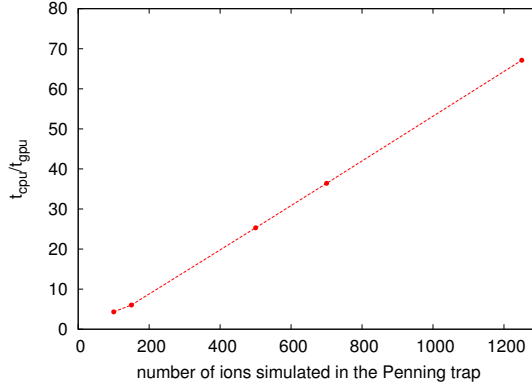
Figure 4.8: The x-axis represents the number of particles that are simulated. The y-axis marks the factor that is gained in time when using a graphics card instead of a conventional CPU (the Coulomb interaction on a CPU is computed on a single core). As can be seen, the GPU is a factor of 50 faster if 1000 particles are simulated. This gain factor increases if more particles are simulated.

behavior is linear up to (at least) 1250 particles. Since a simulation with more than 1250 particles takes too long on a CPU the behaviour was not investigated further.
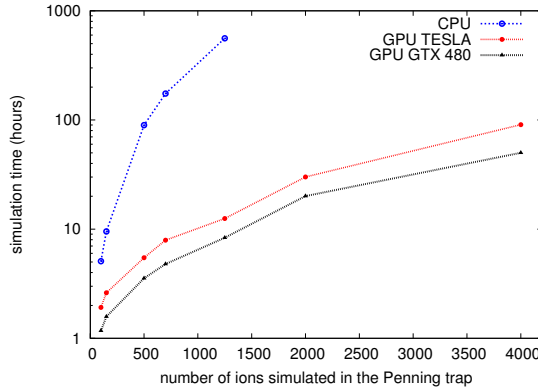


Figure 4.9: Comparison of the simulation time needed on a CPU and on a TESLA or GTX 470 GPU to simulate N ions moving during 100 ms in a buffer–gas filled Penning trap with a quadrupole excitation being applied.

Figure 4.9 shows the simulation time needed versus the number of particles simulated. Simulating 4000 ions moving in a Penning trap for 100 ms with buffer–gas and a quadrupolar rf excitation takes 50 hours on a GTX 470 GPU while a simulation time of 6000 hours or 250 days is expected for a normal CPU. Simulations using only the CPU

on the two pc's used (for the TESLA and the GTX GPU), showed that the pc with the GTX card is a factor 1.5 faster. Taking this factor into account the simulation times for the TESLA and the GTX card turns out to be similar, i.e. the red and black curves in Fig. 4.9 nearly coincide.

For simulations with up to 3000 particles the simulation time seems to scale linearly with the number of particles on the GPU, while an $\mathcal{O}(N^2)$ dependence is found immediately for simulations on a CPU. To get an idea of the *Simbuca* package performance a simulation for 10 000 particles moving for 100 ms in a buffer–gas filled Penning trap was performed. This was found to take 5.5 days of simulation time on a GTX 470 GPU. From extrapolation, one can conclude that doing the same simulation on a CPU would take roughly about 4.5 years.

## 4.6.2 Further improvements

GPU programming is a rapidly evolving field and other, faster, computer codes are regularly becoming available. In contrast to the *Chamomile* scheme used in this work, the computer codes listed below do not have a library structure but are collections of files which require separate compilation and thus more programming knowledge. These codes are compared in performance with the first version of the *Chamomile* scheme. The second version, discussed in this paper and implemented in *Simbuca*, is a factor of two better. Both the *Chamomile* and the *Kirin* library can be used in combination with a Barnes Hut tree code (see section 4.4.1).

1. The *Kirin* library has been developed by Belleman and co-authors in 2008 [Belleman et al., 2008]. This library does not only provide the force calculation but also a predictor–corrector integrator, like the Gear method (see section 4.5.2). In its implementation the force calculation, potential and jerk (the derivative of acceleration with respect to time) is performed on the GPU. The prediction and correction steps are performed on the CPU, because double precision is required for a correct simulation including round-off errors. GPUs of the modern generation (e.g. the Quadro FX3900, GTX and TESLA GPUs) achieve double precision but at the time of the writing of the *Kirin* library, GPUs only reached single precision so the critical prediction and correction steps were performed on the CPU. This library was proven to be twice as fast as the Chamomile scheme used in this paper, see table 3 in Ref. [Belleman et al., 2008].

2. The *Sapporo* library is an improvement of the *Kirin* library since it emulates double precision on the GPU [Gaburov et al., 2009]. The loss in simulation time of this operation is less than 20%. The prediction and calculation steps are carried out on the GPU, while the correction factor is computed on the CPU. If the prediction for all particles is carried out on the CPU, as in the *Kirin* library, the integration is dominated by the communication and calculation of the prediction step. One can thus expect the Sapporo library to be faster than the *Kirin* library, but real comparisons are not described in Ref. [Gaburov et al., 2009].

3. The $N - body$ library comes with the CUDA environment software [Nyland et al., 2007, chap. 31]. The main stress in this library is on calculating the pairwise

interaction as fast as possible. To this end a number of different optimizations, e.g. *loop unrolling*, are applied. The authors believe to achieve a nearly two times greater performance than the Chamomile scheme, but no hard numbers are given in their publication.

## 4.7   Simulation examples

### 4.7.1   Comparison with theory

*Simbuca* was first compared with the theoretical equations of motion to check the correctness of the program. To this end a Penning trap with a magnetic field of 6 T and trap depth of $U_0/d^2 = 1.8 \cdot 10^4$ V/m$^2$ was utilised in the simulation. The ion cloud consists of 1000 $^{39}$K$^+$ ions which initially are distributed in the center of the trap inside a sphere with radius 0.05 mm and a velocity of 10 m/s in each direction. No buffer gas nor Coulomb interactions are taken into account.

A dipolar rf excitation at the eigenfrequency $\nu_-$=1500.15 Hz is being applied for 5
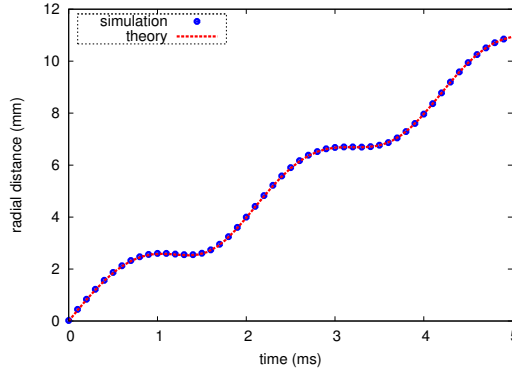


Figure 4.10: Test of *Simbuca* by comparing it with the equations of motion of a dipolar excitation at the eigenfrequency $\nu_-$. Perfect correspondence between simulation and theory is found.

milliseconds (see section 4.3). The equations of motion for an ion in a Penning trap with a dipolar excitation applied are given in Ref. [Coeck, 2007]. Figure 4.10 shows both the simulation results and the theoretical equation for the given parameters. A perfect correspondence can be seen between the expected theoretical calculation and the simulation for the ion moving in the Penning Trap under the influence of an excitation. Furthermore, since the buffer–gas model and the Coulomb interactions have been tested and give consistent results, we conclude that *Simbuca* is a reliable package to simulate ions in a Penning trap.

## 4.7.2   Coulomb interaction example

As an example an ensemble of 3000 $^{35}$Ar$^+$ ions moving in a Penning trap is simulated. The velocities are chosen according to a Maxwell–Boltzmann distribution with its peak at 1.5 eV. The direction of the velocity is chosen randomly. The positions are chosen randomly as well in a cube with edges of 4 mm and centered in the Penning trap. An ideal Penning trap is used in the simulation with a magnetic field of 6 T and a characteristic trap depth $U_0/d^2 = 1.8 \cdot 10^4$ V/m$^2$. Buffer–gas interactions and excitations were excluded in this simulation in order to clearly see the effect of the Coulomb interaction on the shape of the ion cloud.

Figure 4.11 shows cuts in time for ions moving in the xy-plane. Each cut is a
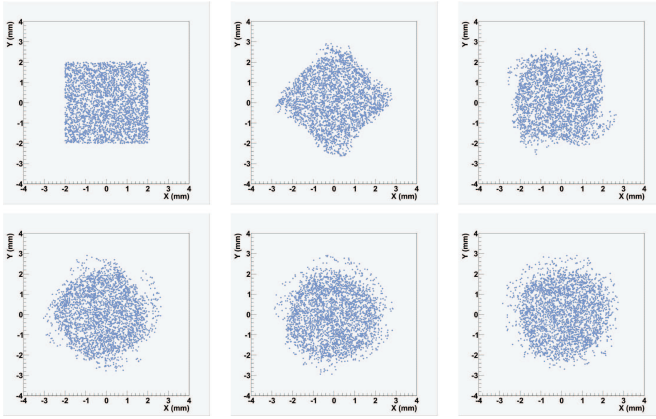


Figure 4.11: Time evolution of the ion cloud in a Penning trap in the xy-plane. The cloud moves 20 milliseconds between each time cut and the first cut is taken when the simulation starts. As can be seen, after 80 milliseconds the initial squarish form is transformed into a circle.

cross–section of the Penning traps through the trap center perpendicular to the B-field. As can be seen, the initial square transforms to a circle due to Coulomb interactions. A similar simulation reveals that without Coulomb interaction between the ions, this transformation does not take place and the cube like structure is maintained.

In the third cut in figure 4.11 tails around the edges of the square can be seen.

# 4.8   Conclusion and outlook

A new Penning trap simulation package, *Simbuca*, was presented. This versatile package is easy to use, powerful and calculates Coulomb interactions between particles on a graphics card to speed up the simulation time tremendously. *Simbuca* can be utilised on

a normal CPU as well and can be applied to simulate charged particles in Paul traps or RFQs with minor modifications.

A reduction in simulation time by a factor 50 is achieved when simulating 1000 particles on a graphics card compared to a CPU. Furthermore, this factor increases with the number of simulated particles. Simulating 10 000 ions, moving for 100 ms in a Penning Trap is performed within 5.5 days on a GTX 470 GPU while the same simulation on a conventional CPU would take at least 4.5 years to finish.

Computing on a graphics card is a new field that is rapidly finding its way towards different research topics. The work presented here is the first application of using a graphics card to calculate the Coulomb interaction between charged particles. Currently, related libraries and simulations codes that were originally written for usage on a normal CPU are being transformed to be used with a graphics card. Thanks to these developments it will soon be possible to simulate up to $10^8$ particles in a relatively short timespan, e.g. by implementing a tree method on the GPU.

# Acknowledgments

# 4.9   Additional improvements

In the past years several improvements to both the Simbuca and CUNBODY code have been made. Due to this and newer versions of the CUDA environment the speed of the program was increased with a factor of about 10 as compared to the results and figures presented in the paper.

Further improvements of the simulation code are certainly possible, mainly on the time integration routine. In general, the simulation time for a time integrator is dominated by the step size. For a Penning trap simulation, the length of the minimum step ($\Delta t$) scales with $\omega_c^{-1}$, since the cyclotron frequency is the fastest frequency to be calculated. For a quick investigation of the behavior of ions, one can thus take a very small magnetic field. Naturally, a magnetic field of $1\,\mathrm{T}$ compared to $6\,\mathrm{T}$ speeds up the simulation 6 times. However, for precise simulations, one does not want to change the magnetic field strength.

Assuming that the magnetic field is constant over the whole Penning trap results in a constant cyclotron frequency (Eq. 3.7), such that the calculation of $\omega_c$ each time step can be brought out of the force equation (Eq. 3.6). This removes the necessity to calculate the fast cyclotron motion each time step, thereby decreasing the simulation time required for a simulation. Ref. [Spreiter & Walter, 1999] discusses a variety of integrators that have this approximation implemented. One of the discussed integrators in this publication is a Velocity-Verlet algorithm, that was applied already successfully for Penning trap simulations [Herfurth et al., 2006].

## 4.9.1   N-body simulations

Tree codes can be applied to speed up the calculation of the Coulomb interaction from $\mathcal{O}(N^2)$ to $\mathcal{O}(N\ logN)$, with $N$ being the number of particles. Such algorithms split the Coulomb interaction calculation between nearby ions and ions that are far away, of which the Coulomb contribution is now estimated. A few of these methods were already described in the paper (Sec. 4.4.1).

The *octgrav* tree library [Gaburov et al., 2010] is the first published tree code that runs on a GPU. Tshis library is now also implemented in Simbuca and was used as a test to compare with the CUNBODY library. Figure 4.12 shows the required simulation times of both libraries for $N$ particles moving $1\,\mathrm{ms}$ in a Penning trap. Surprisingly, the CUNBODY library outperforms the octgrav library, most likely due to to the difficulty to implement such tree codes on a GPU. However, due to the novel approach and high interest of the astrophysics community to use the GPU for simulations; tree codes will most likely become available on a GPU soon. Also Toshi Iitaka (Riken Laboratory), who developed CUNBODY, is working on a tree code that will be released in due time [Iitaka, 2012].
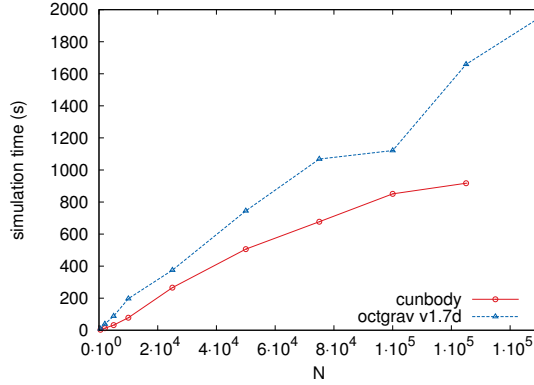
Figure 4.12: Simulation time of the CUNBODY and *octgrav* tree code for N ions moving 1 ms in a Penning trap. As can be seen the CUNBODY code is faster than the *octgrav* tree code.

## 4.9.2 Use of Simbuca by other experiments

Currently the program has been used to aid analysis or restrict the parameter space of various experiments. It has been applied at SMILETRAP to investigate evaporative cooling of highly charged ions. At ISOLTRAP it was used for simulations of the electrostatic mirror [Wolf et al., 2011]. This electrostatic mirror device separates ion bunches by TOF. Via simulations with Simbuca it was shown that when the ions were injected in the device with a low energy, ions would cluster in groups due to their mutual Coulomb interaction. As one would expect, this cluster of ions (the so-called negative mass effect) had a negative influence on the mass resolution. Simulations also showed that when injecting ions with a higher energy this clustering did not occur, and the isobar separator could be used as intended.

Recently, there has also been interest from the CLIC accelerator community to investigate this negative mass effect in particle accelerators. Interest was also shown to use the program for the development of a REXTRAP-like Penning trap for SPIRAL-2.

# Chapter 5

# Data Analysis of the June 2011 experiment

In 2011 two experimental runs on $^{35}$Ar were planned with the WITCH setup. A first experiment at the end of June and a second one in October. Due to technical issues at the WITCH setup as well as with ISOLDE target efficiency only a limited amount of statistics was gathered in the June 2011 experiment. Analysis of this data set, however, allowed the commissioning of the WITCH setup as well as the analysis method to extract $a$. The draft of an article about this analysis is presented in this chapter and will be submitted for a publication in Physical Review C.

A second experiment in October 2011 resulted only in minor improvements due to issues with a new type of (nanostructured) CaO ISOLDE target. Therefore a third run in November 2011 was scheduled with a properly operating CaO ISOLDE target, which allowed to gather a large dataset that is currently being analysed. Since this experiment took place while writing this thesis, only a short description and outlook will be given about it (Sec 5.9).

In this chapter the article entitled *Determination of the beta-neutrino angular correlation coefficient, a, from $^{35}$Ar decay* is presented. Later in this chapter additional information on the data analysis will be given.

---

### *Determination of the beta-neutrino angular correlation coefficient, $a$, from $^{35}$Ar decay with the WITCH setup*

**S. Van Gorp**[1]**, M. Beck**[2]**, M. Breitenfeldt**[1]**, V. De Leebeeck**[1]**, P. Friedag**[2]**, F. Glück**[5]**, A. Herlert**[3]**, V. Kozlov**[5]**, T. Porobic**[1]**, G. Soti**[1]**, M. Tandecki**[1]**, Ch. Weinheimer**[2]**, D. Zákoucký**[4]**, N. Severijns**[1]

[1] *K.U.Leuven, Instituut voor Kern- en Stralingsfysica, Celestijnenlaan 200D, B-3001 Leuven, Belgium*
[2] *Universität Münster, Institut für Kernphysik, Wilhelm-Klemm-Strasse 9, D-48149 Münster, Germany*
*University of Manchester, School of Physics and Astronomy, M13 9PL Manchester, UK*
[4] *Nuclear Physics Institute, ASCR, CZ-250 68 Rež, Czech Republic*
[5] *Karlsruhe Institute of Technology, Institut für Kernphysik, Postfach 3640, D-76021 Karlsruhe, Germany*

# 5.1 abstract

A measurement of the beta-neutrino angular correlation coefficient $a$ yields information on possible exotic couplings in the weak interaction. We report on the first measurement of $a$ for $^{35}$Ar with the WITCH setup, which uses a double Penning trap and a MAC-E retardation spectrometer, and outline the procedure to analyze such data. Simulations cross checked with experimental data are used to take into account the behavior of the ions in the Penning trap. It will be shown that a statistical precision of about 0.5% is reachable, opening up the possibility of contributing to searches for exotic interactions.

# 5.2 Introduction

The most general Hamiltonian for beta decay consists of 5 Lorentz-invariant weak currents with corresponding coupling constants: vector (V), axial vector (A), tensor (T), scalar (S) and pseudoscalar (P) currents [Severijns et al., 2006; Lee & Yang, 1956]. The Pseudoscalar contribution is negligible in $\beta$ decay since nucleons can be treated non-relativistically. Further, scalar and tensor interactions are not included in the vector-axial vector weak-interaction theory of the Standard Model [Severijns et al., 2006; Herczeg, 2001]. Although this provides a good description to date, scalar and tensor currents are not fully ruled out experimentally. Experimental limits on these exotic interactions with respect to their vector and axial vector counterparts (95.5% CL) are $\frac{|C_S|}{|C_V|} < 7\%$ on scalar and $\frac{|C_T|}{|C_A|} < 9\%$ on tensor currents [Severijns et al., 2006; Severijns & Naviliat-Cuncic, 2011]. A possible presence of these currents implies the existence of corresponding mediator bosons [Severijns et al., 2006; Herczeg, 2001], particles which are searched for directly with the LHC accelerator. In low-energy processes, such as nuclear beta decay

and free neutron decay, scalar or tensor currents would induce small shifts in the values of experimental observables that can be looked for in precision measurements [Severijns et al., 2006; Jackson et al., 1957]. In particular, measuring the $\beta$-$\nu$ angular correlation coefficient, $a$, provides high sensitivity to both scalar and tensor currents and has therefore been addressed a number of times already (see e.g. [Johnson et al., 1963; Adelberger et al., 1999; Scielzo et al., 2004; Gorelov et al., 2005; Vetter et al., 2008; Fléchard et al., 2011]). Most recent experiments use ion or atom traps which offer the advantage of a scattering-free source. This is essential as one has to observe the very low-energy daughter ion (with a typical kinetic energy of the order of 100 eV) to determine the kinematics of the decay (i.e. of the mother ion into a daughter ion, beta particle and (anti-)neutrino). The majority of these experiments observe coincidences between the $\beta$ particle and the recoiling nucleus created in $\beta$ decay. The WITCH experiment [Beck et al., 2003; Kozlov et al., 2008; Beck et al., 2010] applies a unique and different method, i.e. it uses a retardation spectrometer to measure the recoil energy distribution, which is correlated via kinematics to the angle between the $\beta$ particle and the neutrino [Kofoed-Hansen, 1954].

## 5.3 Experimental setup

### 5.3.1 General overview

At the WITCH experiment [Beck et al., 2003; Kozlov et al., 2008; Beck et al., 2010] (see Fig. 5.1), located at CERN/ISOLDE [Kugler, 2000], the $\beta$-$\nu$ angular correlation coefficient is determined by measuring precisely the shape of the recoil energy distribution after $\beta$ decay. A continuous 30 keV beam of ISOLDE is bunched in the REXTRAP cooler and buncher [Ames et al., 2005], and the ion packages are transferred to the WITCH setup. In the Pulsed Drift Tube (PDT) [Coeck et al., 2007] in the Vertical Beamline (VBL) of WITCH, the energy of the beam is brought down from 30 keV to an energy between 0 and 250 eV, allowing to capture the beam in the first of two Penning ion traps. In this first Penning trap, the cooler trap, the ions are cooled to a few eV by collisions with helium buffer gas. Radial centering of the trapped ions can be performed by applying a quadrupole excitation on the mass specific frequency $\nu_c = \frac{1}{2\pi}\frac{qB}{m}$ where $B$ is the magnetic field strength and $q$ and $m$ are the charge and mass of the ions, respectively. After preparation in the cooler trap the ions are transferred to the second Penning trap, the decay trap, where they are kept for up to about 5 s and are left to decay. Typically, a potential between 1 V and 5 V is applied to trap the radioactive ions in the decay trap. A stored ion is escaping from the decay trap when it undergoes $\beta$ decay since the total recoil energy it obtains is typically up to a few 100 eV (e.g. maximum 452 eV in the decay of $^{35}$Ar). The total recoil energy is divided among the radial and axial components. When the latter is sufficiently large to overcome the potential barrier of the decay trap (typically of the order of 0.5 eV), the ion will escape the trap.

The total energy of ions is probed with the MAC-E filter principle [Lobashev & Spivak, 1985], see Figure 5.2. As can be seen, the magnetic field varies from 6 T in the Penning trap region to 0.1 T in the analysis plane and undergoes a sudden drop at z=210 cm
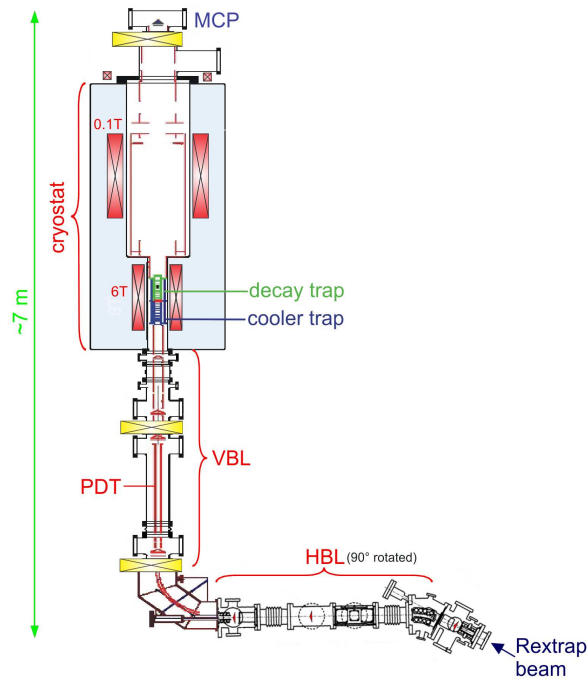
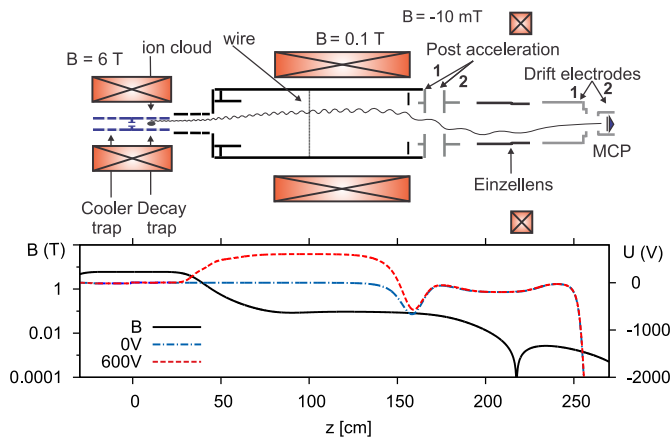Figure 5.1: Layout of the WITCH setup.



Figure 5.2: Overview of the magnetic field and the electrical potential in the WITCH spectrometer. The change in electrical potential along the symmetry axis is shown for the cases without retardation voltage (dash-dotted line) and with 600 V retardation (dotted line). $z$=0 corresponds of the middle of the Penning trap structure.

due to the recently added compensation magnet. In the spectrometer section, a voltage barrier is applied that can only be passed by decayed ions with a sufficiently large recoil energy. The number of ions that make it over this retardation barrier are counted, while varying the voltage of the barrier. From this the integral recoil energy spectrum of the ions after $\beta$ decay is obtained. Because of the operating principle of the spectrometer, with a 6 T magnetic field in the Penning traps and 0.1 T in the retardation region, as much as 98.3% of the ion radial energy is converted into axial energy at the analysis plane (at z=100 cm), where the applied retardation voltage reaches a maximum, such that the total recoil energy can be probed. Ions that pass the analysis plane are pulled off the magnetic field lines towards the ion detector by applying a high negative voltage in the post-acceleration section. An einzel lens and two drift electrodes then focus the ions onto the MCP, which is at -6.4 kV.

This MCP on top of the WITCH setup has an active radius of 41.5 mm, and is comparable to the one described in Ref. [Liénard & et al., 2005]. The DAQ provides, aside from a fast counting branch, also a slower branch that registers the pulse height and position of the incident ion. The fast branch is used to collect the counts, for data analysis, while the slow branch can be used for additional checks on the data (e.g. cuts in radius, time bin, ion charge, ...). More information on the WITCH data-acquisition system can be found in Ref. [Kozlov et al., 2008].

It should be noted that the combination of magnetic and electrical fields can also lead to unwanted trapping of positively and/or negatively charged particles in different parts of the system. These can influence the background count-rate or prevent high-voltage electrodes to be used at their nominal values. We will not elaborate on this in detail here but forward the interested reader to Refs. [Kraus et al., 2005; Baeßler et al., 2008] for general information on these processes in spectrometers or to Ref. [Tandecki, 2011] for the specific case of the WITCH experiment. One such unwanted Penning-like trap in the setup was removed by installing in the einzel lens region a compensation magnet providing a field of $\mathbf{B}$=-10 mT. Prior to installing this magnet, electrons which are created by field emission of electrodes could be stored in the einzel lens region due to a combination of high negative potentials on neighboring electrodes and magnetic field lines connecting these electrodes. The compensation magnet removed this unwanted trap for electrons by modifying the magnetic field lines in the einzel lens region. Further, a wire was installed in the analysis plane in the spectrometer to remove an unwanted Penning trap for electrons at that position, see Ref. [Tandecki, 2011].

## 5.3.2 Selected isotope $^{35}$Ar

The selected isotope for a measurement should fulfill several constraints. It should preferentially have a high production yield at ISOLDE ($10^6 - 10^7$ particles/second), a half-life between 0.5 s and 2 s, a stable daughter isotope, minimal isobaric/isomeric contamination, a simple decay scheme and, if possible not be a $\beta^+$-emitter. Indeed, the larger fraction of the daughter nuclei from the $\beta^+$ decay of a $1^+$ ion, will have zero charge and thus be undetectable. The isotope $^{35}$Ar$^+$ ($t_{1/2} = 1.775(4)$ s) fulfills most of these constraints but has the drawback that it is a $\beta^+$ emitter. After $\beta^+$ decay, 72(10)% of the $^{35}$Cl daughter ions are neutral and are thus lost, while the remaining 28(10)% can undergo

shake-off to provide charge states from $1^+$ up to $5^+$. The charge state distribution after the $\beta^+$ decay of $^{35}$Ar was determined in a measurement performed with the LPC trap setup at GANIL [Couratin, 2012]. This showed that of the about 28 % charged recoil ions about 75% ends up in the first charge state and the remainder in higher charge states.

If stable $^{35}$Cl ions are contaminating the beam composition with a large fraction, they will fill the REXTRAP and WITCH Penning traps, thereby limiting, the number of $^{35}$Ar ions that can be loaded in the decay trap, as has been an issue in the past. Recently, however, the ratio $^{35}$Cl to $^{35}$Ar ions has been brought down by more than two orders of magnitude taking special care in the preparation of the CaO target [Fernandes et al., 2011]. During the experiment described here, the contamination of $^{35}$Cl ions in the beam was only around 1%, allowing a proper transfer of $^{35}$Ar ions to the decay trap.

### 5.3.3 Experimental conditions

The parts of the setup that have a profound impact on the data analysis will be discussed in more detail in this section. These are the timings for efficient loading of ions into the decay trap, the storage conditions of the ions in this trap, and the settings of the spectrometer to probe the energy of recoil ions emerging from the decay trap.

**Penning trap timings**

Ions which leave the PDT section in the VBL with an energy between $0\,\mathrm{eV}$ and $250\,\mathrm{eV}$ are captured in the cooler trap. When the ion bunch has entered this trap the entrance electrode voltage is raised to block the ions from going back into the vertical beam line after they have been reflected at the potential of the endcap electrode. Once captured, the ions are prepared in the cooler trap, during $500\,\mathrm{ms}$, and then transferred to the decay trap where they are stored for $1.5\,\mathrm{s}$ and are let to decay. The total trapping cycle can be divided into five steps. Each step has a certain duration and different potentials are applied on the Penning trap electrodes:

1. In the beginning of the cycle the $^{35}$Ar$^+$ ions are stored for $500\,\mathrm{ms}$ in the buffer-gas-filled cooler trap while a quadrupole excitation is applied. The parameters of this quadrupole excitation were optimized during the experiment resulting in a frequency ($\nu_c$) of $2.634374$ MHz and an amplitude of $2.5$ V. The combination of buffer gas and the excitation leads to the centring of the ions [Savard et al., 1991].

2. The well-cooled and centred ion cloud in the cooler trap is then transferred to the decay trap by switching the potentials in both traps for $31.5\,\mu\mathrm{s}$.

3. The ions are subsequently kept for $2.005\,\mathrm{ms}$ in an asymmetric decay trap (see inset in Fig. 5.3).

4. The potentials in the decay trap are then made symmetric and the argon ions are stored here for $2\,\mathrm{s}$ while they can undergo $\beta^+$-decay.

5. Finally, any leftover ions are shot downwards at the end of the cycle, through the cooler trap, and the cycle is started again.
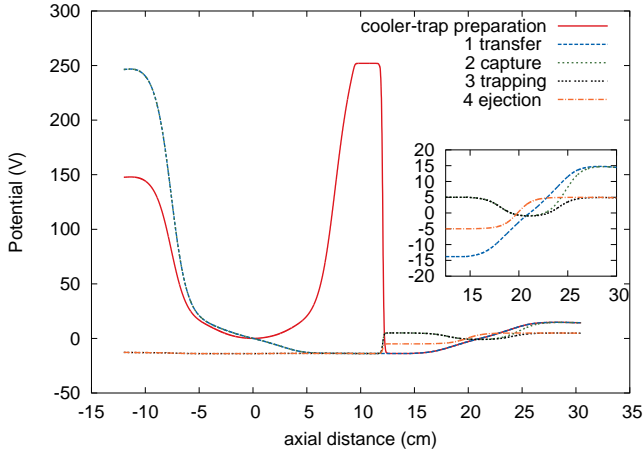
Figure 5.3: Evolution of the electrical potential in the Penning trap system for the different steps in the experimental cycle. The cooler trap is at z=0 cm, the decay trap at z=21.1 cm. The inset shows a zoom of the region of the decay trap.

The applied Penning trap electrode voltages for these steps are shown in Fig. 5.3. Initially 250 V are required on the endcap electrodes of the cooler trap so as to capture the ions coming from the vertical beamline (i.e. the pulsed drift tube). After the cooling process and the transfer to the decay trap, a voltage of 5 V is sufficient to keep the ions trapped there.

### Decay trap

Normally, ions can be stored in the decay trap for up to about 5 s and even longer. This was not the case, however, with the data discussed in this paper (see below). Therefore, the losses in the decay trap have to be taken into account in the analysis.

The decay trap storage efficiency for the settings used in the experiment, was determined using stable $^{39}K^+$ ions, right after the radioactive beam time. Potassium ions were injected in REXTRAP, bunched and transferred to the WITCH setup. The same experimental cycle as during the $^{35}Ar$ run was used in order to exclude other effects. As such, during the first 500 ms the ions were prepared in the cooler trap and afterwards transferred to be stored in the decay trap. Here the amount of $^{39}K^+$ ions was measured as function of the decay trap storage time, see Figure 5.4. One can see that for typical settings of timing pattern and applied voltages in the decay trap there are no severe losses. However, during the experiment, when slightly different timings and voltages were applied, the amount of ions in the decay trap drops gradually from 0.7 s to 1.7 s before flattening out at the level of about 40% of the initial amount. This indicates that the decay trap was not optimally tuned during the experiment and losses occurred,

independent of charge-exchange and effects correlated to radioactivity, but due to the fact that slightly different timing patterns and voltages were applied.
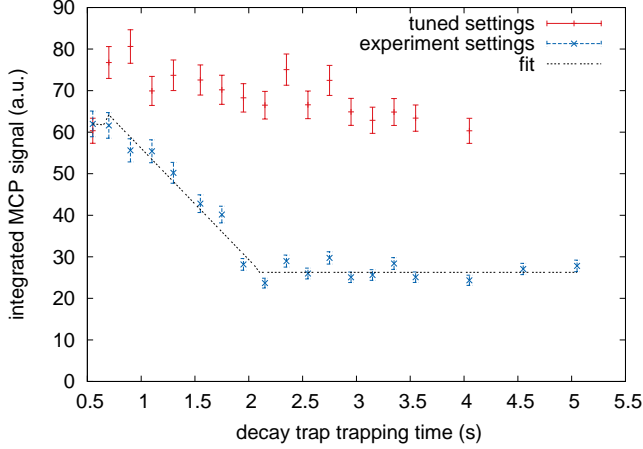


Figure 5.4: Signal intensity on the MCP as a function of the trapping time in the decay trap for $^{39}$K$^{+}$ ions. During the first 500 ms of the measurement cycle the ions are prepared in the cooler trap, which is not shown.

The reason for this is not understood and an in-depth determination of these losses is, unfortunately, not possible anymore due to an upgrade of the mechanical and electrical trap-structure, shortly after the data were taken, which now allows to store ions up to 6 s without noticeable losses. Since the physics mechanism behind these losses is not known, but it nevertheless has to be taken into account, as a first approximation the behavior of the ion losses in function of the trapping time was fitted with a straight line. A first one for times between 0.7 s and 2 s, representing the loss of ions and yielding $f(t) = 82.9(8) - 26.8(5)t$. Since before 0.7 s and after 2 s of storage in the decay trap no significant losses were observed, these data were fitted to a constant, yielding the value 61.8(9) and 26.4(4) respectively. The total fit function can thus be summarized as:

$$f_{dt}(t) = \begin{cases} 61.8 & \text{for } t \leq 0.7 \, \text{s} \\ 82.9 - 26.8 \, t & \text{for } 0.7 < t < 2 \, \text{s} \\ 26.4 & \text{for } t \geq 2 \, \text{s} \end{cases} \tag{5.1}$$

and resulted in a reduced $\chi^2$ of 2.3. Eq. 5.1 will be used to correct the data in the analysis (see below).

## Spectrometer

Table 5.1 summarizes the calculated optimal spectrometer electrode settings [Friedag & et al., 2012] and the values actually used during the experiment. Due to technical

| Electrode name | optimal values (V) | Actual values(V) |
|---|---|---|
| SPACC01 | -2000 | 0 |
| SPACC02 | -9000 | -1000 |
| SPEINZ | -600 | -200 |
| SPDRIF01 | -9000 | 0 |
| SPDRIF02 | -9000 | -6400 |
| MCP | -9000 | -6400 |

Table 5.1: Optimal values and actually used values for the spectrometer electrode settings in the post acceleration section (SPACC01-2), einzel lens (SPEINZ) section, drift section (SPDRIF01-2) and the MCP detector. The positions of the different electrode sections are indicated in Fig. 5.2.

difficulties, which have been solved in the meantime, the electrode settings could not be operated at the optimal values, causing a non-optimal focusing of the ions. Especially the too low voltages in the acceleration section made it difficult to focus all recoiling daughter ions onto the MCP detector. In turn, this resulted in an energy and charge-dependent focus that will be discussed in the section about ion tracking simulations 5.5.2 .

## 5.4   Measurements

### 5.4.1   Acquired data set

The measurement cycle starts by cooling the ions for 500 ms in the cooler trap prior to transferring them to the decay trap. The ions were stored in there for 2 s while their decay was observed. Significantly more counts are observed in the time bins at 0 and 0.5 s, which is respectively due to overshoot of ions from the VBL to the cooler trap and overshoot of the decay trap when transferring the ions from the cooler trap to the decay trap.

For the first spectrum, which we will name spectrum 1, no retardation voltage was applied, see Figure 5.5a. This spectrum was used to check the stability of the system and served as normalization for the analysis. Thereafter the measurement was repeated, this time applying a retardation voltage in certain time bins so as to measure the recoil energy distribution, see Figure 5.5b. This spectrum will further be called spectrum 2. During the last second of the measurement cycle no retardation voltage was applied.

### 5.4.2   Pulse height distribution of the recoil ions

The magnitude or pulse height of an MCP signal, caused by an incident particle, can vary depending on the number of electrons created by the event in a channel and on the number of channels excited by the incoming particle. The Pulse Height Distribution (PHD) of MCP signals has a certain shape [Scielzo et al., 2003], showing a sharp rise
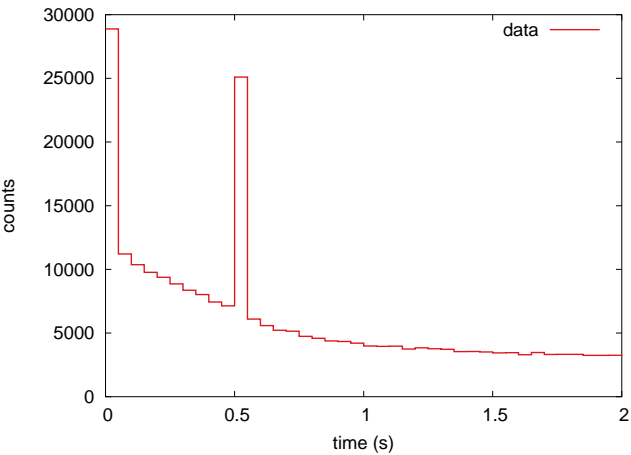
(a) Measurement without retardation voltage (spectrum 1)
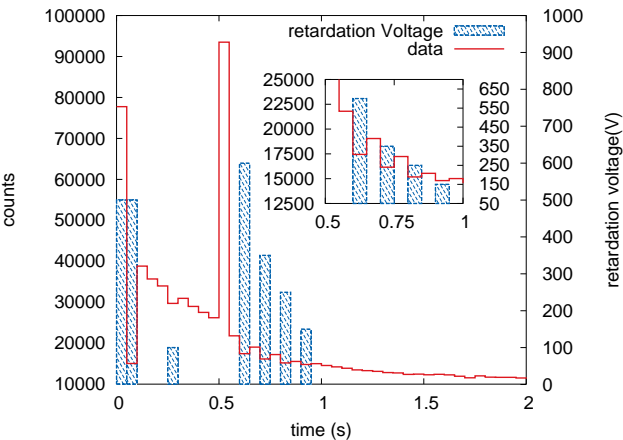


(b) Measurement with retardation voltage (spectrum 2)

Figure 5.5: Resulting spectra (note the difference in the amount of counts collected). Panel (a) shows the measurement with no retardation barrier applied, and was used for normalization. Panel (b) shows the results of the measurement with retardation voltages applied in some of the time bins (see inset).

followed by an exponential drop in counts for both beta-particles and dark counts, while for ions the PHD distribution has a bell-like (Gaussian) shape. Therefore, the PHD can be used to demonstrate the presence of recoil ions. The upper graph in figure 5.6 shows the PHD at times when recoil ions are expected to arrive on the MCP detector (i.e. for the time between t=0.55 s and t=0.60 s in spectrum 2, Figure 5.5(b)) and when not (t=0.60 s to t=0.65 s in spectrum 2, when a retardation voltage of 600 V was applied, Figure 5.5(b)). Subtracting these two distributions results in a Gaussian distribution, as can be seen in the bottom graph of figure 5.6, indicating that the difference in the counts collected in these two time bins is indeed due to recoil ions.
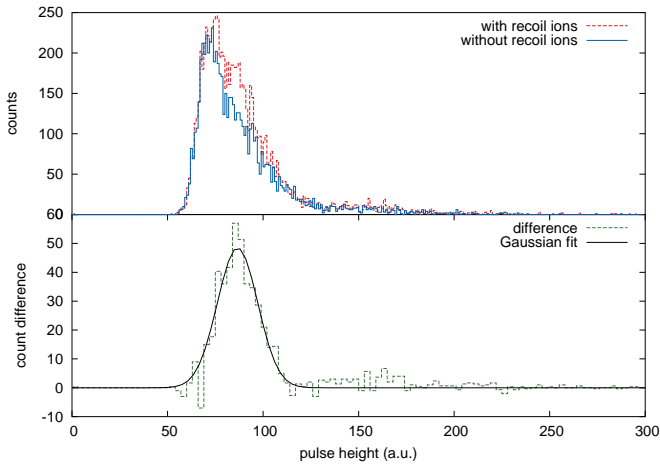


Figure 5.6: Upper panel: PHD of particles arriving on the MCP detector within a radius of 30 mm, without retardation voltage (t=0.55 s to t=0.60 s) and with 600 V (t=0.60 s to t=0.65 s) being applied. Bottom panel: difference in counts for the two PHDs in the upper panel with a Gaussian fit, which is typical for recoil ions.

## 5.4.3 Amount of trapped ions

The total amount of ions trapped in the decay trap can be estimated from the amount of argon ions delivered by ISOLDE or from the amount of collected recoil ions on the MCP. Due to experimental time constraints, the efficiency of the WITCH beamline and Penning traps, as well as the amount of argon ions in a single REXTRAP bunch could not be determined precisely. Therefore the amount of trapped ions in the decay trap was estimated from the amount of recoil ion events counted on the MCP.

The total amount of collected recoil ions is obtained by correcting the observed signal for background and dead counts, both of which are also registered. Therefore the difference is made between the amount of counts in the time bin when recoil ions can reach the MCP (see spectrum 2 at t=0.55 s to t=0.60 s, Figure 5.5(b)), with the counts in the time bin when recoil ions can not reach the MCP due to the 600 V potential in the spectrometer

(see spectrum 2 at t=0.6 s to t=0.65 s, Figure 5.5(b)). This difference equals 2500(300) counts and thus represents the total amount of recoil ions, in the time bin between t=0.55 s and t=0.6 s of spectrum 2, which were collected over all 1771 measurement cycles (4 hour measurement). This result in an average of 1.4(0.2) recoil ions detected per cycle in the time interval between t=0.55 s and t=0.6 s. This number has to be corrected for the efficiency of several processes to obtain the corresponding amount of ions that were stored in the decay trap. The following effects play a role in this with the percentage of ions contributing to the signal due to each effect listed between brackets. Charge state distribution (28(10)%, the rest being produced as neutrals, see section 5.3.1), magnetic field focusing (50%, half of the ions is focused upwards and half is focused downwards), electric field focusing (40%, see section 5.5.2), MCP open area ratio of 52.3(3)% (see Ref. [Liénard & et al., 2005]), percentage of decayed ions in the first time bin after the ions have been transferred to the decay trap (1.85%). Combining all numbers finally results in a total of 2600(900) ions being present in the decay trap after each trap load, with the error being determined mainly by the error on the fraction of charged ions resulting from the $\beta^+$ decay.

# 5.5 Data analysis

The value of the beta neutrino angular correlation coefficient, $a$, is extracted from the data by comparing the experimentally acquired integral recoil distribution with the simulated distribution for the actual experimental conditions. Any mismatch between these two distributions could reveal new physics. The integral recoil distribution is obtained from the acquired spectra (see following paragraph). The simulated distributions are generated with Penning trap and tracking simulations, taking into account the experimental conditions.

## 5.5.1 Reconstruction of the recoil energy spectrum

In general, the recoil energy distribution can be reconstructed from the spectra by using two methods; either by fitting, or by subtracting both spectra from each other after proper normalization. Both methods will be shown in this section.

### Data set 1

Since both spectra (see Fig. 5.5a,b) were acquired over different time intervals, straightforward subtraction is not possible. Instead, scaling of spectrum 1, prior to subtracting both spectra from each other, is required. To obtain data set 1 the appropriate scaling factor, $f$, was obtained by applying a regression analysis on the data. To this end, the data from spectrum 1 (Fig. 5.5(a)) are multiplied with $f$ and subtracted from spectrum 2 (Fig. 5.5(b)). The sum of the squares to be minimized is
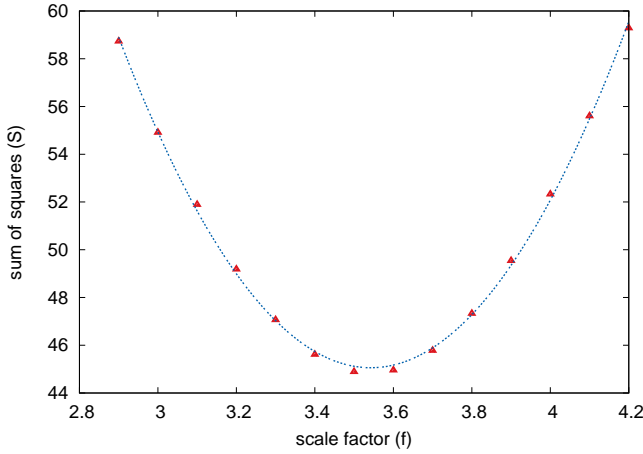
Figure 5.7: Determination of the scale factor $f$ from the regression analysis. The optimal scale factor $f$ was found to be 3.540(3).

than calculated as:

$$S = \frac{\sqrt{\sum_{n=1}^{26} (x_i - \bar{x})^2}}{N}, \tag{5.2}$$

with N the number of time bins, $x_i$ the difference in counts between the data set with retardation voltages applied and the scaled normalization data set, and $\bar{x} = \sum x_i$. Note that the bins at times when a retardation barrier was applied were left out of the regression analysis. Figure 5.7 shows the result of this analysis, leading to $f = 3.540(3)$ for the scaling factor. Figure 5.8a shows the subsequent result of subtracting both spectra, after applying this scaling factor. This result still has to be corrected for the half-life of $^{35}$Ar of 1.775(4) s and for losses in the decay trap (Eq. 5.1) which is shown in Figure 5.8 as well. We will refer to this result as data set 1. The excess of counts in time bins where a retardation voltage was applied is due to stopped recoil ions. It can be seen that this difference is larger for 600 V compared to 150 V. Although data were taken for only four retardation voltages, the recoil energy distribution can be reconstructed from this.

## Data set 2

Instead of applying a regression analysis, the scaling factor can also be obtained from the ratio of the number of counts in a single bin in both data sets. Naturally, this approach is only valid when the counts in this bin directly relate to the total amount of collected ions in the data set, and thus, in turn, to the amount of stored ions in the decay trap. During the transfer of ions from the cooler trap to the decay trap, at t=550 ms, a fraction of the ions has a too large energy to be captured in the decay trap. These will be collected on the MCP and result in the overshoot peak (Fig. 5.5(b)). Since the buffer gas pressure
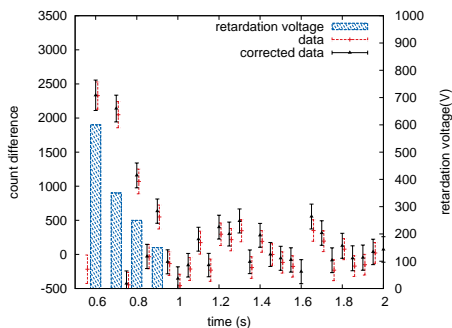
(a) Data set 1.
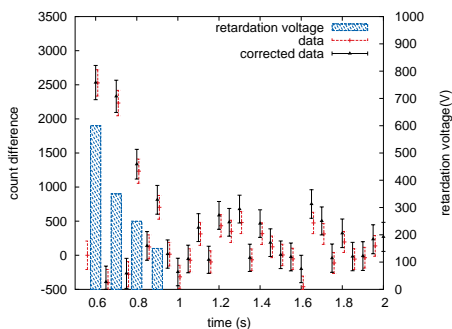


(b) Data set 2.
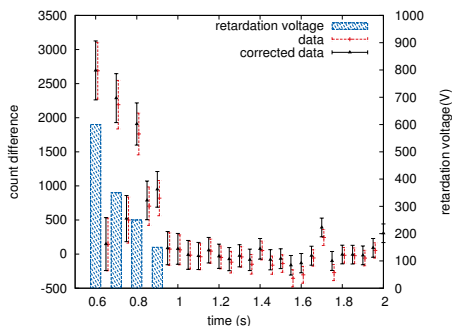


(c) Data set 3.

Figure 5.8: Difference in counts between the spectra obtained with retardation voltages applied and the scaled spectra without retardation voltages applied. Shown is the raw data and the data corrected for the $^{35}$Ar half-life and losses in the decay trap, see text for details. Both data set 1 (with the regression analysis), data set 2 (normalization with the amount of counts in the overshoot peak) and data set 3 (by fitting the data) are shown.

and trapping time in the cooler trap were kept constant during the measurements, it can be assumed that the energy distribution was identical during all cycles, leading to an identical fraction of well-cooled and less well-cooled ions and hence to the same fraction of overshoot and stored ions in the decay trap. Therefore the amount of collected counts in the overshoot peak relates to the amount of ions stored in the decay trap, and can thus be used as normalization. The ratio of the overshoot peaks in both spectra equals $f = 3.575(25)$. Note that the error bar is around an order of magnitude larger as that obtained in the regression analysis. The final result obtained for $a$ will thus also have a larger error bar when determining $f$ by normalizing on the overshoot peaks. Figure 5.8b represents the resulting difference in counts between both measurements when this scaling method is used. As can be seen, comparable results are obtained as with the previous method. For future use we will call this data set, data set 2.

A more careful investigation of data set 2 shows that the overall background value, obtained by averaging the counts in all bins where no retardation voltage was applied, is found to be 143(40), which is off the expected value of zero. A raise in background counts can e.g. originate from ionization of rest gas atoms in the system when switching the retardation voltage barrier (which is different in both data sets). However this process should reveal itself in the bins next to the bins when the retardation voltages are switched, i.e. between t=0.55 s and t=1 s. In these bins the background averages to -91(100) which is within the expected value of zero. Therefore ionization processes can be excluded. It might also be that the MCP is, or some of the MCP channels are, in saturation when the overshoot ions hit the MCP [Coeck et al., 2006]. Due to fluctuations over time in the ion-beam intensity the average amount of counts during both measurements (Fig. 5.8a,b) can then vary slightly , while the overshoot peak is always in saturation, independent of the amount of ions, and this does not change in intensity. This effect will result in a non-zero background. In any case the observed mismatch hints that the normalization method using the amount of counts in the overshoot peak is not an appropriate approach. For comparison, the average background for data set 1 equals 7(35), well within the expected value of zero.

## Data set 3

Finally, one can also take the data of spectrum 2 (Fig.5.5(b)), omitting the time bins where a retardation voltage was applied, fit this with an appropriate function, and subtract this from the full data set, now including all time bins, to obtain the difference in counts due to the applied retardation voltages.

To this end the data was fitted with a convolution of an exponential and the losses in the decay trap ($f_{dt}$):

$$f(t) = A + b \cdot e^{-tc} f_{dt}(t) \tag{5.3}$$

with $f_{dt}(t)$ as given in Equation 5.1. The results of this fit for the data of spectrum 2 (Fig. 5.5(b)) is shown in Fig. 5.9 and yields $A$=11342(25), $b$=33400(1000), $c$=2.22(4) with $\chi^2/\nu$=3.1. The large reduced error indicates that the fit function is too simplistic. Applying the same procedure to the data of spectrum 1 (Fig. 5.5(a)) yielded c=2.32(11) ($\chi^2/\nu$=1.8), in good agreement with the fit for the data of Fig.5.5(b) (the larger error
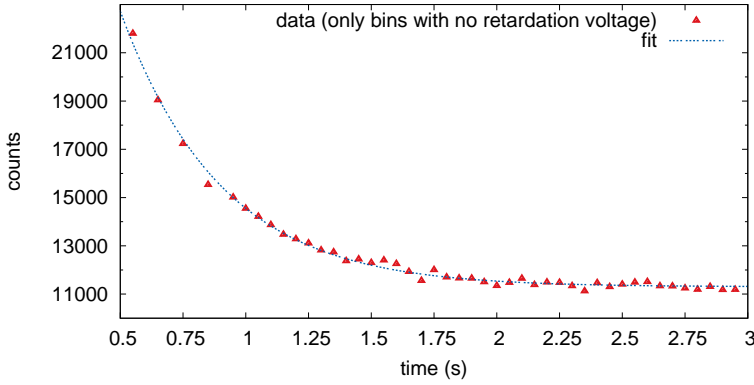
Figure 5.9: Fit of the dataset of Fig.5.5(b) with time bins where a retardation barrier was applied left out. See text for a summary of the fitted parameters.

bar being due to the smaller amount of statistics collected). The differences between the actually measured number of events for the time bins where a retardation voltage was applied and the values expected from the fit with Eq.(5.3) will further be referred to as data set 3 (see Fig. 5.8(c)). As will be shown later (sec. 5.5.4) the results of this additional analysis method are less precise than the results, for data sets 1 and 2 due to the uncertainty on the slope and amplitude of the fit, leading to a larger error on the expected amount of recoil ions.

## 5.5.2 Simulations

Simulations were applied to generate the expected recoil energy spectrum, taking into account the different experimental effects that modify the ideal spectrum shape. The Simbuca simulation package [Van Gorp et al., 2011] allows to investigate the behaviour of ions in a Penning trap and is applied to obtain the position and velocity distributions of ions in the ion cloud stored in the decay trap. These input parameters are given to the SimWITCH simulation package which adds a random recoil energy to the daughter ion and calculates the path of the recoiling ion tracks with a particle tracking routine. The tracking follows the recoil ions from their creation from $\beta$ decays in the ion cloud in the decay trap, trough the spectrometer, up to their arrival on the MCP detector [Friedag & et al., 2012] or their loss in the system.

**Penning trap simulations**

The input data for the ion tracking routine are the initial positions and velocities of the ion cloud in the decay trap. These parameters are obtained with the Simbuca simulations program [Van Gorp et al., 2011]. Simbuca is a versatile Penning trap simulation program, that can handle ion excitations, electric and magnetic field maps, buffer gas collisions and Coulomb interactions between the ions. The latter are calculated in Simbuca with a graphics card (GPU) to dramatically reduce the simulation time. The simulations described here were performed for a cloud consisting of 2600 $^{35}Ar^+$ ions (cf. Sec 5.4.3) with the Coulomb interaction applied between them.

The helium background pressure in the decay trap, due to leaking of buffer gas from the cooler trap, can be obtained from gas flow calculations [Neidherr et al., 2008]. Given the diameter (2 mm) and length (5 cm) of the differential pumping diaphragm between the cooler trap and the decay trap, the helium pressure was calculated to be $4 \cdot 10^{-8}$ mbar, a factor of about 2600 times less than in the cooler trap, which is comparable to the gauge read-out. Due to this low pressure in the decay trap, the chance for recoil ions to collide with buffer gas atoms is small. If the ion cloud is stored for 0.5 s in the decay trap, the influence of the helium pressure in the decay trap causes a 2% decrease in average kinetic energy of the ion cloud and a 2% increase in average ion cloud radius.

In order to take into account the experimental settings, the COMSOL [comsol, 2011] package was used to calculate the field map due to the electric potentials applied on the Penning trap electrodes. The magnetic field map was provided by the magnet manufacturer. Note that the ion cloud properties are simulated for the entire duration of the experimental cycle, i.e. from the capture of the ions in the cooler trap until they are transferred to and then stored in the decay trap, see Sec 5.3.3. The exact value of the initial velocities and positions of the ions in the cloud in the cooler trap are not of too big importance, since a quadrupole excitation was applied for a long enough period (500 ms) for the ions to be cooled down to their minimal possible energy (i.e. ≈0.1 eV) and for them to be centred. Note that our simulations have shown that the maximum energy of the cooled and stored ions at room temperature is not 0.025 eV, but rather 0.1 eV due to buffer gas heating. The bunch with $^{35}Ar^+$ ions that arrives in the cooler trap has a Gaussian position distribution with a FWHM of 6 mm after being switched down from 30 keV to ground potential in the pulsed drift tube section (see Figure 4.16 in Ref. [Coeck et al., 2007]). The initial velocities are randomly chosen according to a Maxwell-Boltzmann distribution with its maximum at 0.2 eV.

After the cooling process, during which the FWHM of the Gaussian distribution was reduced to 0.1 mm the ion cloud was transferred to the decay trap in 31.5 μs. An optimal transfer does not provide the ions with additional energy nor does it influence the spatial distribution. Simulations later showed that during the experiment the trap was, unfortunately, not optimally tuned and that the optimal transfer time would have been 38.2 μs. Figure 5.10 shows the mean energy and axial position of the ion cloud as a function of the transfer time. As can be seen, a non-optimal transfer leads to a higher energy of the ions in the decay trap, in this case 4.5 eV. During the experiment the trap voltages are always tuned to be as low as possible, with a minimal amount of ion losses. This resulted in a 5 V potential, in good agreement with the maximum ion energy of 4.5

| | | Exp. settings | | Optimal settings | |
|---|---|---|---|---|---|
| | $\mu$ | $\sigma_{100}$ | $\sigma_{2600}$ | $\mu$ | $\sigma$ |
| $x$ (cm) | 0 | $4.1 \cdot 10^{-3}$ | $5.0 \cdot 10^{-3}$ | 0 | $3.3 \cdot 10^{-3}$ |
| $y$ (cm) | 0 | $4.1 \cdot 10^{-3}$ | $5.0 \cdot 10^{-3}$ | 0 | $3.3 \cdot 10^{-3}$ |
| $z$ (cm) | 0.032 | 3.0 | 2.8 | 0 | 0.4 |
| $v_x$ (m/s) | -0.2 | 379.5 | 460 | 0 | 386 |
| $v_y$ (m/s) | -0.1 | 379.7 | 460 | 0 | 385 |
| $v_z$ (m/s) | -5 | 3400 | 3290 | 0 | 424 |

Table 5.2: Overview of the simulated Gaussian position and velocity distribution (mean value, $\mu$, and spread, $\sigma$) in the decay trap for the settings as applied during the experiment (first column) and for the optimal settings when a perfect transfer between the traps is assumed. The Gaussian distributions are determined from a fit to all velocities and positions of the ion cloud during 0.5 s of storage in the decay trap. The subscript 100 and 2600 indicates the amount of simulated $^{35}$Ar$^+$ ions.

eV as determined with simulations. Due to this too short transfer time the resulting ion cloud was located 1.5 cm below the centre of the decay trap.

The position and velocity parameters of the ion cloud in the decay trap follow a Gaussian distribution. The values calculated by Simbuca for the actual experimental conditions as well as for the optimal settings are listed in Table 5.2 (for both 100 and 2600 ions in the traps). It can be concluded that the offset of about 7 $\mu$s in optimal transfer time leads to an almost 10 times broader axial velocity ($v_z$) and axial position ($z$) distribution.

Comparing the simulations with 100 and with 2600 ions stored in the decay trap shows that when more ions are trapped the radial position and velocity distributions become slightly wider, while the axial distribution shrinks. Due to the Coulomb repulsion between ions, the ion cloud will broaden if the ions are close together. This effect, however, is in our case here is only visible in the radial direction, since in the axial direction the harmonic-oscillator-like motion of the ions is spread over too large a distance ($\sigma$=3 cm, due to the non-optimal conditions) so that the cloud will be *cooled* due to the Coulomb interaction between the particles. Cooling by Coulomb interaction is thus the same as due to buffer gas collisions; the cloud is cooled axially and heated in radial direction. Note that this simple picture is not valid anymore when at least 10000 ions are stored in the decay trap [Van Gorp, 2012], as in the latter case the ion cloud starts to behave as a non-neutral plasma [Dubin & O'Neil, 1999].

**Monte Carlo tracking simulations.**

Once the position and velocity distributions for the ion cloud in the decay trap are established, these are used as input for the SimWITCH [Friedag & et al., 2012] Monte Carlo (MC) simulation program that tracks the recoil ions created by $\beta$ decays in the decay trap on their way to the MCP detector. For this the electrode and magnetic field
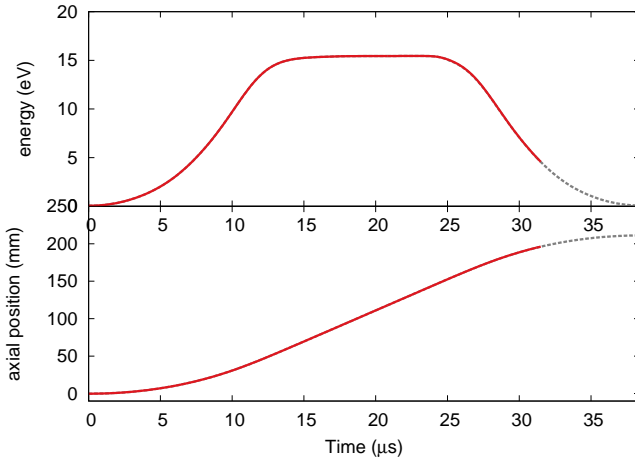
Figure 5.10: Average kinetic energy (top panel) and axial position (bottom panel) of the ion cloud in the decay trap as a function of the transfer time. In the experiment the duration of the transfer was set to be $31.5\,\mu s$ (end of the solid line) instead of $38.2\,\mu s$ (end of the dashed line), the optimal value that was later found in simulations.

configurations in the retardation spectrometer are used. The electric and magnetic field calculations in SimWITCH are based on the work described in Refs. [F. Glück, 2011a,b]. The path of an ion in the spectrometer is calculated via a Runge-Kutta routine of eight order [Verner, 1978]. Further, SimWITCH takes into account various effects like velocity Doppler broadening and losses due to trap depth.

SimWITCH simulations were performed for the different retardation voltages used in the experiment (i.e. 0, 150, 250, 350 and $600\,V$) and for $1^+$ up to $5^+$ charge states. Figure 5.11 shows the simulated expected number of counts for $1^+, 2^+$ and $3^+$ charged daughter ions as a function of their recoil energy. As can be seen, around 60% of the singly charged ions will be lost, which is due to the non-optimal high voltage settings in the spectrometer (see Table 5.1). The applied negative voltages in the post-acceleration section are not high enough in absolute value to pull the positively charged ions off the magnetic field lines and focus them onto the detector. As can be seen, for $^{35}Cl^{X+}$ daughter ions with recoil energies above about $150\,eV$ the transmission efficiency starts to drop considerably. This can be explained since ions with a lower energy have to spend a longer time to travel from the decay trap to the MCP detector and can thus more easily be manipulated, and thus focused, by electromagnetic fields. The same figure also reveals that the transmission efficiency is larger for higher charge states which is due to two effects. Since the electric force on a $X^+$ charge is X times higher than on a $1^+$ charge it is much easier to focus the higher charge states onto the detector, leading to less losses for the latter. Further a higher charge state has a smaller cyclotron radius in the magnetic field, and is thus easier to focus on the MCP. Figure 5.12 shows where the $1^+$ and $2^+$ ions are lost in the system as function of the axial distance $z$. As can be seen, quite some ions are not pulled
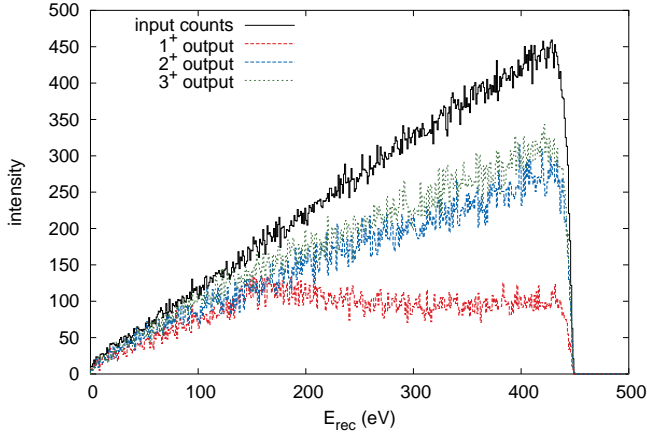
Figure 5.11: Simulation input (solid black curve) and corresponding output results as a function of the recoil energy for different charge states of the $^{35}Cl^+$ recoil ions (dashed colored curves). The scatter on the curves is not physical but stems from the statistics of the simulation. Note that the original input spectrum has already been reduced by a factor of two for good comparison with the output spectra for the different charge states, since only half of the recoil ions are focused into the retardation spectrometer by the magnetic field.
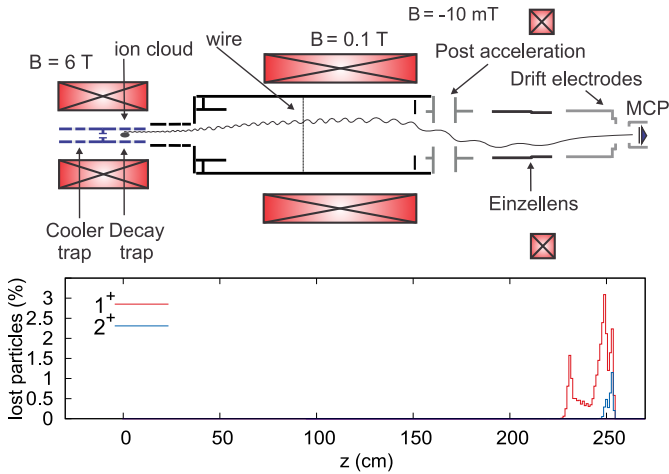


Figure 5.12: Simulated ion losses distribution for the $1^+$ and $2^+$ recoil charge states with $0\,V$ retardation voltage applied.

off the magnetic field lines (which go outwards in the einzellens region, see Fig. 5.2) by the electrodes in the post-acceleration section. A considerable fraction of the ions is thus not focused onto the MCP but hit the first drift electrode instead. When design values are applied, no losses are expected.

## 5.5.3 Simulation validity

The simulated position distribution of the recoil events on the MCP detector can be compared with the experimentally obtained one. Due to the low efficiency of the slow data acquisition and the available statistics, it is opted to compare the radial distribution of events on the MCP instead of the position distribution. This radial distribution can be simulated by assuming the Standard Model value of $a$=0.9004 [Severijns et al., 2008] to create the recoil ions energy distribution. Simulation results for the different recoil ion charge states from $1^+$ to $5^+$ were then combined according to their relative abundances [Couratin, 2012].

The radial distribution for the experimental data was obtained by calculating the difference in the number of counts in a time bin where recoils are being observed (i.e. at t=0.55 s to t=0.60 s) and the next bin where 600 V was applied to block all recoil ions, automatically also subtracting the background counts and counts from $\beta$ particles on the MCP detector.

Figure 5.13 shows the experimental and simulated radial distributions. As can be seen in the central part of the detector, either the simulations overestimate the data or experimental counts are missing. Inspecting the experimentally observed position distribution, it was found that central counts (i.e. $|x| < 1$ mm) are missing consistently along the y-axis. This was found to be an artefact of the MCP caused by non-optimal fine-tuning of the y-delay line, leading to missing counts in that area. Apart from this, Fig. 5.13 shows good agreement between the simulated and experimental radial distributions.

## 5.5.4 Deducing the beta-neutrino angular correlation coefficient

The goal of the WITCH experiment is to determine the $\beta$-$\nu$ angular correlation coefficient, $a$. This is done by comparing the result of the full MC simulation for $a$=1 and $a = -1$ with the experimental data. Both MC simulations were performed for all applied retardation voltages and all recoil ion charge states ranging from $1^+$ to $5^+$. Results for the different charge states were then combined, taking into account the measured charge state distribution [Couratin, 2012], to obtain the expected amount of recoil ions events on the MCP detector for each retardation voltage used.

Equation 5.4 shows the fit function to extract the value for $a$ by comparing the experimental data with a linear combination of the simulated results for $a$=1 and $a = -1$, with the correlation coefficient $a$ and the amplitude as fit parameters. This can be done
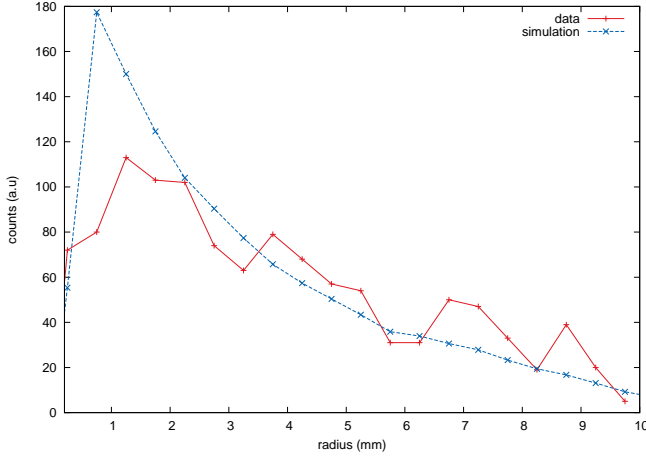
Figure 5.13: Radial distributions of events on the MCP detector obtained from the data and from simulations.

since the expression for the recoil energy spectrum is linear in $a$ [Kofoed-Hansen, 1954].

$$f(a) = \text{amplitude} \left( \frac{1-a}{2} f_{a=-1} + \frac{1+a}{2} f_{a=1} \right) \tag{5.4}$$

Figure 5.14 shows the result of this fit to the data set 1 (see section 5.5.1), yielding $a=1.12(33)$ for the beta-neutrino angular correlation coefficient. Although $a > 1$ is non-physical, within error bars the value agrees with the Standard Model value of 0.9004(16) [Severijns et al., 2008]. Also shown are the simulated, expected spectra for $a=1$ and $a=-1$ for the experimental conditions used. It can be seen that the expected amount of counts is higher for $a=-1$ than for $a=1$. A recoil energy distribution for $a=-1$ favors lower recoil energies. At these lower recoil energies the higher charge states will contribute more to the observed counts, since a $X^+$ charge is blocked in the spectrometer section with a maximum retardation voltage of $452/X\,V$. Since further the detection efficiency is higher for higher charge states (see Sec.5.5.2), more recoil ions will be observed if the recoil energies are distributed with a value of the angular correlation coefficient more towards $a=-1$ than towards $a=1$.

Table 5.3 summarizes the results of the analysis for the different data sets discussed in section 5.5.1. As explained in section 5.5, data set 1 and set 2 are obtained in a similar way, i.e. by scaling the measurement without retardation voltages applied with a factor $f$, prior to subtracting this measurement from the measurement with retardation voltages applied. This factor can be obtained by regression analysis, which leads to data set 1, or by looking at the overshoot peak, data set 2. As discussed before, data set 2 is less precise and less trustworthy due to the offset in its background. For data set 3 a fit of the data was used to reconstruct the expected number of events when a retardation voltage was applied. The value for $a$ obtained for data set 3 has a larger error bar, which is mainly due to the uncertainty on the slope and amplitude of the fit. Nevertheless the
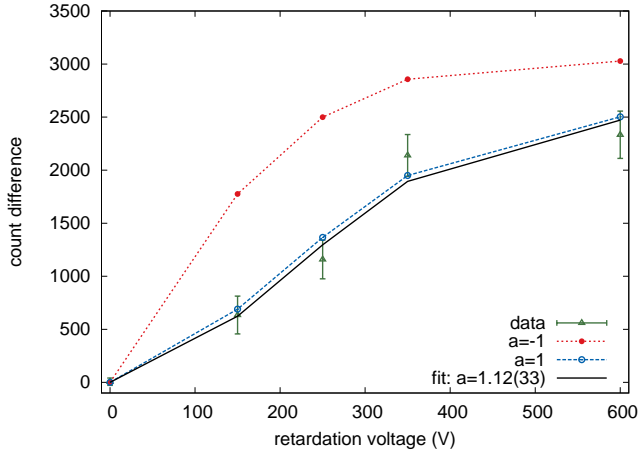
Figure 5.14: Results of the analysis of data set 1. The black line corresponds to the best fit to the data, yielding a=1.12(33). For comparison the curves expected for $a$=1 (pure vector interaction) and $a$=-1 (pure scalar interaction) are also shown. Lines were drawn to guide the eye.

| data set | $\chi^2$/NDF | $a$ | amplitude |
|---|---|---|---|
| 1 | 0.64 | 1.12(33) | 0.43(4) |
| 2 | 0.86 | 0.90(40) | 0.45(5) |
| 3 | 0.36 | 0.71(55) | 0.46(8) |

Table 5.3: Summary of the obtained fit results for the $\beta$-$\nu$ angular correlation coefficient $a$ and the amplitude, for the three data sets described in Sec. 5.5.1. Error bars are only statistical.

procedure described here and the result showed in Fig. 5.14 demonstrate the proof of principle for measuring the $\beta$-$\nu$ correlation coefficient with a Penning trap and MAC-E filter retardation spectrometer based setup as well as the procedure adopted for analysis of such data.

Note, finally, that if the data are analyses with a transfer time between the traps of $38.5\,\mu$s instead of $31.5\,\mu$s, i.e. assuming optimal conditions for the transfer between the two traps instead of the actual experimental conditions, this would have resulted in a value of $a$=2.62(42) with a $\chi^2/\nu$=1.1, i.e. 4 standard deviations from the expected value of 0.90. This shows that using the exact source conditions, as obtained with the Simbuca code, is crucial for a correct determination of the $\beta$-$\nu$ angular correlation coefficient.

### 5.5.5 Systematic error

The total systematic error in this measurement was estimated to be at most about 10%, see Ref. [Tandecki, 2011]. As this is low compared to the still large statistical error, we will not deal with this in detail here. The main contributions to the systematic error stem from the knowledge of the energy distribution in the trap, the axial size of the ion cloud and the detection efficiency over the MCP surface. Other effects, like, the knowledge of the magnetic field ratio, the electric potential barrier and the $^{35}$Ar half-life, are estimated to have a much smaller influence [Tandecki, 2011].

Clearly, a good understanding of the ion cloud energy and position distribution, as well as measurements of the energy distributions of the ions in the decay trap will be required for a precise determination of $a$. Methods to both simulate and measure the energy distributions are currently available and being improved. Also, a method to map the MCP efficiency is being developed. Further, the mono-energetic recoil ion peak expected at $542$ eV, which corresponds to electron capture decays between the $^{35}$Ar and $^{35}$Cl ground states, would yield an additional measurement of the energy resolution. However, the branching ratio of 0.06% for this process renders observation of this peak very difficult and requires much more statistics.

## 5.6   Summary

We have presented the commissioning of the WITCH experiment with its prime physics candidate, $^{35}$Ar, leading to a first determination of the $\beta$-$\nu$ angular correlation coefficient $a$ with the WITCH setup, albeit still with limited statistical precision. The observation of recoil ions was shown by using the pulse height information from the MCP detector. The analysis methods used show consistent results and point to the importance of simulations of the properties of the ion cloud in the Penning trap and of tracking simulations, that were both successfully applied for the data analysis. The validity of the simulations was checked by comparing the experimental and simulated radial distributions of the ions on the MCP, which was found to be in good agreement.

## 5.7   Outlook

The measurement discussed here can be improved at many places to increase the amount of recoil ions that are collected. First the target/ion source combination used here was not operating at optimal conditions yet. The intensity of the ISOLDE beam sent to the WITCH setup can still be increased with a factor of about 10. Also, the measurement time can be up to 50 hours instead of the 5 hours of data that were available for this analysis. A factor of two to three in statistics can still be gained as well by modifying the measurement cycle, i.e. observing the ions in the decay trap for 1.5 s instead of 500 ms. Further, optimum voltage settings on the spectrometer electrodes would focus all ions, which yields another factor of two. Finally, general tuning in WITCH, and especially tuning the injection of the slowed down ion beam into the magnetic field,

would allow for an improvement factor of 4. All these improvements will result in an increase in statistics by a factor of about 8000, bringing down the statistical error below 0.5% thereby allowing a precise determination on the $\beta$-$\nu$ angular correlation coefficient, $a$, with the present setup.

A new measurement was performed in November 2011. At this time no losses in the by then renewed decay trap were observed, and, due to an improved injection in the magnetic field, an increased $^{35}$Ar yield, and a longer measurement time, data corresponding to a statistical precision below 5% could be collected, thereby opening up the next phase of the WITCH experiment, i.e. an extensive investigation of systematic effects. These data are currently being analysed and results will be reported in due time.

## acknowledgments

# 5.8   Additional Information

In this section additional items about the analysis are discussed in more detail. This list is in a rather random order.

## 5.8.1   Beam composition

Figure 5.15 shows the decay of implanted 20 to $250\,\mathrm{eV}$ $^{35}$Ar ions on the MCP detector at the top of the WITCH setup. The beam was around 99% pure, with the other 1% being $^{35}$Cl ions.

The fitted half-life of the implanted ion species is determined as $1.70(1)\,\mathrm{s}$. This value is lower than the literature value of $^{35}$Ar of $1.775(4)\,\mathrm{s}$ [Severijns et al., 2008].
The MCP consists of a glass core with a $200\,\mathrm{nm}$ conductive NiCr layer on it, on top of which a thin, $21\,\mathrm{nm}$, $SiO_2$ coating is applied. Simulations performed with SRIM [srim, 2011] show that the implantation depth of the $^{35}$Ar ions is between 13 and 19 nanometer only, as such that the argon ions are implanted in the silicon-oxide layer. The difference in observed half-lives can then be explained by the fact that part of the argon ions diffuse out of the $SiO_2$ coating, leading to a shorter half-life being observed. Note that correcting this value for the (small) dead-time will cause it to deviate slightly more from the literature value.
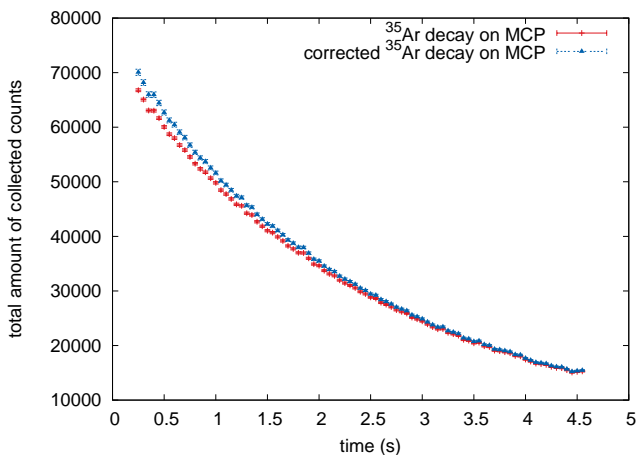


Figure 5.15: Decay curve of $^{35}$Ar implanted on the MCP detector yielding a half-life of $t_{1/2}{=}1.697(12)\,\mathrm{s}$. Correcting for dead time (see text) the decay-curve becomes slightly steeper leading to a half life of $1.642(13)\,\mathrm{s}$. This value is off the literature value of $1.775(4)\,\mathrm{s}$, which can be attributed to the fact that argon atoms, as a noble gas, can diffuse out of the MCP detector after implantation.

|         | data set 3   | data set 4.  |
| ------: | :----------: | :----------: |
| $A$     | 11342(25)    | 3202(28)     |
| $b$     | 33400(1000)  | 10500(700)   |
| $c$     | 2.22(4)      | 2.34(10)     |
| $\chi^2/\nu$ | 3.1     | 1.8          |

Table 5.4: Overview of the fitted parameters.

The total dead-time is in fact the convolution of two dead-times: the electronics (discriminator) can be busy processing a signal and thus not being able to deal with the signal of a newly arriving particle, and an MCP channel can be in saturation from a previous event when a new one arrives. The dead-time of the DAQ readout system is negligible.

The discriminator can only accept events that are arriving within at least 20(5) ns of each other. The observed counts $N$ have to be corrected taking into account the dead time $\tau_1$ so that

$$N^{'} = \frac{N}{1 - N\frac{\tau_1}{t_b}}, \tag{5.5}$$

with $t_b$ the length of the measurement bin. For the data taken this error turns out to be between 2.5 to 0.5% depending on the amount of collected counts in a single bin.

The spot-size during the measurement covered about 7.5% of the entire MCP surface. Given that the typical dead time of one channel is $\tau_c = R \cdot C = 32 \cdot 10^6 (\Omega) \cdot 213 \cdot 10^{-12} (F) = 6.8$ ms, and that the MCP has $6 \cdot 10^6$ channels: the average dead time due to saturation of the MCP equals $\tau_2 = \frac{\tau_c}{6 \cdot 10^6 \cdot 0.075} = 15.1$ ns. The final count rate $N^{''}$ is then obtained by correcting $N^{'}$ with $\tau_2$ via Eq. 5.5. The correction of the data for both dead times yields a half-life of 1.642(13) s. No other species except $^{35}$Cl were $^{35}$Ar are expected to be present in the beam, as this measurement confirms.

## 5.8.2 Decay Trap halflife uncertainty

The error bars on the points in Fig. 5.4 were not determined during the measurement (although each point is the average of 16 points). To overcome this, typical fluctuations in the observed ion signal (due to ion-source fluctuations, voltage drift and possible timing offsets) were measured separately (see Fig. 5.16), yielding a maximum fluctuation of about 5%. The obtained 5% deviation was then used as uncertainty for the decay trap losses, which is a conservative (overestimated) value considering the losses in the decay trap were averaged over 16 points.

## 5.8.3 Extra (less sensitive) analysis

Here an extra analysis will be applied to reconstruct the recoil energy spectrum, we will refer to the resulting data set as data set 3. As briefly mentioned in section (5.5)
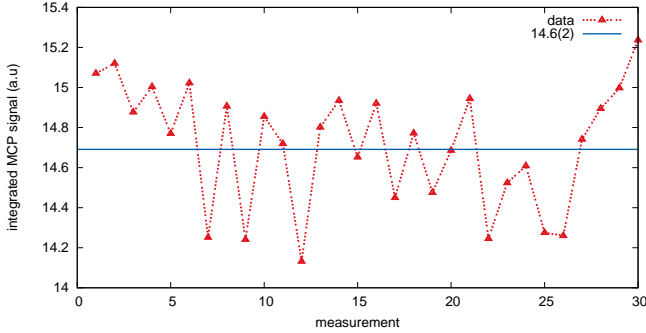
Figure 5.16: Measured fluctuations in the ion signal.

one can also fit spectrum 1 (Fig. 5.5(a)) instead of spectrum 2, which was applied to construct data set 3. Also here equation 5.3 is used to fit the data, of which the results are summarized in 5.4. Compared to data set 3, there are more points to fit trough the function where it drops exponentially, so one might expect a more precise result. However since this is only a one hour measurement (instead of four hours) the error on the points is larger which in turn reflects in a larger error bar on the fitted slope, i.e. 4% instead of 1.8%. Therefore this data set results in a less precise result $a$=0.57(89) with a $\chi^2/\mu = 0.19$, compared to data set 3.

## 5.8.4 Radial distribution as a function of charge state.

Figure 5.18 shows the radial distribution on the MCP detector for the different charge states of the $^{35}$Cl-daughter ion. As can be seen, daughter ions with a higher charge state hit the MCP more in the center, compared to daughter ions with a lower charge state. Since the cyclotron radius in a magnetic field is $r = \frac{mv}{qB}$, a higher charge has a smaller radius. When an ion is passing from a high magnetic field of 6 T to a low magnetic field of 0.1 T, its radius is blown up with a factor of $\sqrt{\frac{6}{0.1}} = 7.7$ due to conservation of the magnetic flux ($\Phi = \pi r^2 |\mathbf{B}|$). This increase is charge-independent but it does cause lower charge states, which have the biggest radius in the decay trap, to have an even larger radial distribution on the MCP position.

As discussed before higher charge states are easier to manipulate with electric fields. Therefore highly charged ions are easier to rip off the magnetic field lines by applying a potential on the electrodes in the post-acceleration section, causing a higher focusing efficiency and thus a better centered distribution for the higher charge states (Fig. 5.18). Both electric and magnetic fields thus have a preference to focus lower charge states more off-center and higher charge states more in the center of the MCP.
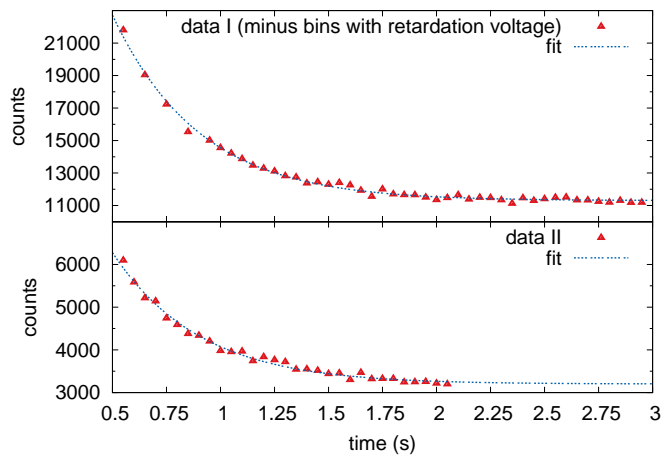
Figure 5.17: Fit of spectrum 1 and 2 with Eq. 5.3. The upper graph represents a fit to the data in spectrum 1 which resulted in data set 3, as was already discussed before (section 5.5.1). The bottom graph represents the fitted data of spectrum 2. See Table 5.4 for a summary of the fitted parameters.
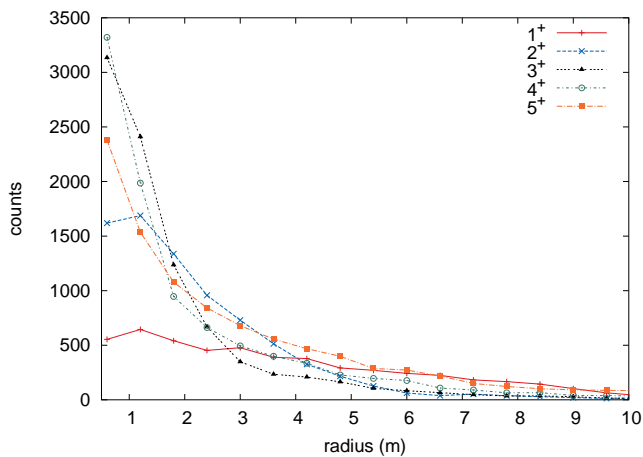


Figure 5.18: Simulated radial distribution for the different charge states of the $^{35}$Cl-daughter ion. Ions with a higher charge state typically have smaller radial distribution.

Figure 5.19 shows the change in radial distribution of ions on the top MCP in function of the applied retardation voltages of 0, 150, 250, 300 and 600 V. One can see that for a higher retardation voltage the radial distribution is broader. Indeed, higher retardation voltages are blocking more ions in the higher charge states thus allowing the relative contribution of detected $1^+$ ions to become higher compared to $2^+, 3^+, 4^+$ and $5^+$, implying a broader radial distribution of the daughter ions over the MCP surface for higher retardation barriers. Unfortunately it is not possible to compare these simulations
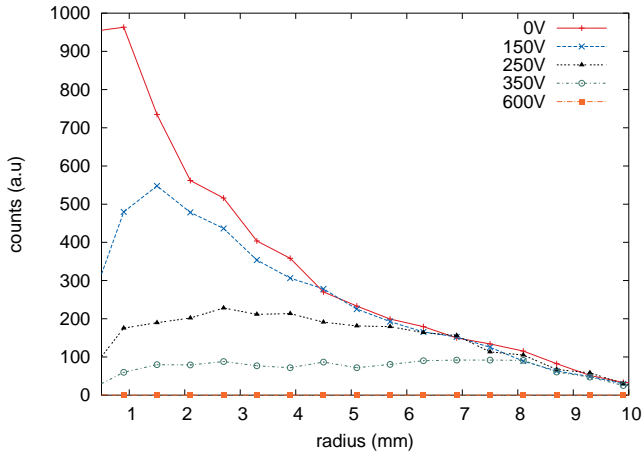


Figure 5.19: Simulated radial distribution of the recoil ions on the top MCP detector. For lower retardation voltages a more central beam-spot is observed. This can be explained by the fact that a lower retardation voltage causes a larger distribution of the higher charge states, which are arriving more in the center of the MCP.

with the experimental data due to the (very) low count rate of recoil ions in the slow data branch for higher retardation voltages. Figure 5.19 can be verified later when more data will be available taken.[1]

## 5.8.5 Estimated charge state distribution from the decay

The information of the charge state distribution is folded in the recoil-energy distribution since the count rate at a higher retardation voltage has relatively more contribution from the lower charge states. It is thus possible to estimate the charge state distribution from the measured recoil-energy distribution.

Since the electric force scales with the charge, the maximum retardation barrier to block all recoil ions with charge $z$ is $452/z$ V, here 452 eV is the maximum recoil energy for a $1^+$ ion. E.g. for a $3^+$ ion the maximum retardation barrier will be 150 V. During the

[1]The distributions obtained here might depend on the quite unique settings that were applied during last run, i.e. the low voltages on the high acceleration section.

measurement, only retardation voltages at 0, 150, 250, 300 and 600 V were applied. Since not much retardation barriers were applied at a low voltage where the sensitivity to the higher charge state is the largest, an estimation of the charge state distribution will thus not be sensitive to the lower charge states $3^+$ up to $5^+$ (which are in total 8% of the ions after decay). Therefore only the ratio of singly charged to double charged recoil ions will be estimated, with the contribution of higher charge states taken from Ref. [Couratin, 2012].

A simulation was performed for all charge states and for $a = 1$ and $a = -1$. The outcome of these simulations were folded with the charge state distribution with a fraction of $x$% to the expected amount of collected $1^+$ recoil ions and $92 - x$ % for the expected amount of $2^+$ recoil ions, the leftover 8% thus being divided among the higher charge states [Couratin, 2012]. Figure 5.20 shows the different values of $a$, when the fraction $x$ of the $1^+$ ions was varied.

Given the large uncertainty on the resulting values, the $1^+$ contribution of the charge state is found to be between 72% and 90% which is in agreement with the 74.6(10)% as given in [Couratin, 2012]. Furthermore a higher contribution of the $1^+$ charge state yields a lower value of $a$, thus making the charge state-distribution an important systematic effect that will directly influence a measurement and will need to be taken into account to extract $a$.
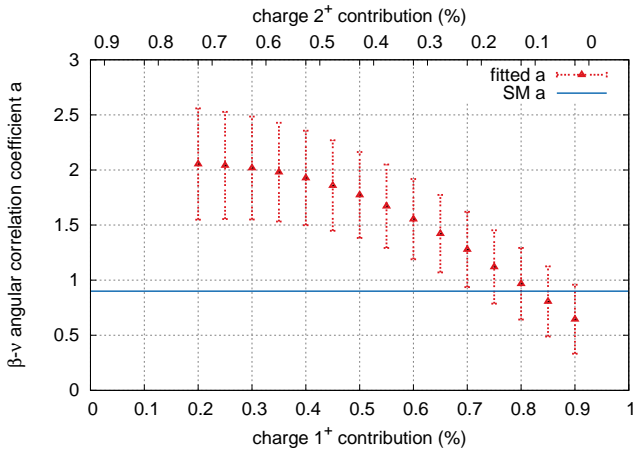


Figure 5.20: The value and the error on $a$ can be extracted for different contributions of the $1^+$ (and $2^+$) charge states, using a 8% contribution for higher charge states as given in [Couratin, 2012]. The contribution of $1^+$ ions changes the value of $a$ and thus constitutes an important systematic effect to be taken into account in a more precise determination of $a$.

## 5.8.6   Recoil ions position Distribution

Figure 5.21 shows the position distribution of events on the MCP detector for measurements with and without retardation voltage applied, for the central part of the detector. The excess of events in panel (a) is due to recoil ions. All ions were found



(a) with recoil ions



(b) without recoil ions
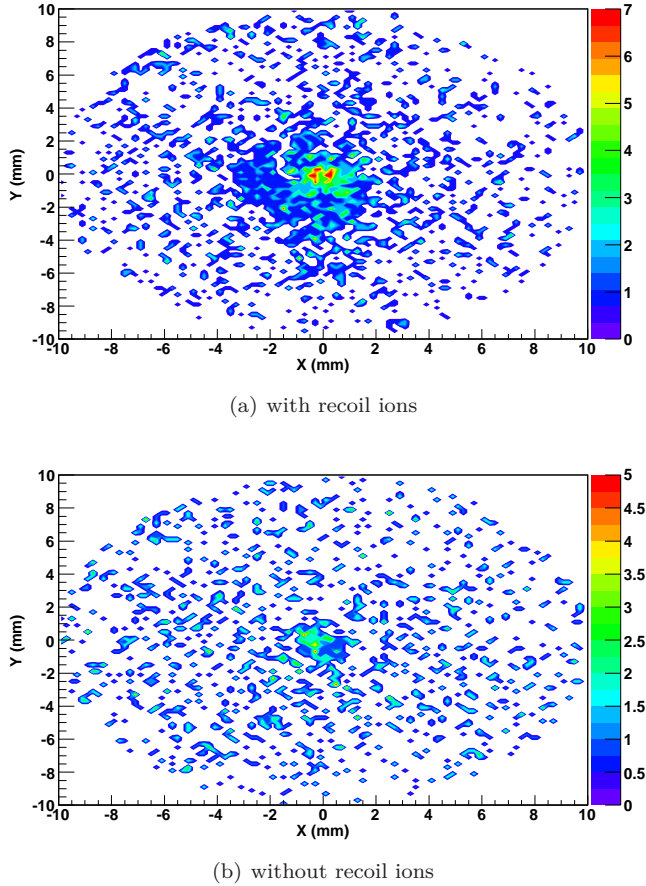
Figure 5.21: Position distribution with $0\,V$ (at t=0.55 s) and $600\,V$ (at t=0.6 s) applied retardation voltages in the analysis plane, respectively. Without voltage applied the daughter ions, coming from the decay trap, can reach the MCP. Applying a retardation barrier of $600\,V$ block these ions. The difference between $0\,V$ and $600\,V$ is thus due to recoil ions. As can be seen the position distribution of the recoil ions is quite narrow, i.e. below $1\,cm$ FWHM. Not that the data was shifted -3.5 mm in y-direction to center the beamspot.

to arrive close to the center of the detector, with the observed spot being offset by 3.5 mm. This misalignment was not observed in off-line tests with the MCP and so must be related to the beam. Detailed inspection of fig. 5.21(a) shows that counts are systematically missing in the central region along the y-axis. This is believed to be an artifact, caused by non-optimal tuning of the delay-lines of the MCP detector.

# 5.9 Autumn 2011 experiments

Two experimental runs with the WITCH setup, both using different CaO targets, were performed in autumn 2011. Initially, only a single experiment was planned in October 2011. For this, a new type of CaO target using nanostructured porous material Fernandes et al. [2011] providing a larger yield of $^{35}$Ar was planned (Section 2.8.1). However, due to technical difficulties (the vacuum seal of the target broke during the baking procedure), the same target that had been used already in the 2011 June run and in the November 2009 run had to be used once more. Therefore, the yield was still a factor of 5 lower than requested.

During a second experimental campaign, in November 2011, the new type of CaO ISOLDE target was available, which greatly enhanced the collected amount of statistics. Furthermore, the efficiency of the ion transmission in the VBL was improved by a better injection of the slow ions in the WITCH magnetic field. Overall around 20 times more statistics were gathered in this experiment compared to the experiment a few weeks earlier. Below we will briefly discuss the quality of the data obtained in both runs and give some reflections as to the analysis of these, which is currently ongoing.

## 5.9.1 October 2011

During this experiment, the ion transmission efficiency trough the WITCH setup improved considerably compared to the June 2011 experiment. In addition, losses were no longer observed in the decay trap, and the spectrometer electrodes could be operated as intended. Overall these efforts allowed to surpass the statistics of the June experiment already after 30 minutes of data taking. During this run a variety of voltage patterns were applied in the spectrometer, with the aim to better understand the setup and investigate whether a certain voltage pattern would be more sensitive to a measurement of $a$ than others. An example of an applied voltage pattern and the resulting collected amount of counts on the MCP can be seen in Figure 5.22. During this measurement the retardation barrier in the spectrometer was switched periodically between blocking the recoil ions (ON) and allowing ions to pass on to the MCP detector (OFF). The measured difference in counts between the ON and OFF periods is thus due to recoil ions. Note that in this resulting spectrum, Figure 5.22, two overshoot peaks appear. A first peak occurs at t=0 s and is due to ions coming from the PDT that fly trough the cooler trap when trying to capture them here. A second peak, at t=200 ms, is due to the transfer between both traps, i.e. ions that cannot be captured in the decay trap. Note that the decay of $^{35}$Ar can be seen as well.

## 5.9.2 November 2011

In this run the newly made nanostructured CaO target could be used for the first time on line. This resulted in an about 4 times higher yield compared to the October 2011 run without putting too much load on the target yet as its properties were still to be studied in more detail. Apart from this, careful retuning of the injection of the ion beam into
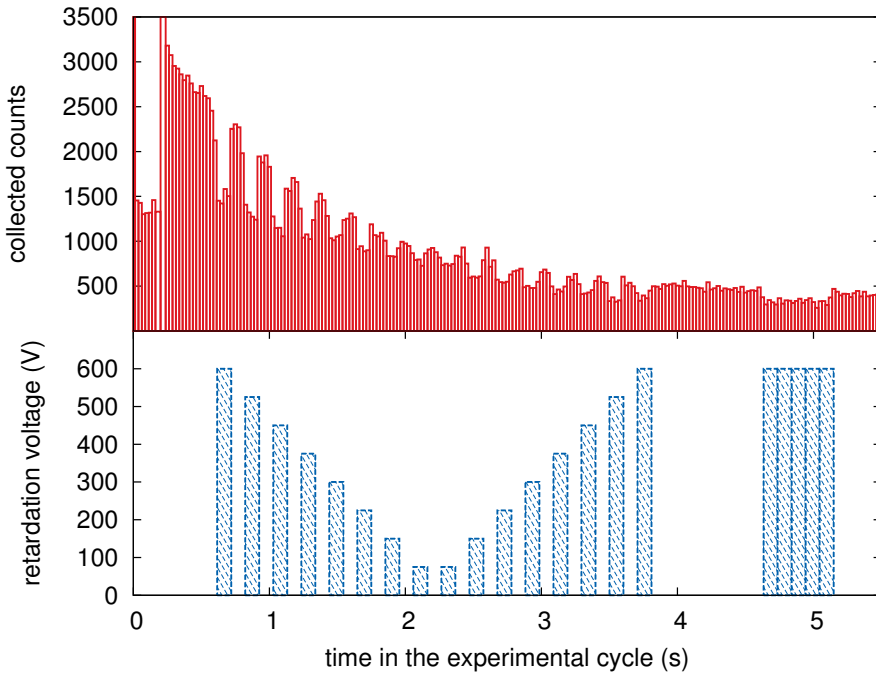
Figure 5.22: Result from one of the measurements from the October 2011 experiment. The X-axis represents the time during the measurement cycle. The bottom panel shows the applied retardation voltages while in the upper panel the collected amount of recoil ions on the top MCP is displayed. The missing counts in the exponential decaying curve thus stem from recoil ions that are prevented from reaching the MCP detector due to the applied retardation voltage.

the WITCH magnetic field had also yielded an about 5 times higher injection efficiency compared to the previous run.

## Data set

Apart from taking measurements with a variety of voltage patterns applied in the spectrometer, as was done in the October 2011 run, also an ON-OFF sequence has been used this time. In total around 16 such ON-OFF measurements were acquired, each of which with a different constant voltage $V$ during the ON period (between t=0.75 s and t=2.4 s in the experimental cycle) (Figure 5.23). During the rest of the cycle no retardation voltage was applied (OFF), except for a period of 0.5 s at the end of the cycle, where a retardation voltage of 600 V was applied such that no recoil ions should reach the MCP.

All 16 measurements, $V$=0, 5, 10, 25, 50, 100, 150, 175, 200, 250, 300, 350, 400, 450, 500, 550, 600 and 700 V, are displayed in the inset of figure 5.23. Note that an unexpected
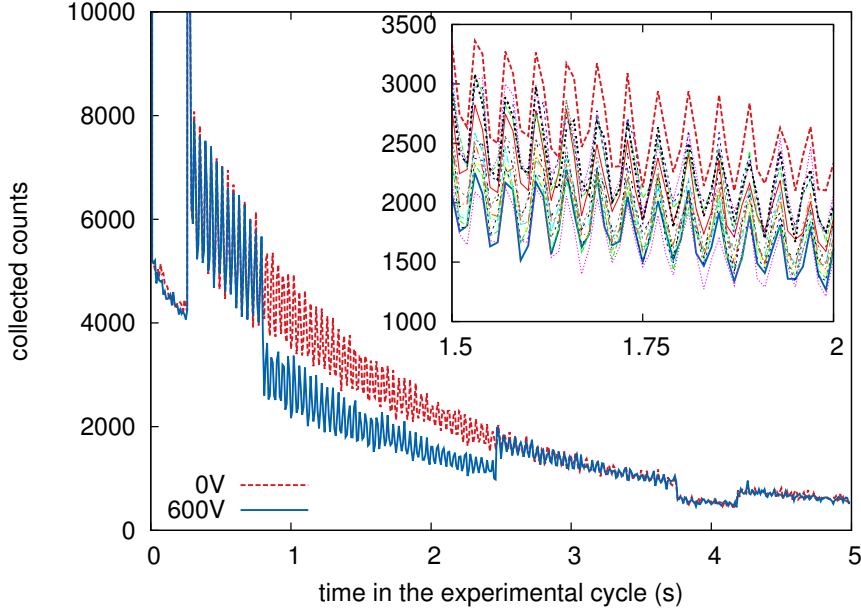
Figure 5.23: Result of a measurement from the November 2011 experiment, showing the ion intensity as a function of time in the experimental cycle. Between t=3.5 s and t=4 s, a retardation barrier of 600 V is applied to prevent all recoil ions from reaching the MCP. Between t=0.75 s and t=2.4 s, a retardation voltage with a chosen voltage $V$ is applied. Shown here are the data from two different measurements, one such measurement with $V$=0 and one measurement with $V$=600. The missing counts in the lower exponential curve, thus stem from recoil ions that are prevented to reach the MCP detector due to the applied retardation barrier of 600 V. The inset shows a zoom of the experimental cycle and displays all different measurements ($V$=0, 5, 10, 25, 50, 100, 150, 175, 200, 250, 300, 350, 400, 450, 500, 550, 600 and 700 V).

oscillation appears on the collected counts. This oscillation has the same period as the magnetron frequency in the decay trap, see Eq.(3.15). Together with other measurements this hints to a misalignment of the magnetic and mechanical axis of the trap electrodes.

The amount of stored ions in the decay trap can be calculated, similar as for the June 2011 experiment (section 5.4.3) as will be demonstrated here. In the time bin between t=1.01 s and t=1.02 s the difference in counts after normalization between the spectra with $V = 0$ V and $V = 600$ V equals 1550(90) and thus corresponds to the amount of recoil ions that are collected in that time bin during the whole measurement that consisted of 200 cycles. Only 0.3% of the ions decay in between the time bins t=1.01 s and t=1.02 s. Part of the ions is also lost due to a non-optimal voltage of the MCP which

causes a non-optimal focus efficiency. This exact number can only be obtained from tracking simulations with a properly simulated ion cloud in the decay trap, given the exact conditions during the experiment. However, for a perfectly cooled ion cloud in the decay trap, around 8% of the ions is lost due to their large radius and subsequent hit with one of the drift electrodes. In this discussion, we will use this 8% of lost ions since the exact source of ions in the decay trap has not been simulated yet. Other corrections due to MCP efficiency, magnetic field focuss and charge exchange are the same as in the June experiment (section 5.4.3). Taking all these effects into account leads to the conclusion that around 40000(14000) ions are stored in the decay trap in each experimental cycle. With this large amount of stored ions the ion cloud will behave like a plasma and the picture of a single trapped ion is not valid anymore (see section 6.2). Simulations with the Simbuca simulation package are therefore required to simulate the parameters of the ion cloud in the decay trap.

## Analysis

The analysis of these data is currently ongoing and will be reported in due time. Different analysis methods will be applied to reconstruct the recoil energy spectrum with the aim to investigate and compare these different methods. E.g. one can subtract the counts in time bins where a certain retardation voltage $V$ is applied, with the counts in time bins where $V = 600 \, \text{V}$. The difference is than only due to counts that stem from recoil ions and can thus be used to construct a recoil energy spectrum after a proper correction for the half-life of $^{35}\text{Ar}$ and possible losses in the decay trap.

The recoil energy distribution can also be reconstructed by fitting the data sets instead of subtracting them. In this case, however, knowledge of all involved physical effects that can create counts on the MCP have to be taken into account. These effects are:

- An MCP will register dark counts ($< 200$ counts/s) which constitute together to a constant background.

- Recoil $^{35}\text{Cl}$ ions which have a sufficiently high energy to pass the retardation voltage barrier. These counts will be convoluted with the half-life of $^{35}\text{Ar}$ and with possible imperfections in the decay trap. Indeed, any change in position and energy distribution of the ion cloud during the storage in the decay trap (see section 6.3.1) can change the transmission efficiency of the recoil ions to the MCP and will thus result in a change in observed half-life of the recoil ions compared to the literature value.

- $\beta$-particles that are created in $\beta$ decays in the decay trap. These particles have a high energy and are not influenced by the electrostatic retardation voltage barrier. They will thus, on average, create an equal amount of counts in each measurement cycle and exhibit the effective half-life of the $^{35}\text{Ar}$ ions in the decay trap (including any losses there).

- $\beta$-particles from the decay of $^{35}\text{Ar}$ ions that were implanted in the MCP, i.e. 'overshoot' $^{35}\text{Ar}$ ions. As discussed before, see section 5.8.1, the half-life of these counts will be different than the half-life of $^{35}\text{Ar}$ due to the volatility of the implanted noble gas. Furthermore, the implantation half-life is dependent on the

implantation energy, which depends on the energy of the incoming ions (which is different for the two overshoot peaks) and on the bias voltage of the MCP. Since the latter was different during the June 2011 (-6.4 kV) and November 2011 (-3.23 kV) experiment the diffusion and hence half-life of the implanted ions will be different as well. Therefore, in principle, this half-life has to be obtained from a separate measurement.

- with each of the above two $\beta$-particle components also goes a component in the spectra coming from $\gamma$ rays de-exciting the 1.2 MeV first excited state of $^{35}$Cl that is populated in about 1.2% of all $\beta$ decays (Fig. 1.5). This component will be small however, also because of the low sensitivity of the MCP to $\gamma$ radiation.

Information on some of the contributions listed above can be obtained/estimated from separate measurements. E.g. an off-line measurement can, in principle, be applied to determine the amount of dark counts on the MCP. A measurement with a continuously high retardation barrier, preventing all recoil ions from arriving at the MCP, will provide the number of counts that stem from $\beta$ particles coming from decays in the decay trap and from implanted $^{35}$Ar ions.

To determine this fraction a separate measurement is not necessarily required as one can also estimate this contribution when the retardation barrier blocks all the recoil ions (Fig. 5.23) in the measurement cycle, i.e. in the time bins where 600 V or 700 V was applied. Similarly the amount of counts in a time bin where the retardation barrier is off (0 V, i.e. no ions blocked) can be used to normalize different measurements with each other. Applying no, a partial or a full blocking voltage will select which type of counts can arrive on the MCP and will thus yield information about the different contributions to the total amount of collected counts. Naturally there is a balance in which fraction of the total time available in each measurement cycle is devoted to no, partial or full blocking voltages being applied. Analysis of the data presented here will be applied to gain more insight into this, as well as in the optimal method to reconstruct the experimentally measured recoil energy distribution.

Note that information of the slow data acquisition of the MCP (section 2.5) can be used as well. From this the ratio of collected $\beta$ particles to ions can be obtained by comparing the respective contributions in the Pulse Height Distribution or by looking at the spot-size, which will be different for $\beta$ particles and for ions Beck et al. [2003]. The main goal of a measurement of the position distribution, however, is to compare it with simulations to verify the validity of the simulations.

## Simulations

The recoil energy distribution will be reconstructed with the use of both ion tracking and Penning trap simulations (see section 5.5.2). For a final determination of the $\beta$-$\nu$ angular correlation with the WITCH setup, however, the wire that was installed in the spectrometer to remove the unwanted Penning-like trap for electrons here will have to be handled more realistically in the SimWITCH program. Currently this wire is implemented as a condition that verifies the coordinates of an ion and *deletes* this ion if its position coincides with the position of the wire. This temporary solution was put forward since SimWITCH assumes cylindrical symmetry in the system, and three-

| charge state | ions that hit the spectrometer wire |
|---|---|
| $1^+$ | 12 % |
| $2^+$ | 20 % |
| $3^+$ | 27 % |
| $4^+$ | 33 % |
| $5^+$ | 38 % |

Table 5.5: Percentage of the ions that are lost in the SimWITCH simulation due to a collision with the spectrometer wire. Note that the resulting percentage was multiplied by a factor 2 to take into account the magnetic field guiding effect, which only ejects half of the ions towards the MCP, the other half being ejected downwards into the VBL.

dimensional field maps can presently not be used. The impact of the wire, however, is significant as is shown in Table 5.5. Here the percentage of the simulated ions that are lost on the wire is shown as a function of the different charge states. For these tracking simulations an ideal ion cloud in the decay trap was assumed, i.e. the ion cloud position and velocity distributions were taken from the Simbuca simulations of the June 2011 experiment, assuming a perfect ion transfer between both ion traps (see Table 5.2). Clearly the amount of ions that hit the wire is large especially for daughter ions with a higher charge state. Since the wire has such a profound impact on the simulation results, a more realistic implementation of the wire, one in which the potential on the wire is taken into account, will thus be required to extract a correct $a$ parameter.

# Chapter 6

# Nonneutral plasma in a Penning trap

When more than one particle is stored in a Penning trap, the Coulomb interaction with other ions will influence the ion motion. This mutual interaction changes the single particle theoretical framework that was described in section (3.2) dramatically.

## 6.1 The nonneutral plasma

### 6.1.1 Introduction

The term nonneutral plasma became common with the publication of Davidson's monograph, Theory of Nonneutral Plasmas in 1974 [Davidson, 1974]. Although the term plasma naturally refers to an ionized gas which is neutral, it has been used in the Penning trap field to describe the nonneutral collection of trapped charges because they have many features of neutral plasmas in common as e.g. the Debye shielding from applied electric fields. This shielding is simply the gas phase analog of the electrostatic screening in electrolytes as described by the chemists Debye and Hückel [Debye & Hückel, 1923]. Debye shielding occurs as a result of the freedom a charged particle has inside the plasma to move in response to the electric fields, and is characterized by the Debye length

$$\lambda_D = \sqrt{\frac{k_b T \epsilon_0}{n q^2}}, \tag{6.1}$$

with $k_b$ the Boltzmann constant, $\epsilon_0$ the permittivity of the vacuum, $T$ and $n$ the plasma temperature and ion density, respectively, and $q$ the charge of the ions. [1]

The collection of charges within a plasma substantially modifies (Debye shield) the externally applied electric fields, such that the ion density is nearly uniform in the ion cloud but drops to zero at the edges of the cloud over the Debye length $\lambda_D$.

The term plasma is only valid if the typical parameters of the plasma, i.e. the radius of the cloud, $r_c$, and the axial length of the cloud $2z_c$, are larger than the Debye length

$$\lambda_D < r_c, z_c. \qquad (6.2)$$

A second, less strong, condition for a non neutral plasma is:

$$n\lambda_D^3 \gg 1, \qquad (6.3)$$

meaning that the numbers of particles within a Debye sphere must be large. The term $1/n\lambda_D^3 \equiv 4\pi\sqrt{3}\Gamma^{3/2}$ is named the plasma expansion parameter, with $\Gamma = \frac{q^2}{ak_bT}$ the so-called coupling parameter and $a$ the Wigner-Seitz radius $4\pi na^3 \equiv 1$. The coupling parameter, $\Gamma$, expresses the strength of the correlations between the collection of charges by taking the ratio of the interaction energy between neighbouring charges $q^2/a$ and the kinetic energy $k_bT$. If the kinetic energy of the particles in the ion cloud is much larger than their interaction energy $\Gamma$ is lower than 1, as is the case for most non-neutral plasmas and also for ion clouds in the WITCH Penning traps. In this case the cloud reveals itself more like a gas than as a liquid or a solid. Analogously, when $\Gamma \geq 2$ the system begins to mimic a fluid and for $\Gamma = 174$ there is a phase transition to a bcc crystal state, which can only be achieved when the ion-cloud is cooled to cryogenic temperatures [Bollinger et al., 2000].

Here we will discuss only weakly correlated plasmas, with $\Gamma < 1$. In this case, the ion density distribution can be calculated starting from the classical Maxwell Boltzmann distribution of the ions, as is done in Refs. [Dubin & O'Neil, 1999; Li et al., 1998].

In the following section the movement of an ion within the ion cloud and the movement of the cloud itself in such a weakly correlated plasma will be discussed. This discussion is mainly based on Refs. [Peurrung et al., 1996; Bollinger et al., 1993], where a phenomenological description of the non-neutral plasma is given. For a more in-depth discussion and a complete theoretical framework, Ref. [Dubin & O'Neil, 1999] is suggested. The motion of a single particle within a charged cloud is very different from the motion of a free isolated particle due to the self-electric field of the non-neutral cloud, even when Eq. 6.2 is not satisfied. Due to the electric fields inside the non-neutral plasma all the eigenfrequencies of a single particle's motion ($\omega_{z,+,-}$) will be affected, either slightly or dramatically depending on the initial size and density of the ion cloud.

---

[1]Sometimes the Debye constant, as well as other variables in the field of plasma physics are given in CGS units instead of MKS units. E.g. the Debye constants in CGS units is $\lambda_D = \sqrt{\frac{k_bT}{4\pi nq^2}}$. In this work all used units are within the MKS system.

## 6.1.2 Motion of a nonneutral plasma

Different methods to obtain the equation of motion of an ion in a non-neutral plasma exist. One way is to start with the spheroidal shape that a plasma has in a cylindrical and hyperbolic Penning trap. The radially outward electric field then has the simple form [Bollinger et al., 1993]:

$$E = a(\alpha)\frac{m\omega_p^2}{q}r, \tag{6.4}$$

with $\alpha = z_c/r_c$ the cloud aspect ratio and $\omega_p$ the plasma frequency, defined as:

$$\omega_p = \sqrt{\frac{nq^2}{\epsilon_0 m}}. \tag{6.5}$$

The plasma frequency is defined for convenience and does not correspond to an actual frequency of the plasma. This equation can be added to the force equation and has two solutions for $\omega$ as given below (Eq. 6.7).

Another method to obtain the solutions for $\omega$, is to calculate in the Lorentz force due to the electric and magnetic fields, which should be equal to the centrifugal force

$$-\frac{nq^2}{2\epsilon_0}r + qB\omega r = m\omega^2 r, \tag{6.6}$$

with $n$ the ion density. The general solution for this equation is:

$$\omega_\pm = \frac{\omega_c \pm \sqrt{\omega_c^2 - 2\omega_p^2}}{2}. \tag{6.7}$$

Note that this equation is similar to the equations of motion for a single particle (Eq. 3.16 and 3.15), but with the single particle axial oscillation frequency $\omega_z$ being replaced by the plasma frequency $\omega_p$. Equation 6.7 also implies that the frequencies are real only if $\omega_c^2/2\omega_p^2 \geq 1$. This inequality sets the maximum density that can be confined, for a given magnetic field $B$ and mass $m$ for a particle and is called the Brillouin limit [Brillouin, 1945]

$$n = \frac{\epsilon_0 B^2}{2m}. \tag{6.8}$$

Note that the Brillouin limit does not depend on the charge of the particle nor on the voltages applied to the trap electrodes. For example for a magnetic field of 6 T and an ensemble of $^{35}\mathrm{Ar}^+$ $\left(^{133}\mathrm{Cs}^+\right)$ ions in the Penning Trap, the Brillouin limit is $2.74 \cdot 10^6$ ions/mm$^3$($7.22 \cdot 10^5$ ions/mm$^3$). Confinement of a nonneutral plasma with density higher than the Brillouin limit is not possible in a Penning trap.

Inside the Penning trap, the ion cloud will have a spheroidal shape. The coefficient $a(\alpha)$ in Eq 6.4 is the cloud aspect ratio, which depends on the ratio of axial to radial length of the spheroid and is given by:

$$a(\alpha) = \frac{1}{2}\left[1 - \frac{1}{\alpha^2 - 1}Q_1^0\left(\frac{\alpha}{\sqrt{\alpha^2 - 1}}\right)\right] \tag{6.9}$$
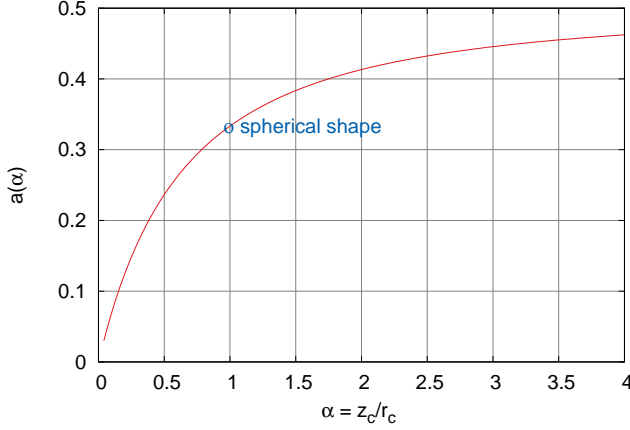
Figure 6.1: Cloud elongation $a$ versus the cloud aspect ratio $\alpha$. For a spherically shaped cloud ($\alpha = 1$) $a = 1/3$, while for a cylindrically shaped cloud of charges ($\alpha = \infty$) $a = 1/3$.

with $Q_l^m$ the Legendre function of the second kind. Note that this Legendre function is different for an oblate ($\alpha < 1$) and prolate ($\alpha > 1$) spheroid [Bollinger et al., 1993]. Figure 6.1 illustrates the relation between the cloud aspect ratio and $a(\alpha)$.

The ion cloud will rotate around its own center of mass with a certain frequency. This can be seen from Eq 6.4; since here the electric field is proportional to $r$ and considering the $\boldsymbol{E} \times \boldsymbol{B}$ drift, the cloud rotates as a rigid rotor with a frequency

$$\omega_r = a(\alpha)\frac{\omega_p^2}{\omega_c} \tag{6.10}$$

$$= a(\alpha)\frac{nq}{\epsilon_0 B}. \tag{6.11}$$

The cloud rotation frequency, $\omega_r$, is thus the frequency with which ions are moving around the cloud centre. Note that this frequency is independent of the mass. From this equation it follows, although this may sound somewhat paradoxical, that the cloud stability is improved with a lower magnetic field and a larger ion density. In an elongated trap with a shallow potential like at WITCH, the ion cloud becomes very long in axial direction and can be approximated as a cylinder. In this limit $\alpha = \infty$ and $a = 0.5$. The ion cloud rotation frequency then becomes:

$$\omega_r = \frac{\omega_p^2}{2\omega_c} \tag{6.12}$$

Furthermore, the plasma frequency $\omega_p$ is related to the axial frequency $\omega_z$, via the aspect ratio $\alpha$ of the ion cloud (see figure 6.2)

$$\frac{\omega_z^2}{\omega_p^2} = \frac{1}{\alpha^2 - 1} Q_1^0 \left( \frac{\alpha}{\sqrt{\alpha^2 - 1}} \right), \tag{6.13}$$

Since $\omega_p^2$ scaler linear with the ion density $n$ and the aspect ratio of the cloud contains
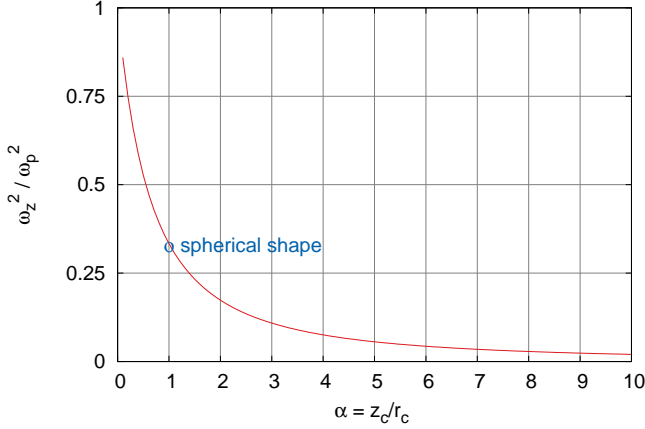
Figure 6.2: Relationship between the cloud aspect ratio $\alpha$ and the squared ratio of the axial frequency over the plasma frequency.

information on its density, a measurement of the axial frequency can in principle be used to extract the density of the ion cloud. To first order the relative frequency shift of $\omega_z$ due to the space charge was determined in Ref. [Winters et al., 2006], for spherical clouds, as:

$$\frac{\Delta\omega_z}{\omega_z} \approx -\frac{nqd^2}{24\epsilon_0}, \tag{6.14}$$

with $d$ and $U_0$ as defined before, i.e. the characteristic length of the Penning trap and the potential difference between the ring and endcap electrodes. The relative shift in $\omega_z$ thus depends linearly on the charge density. A determination of $\omega_z$ is thus a probe to obtain the ion cloud density.

Another convenient relation, finally, relates the total number of ions $N$ and the ion density $n$, since the ion cloud has a spheroidal shape:

$$\frac{N}{n} = \frac{4}{3}\pi r_c^2 z_c. \tag{6.15}$$

## Change in magnetron motion due to image charges

The attraction between the space charge of the ion cloud and the induced image charges on the trap walls causes a slow drift around the trap center in addition to the magnetron motion. This motion is called the diocotron motion [White et al., 1982], and its frequency is given by [Peurrung et al., 1996]

$$\omega_D = \left(\frac{r_c}{r_w}\right)^2 \omega_r \qquad (6.16)$$

with $r_w$ the distance from the center of the trap to the outer wall. In principle image charges are only of importance when the trapped ions are highly charged or moving on a radius close to the trap walls. In case of the WITCH setup, both conditions are not fulfilled, therefore any influence from image charges can be neglected in our case.

## nonneutral plasma simulations

Simulations were performed with the Simbuca code (Chapter 4) to illustrate the principle of nonneutral plasmas, as well as to show that simulations can be applied to simulate the plasma behavior.

In these simulations, an ideal Penning trap with the WITCH parameters as described in Table 3.1 is assumed. The presence of buffer gas ($p = 1 \cdot 10^{-4}$ mbar) was included via the $K_0$ realistic collision model (see section 4.5.3). A cloud of 1000 cesium $1^+$ ions is Gaussian distributed in the center of the trap with $\sigma$ arbitrarily chosen as 2.5 mm. The charge of each ion is scaled with a factor $10^4$ during the cooling and dipole excitation in order to mimic a cloud of $10^7$ ions.
Initially no excitation is applied for 4 ms, such as to let the ions cool down. In a second step all ions are brought out of the centre of the trap by applying a dipole excitation with 0.5 V amplitude for 5 ms on $\nu_-$ (1500.14 Hz). This resulted in an average radius of the ions of about 11 mm. As a final step the cloud is left untouched for another 200 ms to let it arrive in a state of equilibrium. Note that the last step is 200 ms long in order to be absolutely sure that the cloud is in a state where all ions are in equilibrium, thus well-cooled and well-arranged due to the mutual Coulomb interactions (see later, section 6.3.1).

After this preparation time the cesium ions are clustered together in an ion cloud with a radius of 3.5 mm. Further simulations are then performed with this ion cloud as initial condition. In these a different scaled Coulomb factor (ranging between 10 and $10^4$) will be given to the ions to carefully investigate the influence of the amount of ions on the ion motion. Figure 6.3 shows the x, y distribution of $10^7$ ions over time both with and without Coulomb interaction. In both cases, one particle is colored, to allow to follow its track in the figure. Without Coulomb interaction, the ions are moving undisturbed with their eigenmotions $\omega_{-,+,z}$ as was explained already in section 3.2. With Coulomb interaction, however, the $\boldsymbol{E} \times \boldsymbol{B}$ drift that is created by the Coulomb interaction between the ions causes the same ions to move around the cloud center with frequency $\omega_r$. The frequency $\omega_r$ can be extracted by plotting the change in radius of a particle over time as shown in Fig. 6.4.
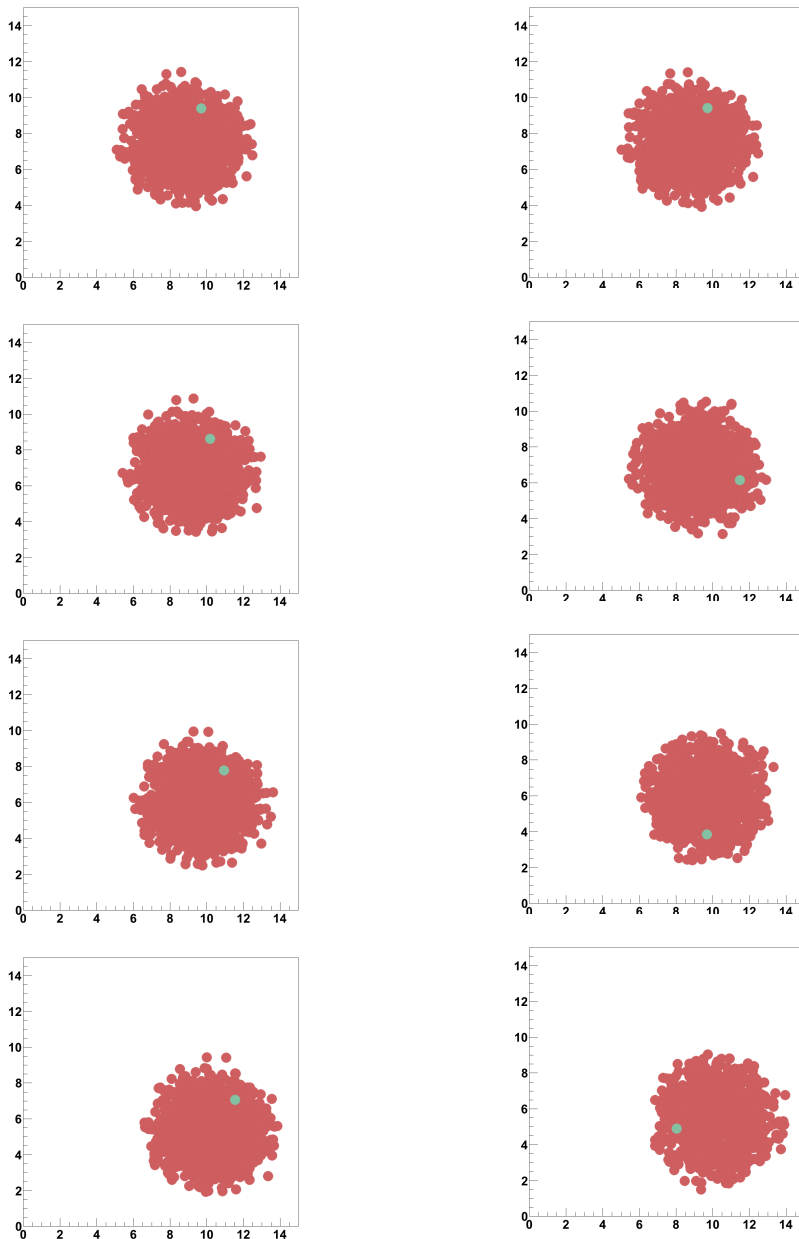
Figure 6.3: Movement of the ion cloud in the X,Y-plane of the trap (in mm). The left column represents 1000 ions without Coulomb interaction. Coulomb interactions between ions are taken into account in the right column. Here 1000 ions are each given a charge of $10^4+$ to represent $10^7$ ions. Ions move 50 $\mu s$ between the frames. Due to the Coulomb interaction in the cloud, the ion rotates around the center of the cloud (right column). Without Coulomb interaction taken into account the ion stays at the same position inside the cloud (left column).
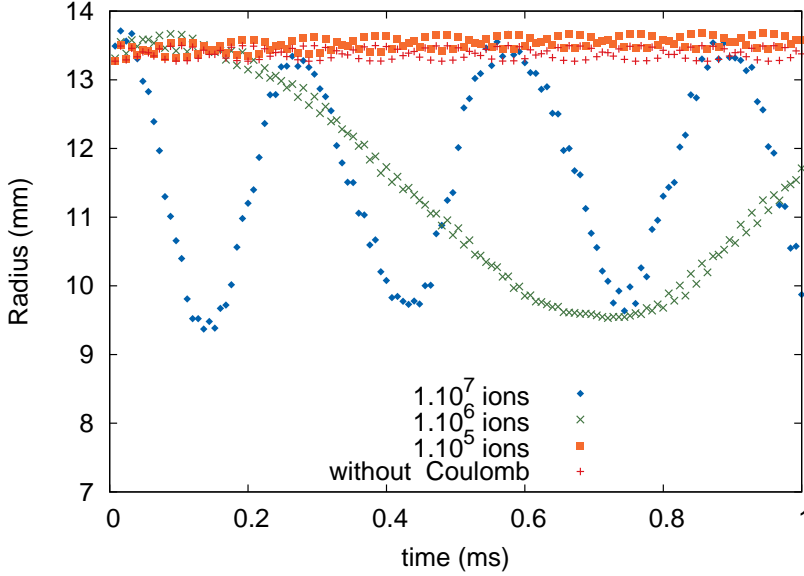
Figure 6.4: Radius at which an ion is movign around the trapcenter versus time, as shown in Fig. 6.3. Under the influence of the Coulomb interaction between the ions in the trap, an ion rotates around the center of the cloud with frequency $\omega_r$. As can be seen, when a cloud contains more ions the rotational frequency increases. Note that the short oscillation observed for $10^5$ ions and for the case without Coulomb interactions is a non-physical phase difference effect caused by the difference between the cyclotron frequency and the frequency with which the simulation data are written to the file.

Applying a Fourier transformation to the change in radial distance of the ion over time allows to extract the rotation frequency $\omega_r$ of the ions motion around the cloud center. This frequency can also be calculated from Eq. 6.11 using as input the density obtained from simulations. Table 6.1 summarizes the simulation parameters and the theoretical frequency $\omega_r$.

Overall there is good agreement between the calculated rotational frequency $\omega_r$ and the one obtained from the fit. The mismatch of a factor $1/2$ (exactly equal to $a(\alpha)$) can have different causes, i.e. a non optimal model for the scaling of the charges, or a too large initial radial distribution. Nevertheless, the global trend is very well reproduced. Simulations under the same conditions but with a mass of 39 u instead of 133 u, resulted in the same rotational frequency, thus showing that $\omega_r$ is indeed independent of the mass. Assuming a spheroidal shape with constant density, taking the maximum radius and half axial size allows to determine the density of the ion cloud. The density for $10^7$ ions is found to e around 6581 ions/mm$^3$, which is still two orders of magnitude below the Brillouin limit. When applying a quadrupole excitation at $\omega_c$ for 400 ms at

| N | $r_c$ | $z_c$ | $n$(ions/mm$^3$) | period | $\omega_r$ (calc) | $\omega_r$ (fit) | $\lambda_D/r_c$ |
|---|---|---|---|---|---|---|---|
| $10^3$ | 3.7 | 7 | 2.5 | N/A | $1.7 \cdot 10^3$ | N/A | 1.74 |
| $10^4$ | 3.7 | 7 | 25 | 160 | 37.5 | N/A | 0.55 |
| $10^5$ | 3.7 | 7.5 | 233 | 17 | 350 | 687(1) | 0.18 |
| $10^6$ | 3.7 | 8.5 | 2052 | 2.0 | 3089 | 5271(11) | 0.06 |
| $10^7$ | 3.7 | 26.5 | 6581 | 0.6 | 9909 | 21055(30) | 0.033 |

Table 6.1: Results of the simulations (see text for details). The calculated frequency of a particle, $\omega_r$, is within a factor of two of the frequency obtained from a fit of the radial motion of the ion. Distances are expressed in mm frequencies in Hz and the displayed times have ms as unit.
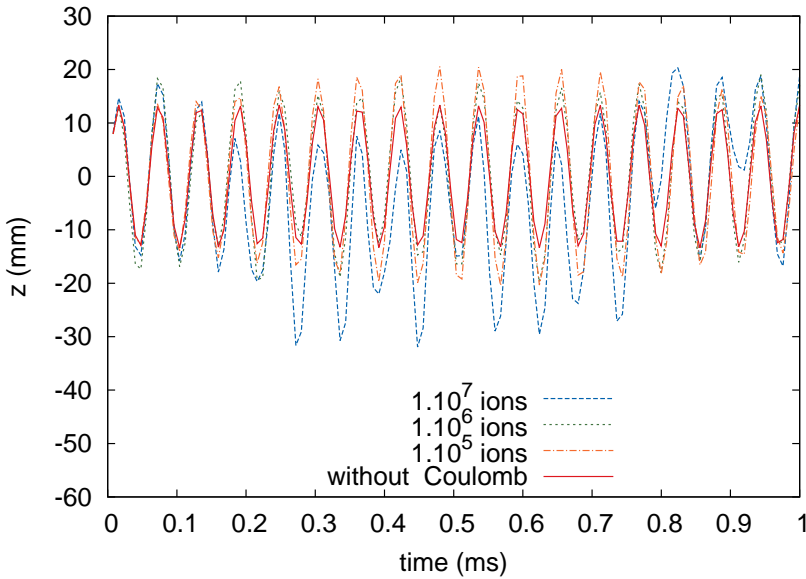


Figure 6.5: Dependence of the axial position of a particle in an ion cloud over time for a different amount of ions in the cloud. Although the axial position of the ion is more unstable when more ions are trapped, the axial frequency remains unchanged.

1.5 V amplitude the cloud becomes more elongated in axial direction and shrinks radially ($r_c$=2.5 mm, $z_c$=40 mm) and the density increases to 9550 ions/mm$^3$.

As hinted by Fig. 6.2 as well as by Eq. 6.14 a measurement of the axial frequency can be used to determine the ion density, $n$. Simulations were performed which show that with the typical parameters involved in the WITCH experiment the axial frequency is

| $N$ | $n$ | $\alpha = \frac{z_c}{r_c}$ | $\frac{\omega_z^2}{\omega_p^2}$ | $\frac{\Delta\omega_z}{\omega_z}$ $(sim)$ | $\frac{\Delta\omega_z}{\omega_z}$ $(theo)$ $(\%)$ [Winters et al., 2006] |
|---|---|---|---|---|---|
| $10^3$ | 7 | 1.9 | 400 | 0 | -0.01 |
| $10^4$ | 25 | 1.9 | 40 | 0 | -0.1 |
| $10^5$ | 233 | 2.0 | 4.3 | 0 | -0.1 |
| $10^6$ | 2052 | 2.3 | 0.5 | 0 | -8.6 |
| $10^7$ | 6581 | 7.2 | 0.15 | 0 | -27.5 |

Table 6.2: Results of the simulation (see text for details). The trend of the expected relation between $\alpha$ and $\frac{\omega_z^2}{\omega_p^2}$ is reproduced. However, the expected theoretical shift in axial frequency (last column) is not observed with simulations (one to last column), where no such shift is noticed.

not sensitive to the exact value of $n$. Instead Eq. 6.13 can be used to extract $n$ if the characteristic parameters $z_c$ and $r_c$ are known.

Figure 6.5 shows the axial position of an ion versus time, for different amounts of ions ($N$) in the ion cloud. As can be seen the axial frequency stays constant at 114 kHz, which is the expected value for the axial frequency for a single trapped ion given the simulated conditions. The results of these simulations are summarized in Table 6.2. The axial length of the cloud increases with $n$, from 2 cm to 5 cm (Fig. 6.5). The axial frequency, however, remains unchanged and thus independent of the amount of ions in the cloud ($N$) as well as independent from the ion density ($n$). Eq. 6.14, which predicts a linear dependency between $n$ and $\frac{\Delta\omega_z}{\omega_z}$, is thus not confirmed by the simulations. This is because of the shallow potential in axial direction, resulting in an axially elongated cloud, while Eq.6.14, only holds when the cloud is spherical, and thus small in axial direction. Therefore we can conclude that the axial frequency in WITCH is not sensitive to the ion density $n$.

Table 6.2 also shows the dependence of $\frac{\omega_z^2}{\omega_p^2}$ as a function of $\alpha$, which follows the predicted behavior (see Eq 6.13 and Figure 6.2). Since simulations have shown that the axial frequency of the WITCH ion cloud is independent of $N$, the ratio $\frac{\omega_z^2}{\omega_p^2}$ scales linearly with $n^{-1}$ (Eq 6.5), and therefore the three observables $r_c$, $z_c$ and $n$ are related via Equation 6.13. Note that observation of these three parameters also yields the absolute ion number $N$ via Eq. 6.15.

## 6.2 boundary between the single particle and the nonneutral plasma regime

The most important systematic effects for a precise measurement of the $\beta$-$\nu$ correlation coefficient $a$ with the WITCH setup are correlated to the position and velocity distribution of the ions in the cloud. It is thus of major importance to get a better

understanding of the ion behaviour in the traps [Tandecki, 2011]. Since the ion behaviour (density, shape, movement) is different for the single particle and non-neutral plasma regimes in the Penning trap, the boundary between those two regimes will be investigated in this section. In both cases the density functions can be extracted from classical Boltzmann theory as is done for example in Ref. [Li et al., 1998]. If the density profile can be calculated, given experimentally determined parameters, it can be used in ion tracking simulations, to determine $a$. The calculated ion density might also be used to determine other observables (e.g. the radial or axial cloud size) as input for the simulations required to create a expected recoil energy spectra (see section 5.5.2).

Substituting the density of the ions in a spheroid (Eq.6.15) in Eq.6.1 that defines the Debye length yields

$$\lambda_D = \sqrt{\frac{4r_c^2 z_c}{3} \frac{\epsilon_0 k_b T}{N q^2}} \tag{6.17}$$

and thus

$$\frac{\lambda_D}{r_c} = \sqrt{\frac{4z_c}{3} \frac{\epsilon_0 k_b T}{N q^2}}, \tag{6.18}$$

which depends only on one parameter, i.e. $z_c$, that is to be obtained from simulations.

Space charges in the ion cloud can be neglected when (see Eq.6.2)

$$\frac{\lambda_D}{r_c} \geq 1. \tag{6.19}$$

The ion cloud is then in the high temperature and low density limit and the term plasma is no longer valid.
When

$$\frac{\lambda_D}{r_c} << 1, \tag{6.20}$$

the cloud is in the low temperature, high density limit and the mutual Coulomb interaction does play a role. Under these conditions the cloud can be described as a nonneutral plasma.

The axial size of the cloud is extracted from simulations and inserted in Equation (6.18) to obtain conditions for a nonneutral plasma in the WITCH Penning traps, see Table 6.1. Figure 6.6 shows both the axial cloud size and $\lambda_D/r_c$ for different $N$. As can be seen, when more than $1 \cdot 10^4$ ions are stored in the Penning Trap, the collection of charges can be considered a non-neutral plasma and the single ion picture is thus no longer valid. Note, however, that the boundary of $1 \cdot 10^4$ ions between the one-particle and non-neutral plasma regimes is not fixed but will most likely depend on the trapping potential, the value of the external magnetic field, and the mass, charge and energy of the particle, among other parameters.

The value of of $1 \cdot 10^4$ as boundary between the two regimes is of the same order of magnitude as in Ref. [Greaves & Moxom, 2008] and as Nikolaev and collaborators showed [Nikolaev et al., 2007]. They found that, for an axially elongated ion cloud,
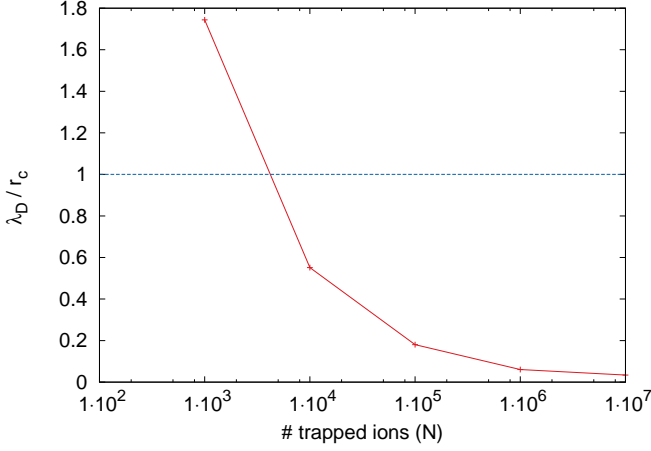
Figure 6.6: The ion cloud in one of the WITCH Penning traps can be described as a nonneutral plasma if around $1 \cdot 10^4$ or more ions are stored.

phase locking of ions sets in when storing between 5000 and 20000 ions. When clouds are more spherical, e.g. by applying a higher axial trapping potential, phase locking happens with fewer ions, i.e. already at 5000 ions.

# 6.3   Relaxation of the ion cloud

## 6.3.1   Ion cloud energy distribution

The Coulomb interaction between ions will cause them to repel each other, thereby increasing their kinetic energy. In turn this raises the maximum of the energy distribution that an ensemble of trapped ions can be cooled down to by buffer gas collisions: from around 0.5 eV for a single trapped ion (see section 3.3) to a few eV when up to $10^7$ ions are trapped simultaneously . Naturally this effect is important for a final determination on $a$ since the temperature of the ions defines, among other parameters, the energy resolution of the spectrometer. It will be shown here that simulations as well as experimental data confirm an increase of ion energy with ion number $N$.

Note that the energy that is discussed in this section is purely the kinetic energy. Figure 6.7 shows the average energy and the energy spread for the simulated ion cloud of cesium ions (as used before in this chapter, see section 6.1.2). It can be seen that the average energy and the spread of the energy distribution both increase when $10^7$ ions are trapped, compared to when the Coulomb interaction between ions is neglected. E.g. after 100 ms the average energy for a cloud of $10^7$ ions is 0.3 eV, while without Coulomb interaction this is 0.08 eV only. Note that the speed of the cooling does not seem to
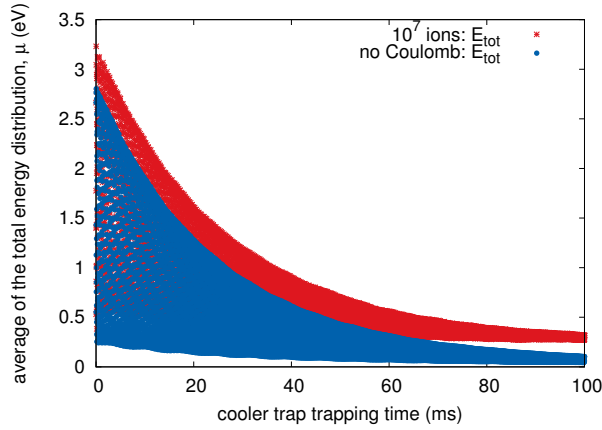
(a) Average energy, $\mu$, of the ion cloud
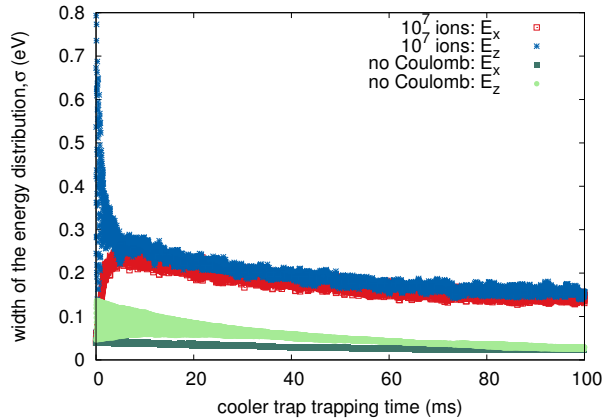


(b) Spread, $\sigma$, of the energy of the ion cloud

Figure 6.7: The average kinetic energy (top panel) and the width of the kinetic energy distribution (bottom panel) as a function of trapping time in the cooler trap, filled with helium buffer gas ($p = 10^{-4}$mbar), for an ion cloud of $10^7$ ions with and without Coulomb interaction enabled. A similar simulation has been performed for $10^4$ ions, resulting in the same energy distribution as shown here for $10^7$ without Coulomb interaction enabled.

be influenced by the Coulomb interaction. Simulations with $10^4$ stored ions were also performed and showed results comparable to when $10^7$ ions are trapped without Coulomb interaction included.
The maximum of the energy distribution of the cooled ensemble of $10^7$ ions without Coulomb interaction still is 0.5 eV like in the single particle regime. It becomes 2 eV when the Coulomb interaction between those ions is enabled.

This effect was also looked into experimentally, by changing the amount of trapped ions and determining their axial and total energy distribution. For this, $^{39}K^+$ ions from the REXTRAP ion source were cooled for 190 ms in the cooler trap, during which a sideband cooling was applied. After this the ion cloud was transferred to the decay trap, where they were trapped for 50 ms followed by a measurement of their energy distribution.

The axial energy of the ions can be determined by lowering the potential of the upper endcap electrodes of the decay trap, and counting how many ions have enough kinetic energy to overcome the voltage barrier on the endcap and hit the MCP. The total energy of the ions can be measured as well due to the unique setup of WITCH with its spectrometer. In a similar way as obtaining a recoil energy spectrum, the retardation barrier in the spectrometer can be scanned to probe the total energy of the ions. However, the applied voltage on the spectrometer walls is different from the actual potential in the centre of the spectrometer, which can cause a discrepancy in the energy determination [Delauré, 1997]. Furthermore, the influence of the wire, which is at the same potential as the spectrometer, will disturb any measurement, and especially a low energy measurement like here. Therefore, ion tracking simulations are required to obtain the correct total energy distribution of the ion cloud. However, to be able to do this, a three-dimensional field map of the spectrometer section with the wire included is required, which is currently not available. Results of total energy measurements should therefore at present be interpreted qualitatively only.

The measured energy spectrum (Fig. 6.8) is an integral spectrum instead of a differential spectrum, and is therefore fitted with an integrated Gaussian function

$$f(x) = A \left[ 1 + erf \left( \frac{x - \mu}{\sigma \sqrt{2}} \right) \right] + b, \tag{6.21}$$

with $A$ the amplitude, $b$ the background and $\mu$ and $\sigma$ respectively the average and standard deviation of the Gaussian energy distribution.[2]. The amount of trapped ion bunches from REXTRAP is increased with the stacking (Sec. 2.7) technique.[3]

Figure 6.8 shows the measurement of the axial energy of a stored ion ensemble with 1 ion bunch and with 18 stacked bunches. The results of the fit to the energy distributions for this measurement as well as for other measurements is summarized in Table 6.3. These measurements confirm the simulations, i.e. when more ions are trapped the energy distribution increases and becomes broader. The total energy of the ion ensemble also seems to be about 6 times higher than the axial energy, from which one may conclude

---

[2]The total energy has a Maxwell Boltzmann distribution. Here, however, the Maxwell Boltzmann distribution will be approximated as a Gaussian distribution.
[3]The exact amount of ions, or even an order of magnitude of the ion intensity in each bunch is not known.
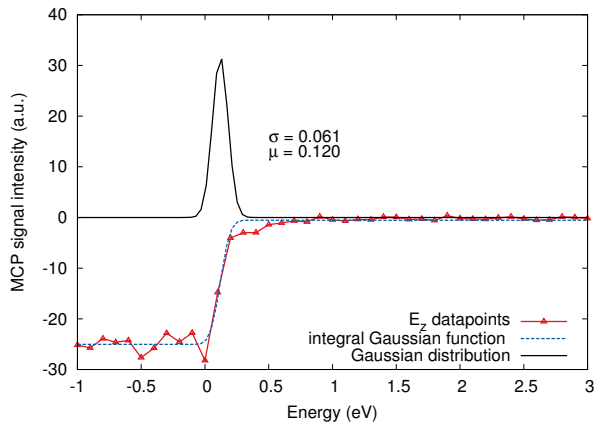
(a) 1 REXTRAP ion bunch
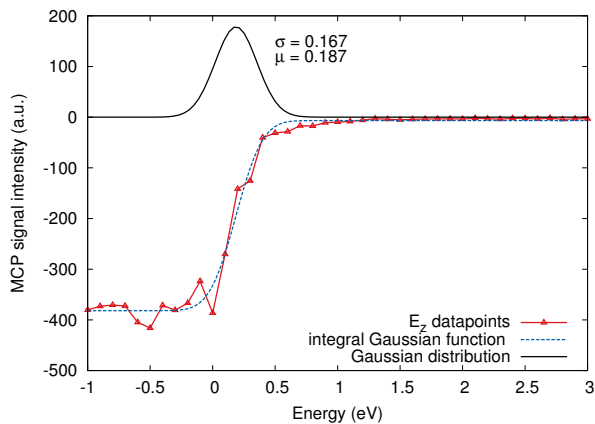


(b) 18 REXTRAP ion bunches

Figure 6.8: Axial energy distribution of ions in an ion cloud. Each panel shows the fit of the data with an integral Gaussian function and the resulting Gaussian distribution. In the bottom panel, a measurement is shown when 18 times more ions are stored in the cooler trap, showing clearly the effect of the mutual Coulomb interaction between the ions on the energy distribution.

| | 50 ms DT | | | | 1 s DT | |
| | 1 bunch | | 18 bunches | | 1 bunch | 18 bunches |
| | $E_z$ | $E_{tot}$ | $E_z$ | $E_{tot}$ | $E_z$ | $E_z$ |
|---|---|---|---|---|---|---|
| $\mu$ | 0.120(7) | 0.673(9) | 0.19(1) | 0.707(9) | 0.063(9) | 0.19(2) |
| $\sigma$ | 0.06(1) | 0.09(1) | 0.18(2) | 0.14(1) | 0.035(8) | 0.09(2) |
| $A$ | 12.2(2) | 11.8(2) | 188(3) | 177(3) | 5.13(9) | 79(3) |
| $b$ | -25.0(3) | -24.2(3) | -382(6) | -365(4) | -10.3(2) | -158(5) |

Table 6.3: Summary of the fitted parameters from Eq 6.21. DT stands for decay trap. When 18 bunches are trapped the mean and average energy of the ion cloud increases.

that the radial energy should be much larger than the axial energy. However, this is in contradiction with simulations which show that the axial energy is twice higher than the energy stored in $X$- and $Y$-direction. It is believed that this discrepancy stems from the experimental measurements of the total energy which are incorrect in absolute numbers, as discussed earlier.

The same energy measurements were repeated with 1 s trapping time in the decay trap instead of 50 ms. Surprisingly the average and the spread of the energy distribution seemed to have decreased over time. Also the ion intensity $A$ decreased. It might be that the hotter ions have left the ion cloud, causing a decrease in energy and in ion intensity. This effect was not seen in simulations and is thus most likely due to some imperfection that is not taken into account in the simulations. Since no more experimental data was acquired about this effect it is at this point not possible to make a conclusive statement about the losses of ions in the decay trap.

## 6.3.2 Stability of the ion cloud.

Knowledge of the movement of the ion cloud in the decay trap is imperative for a final determination of $a$. Ideally, the ion cloud conditions do not change during trapping in the decay trap. However, a number of parameters can influence this equilibrium as will be outlined in this section.

An ion cloud is, and will remain in equilibrium if three conditions hold [Peurrung & Kouzes, 1994]:

- The ion cloud must have a single energy, i.e. the axial and radial energy must be equal. If this condition is not fulfilled, the energy will be divided among the radial and axial directions of the ion cloud such that the ion cloud will, over time come to equilibrium. If buffer gas is not included, e.g. in the decay trap, this energy can be divided due to Coulomb collisions between the ions. The rate $\nu$ with which this process happens is mainly influenced by the average ion energy since this will

directly influence the distance of closest approach between ions:

$$\nu_{ii} = \frac{nq^4 ln(\Lambda)}{2\pi\epsilon_0^2 m^2 \overline{v}^3} \tag{6.22}$$

with $\Lambda$ the average number of ions in the Debye sphere $\frac{4}{3}\pi n\lambda_D^3$ and $\overline{v}$ the average ion energy.[4] Note that the total radial arrangement of the ion cloud is much smaller. Total radial arrangement is achieved when the positions of all ions with respect to their neighbours is fixed. The rate at which the ion cloud approaches this equilibrium is given by [O'Neil & Driscoll, 1979]:

$$v = \frac{3}{8}\left(\frac{\omega_p}{\omega_c}\right)^4 v_{ii} \tag{6.23}$$

$$= \frac{3}{8}\left(\frac{n \cdot m}{\epsilon_0 B^2}\right)^2 v_{ii} \tag{6.24}$$

Note that for most Penning traps, like the WITCH Penning traps, the plasma frequency is much smaller than the cyclotron frequency. The equilibrium in the radial arrangement of the ions is thus much slower then for the arrangement of the energy in an ion-cloud.

- The density of the ion cloud has to decrease with the radius of the cloud. An instability can thus be caused by holes in the plasma, and thus holes in the transported beam bunch, which is assumed not to be the case for the WITCH experiment. If however, an instability takes place, the ion cloud will suffer a complex rearrangement which is the diocotron motion [Levy, 1965]. This motion is similar to the influence of mirror charges on the electrodes, see section 6.1.2. Another electromagnetic instability can be created by applying excitations, which will thus influence the radial and energy distributions, as will be discussed in the following section.

- An ion cloud should be independent of external interactions to maintain its equilibrium. Following processes will influence the ion cloud stability: charge-exchange or other sources of particles loss, the decay of radioactive ions, interaction with time-dependent electric fields arising from mechanical vibrations or electric noise and collisions from the ions in the cloud with the rest-gas or with buffer gas that is leaked from the cooler trap [Eggleston et al., 1984; Driscoll et al., 1986; Notte & Fajans, 1994]. Obviously, any real experiment suffers from these interactions. Note that an excitation can be applied to counter these effects and to recenter the ion cloud as will be discussed in the following section.

Clearly a trapped ion cloud in the decay trap will suffer from buffer gas collision and from the radioactive decaying ions. As shown in the last column of Table 6.3 losses in the decay trap do happen over time. In order to investigate these effects, careful measurements have to be performed, as e.g. changing the buffer gas pressure in the cooler trap and investigating if the radial distribution of the ion cloud, as seen with the top MCP, changes.

_____

[4]In principle $r_c$ should be used instead of $\lambda_D$ for weakly magnetized plasmas as are being described here.

# 6.4  Penning trap excitation of a plasma

Since trapped charged particles inside a non-neutral plasma are Debye shielded from applied electrical fields, the application of rf-excitations will have a different effect compared to the single particle picture. In some cases, the response of a plasma to such an excitation will reveal intrinsic parameters of the plasma like e.g. the plasma density

## 6.4.1  Quadrupole excitation

When a quadrupolar rf excitation is applied, the collective motion of multiple ions in the trap is known to shift and broaden the resonant quadrupole excitation frequency $\omega_c$, see e.g. Ref [Herlert et al., 2011]. The influence of Coulomb interaction on the resonant quadrupole excitation frequency has been investigated experimentally (e.g. Ref. [Ames et al., 2005; Gustafsson et al., 2011]) as well as a theoretically (e.g. Ref. [Mitchell & Smith, 1995]). The magnitude of the shift and/or broadening of the resonant excitation frequency is highly dependent on the amount of ions and ion species as well as on the initial conditions like charge, position and velocity distribution, and ion density.

When particles with different mass are trapped they tend to cluster in ion clouds that each constitute of particles with the same mass. This process depends on the initial conditions and occurs if the amount of ions is high enough (around $1 \cdot 10^4$ ions, see section 6.2) [Nikolaev et al., 2007]. The influence on the resonant excitation frequency due to the mutual Coulomb interaction between these different ion clouds has a much larger influence, around an order of magnitude, on the value of the resonant excitation frequency than when only one species of ions is trapped [Wong & Amster, 2007]. Indeed, on top of the complex ion-ion interaction in a cloud, these two ion clouds will influence each other's motion via Coulomb interaction and will hence largely disturb the resonant excitation frequency. A literature search yields more results for the influence of Coulomb effects in the presence of multiple ion species compared to Coulomb effects for a single trapped ion species. This can be attributed to FT-ICR measurements which are significantly affected by the influence of multiple mass clouds on each other [Marshall & Hendrickson, 2002].

Since the addition of more masses adds extra complexity to the picture the following section will be split in two parts: one part about Coulomb effects if only a single ion species is present in the trap and a second part dealing with multiple ion species being stored in the trap. Note that FT-ICR measurements tend to measure the reduced cyclotron frequency $\omega_+$ instead of the $\omega_c$ frequency, which is the resonant frequency for quadrupole excitation. However, publications by the FT-ICR community potentially give an interesting view on the ion cloud kinematics involved and their possible influence on observables.

## one ion species trapped

Buffer gas can get ionized in a Penning trap and consequently also be trapped, as happens for example in the REXTRAP Penning trap. The ionized buffer gas has the potential to form into an ion cloud, which, if consisting of many ions, will influence the cloud of trapped particles, thereby distorting the single ion species picture. In the latter case the description for a single ion species given in this section is not valid anymore, and one refer to the description when more ion species are trapped (Sec. 6.4.1).

For a long time since the publication of Wineland and Dehmelt [Wineland & Dehmelt, 1975] it was assumed that when only one ion species is stored in a Penning ion trap, the eigen frequencies of a trapped ion will not be effected. They argue that according to the third law of Newton, the action and reaction between particles is equal in size but opposite in direction, thus $F_{z,12}$ equals $-F_{z,21}$. The centre of motion of the ion cloud will thus follow the single particle motion. Although this argument indeed holds for the axial direction, they also, incorrectly, extended it to the radial direction. The radial force field, which is perpendicular to the magnetic field, depends on the Lorentz force from the magnetic field $F_L = q\mathbf{v} \times \mathbf{B}$ and thus on the velocity of the ions, which is non-central. In other words, the force vector between two particles does not align with a line trough those particles. Consequently the forces between two ions do not cancel completely and the center of mass will change in radial direction. Newton's third law is thus not applicable to a Lorentz force [Cornille, 1995].[5]

When more ions are added, the ion cloud will occupy a larger radial and axial volume in the Penning trap. The cloud will stretch to regions where imperfections of the magnetic and electric field are more pronounced, causing the eigen frequencies of a trapped particle to change slightly, as was discussed before in section 3.2.2. Due to the mutual Coulomb repulsion between ions not all ions can be stored in the trap centre, i.e. some of the particles will move into regions where they are more prone to magnetic and electric field imperfections. Since the eigenfrequency changes quadratic with the distance of an ion to the centre of the trap, even a slight radial or axial offset of the ion cloud has a large effect. The overall effect of the Coulomb interaction will thus most probably be a broadening of the eigenfrequency. The more ions are trapped, the larger the broadening. Note that this behavior was observed before [Ames et al., 2005], but never explained. Although the magnitude of this effect is unknown and depends on the mechanical and magnetic alignment and design of a Penning Trap, it is possible to investigate this effect with the Simbuca program, that was developed as part of the WITCH project (see Chapter 4), by importing the magnetic and electric field map in the simulations.

A simulation has been performed starting from an off-centre ion cloud of $10^7$ cesium ions with initial conditions as given in the beginning of this chapter (Sec. 6.1.2). This off-centre ion cloud is made subject to a quadrupole excitation with an amplitude of 1.5 V, during 400 ms. The excitation is applied at different frequencies around the theoretical resonant frequency of a quadrupole excitation: $\omega_c$. It will be shown here that the resonance frequency will shift slightly towards positive values like previous measurements and simulations also showed [Gustafsson et al., 2011; Ames et al., 2005].

---

[5] However conservation of angular momentum (which is the foundation of Newton's third law) still holds, since the electromagnetic field can carry away angular momentum.
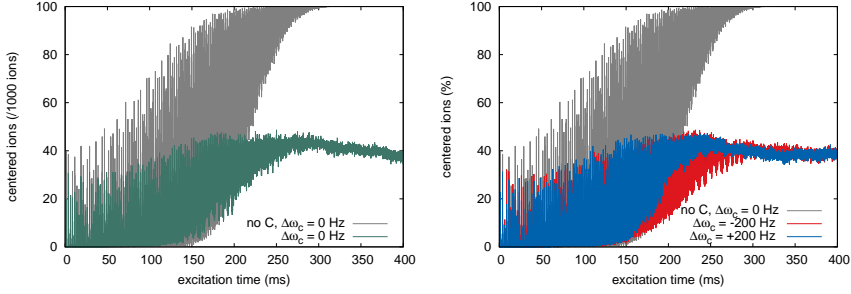
Figure 6.9: Amount of centered $^{133}$Cs ions as a function of the duration of the quadrupole excitation. In the left panel the situations with and without Coulomb interaction are compared. It can be seen that due to Coulomb interaction only about half of the ions can be centered. In the right panel the influence of a positive and negative shift of 200 Hz on the cyclotron excitation angular frequency $\omega_c$ is shown. This figure already hints that applying a more positive excitation frequency results in the centering of more ions.

Unfortunately, this simulation was performed assuming an ideal Penning trap, i.e. without any electromagnetic imperfection. Although the simulation already showed a positive shift of the frequency, the magnitude of the shift and the broadening are not as large as observed experimentally. This is most likely due to the fact that imperfections in the electric and magnetic field were not taken into account in the simulation.

Figure 6.9 shows the amount of centred ions as a function of the duration of the quadrupole excitation. It is expected that the longer the excitation is applied the more ions are centred in the trap. An ion is considered *centred* when the diameter of its orbit is smaller than the diameter of the pumping diaphragm, between the cooler and the decay trap, which is 1.5 mm. Only the centred ions can be transferred to the decay-trap.[6] As one can see the Coulomb repulsion between the ions hinders complete centring of the ion cloud; around 50% of the ions can thus not be transferred to the decay trap. This loss of ions during a sideband excitation is surprising. However, this might have been observed during the November 2011 experiment of WITCH as when a quadrupole excitation was applied, ions losses were indeed registered. During these measurements around $10^6$ ions were stored in the WITCH cooler trap, which is close to the $10^7$ ions described here. Losses of ions are a topic that might need some further investigation, both experimentally as via simulations, since precious radioactive ions can be lost like this. It might well be that rotating wall cooling (see section 6.4.2) is needed to squeeze the ion cloud so that a maximum amount of ions can be centred, prior to the transfer between the traps.

_____

[6]Only in first approximation the amount of centred ions equals the ions that are transferred to the second Penning trap. In principle, the transfer depends on both the axial and the radial position, as well as the velocity and transfer potentials. Stating that the centred ions are the ones that are transferred to the decay trap is thus over simplified.
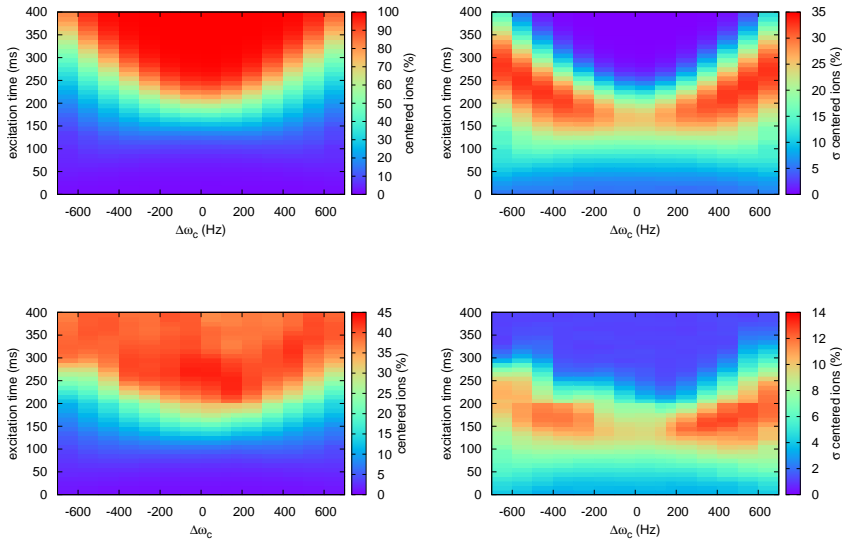
Figure 6.10: The left panels shows the average of centered $^{133}$Cs ions as a function of the quadrupole excitation frequency and excitation time. The panels at the right show the standard deviation of the distribution of centred ions as a function of the quadrupole excitation frequency and excitation time. The top row shows simulation results when the Coulomb interaction between the ions is neglected, while in the second row the Coulomb interaction between the ions is included. Note different vertical scales between the top and bottom rows (without and with Coulomb interaction).

In the second panel of Figure 6.9 the influence of an excitation at $\omega_c \pm 200$ Hz is shown. As can be seen, the ion cloud tends to be more centered with a positive offset. Also it has a smaller radial distribution when applying an excitation at $\omega_c + 200$ Hz compared to an excitation at $\omega_c - 200$ Hz.

A global overview of the change of centred ions (as a function of duration of the excitation and of the frequency) is obtained by grouping all values for the amount of centred ions in 10 ms intervals and fit the set of data in each such interval with a Gaussian distribution. Figure 6.10 shows the mean (left column) and standard deviation (right column) of the distribution of the amount of centred ions for each such interval. For comparison the data without Coulomb interaction are shown on the first row, while the data with $10^7$ ions and Coulomb interaction enabled are presented in the second row. Without Coulomb interaction enabled a symmetric structure is expected and obtained as well. Ions are more easy to centre when the excitation is applied with the resonant frequency $\omega_c$ but nevertheless for excitation frequencies which deviate a couple of 100 Hz from the central

frequency all ions can still be centred provided the excitation is applied for a longer time. When Coulomb interaction is enabled, however, mutual repulsion between the ions distorts this ideal picture. Due to this repulsion it is not possible anymore to centre all the ions, but only a maximum of 45%, as discussed before (see figure 6.9). Furthermore the distribution is asymmetric, i.e. the maximum amount of centred ions is reached earlier in time when a more positive frequency is applied.

Although the sign of the frequency shift is in agreement with earlier observations, the magnitude of the shift is around $\Delta\nu \approx \frac{+170}{2\pi} = +27$ Hz which is much smaller than a frequency shift of $+7000$ Hz as observed with the REXTRAP setup for $1 \cdot 10^7$ trapped ions [Ames et al., 2005]. Most likely this is due to the electromagnetic field maps which were not included in this simulation since they can shift the eigen frequencies 3.2.2. This discrepancy between the magnitude of the frequency shift can also stem from the initial ion conditions since in these simulations a dipole excitation was applied prior to the quadrupole excitation, whereas this is not the case in REXTRAP measurements.
There is, however, also some discrepancy in the experimentally obtained frequency shifts. E.g. a frequency scan of $\omega_c$ with $^{133}$Cs ions trapped in the ISOLTRAP Penning traps does not show a shift when measuring with up to $6 \cdot 10^5$ trapped ions [Herlert et al., 2011], while a measurement with this amount of trapped ions with the REXTRAP setup increased the resonant excitation frequency with $\approx 200$ Hz and doubled the frequency broadening [Ames et al., 2005]. Comparison between simulations and a REXTRAP measurement on $^{133}$Cs were found to be in good agreement in Ref. [Sturm et al., 2009]. In this publication Sturm used a scaled Coulomb approach for the simulation. Also in Ref. [Beck et al., 2001] scaled Coulomb simulations are shown to be applicable for up to a few $10^7$ particles in the WITCH Penning traps indicating in a shift of the eigenfrequency of $+2000$ Hz when trapping $10^7$ ions. In this simulation an ideal Penning trap was assumed with the ion cloud initially distributed in the centre of the Penning trap. It thus seems that both the electromagnetic field maps as well as the initial conditions prior to the quadrupole excitation plays a large role in the magnitude of the frequency shift.

The most in depth investigation with simulations was performed by Nikolaev et al. [Nikolaev et al., 2007]. Although this paper discusses a dipolar excitation at $\omega_+$, the effect of the amount of ions on the ion cloud is investigated in depth. In this publication it is concluded that the phase locking of the ions has a large influence on the magnitude and the sign of the shift in $\omega_+$. It is sated that: "*The excitation frequency depends largely on the portion of total number of ions redistributed between phase-locked and dephased ensembles*". Clearly this statement hints that the initial energy and position distribution of the ions, which influence the phase locking mechanism, play a large role in the magnitude of the frequency shift.

The shift of the resonant quadrupole frequency is thus a complex mechanism that seems to depend on an uncertain number of parameters. It is at this moment unclear what exactly the influence of parameters like initial ion cloud and Penning trap potentials as well as the magnetic field strength is. Nevertheless for WITCH the exact frequency does not matter that much. The amount of ions lost during an excitation is a potentially much more harming mechanism.
When the frequency shift and broadening will be understood better in the future, it has the potential to be a useful tool for comparing simulations with experiment, depending
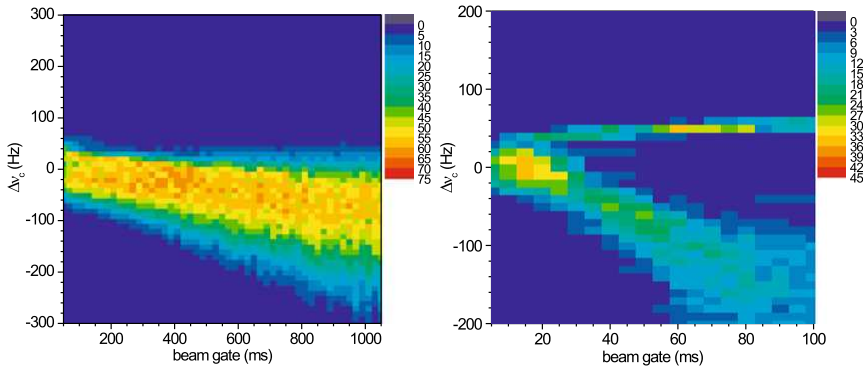
Figure 6.11: Shift of the quadrupole excitation frequency for both stable rubidium isotopes. The scan of the quadrupole excitation frequency for $^{85}$Rb is shown in the left panel, and gives good agreement with the theoretical prediction (Eq. 6.25). The same measurement on the less abundant isotope $^{87}$Rb on the other hand shows no agreement with theoretical predictions (right panel). Figures taken from [Herlert et al., 2011]

on how the shift and broadening depend on the possible parameters. For example, if the exact electromagnetic field maps are the most critical parameter, information about this can be extracted when the amount of trapped ions and the initial conditions are known. Or it can be used as a tool to directly probe the amount of particles or the initial ion density when other observables are known with better precision.

**two ion species trapped**

When two ion species are trapped simultaneously in a Penning trap the optimal quadrupole excitation frequency, $\omega_c$, will be affected by the Coulomb interaction between both ion clouds. Due to this the optimal frequency range can broaden, split or shift in either direction. Not much is known about this process, although the effects have been investigated by the FT-ICR community. With the REXTRAP setup multiple trapped ion clouds were examined in Ref. [Ames et al., 2005; Gustafsson et al., 2011]. Showing a broadening and shift of the optimal quadrupole excitation frequency for transferring $^{39}$K ions. This change in frequency is determined by the presence of $^{41}$K ions, even tough they have a low natural abundance of 6.73%.

Similarly, measurements of the optimal quadrupole excitation frequency as a function of amount of trapped rubidium ions, were performed with the ISOLTRAP setup [Herlert et al., 2011]. To this end $^{85}$Rb ions (72.2% abundance) and $^{87}$Rb ions (27.8% abundance) were loaded simultaneously in the ISOLTRAP preparation Penning trap. Figure 6.11 shows a scan of the quadrupole frequency, for both rubidium isotopes as a function of the beam gate, the length of this being related to the the amount of ions. The number of $^{85}$Rb ions equals 16 ions/ms and $^{87}$Rb ions equals 6.4 ions/ms. As can be seen, a

simple behavior occurs when performing the excitation on the dominant ion mass, i.e. a gradual decrease and a broadening of the optimum frequency. For the less abundant ion species, on the other hand, the behavior is more complex and a splitting of the resonant eigenfrequency occurs. Note that this already happens at around 1200 stored ions (at t=50 ms). With this low number of ions, simulations certainly have the potential to investigate the origin of this splitting. However an in-depth investigation of this is beyond the scope of this thesis. Similarly an in-depth investigation of the parameters that have a high influence on the shift and/or broadening of the frequency range is not discussed here. Instead, the effect of the mutual Coulomb interaction between different ion species will be qualitatively investigated by simulations here.

Theoretically there was a first effort in 1991 to find a model to describe interacting ion clouds in a Penning trap. This was achieved by modeling the ion clouds as point charges and infinitely long line charges [Chen & Comisarow, 1991]. Later these authors modified this model to charged disks [Chen & Comisarow, 1992]. Both models have not been cross checked by experiments, probably meaning that their predictive power was rather limited. Finally in 1995 numerical calculations were applied to investigate the movement of ion clouds and the shift of the cyclotron frequency for both the line model and the charge model [Mitchell & Smith, 1995]. In the latter publication much of the discussion is about the rotation of ion clouds around each other. This process is called phase-locking of one cloud with respect to the other. Also here, it is hinted that phase-locking between the ion clouds plays a large role in the shift of the cyclotron frequency. The phase locking between two ion clouds also determines the achievable mass precision. If ion clouds are rotating around each other they will influence any measurement of $\omega_c$. A formula for the maximum mass resolution $m/\Delta m$ for FT-ICT measurements is given in [Mitchell & Smith, 1995]. In this reference an equation for the shift in the quadrupole excitation frequency is extracted as well:

$$\Delta\omega_{c_1} = \frac{-q_2 N_2}{2\pi\epsilon_0 B z_c r_{+,1}^2} \tag{6.25}$$

With the subscript denoting the respective ion species and $r_+$ the cyclotron radius of an ion.[7] This simple model has successfully been tested [Gorshkov et al., 1993]. Note that the negative sign shows a negative mass shift, as is observed experimentally as well, see Fig 6.11. This model only holds in first approximation while Ref. [Mitchell & Smith, 1995] also discusses more advanced models. These more advanced models also predict a positive phase shift when the radii of the excited ion cloud is smaller than the contaminating ion-cloud.

Since this effect is important for mass measurements, and thus at ISOLTRAP [Mukherjee et al., 2008a], the Simbuca code has been applied to investigate this behavior [Kowalska, 2012].[8] However, the results of these simulations were never published. Therefore, these data will be used here to demonstrate that simulations confirm this simple model. In the simulation first a dipole excitation is applied first for 25 ms, with a frequency of $\omega_- = 1906.4$ Hz and an amplitude of 0.05 V, bringing the ions to a radius of around 6.5 mm. The dipole excitation was followed by a quadrupole excitation on the cyclotron frequency for the less abundant $^{87}$Rb isotope, i.e. $\omega_c = 5.21787 \cdot 10^6$ Hz. This excitation was applied

---

[7]The factor 2 in the denominator is dropped when $r_{+,1} \neq r_{+,2}$.
[8]Simbuca was used by Kristian Petrik, a CERN summer student for ISOLTRAP in 2011.
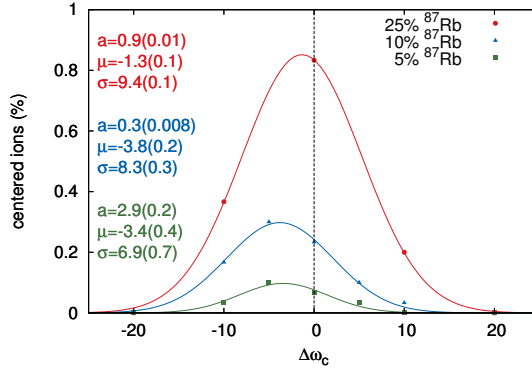
Figure 6.12: Simulated percentage of centred $^{87}$Rb ions as a function of the cyclotron frequency for a different ratio of $^{87}$Rb over $^{85}$Rb ions. To good approximation, this data set can be fitted with a Gaussian distribution [Naimi et al., 2011] of which $a$ is the amplitude, $\mu$ the mean and $\sigma$ the standard deviation.

with an amplitude 0.115 V and during 75 ms. A total of 100 ions were simulated with a scale factor of 30 to represent 3000 trapped ions. Figure 6.12 shows the outcome of the simulations, for different abundances of $^{87}$Rb ions. As can be seen, the cyclotron frequency is shifted towards more negative values, as theory predicts. Furthermore, the lower the abundance of the $^{87}$Rb, the lower the relative amount of centred $^{87}$Rb ions. It is thus *harder* for the excitation to centre the ions when the abundance of an ion species is lower.

More insight in this process is given in Figure 6.13 where the change in radial distance of an ion to the centre of the trap is plotted throughout the experimental cycle. $^{87}$Rb ions are trapped within the cloud consisting of $^{85}$Rb ions, such that the applied quadrupole excitation must be strong enough to overcome and *break* the Coulomb interaction between the two ion clouds. The figures in the first row stem from the simulation where the Coulomb interaction between ions was disabled. No shift in optimum frequency is expected, as is indeed observed.
Coulomb interaction is enabled between the ions in the second row of the figure. With a more negative excitation frequency the average radius of the ions at the end of the cycle is smaller. There also is a certain *resistance* to the excitation due to space charge effects in the cloud, which is visible in the late reaction of the ions to the excitation. It is thus harder for the applied excitation to pull the ions away under the influence of the Coulomb interaction of the $^{87}$Rb ion cloud.

When the abundance of $^{87}$Rb ions is lower (the third row compared to the second row), the ions are more attracted towards the ion cloud that consists of $^{87}$Rb ions, and hence more difficult to focus. When the ratio of the less abundant $^{87}$Rb ions is higher, they will group themselves into one cloud and be more resistant to the Coulomb effect of the
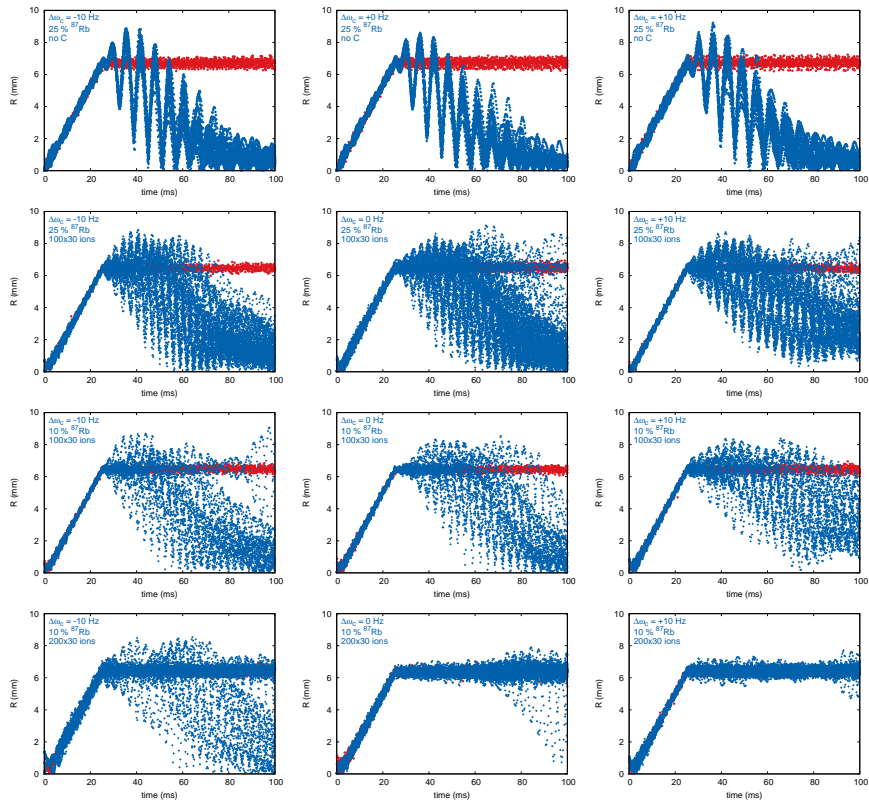
Figure 6.13: The Radius $R$, in mm, of a simulated ion cloud versus excitation time, in ms. For each ion the couple $(t, r)$ is shown on each graph for each time step ($= 0.1$ ms) in the simulation. The left column shows an offset of $\Delta\omega_c = -10$Hz, the middle column the central frequency $\Delta\omega_c = 0$Hz and the right column $\Delta\omega_c = +10$Hz. Each row is the result of a simulation with the same initial conditions, as discussed in the text.
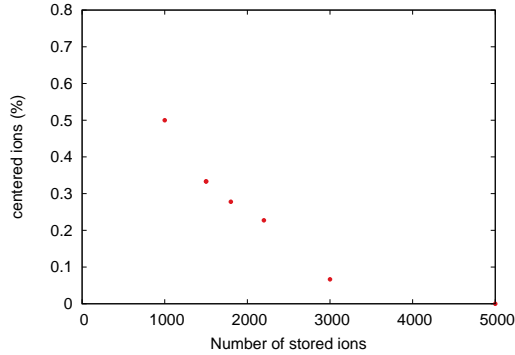
Figure 6.14: Percentage of centered $^{87}$Rb ions as a function of the total amount of trapped rubidium ions. Only 5% of the total amount of ions are $^{87}$Rb ions, the rest being $^{85}$Rb ions.

cloud that consists of $^{85}$Rb ions.

A similar effect can be seen in the bottom row of the figure, when double the amount of ions of both species are trapped. Centering of the $^{87}$Rb ions is even more difficult under these conditions. This indicates that the shift in excitation frequency depends on the total amount of ions and not on the ratio between the ion species.

The influence of the total amount of ions on the amount of centred ions is also shown in figure 6.14. Here the amount of centered ions during a quadrupole excitation with frequency $\omega_c$ as a function of ion number is shown. This simulation was performed with an abundance of 5% for the $^{87}$Rb ions. As can be seen, the higher the total amount of ions the more difficult it is to centre the ions. The centring thus depends on the total number of ions and not on the ratio. This is not surprising, as a cloud consisting of more ions has a higher internal electric field due to the space charges and thus attracts the $^{87}$Rb ions more easily, making it harder to centre them with an excitation.

For the WITCH experiment this topic currently does not need more investigation since the $^{35}$Cl contamination in the $^{35}$Ar beam has been brought down from about 50 times more to about 1%, and will hence not hamper the preparation of the argon ions in the cooler trap anymore. However, when performing a measurement on other nuclei, these effects might hamper the normal operation of the Penning traps. For example a measurement on a radioactive nucleus that undergoes electron capture decay, would yield information about the energy resolution of WITCH. However, the beams delivered by ISOLDE for the most suitable candidates for such a measurement with WITCH, i.e. $^{144}$Eu or $^{140}$Eu, are in both cases in cocktail beams.[9] Hence in this case both REXTRAP and WITCH will suffer from this effect, unless the dependence of the effect on the variety of parameters is understood better and a solution can be put forward.

_____

[9]Although laser ionization schemes are being developed to produce more pure beams of these nuclei.

## 6.4.2 Rotating Wall excitation

In theory, due to conservation of energy and momentum, a trapped ion cloud will be trapped forever in a Penning trap. In practice, however, imperfections can cause a loss of ions inside the plasma, see section 6.3.2. Apart from sideband cooling (Sec.3.4.2) also *rotating wall* cooling can be applied to prevent such losses to occur. This excitation can increase the density of the plasma and can therefore be applied to store plasmas up to weeks in a Penning trap.

A rotating wall excitation is performed by applying an oscillating electric potential $\phi_j$ on all eight wall sectors of the ring electrode at $\theta_j = 2\pi j/8$. The potential on the $j$'th segment of the ring is defined as:

$$\phi_j(t) = U_{rw} cos[m(\theta_j - \omega_{rw}t)] \tag{6.26}$$

with $m$ the order of the rotating wall excitation. The most effective one is $m = 1$, the so called dipole rotating wall excitation, since it rotates with the cloud. When $m = 2$, the quadrupole rotating wall excitation will change the cloud shape significantly [Huang et al., 1997; Hasegawa et al., 2005]. The dipole rotating wall electric field is defined as:

$$\mathbf{E}_{rw,1} = -\frac{U_{rw}}{r_0} \cdot [cos(\omega_{rw}t)\hat{\mathbf{e}}_x - sin(\omega_{rw}t)\hat{\mathbf{e}}_y], \tag{6.27}$$

while the quadrupole rotating field is given by:

$$\mathbf{E}_{rw,2} = -2\frac{U_{rw}}{r_0^2} \cdot \Bigg( [x \cdot cos(2\omega_{rw}t) - y \cdot sin(2\omega_{rw}t)] \hat{\mathbf{e}}_x$$
$$\tag{6.28}$$
$$- [x \cdot sin(2\omega_{rw}t) + y \cdot cos(2\omega_{rw}t)] \hat{\mathbf{e}}_y \Bigg).$$

The oscillation frequency of the rotating wall excitation $\omega_{rw}$ is chosen to be close to the rotation frequency of ions in a plasma $\omega_r$, such that the oscillation forms a *wall* that moves with the excitation, as is illustrated in Fig 6.15. The applied excitation frequency should be slightly higher then the rotation frequency of the cloud so as to increase the cloud's density and make it more compact. In the opposite case, when the drive rotates slower than the plasma, the latter expands. Note that this is the same principle as the slip of an induction motor.

Rotating wall cooling is thus known to squeeze the cloud to a high density close to the Brillouin limit (see Eq 6.8) [Huang et al., 1997]. Initially this method has been applied to cool trapped electrons or positrons [Greaves & Surko, 2000]. As of today rotating wall cooling is still used mainly to prepare dense bunches of positrons (used to create antihydrogen). In 1993 the rotating wall method for ions has been pioneered on Beryllium atoms by means of laser cooling [Bollinger et al., 1993; Hollmann et al., 2000] and in 2002 rotating wall excitation with cooling by buffer gas was performed for the first time with the REXTRAP setup [Ames et al., 2005; Podadera-Aliseda & Lindroos, 2006]. At present REXTRAP is the only setup that has applied rotating wall excitation with buffer gas cooling and on trapped ions. Although (nitrogen) buffer gas was already demonstrated
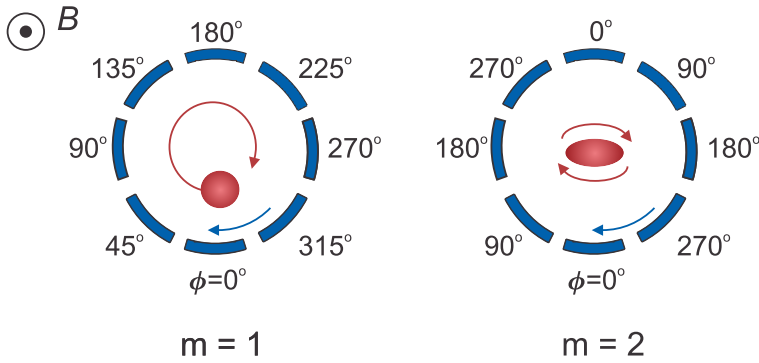
Figure 6.15: Rotating wall application on the segmented ring electrodes. Left: Dipole rotating wall excitation ($m$=1). Right: Quadrupole rotating wall excitation ($m$=2)

to work to cool trapped positrons while applying a rotating wall excitation [Jørgensen et al., 2005].

From a first test with rotating wall cooling in REXTRAP it was shown that rotating wall cooling is beneficial over sideband cooling when more then $1 \cdot 10^7$ ions are trapped [Ames, 2002]. On the downside the cooling seems to be less efficient when measured with an emittance meter [Podadera-Aliseda & Lindroos, 2006]. Note that for WITCH this does not necessary holds as well. REXTRAP typically uses a short cooling time, while at WITCH a longer cooling cycle is used, such that the ion cloud at WITCH will have more time to relax to the state of a nonneutral plasma, whereafter the excitation can successfully be applied. However, more investigation of this topic is needed to extract a firm statement about the possibility of rotating wall excitation at WITCH. It might well be that relaxation for a few ms in REXTRAP, prior to rotating wall cooling is also beneficial. A relaxation time of around 10 ms after which the Coulomb interaction has re-arranged itself should be sufficient. After this, the ion behavior will be more that of a plasma, most likely resulting in an improved efficiency of the rotating wall excitation.

Note that recently it was shown that rotating wall excitation also works in the one-particle regime [Greaves & Moxom, 2008], i.e. when the amount of ions is around or below 1000. Rotating wall excitation can then be used to achieve very fast (within a few ms) a high density. Furthermore, it was shown that the time needed to increase the density of the ions increased linearly with the magnetic field. The resonant excitation frequency equals the sum of the axial frequency and the $m$ times the magnetron frequency, with $m$ the rotating wall excitation mode.

Taking this in to account, rotating wall excitation should be tried again at REXTRAP, with special care taken of the relaxation time prior to the excitation. The excitation amplitude and time which were taken between 2.5-15 V amplitude and from 10 to 50 ms only [Podadera-Aliseda & Lindroos, 2006] should be looked at more carefully. Especially since for a rotating wall excitation on positron plasmas the excitation amplitude is

maximum only 1 V as well as that the duration of the excitation is up to seconds before the maximum plasma density (for that given frequency is reached) [Danielson & Surko, 2005]. Most likely for ions in REXTRAP or in the WITCH experiment, the parameter space is different, but nevertheless has to be looked into more detail before a statement can be made whether rotating wall excitation is useful or not for REXTRAP or for WITCH. Due to the short trapping time in REXTRAP (only 80 ms), rotating wall excitation will most likely not have a major improvement. However at the WITCH experiment, typical cooling times are up to 500 ms. At this timescale, rotating wall excitation might be preferred over sideband cooling, due to an increase in the ion density, which prevents ion losses in the cooler trap during the quadrupole excitation, see section 6.4.1.

It was tried to simulate rotating wall excitations with the Simbuca code, but no centering nor an increase in ion density was observed compared to an ion cloud that is not subject to an excitation, except that when a rotating wall excitation is applied in the direction opposite to the rotation of the ion cloud the whole ion cloud is strongly distorted due to the applied electric field. In this case, within 10 ms the whole ion cloud is lost on the walls of the Penning trap. Further investigation is needed to investigate the need of a rotating wall excitation for WITCH. And to determine the possibility to use rotating wall excitation to overcome the losses observed in the cooler-trap and during a quadrupole excitation.

# Chapter 7

# Conclusion and outlook

In this work the first measurement on the beta neutrino angular correlation cofficient of the WITCH experiment has been presented. The theoretical framework as well as the experimental setup have been discussed.

An important part of the research reported here was the development and application of the *Simbuca* Penning trap simulation package to calculate the Coulomb interaction between ions. Due to the novel approach of using a graphics card for the calculation of the Coulomb interaction (instead of a CPU) the simulation time is incredibly shorter by 2 to 3 orders of magnitude. Further, this complete simulation package was applied to investigate nonneutral plasmas in the WITCH Penning traps. It has been shown that an ion cloud can be considered a plasma when it consists of more than $1 \cdot 10^4$ ions. Furthermore the mutual Coulomb repulsion between ions influences their energy distribution in the trap, as was demonstrated with simulations as well as with experimental data.

The final commissioning of the WITCH experiment, with its prime physics candidate $^{35}$Ar, has also been discussed in this work. This has led to a first determination of the $\beta$-$\nu$ angular correlation coefficient $a$ with the WITCH setup, albeit still with limited statistical precision. It has been shown that an improvement on different parts of the setup is still possible, which would allow reaching a statistical uncertainly below 0.5%. Data sets with a statistical significance below 5% have been acquired already, in October and November 2011. The analysis of these data will provide valuable information on the main systematic effects and will learn how the setup, the measurement cycle and the analysis can be further improved in view of a final result.

# Appendix A

# In trap decay of ions

Simbuca was used as a simulation tool to investigate in-trap-decay efficiency of $^{61}$Mn,$^{62}$Mn,$^{63}$Mn ions in the ISOLTRAP setup. A paper on this topic will be submitted soon and its draft is attached below. In this paper, Penning trap parameters were varied and their influence on the in-trap-decay efficiency was examined. Furthermore, simulations confirm the experimentally determined in-trap-decay efficiency or around 50%.

# Recoil-ion trapping for precision mass measurements

A. Herlert[1,a], S. Van Gorp[2], D. Beck[3], K. Blaum[4], M. Breitenfeldt[5,b], R.B. Cakirli[6,c], S. George[3,7,d], U. Hager[8,e], F. Herfurth[3], A. Kellerbauer[4], D. Lunney[9], R. Savreux[3], L. Schweikhard[5], and C. Yazidjian[3]

[1] CERN, Physics Department, 1211 Geneva 23, Switzerland
[2] K.U. Leuven, Instituut voor Kern- en Stralingsfysica, Celestijnenlaan 200 D, 3001 Leuven, Belgium
[3] GSI Helmholtzzentrum für Schwerionenforschung GmbH, Planckstr. 1, 64291 Darmstadt, Germany
[4] Max-Planck-Institut für Kernphysik, Saupfercheckweg 1, 69117 Heidelberg, Germany
[5] Ernst-Moritz-Arndt-Universität, Institut für Physik, 17487 Greifswald, Germany
[6] Istanbul University, Department of Physics, 34134 Istanbul, Turkey
[7] Johannes Gutenberg-Universität, Institut für Physik, 55099 Mainz, Germany
[8] University of Jyväskylä, Department of Physics, P.O. Box 35 (YFL), 40014 Jyväskylä, Finland
[9] CSNSM-IN2P3-CNRS, Université de Paris Sud, 91405 Orsay, France

**Abstract.** For the first time masses of recoiling daughter ions have been measured that were held after beta-decay in a buffer-gas-filled Penning trap. From the masses of the trapped beta-decaying manganese ions $^{61-63}\mathrm{Mn}^+$ and the daughter recoil-ions $^{61-63}\mathrm{Fe}^+$ the $Q$ values of $^{61-63}\mathrm{Mn}$ have been deduced with an absolute uncertainty of about 5 keV. The observed yield of iron ions is compared to results from simulations, which confirm a recoil-ion trapping efficiency of about 50 %.

**PACS.** 82.80.Qx Ion cyclotron resonance mass spectrometry – 21.10.Dr Binding energies and masses – 27.50.+e $59 \leq \mathrm{A} \leq 89$ – 07.05.Tp Computer modeling and simulation – 23.40.-s $\beta$ decay; double $\beta$ decay; electron and muon capture

## 1 Introduction

The region of neutron-rich nuclei around $N = 40$ has been subject of many investigations to shed light on the question how nuclear structure evolves between the major shells $N = 28$ and 50. Indeed, data, e.g., on neutron-rich chromium [1,2], vanadium [3] and iron isotopes [4–6] at $N = 40$ showed a variation of collectivity and deformation with an increase of collectivity near $N = 40$ [7]. The onset of collectivity is seen as an indication supporting a new island of inversion [8] in analogy to the one known at $N = 20$, e.g., for $^{32}\mathrm{Mg}$ [9]. Mass measurements on neutron-rich nickel, copper and gallium isotopes showed no indication of a sub-shell behavior [10]. Nevertheless, data across $N = 40$ were still missing, e.g., for neutron-rich manganese

and iron isotopes, which would give further information on the mass surface in that region.

Penning trap mass spectrometry is presently the method of choice for high-precision mass determination on stable as well as short-lived nuclei [11,12]. Numerous such measurements have been performed so far at the ISOLDE facility at CERN using the double Penning trap mass spectrometer ISOLTRAP [14]. ISOLTRAP makes use of the large variety of radioactive ion beams available at ISOLDE. However, although more than 900 isotopes can be delivered with yields sufficiently high for mass measurements at ISOLTRAP, the production process with protons impinging on thick targets and subsequent diffusion and ionization leads to gaps in the chart of nuclides: Due to their chemical and physical properties, certain isotopes are not released from the target and are therefore not available, e.g., iron isotopes as required for the study of nuclear structure in the region around $N = 40$.

Nevertheless, with a Penning trap it is possible to store ions for a long time without significant losses. This can be used to produce nuclides by transmutation, e.g., nuclear $\beta$ decay in the trap volume: The short-lived ions are stored and eventually decay, and the daughter-nuclide ions are trapped afterwards. This has been shown in a preliminary study with $^{37}\mathrm{K}$ isotopes which transformed into $^{37}\mathrm{Ar}$ in the trap by $\beta^+$ decay [15]. In the present work, this proce-

---

[a] *Present address:* FAIR GmbH, Planckstr. 1, 64291 Darmstadt, Germany, e-mail: a.herlert@gsi.de
[b] *Present address:* K.U. Leuven, Instituut voor Kern- en Stralingsfysica, Celestijnenlaan 200 D, 3001 Leuven, Belgium
[c] *Present address:* Max-Planck-Institut für Kernphysik, Saupfercheckweg 1, 69117 Heidelberg, Germany
[d] *Present address:* NSCL, Michigan State University, East Lansing, MI 48824-1321, USA
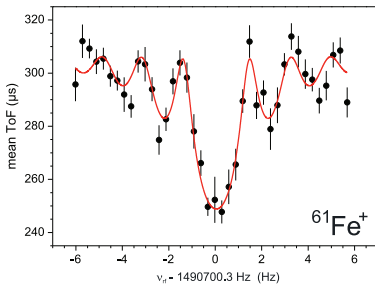[e] *Present address:* Colorado School of Mines, Golden, CO 80401, USA

2                                A. Herlert et al.: Recoil-ion trapping for precision mass measurements



**Fig. 1.** Ion-cyclotron resonance of $^{61}$Fe$^+$ ions. The solid line is a fit of the theoretical line shape [20] to the data points.

dure was applied to the decay of neutron-rich manganese isotopes into iron isotopes in order to allow one to access these nuclides for mass measurements for the first time at ISOLDE. In addition, the observed iron yields are compared to ab-initio simulations [16] which can provide more quantitative information on the efficiency of the recoil-ion trapping in a buffer-gas-filled Penning trap.

## 2 Experimental setup and procedure

The ISOLTRAP mass spectrometer is described in detail in [14]. It consists of a radiofrequency quadrupole buncher and cooler (RFQ) to prepare the 30-60 kV quasi-continuous beam from ISOLDE for subsequent trapping, and two Penning traps for further mass purification and high-precision mass measurements. In the first buffer-gas-filled Penning trap the ions of interest are selected using the buffer-gas-assisted quadrupolar rf excitation [17]. As part of the ion cooling process, the ions are initially kept in the trap for 150 ms to axially center them before application of the rf excitations. For the in-trap-decay scheme this duration is increased to one second in order to allow the stored manganese ions to decay in the trap. The most important experimental steps and their duration are given in Tab. 1.

The recoil-ion-trapping method is described in detail in [15]. In contrast to the results shown for $\beta^+$ decay in [15], the manganese isotopes studied here decay by $\beta^-$ emission, i.e. the daughter nuclide will be in principle doubly charged after the decay (neglecting additional electron shake-off). Nevertheless, only the singly charged iron ions were selected by tuning to the proper cyclotron frequency, i.e. charge-exchange reactions in the buffer-gas environment most likely occured as has been observed, e.g., in the case of doubly charged xenon ions [18].

Since neither the masses of the neutron-rich manganese isotopes nor those of the iron isotopes are well known,

both are of interest and can be accessed in one experimental run using the in-trap-decay method. In order to have enough decays of the parent ions on the experimental time scale (half-lives below one second), the iron isotopes $^{61-63}$Fe have been studied only. The neutron rich manganese ions were produced by impinging 1.4-GeV protons from the Proton Synchrotron Booster at CERN on to a uranium carbide target equipped with a tungsten cavity for selective laser ionization [19]. The ISOLDE ion source was operated at 30 kV and isobars were separated with the GPS mass separator.

## 3 Results

### 3.1 Mass determination

The cyclotron frequencies $\nu_c = qB/(2\pi m)$ of $^{56-63}$Mn$^+$ have been measured, where $B$ is the magnetic field strength in the Penning trap and $m$ and $q$ are the mass and charge of the stored ion. After in-trap decay the $^{61-63}$Fe$^+$ ions were transferred to the precision Penning trap where their cyclotron frequencies were measured, too. As an example, a cyclotron resonance measured for $^{61}$Fe$^+$ is shown in Fig. 1.

A summary of all measured frequency ratios $r = \nu_{c,ref}/\nu_c$ is given in Tab. 3. The atomic mass $m$ of the nuclide of interest can be derived by

$$m = r(m_{ref} - m_e) + m_e \qquad (1)$$

with the atomic mass $m_{ref}$ of the reference nuclide and the electron mass $m_e$. By convention not the atomic mass but rather the mass excess $ME$ is listed, which is defined as the difference $ME = m - A$ between the atomic mass and the mass number $A$, taking the conversion factor 1 u= 931494.0090(71) keV [21].

Data on the stable isotopes $^{41}$K and $^{85}$Rb as well as the masses of $^{56,57}$Mn were taken as cross-checks of all data recorded. For $^{85}$Rb a deviation by more than two standard deviations to the literature mass-value was obtained, which is probably due to a non-optimal injection of ions much heavier than the reference ions $^{39}$K$^+$. Although no deviation for the mass of the stable $^{41}$K isotope was observed, all uncertainties for the frequency ratios given in Tab. 3 were modified by adding in quadrature $6 \times 10^{-8}$ as an additional systematic error. This brings the measured mass-excess of $^{85}$Rb within one standard deviation of the literature value. Otherwise, the analysis procedure followed the one described in [22]. Despite the additional systematic uncertainty, the mass excess values obtained have absolute uncertainties below 4 keV except in the case of $^{63}$Fe, for which only one resonance was recorded, resulting in a larger statistical uncertainty.

### 3.2 Identification of isomers

The even-mass neutron-rich manganese isotopes have isomers with half-lives long enough to be possibly delivered

A. Herlert et al.: Recoil-ion trapping for precision mass measurements      3

**Table 2.** Half-life, spin and parity of ground and isomeric states of manganese isotopes. Data taken from [29] (values marked with # are estimates deduced from systematic trends). Note that for $^{62}$Mn the assignment of the ground and isomeric state is not known.

| isotope | $\Delta E$ (keV) | half-life | $J^{\pi}$ |
|---|---|---|---|
| $^{56}$Mn | | 2.58 h | $3^{+}$ |
| $^{57}$Mn | | 85.4 s | $5/2^{-}$ |
| $^{58}$Mn | | 3.0 s | $1^{+}$ |
| $^{58m}$Mn | 71.78 | 65.4 s | $(4)^{+}$ |
| $^{59}$Mn | | 4.59 s | $(5/2)^{-}$ |
| $^{60}$Mn | | 280 ms | $1^{+}$ |
| $^{60m}$Mn | 271.90 | 1.77 s | $4^{+}$ |
| $^{61}$Mn | | 670 ms | $(5/2)^{-}$ |
| $^{62}$Mn | | 671 ms | $(4^{+})$ |
| $^{62m}$Mn | 0#(150#) | 92 ms | $(1^{+})$ |
| $^{63}$Mn | | 275 ms | $(5/2^{-})$ |

by ISOLDE. In some cases these isomers can be more strongly populated in the production process than the ground state. A list of ground states and isomeric states of the manganese isotopes studied in this work is given in Tab. 2. Usually, with proton-induced fission, the high-spin isomeric state is more strongly populated than the ground state (see e.g. [23,24] or [25] for far asymmetric fission). In case of $^{62}$Mn the spin assignment of the isomers is not known and therefore careful analysis is needed.

As an example the cyclotron resonance of $^{58}$Mn$^{+}$ is plotted in Fig. 2 for two different rf-excitation durations. While for a duration of $T_{rf} = 300$ ms the two states are not fully resolved, the cyclotron resonance for $T_{rf} = 1200$ ms shows the presence of the ground state. The latter has a much lower abundance as compared to the isomeric state at lower cyclotron frequency, i.e., at higher mass. Thus, as only a few ions are present in the trap in each experimental cycle, the amount of contaminating isomeric ions is negligible and there is no significant influence on the mass determination of the isomeric state.

While in the case of $^{58}$Mn both states were observed and thus their relative abundance is known, the situation for $^{60}$Mn and $^{62}$Mn is more complicated. In both cases no traces of two states were observed in the ToF spectra or cyclotron resonances. Especially in the case of $^{62}$Mn the excitation energy of the isomer is not known and therefore no suitable excitation duration can be chosen in order to achieve separation. Furthermore, in both cases the high-spin state is most probably more strongly populated and delivered by ISOLDE, independent of the respective half-life and resulting losses due to $\beta$ decay.

In order to obtain additional information to help identify the ground or isomeric state, the data were analyzed with respect to the absolute number of ions in the precision trap as a function of storage time. Note that the decay loss of the parent ions can only be monitored by looking at the number of surviving parent ions and not at the number of appearing daughter ions. The latter mostly leave the trap due to the shallow trapping potential.
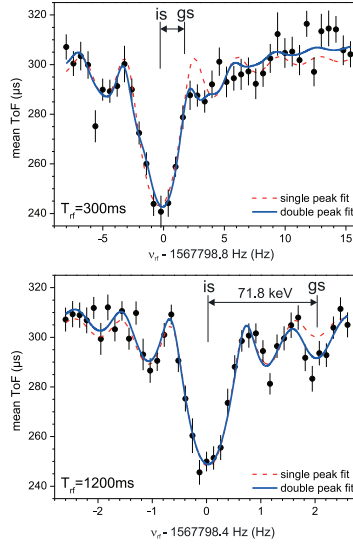


**Fig. 2.** Ion cyclotron resonances of $^{58}$Mn$^{+}$ for excitation durations $T_{rf} = 300$ ms (top) and $T_{rf} = 1200$ ms (bottom). The solid and dashed lines are fits of the line shape [20] to the data points. The dashed line shows a fit for a single resonance ($\chi_{\nu}^{2} = 1.6$ and 1.5 for $T_{rf} = 300$ ms and $T_{rf} = 1200$ ms, respectively) while the solid line gives the result for two resonances within the frequency range ($\chi_{\nu}^{2} = 1.0$ and 1.1 for $T_{rf} = 300$ ms and $T_{rf} = 1200$ ms, respectively). The ground state (gs) and isomeric state (is) are marked together with the energy difference. For details see text.

As an example, the absolute number of ions per cycle in the precision trap is plotted as a function of the cyclotron rf excitation duration for $^{62}$Mn$^{+}$ in Fig. 3 (top). The ion signal was integrated over the expected time-of-flight-range of parent ions only (taking into account the shorter time-of-flight due to in-resonance quadrupolar rf excitation). Since the experimental time was limited, only a few different excitation durations were applied. The resulting values for the half-lives are shown in Fig. 3 (bottom) together with the literature values for the ground and isomeric states.

For $^{60}$Mn the half-life of the ground state is 0.280 s [31] while the excited state isomer has a half-life of 1.7 s. In the case of $^{62}$Mn a short-lived isomeric state was identified by

4                     A. Herlert et al.: Recoil-ion trapping for precision mass measurements
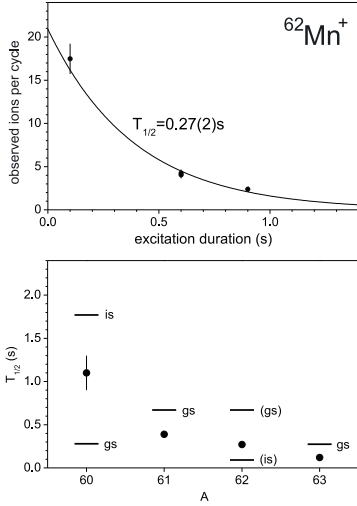


**Fig. 3.** Top: Number of $^{62}$Mn$^+$ ions observed at the ToF ion detector as a function of the duration of the quadrupolar rf excitation in the precision Penning trap. The solid line is a weighted fit of an exponential decay to the data points. Bottom: Half-lives of $^{60-63}$Mn as deduced from exponential fits as shown in the top graph (filled circles). The expected half-lives of the ground state (gs) and isomeric state (is) are given with lines. In the case of $^{62}$Mn the assignment to either the ground state or the isomeric state is not clear.

Gaudefroy *et al.* [33] which has a half-life of 92 ms. An assignment of the ground state was, however, not possible and therefore it is not clear if the high or the low-spin state is the ground state. It is assumed in the following, that the longer-lived state is the ground state.

In all cases the determined half-lives are about a factor 2 smaller than the literature value of the longer-lived state. Additional loss mechanisms cannot be excluded. Furthermore, fluctuations in the ISOLDE ion production may lead to systematic deviations in the measured absolute ion numbers. Therefore, the half-lives obtained from the decay loss in the measurement Penning trap are not sufficient for unambiguous identification.
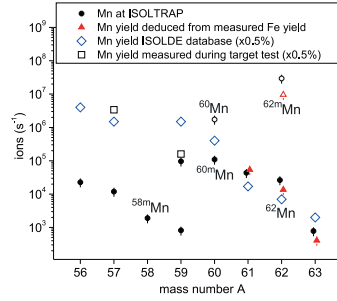


**Fig. 4.** Yield of manganese ions as observed at ISOLTRAP (filled circles). In addition, the yield of manganese ions as expected from the ISOLDE yield data base is shown (empty diamonds) together with data points measured in the beginning of the run as target test (empty squares). A transport efficiency of 0.5 % from the ISOLDE ion source to the ToF ion detector of ISOLTRAP is assumed to rescale the ISOLDE data. Data points denoted by filled triangles give the manganese yield as deduced from the observed iron yield measured at the ion detector. Data points denoted by empty circles and triangles show the deduced manganese yields if the shorter-lived isomers of $^{60,62}$Mn are assumed.

### 3.3 Ion yields

As an additional check, the yield observed at ISOLTRAP can be compared to the manganese yield as delivered by ISOLDE using a resonance ionization laser ion source (RILIS) [32]. The measurement cycle had a fixed duration as shown in Tab. 1 and therefore the measured yield can be corrected for decay losses during the storage in the various ion traps. The result is shown in Fig. 4 where the filled circles are the corrected yields of manganese ions from the RFQ buncher and cooler and the empty diamonds indicate the ISOLDE yields as tabulated in the yield data base (data from [32]) scaled by the stopping and trapping efficiency of 0.5 % of the ISOLTRAP RFQ. The empty squares denote yield data taken during the experimental run at the ISOLDE tape station system (also scaled by 0.5 %). Up to mass number $A = 59$ a lower yield was observed as compard with the expected (scaled) ISOLDE yield, which is most probably due to a detuned ion transport (as well as beam sharing at the GPS mass separator). After retuning of the ion transport (measurements from $A = 59$ to 63) a satisfying agreement of the measured ISOLDE yield with the yield at ISOLTRAP can be seen. For the more neutron-rich manganese isotopes the trend of the observed yield follows the expected yield data.
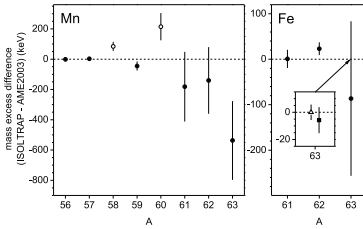
**Fig. 5.** Mass-excess values from the Atomic-Mass Evaluation 2003 data [21] (filled and empty circles for ground and isomeric states, respectively) relative to the values for manganese and iron isotopes determined in this work. The inset shows an additional recent result for $^{63}$Fe from the LEBIT Penning trap experiment [35] (filled square) which is compared to the ISOLTRAP value (empty triangle).

In the case of $A = 60, 62$ the observed yield was corrected according to the shorter half-life of the respective isomers (see Tab. 2) and the resulting yield data are plotted as empty circles in Fig. 4. Clearly, the yields are much higher than expected from the trend, especially in the case of $^{62}$Mn, which, together with the deduced half-life data, gives a strong indication that in the case of $^{60}$Mn and $^{62}$Mn the longer-lived states have been observed in the measurement trap, i.e. for $^{60}$Mn the isomer.

For an estimate of the recoil-ion-trapping efficiency, the initial yield of the precursor manganese ions is determined from the number of iron ions observed at the ToF ion detector by correcting for the in-trap decay in the preparation Penning trap as well as decay losses during the transport to the preparation trap. The resulting manganese yields are plotted in Fig. 4 (filled triangles).

## 4 Discussion

### 4.1 $Q$-values from mass measurements

The mass-excess values determined in this work are compared to the literature values as given in the 2003 Atomic-Mass Evaluation (AME2003) [21]. The filled and empty circles in Fig. 5 denote the AME2003 data relative to the ISOLTRAP values for the ground and isomeric states, respectively. In general, there is good agreement for the ground-state data within the uncertainties of the literature values. The new data mainly improve the uncertainties of the mass-excess values.

For the manganese isotopes, a trend towards smaller mass-excess values is observed when going to more neutron-rich isotopes. The literature value of $^{63}$Mn is deviating by more than 500 keV, however, with an uncertainty of 260 keV. In the case of the isomeric states $^{58m}$Mn and

**Table 4.** $Q$-values as deduced from the experimental data and resulting maximum recoil energies of the daughter nuclei.

| nuclide | Q (keV) | max. recoil energy (eV) |
|---------|---------|-------------------------|
| $^{61}$Mn | 7178(4) | 518 |
| $^{62}$Mn | 10697(4) | 1086 |
| $^{63}$Mn | 8750(7) | 729 |

**Table 5.** Fraction of product ions trapped after in-trap decay of manganese isotopes in the Penning trap as simulated for two different charge states $z$ (see text for details). The branching ratios for the case of additional gamma decays are discussed in the text. The experimental values are taken from Fig. 4 to calculate the ratio.

| parent ion | product ion | $z = 1$ | $z = 2$ |
|------------|-------------|---------|---------|
| ratio of experimental yield | | | |
| $^{61}$Mn$^+$ | $^{61}$Fe$^{z+}$ | 1.22(52) | |
| $^{62}$Mn$^+$ | $^{62}$Fe$^{z+}$ | 0.51(22) | |
| $^{63}$Mn$^+$ | $^{63}$Fe$^{z+}$ | 0.52(22) | |
| $\beta$ decay to gs (%) | | | |
| $^{61}$Mn$^+$ | $^{61}$Fe$^{z+}$ | 52.6 | 74.6 |
| $^{62}$Mn$^+$ | $^{62}$Fe$^{z+}$ | 35.0 | 51.1 |
| $^{63}$Mn$^+$ | $^{63}$Fe$^{z+}$ | 43.6 | 63.2 |
| $\beta$ decay and $\gamma$ decay to gs (%) | | | |
| $^{61}$Mn$^+$ | $^{61}$Fe$^{z+}$ | 53.9 | |
| $^{62}$Mn$^+$ | $^{62}$Fe$^{z+}$ | 38.7 | |
| $^{63}$Mn$^+$ | $^{63}$Fe$^{z+}$ | 46.9 | |

$^{60m}$Mn, a deviation by the amount of the excitation energy is observed, which possibly indicates a wrong assignment of levels in the results from previous $\beta$-decay experiments that are included in the mass evaluation AME2003. A thorough investigation is pursued in a separate publication which includes in addition to the data presented in Tab. 3 also new data on neutron-rich manganese isotopes up to $^{66}$Mn and a full new mass evaluation [34]. The present work concentrates on the recoil-ion trapping and its efficiency.

In the case of the iron isotopes, a recent result [35] from the LEBIT Penning trap mass spectrometer has been added for comparison as well (see inset of Fig. 5, filled square). This shows the good agreement of the ISOLTRAP and LEBIT data for $^{63}$Fe, indicating an accuracy of independent experimental data on the level of a few keV.

Since precise mass-excess values are available for three pairs of mother-daughter nuclei, measured in the same experiment under the same conditions, the $Q$-values of the manganese isotopes $^{61-63}$Mn can be deduced as summarized in Tab. 4. These values will be used in the following simulations of the in-trap decay of the manganese ions and the recoil-ion trapping.

### 4.2 In-trap decay efficiency and simulations

The observed yield of iron isotopes can be used as a measure of the in-trap decay efficiency. The ratios of the averaged observed manganese and iron yields are given in

6                                   A. Herlert et al.: Recoil-ion trapping for precision mass measurements

Tab. 5 (top). In the case of $^{61}$Mn, the yields for manganese and iron are about the same, while for $^{62}$Mn and $^{63}$Mn the deduced yields for the iron ions are smaller than those for manganese, most probably due to losses of the recoil ions after $\beta$ decay.

For a more quantitative approach, ab-initio simulations have been performed using the SIMBUCA simulation package [16]. This code allows calculation of the ion motion in a Penning Trap. Furthermore, it utilizes the GPU of a graphics card in order to speed up the calculation of the ion-ion interactions in a Penning trap and thus enables the investigation of the properties of an ion cloud of more than a thousand ions. The geometry of the preparation Penning trap [36] and the applied potentials as well as realistic buffer-gas collisions have been taken into account.

All nuclides investigated in the present work decay by emission of a $\beta^-$ particle and an anti-electron-neutrino:

$$^A_Z X \longrightarrow ^A_{Z+1} Y + \beta^- + \bar{\nu}_e \qquad (2)$$
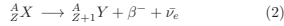
The daughter nucleus has maximum recoil energy when the anti-electron-neutrino is at rest after decay. In this case momentum conservation requires

$$p_{recoil} + p_e = 0 \qquad (3)$$

for the sum of the momenta of the recoil nucleus and the emitted electron. In the decay the energy $Q$ is released, which for $p_\nu = 0$ is shared between the daughter nucleus and the electron:

$$E_{kin,recoil} + E_{kin,e} = Q. \qquad (4)$$

Taking the relation

$$E = E_{kin} + mc^2 \qquad (5)$$

between the total energy $E$, the kinetic energy $E_{kin}$, and the rest mass energy $mc^2$, and the relativistic energy-momentum relation

$$E^2 = p^2 c^2 + m^2 c^4 \qquad (6)$$

one obtains the maximum recoil energy for the daughter nucleus in case of $\beta^-$ decay:

$$E_{recoil,max} = \frac{Q^2 + 2E_{0,e}Q}{2(Q + E_{0,recoil} + E_{0,e})} \qquad (7)$$

$$= \frac{Q^2 + 2m_e c^2 Q}{2(Q + M_{recoil}c^2 + m_e c^2)}. \qquad (8)$$

Due to the large mass of the recoil nucleus ($M_{recoil} \gg m_e$) this can be approximated by:

$$E_{recoil,max} \approx \frac{Q(Q + 2m_e c^2)}{2M_{recoil}c^2} = E_0. \qquad (9)$$

The maximum recoil energies for the cases studied in this work are listed in Tab. 4. Since the potential wall of the preparation trap is about 100 V at both ends, a loss of
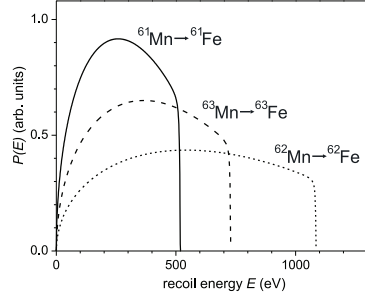


**Fig. 6.** Calculated recoil-energy probability distribution for the daughter nuclides after $\beta$ decay of $^{61-63}$Mn. Data have been normalized with respect to the area of $P(E)$.

ions due to the larger recoil energy can be expected. Aside from the recoil energy, also the angle of the momentum of the recoil nucleus relative to the magnetic field axis varies. This makes trapping of recoil ions possible even if the recoil energy is higher than the trapping potential.

The distribution of recoil energies after $\beta$ decay is determined by the $\beta$-$\nu$ angular correlation as described in [37,38]. For unpolarized nuclei and with a Fierz interference coefficient $b = 0$ this correlation can be written as:

$$\omega(\theta_{\nu\beta}) = 1 + a \frac{p_\beta p_\nu}{E_\beta E_\nu} \cos(\theta_{\nu\beta}) \qquad (10)$$

with the $\beta$-$\nu$ angular correlation coefficient $a$, the total energies $E_\beta$ and $E_\nu$ of the emitted $\beta$ particle and neutrino, respectively, and $\theta_{\beta\nu}$ the angle between the momentum $p_\beta$ and $p_\nu$ of the $\beta$ particle and the neutrino, respectively. For pure Fermi decays $a = 1$ and for pure Gamov-Teller transitions $a = -1/3$. For the neutron-rich nuclides in this work $a = -1/3$ is considered only as Fermi transitions in their $\beta^-$ decay are energetically forbidden and admixtures due to isospin breaking can be neglected. In order to obtain the distribution of recoil energies, Eq. (10) is transformed into a distribution $P(E_{recoil}, E_\beta)$ as described in [38], followed by an integration over all $\beta$-particle energies $E_\beta$. The resulting distributions $P(E_{recoil})$ (see Fig. 6) are used for the simulations. The shape of the distribution is governed by the $\beta$-$\nu$ angular correlation coefficient $a = -1/3$ and the only major difference between isotopes is the maximum recoil energy $E_0$, which is largest for $^{62}$Mn.

The stored ions are expected to have an initial spatial distribution with a FWHM of less than 2 mm. The velocity distribution of the ions is determined by their recoil energy distribution as mentioned above. Within the SIMBUCA simulation, the initial position and initial momentum (due to the recoil process) are randomly set according to the underlying probability distributions. The angle of the re-

A. Herlert et al.: Recoil-ion trapping for precision mass measurements          7
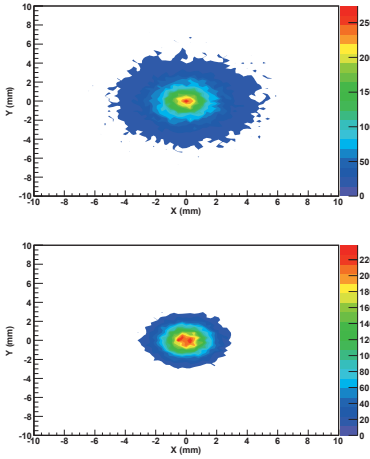




**Fig. 7.** Number of recoil ions $^{62}Fe^{z+}$ (top: charge state $z = 1$, bottom: $z = 2$) lost in the region of the bottom electrode of the preparation Penning trap after in-trap decay of a total of 100,000 $^{61}Mn^+$ ions. The number of events is plotted as a function of the distance from the trap axis ($x = y = 0$).

**Fig. 8.** Number of ions lost as a function of the recoil energy and the angle of the momentum vector of the recoil ion directly after $\beta$ decay ($\phi = 0$ and $\phi = \pi$ are in the direction of the bottom and the top of the preparation Penning trap, respectively).

coiling ion relative to the experiment axis is isotropically distributed. The magnetic field strength was set to 4.7 T, i.e. that of the preparation Penning trap. All simulations were performed for 100,000 ions with one ion in the trap in each cycle. Note that Coulomb interaction was tested in the simulation but showed no effect on the resulting ion loss for an initial distribution of ions within an FWHM of 2 mm and a total number of up to 500 ions stored at once. Since less than 20 ions are typically stored in each experimental cycle in the trap, the density of the ions was not high enough for Coulomb interaction to play a role and was therefore neglected in the following simulations.

The situation is different with respect to the charge state of the recoil ions. Due to the $\beta^-$ decay the daughter nuclides are expected to be doubly charged unless other charge-changing reactions occur, e.g. electron shake-off or charge exchange in the collision with atoms or molecules present in the trap volume. The influence of a sudden change of the charge state on the ion trajectory in a Penning trap was studied in detail in [39]. The main result of reducing the charge state from $z = 2$ to $z = 1$ is an increase of the orbit radius in the trap by a factor of up to three, which can lead to ion loss. In the present experiment, only singly charged iron ions were taken into ac-

count and their cyclotron frequency applied to re-center them in the preparation trap. It is assumed that the majority of daughter ions ends up in the $z = +1$ charge state. Nevertheless, it is not known when the change from $z = +2$ to $z = +1$ occurs. Therefore, the simulation was performed for singly and doubly charged recoil ions, where the charge state does not change throughout the duration of the simulation of the ion trajectory, starting after beta decay until the ion is either lost or brought back to the center of the trap. Note that in the simulation the ions are lost within less than 10 $\mu s$ after $\beta$ decay.

As an example, Fig. 7 shows the number of ions lost in the region of the bottom electrode of the preparation trap (hitting an electrode or leaving the trapping potential) after a simulation of 100,000 ions under experimental conditions. The initial parameters were a FWHM of 2 mm and only $\beta$ decay (no $\gamma$ decay, which will be discussed below). The top and bottom graph give the results for singly and doubly charged recoil ions $^{61}Fe^{z+}$. The main ion loss occurs at small angles while the general shape of the distribution resembles a Gaussian, which is the initial ion distribution in the trap. For the doubly charged ions the distribution of ion loss is much more focused toward the experiment axis, due to the effect of the better radial storage in the homogeneous magnetic field.

In order to illustrate the influence of the recoil angle and the recoil energy on the ion loss, Fig. 8 shows the outcome of another simulation: Above the threshold energy (100 V in the present case) ion loss occurs which increases for larger angles $\phi$ relative to the experiment axis. Thus, depending on the $\beta$-$\nu$ angular correlation coefficient $a$ the ion loss can be very different, especially Fermi transitions ($a = 1$) favor higher recoil energies and thus ion loss is more likely to occur.

Concerning the radial ion loss, an additional simulation was performed where the FWHM of the initial ion distribution was varied. The result for the ion loss is shown

8                          A. Herlert et al.: Recoil-ion trapping for precision mass measurements
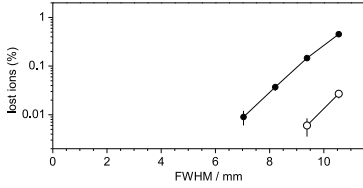


**Fig. 9.** Fraction of recoil ions $^{61}Fe^{z+}$ lost on the radial trap electrodes of the preparation Penning trap after in-trap decay as a function of the FWHM of the initial ion distribution (filled circles: $z = 1$, empty circles: $z = 2$). The potential wall was set to 100 V as in the experiment.
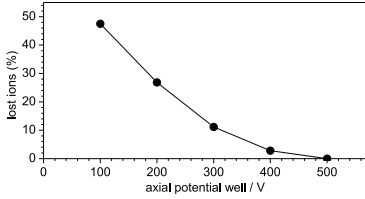


**Fig. 10.** Fraction of recoil ions $^{61}Fe^{1+}$ lost axially as a function of the potential applied to the outer Penning trap electrodes.

in Fig. 9. While for small ion clouds almost no ion loss occurs radially, it increases with increasing FWHM.

The fraction of ions that remain stored after in-trap decay under the different conditions are listed in Tab. 5. As mentioned above, the ion loss for doubly charged recoil ions is suppressed and thus a larger fraction should remain in the trap volume.

### 4.3 Additional $\gamma$ decay

After $\beta$ decay, excited energy levels of the daughter nuclide can be populated with subsequent emission of one or several gammas at energies of the order of hundreds of keV to several MeV. Therefore, the daughter nucleus experiences further two-body decay events which lead to additional recoiling effects. These change the velocity (magnitude and direction) of the daughter ion. It is assumed that the $\gamma$ decay happens instantaniously after the $\beta$ decay. This is a valid assumption since the maximum half-life of an excited state is nanoseconds and the ion has to travel more than $3\,\mu s$ before it hits the wall of the Penning trap and is lost.

For the nuclides studied in this work, the level schemes are shown in Fig. 11. In the case of $^{61}$Fe, the $\beta$-decay feed-

ing to the different energy levels is known [29,40]. In the other two cases recent experiments provided new data on the level schemes [41,42] and some of the levels with strong $\beta$ feeding are marked with an arrow. If several gammas are emitted sequentially, all the recoil effects have to be combined, leading to a complicated shape of the recoil energy spectrum. Since the branching is not always well known and the uncertainty of the experimental data is too large for a precise comparison, only single-$\gamma$ emission-events after $\beta$ decay are considered.

If $E^*$ is the excitation energy of the daughter nuclide after $\beta$ decay of the parent nuclide, energy and momentum conservation requires

$$E^* = E_R + E_\gamma \qquad (11)$$
$$0 = p_R + p_\gamma \qquad (12)$$

with $E_R = (p_R)^2/(2M)$ with $M$ the mass of the nuclide and $p_\gamma = E_\gamma/c$. The recoil energy due to emission of a $\gamma$ is then simply given by

$$E_R = \frac{E_\gamma^2}{2Mc^2}. \qquad (13)$$

A transformation to the moving frame, i.e. the daughter nuclide after initial $\beta$ decay, can be performed using momentum conservation

$$\boldsymbol{p_R}' = \boldsymbol{p_R} - \boldsymbol{p_\gamma} \qquad (14)$$
$$p_R'^2 = p_R^2 + p_\gamma^2 - 2p_Rp_\gamma\cos(\theta) \qquad (15)$$

resulting in the final recoil energy of the daughter nuclide

$$E_R' = E_R + \frac{E_\gamma^2}{2Mc^2} - \cos(\theta)\sqrt{\frac{2E_RE_\gamma^2}{Mc^2}}. \qquad (16)$$

In case the $\gamma$ is emitted in the direction of the moving daughter nuclide ($\theta = 0°$) the kinetic energy is reduced and if the $\gamma$ is emitted in the opposite direction ($\theta = 180°$) the daughter nuclide is accelerated to the maximum recoil energy. In the simulation, the angle $\theta$ is randomly distributed within the Monte Carlo approach.

In Fig. 12 the recoil-energy spectrum is shown for $^{63}$Fe where the $\gamma$ recoil is taken into account. For comparison, the dashed line gives the recoil energy spectrum without additional $\gamma$ decay, i.e. for ground-state to ground-state transitions. The dotted line shows the result for beta decay only to the excited state at 357 keV. The solid line gives the final result including the $\gamma$ transition to the ground state. Since the $\gamma$ energy is much smaller than the $\beta$ decay energy $Q$, the effect of the additional $\gamma$ recoil can only be seen at higher recoil energies.

For the simulation of the in-trap decay including $\gamma$ recoil, the following approximations and considerations have been made:

(i) $^{61}$Mn decay: 74 % of the $\beta$-decay feeding goes to the ground state of $^{61}$Fe, i.e. no $\gamma$ decay is involved. About 7 % is fed into the level at 207 keV and about 18 % into the level at 629 keV. The $\gamma$ cascades from the latter are not considered since the 629-keV $\gamma$ transition to the ground

A. Herlert et al.: Recoil-ion trapping for precision mass measurements 9
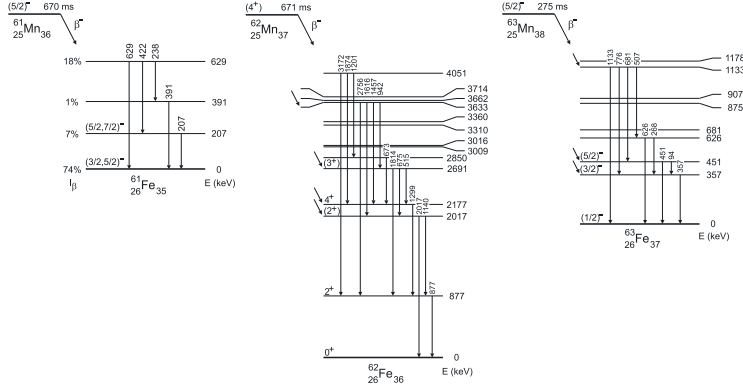


**Fig. 11.** Energy levels of $^{61-63}$Fe populated after $\beta$ decay of $^{61-63}$Mn. Data from [29,40–42].
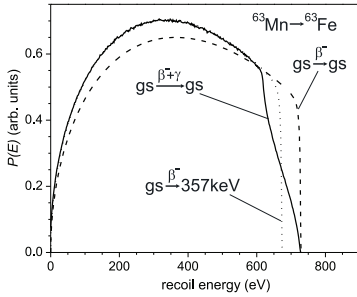


**Fig. 12.** Recoil energy distribution for the daughter nuclide after $\beta$ decay of $^{63}$Mn to the ground state of $^{63}$Fe (dashed line), to the excited state at 357 keV (dotted line), and to the excited state at 357 keV with subsequent $\gamma$ decay to the ground state (solid line). Data have been normalized with respect to the area of $P(E)$.

state carries most of the relative intensity, i.e. in the simulation a fraction of 18 % performs a $\gamma$ decay to the ground state at the respective energy of 629 keV.

(ii) $^{62}$Mn decay: As recently found by Hoteling and coworkers [41], it is the $4^+$ state that $\beta$ decays and therefore the decay to the $0^+$ ground state of $^{62}$Fe is strongly suppressed. The most intense $\beta$ feeding goes into the 3633-

keV level, the level at 2691 keV and the levels at 2177 keV and 2017 keV, respectively. All but one decay proceed by $\gamma$ cascades to the 877-keV level and from there (with the highest relative intensity) by $\gamma$ decay to the ground state. Since a complex decay scheme has to be considered, a rough estimate was performed taking into account only $\beta$-decay feeding to and subsequent $\gamma$ decay from the 877-keV level.

(iii) $^{63}$Mn decay: The level scheme shown in Fig. 11 is the result of a recent experiment [42] at ISOLDE/CERN and new data have been recorded but are not evaluated yet. The proposed scheme [42] shows a strong $\beta$ feeding to three levels as marked with arrows. Most of the $\gamma$ cascades end up in the 357-keV level. In addition, the 1133-keV level decays directly to the ground state. For the simulation, it was decided to take 25 % of $\gamma$ decay from the 1133-keV level and 75 % from the 357-keV level with no $\beta$ feeding to the ground state.

The results from these simulations are listed in Tab. 5. Note that the simulation was performed only for singly charged daughter nuclei. Comparing these values with the ones for the case of $\beta$ decay only, a slight increase of the surviving fraction of daughter ions can be seen. Similarly, an increase for doubly charged recoil ions can be expected.

The simulation results can now be compared to the experimental values, which are deduced from the yield measurements shown in Fig. 4. In the case of $^{61}$Mn no ion loss is observed. There is, however, a large uncertainty due to fluctuations in the production at ISOLDE (variation of the proton beam intensity and of the RILIS ionization at ISOLDE). Nevertheless, in agreement with the simulation results, the largest trapping efficiency is observed for $^{61}$Fe$^+$. For $^{62}$Fe and $^{63}$Fe similar experimental results are

10                          A. Herlert et al.: Recoil-ion trapping for precision mass measurements

obtained with about 50 % trapping efficiency, which agrees with the simulation results within the uncertainties given by the fluctuations of the beam intensity.

Thus, ab-initio simulations confirm the experimental findings, i.e. the possibility to store daughter ions after $\beta$ decay with efficiencies of about 50 %. As shown by the simulations, the efficiency of the trapping depends on various experimental parameters and the parameters of the $\beta$ decay itself. First of all, the $Q$ value defines the maximum recoil energy which is directly linked to the axial potential wall of the Penning trap. In addition, the magnetic field strength $B$ influences the radial storage, i.e. radial ion loss after $\beta$ decay is more likely for smaller $B$ values. Similarly, if the ion cloud is not compressed in the trap center after injection, radial ion loss may occur. The influence of the buffer-gas pressure was not studied, but in principle it is also a parameter relevant for the re-centering of the daughter ions after $\beta$ decay.

A transfer of recoil-ion trapping to other Penning trap systems seems thus feasible. Recently, $^{61}$Fe was produced by $\beta$ decay of $^{61}$Mn in the electron-beam ion source REX-EBIS of ISOLDE to deliver post-accelerated iron isotopes after charge-breeding [43]. However, in-trap decay and recoil-ion trapping in the REX-TRAP Penning trap system, which cools and bunches the radioactive ion beam from ISOLDE for subsequent injection into REX-EBIS, was found to be inefficient as compared with the REX-EBIS system. Some of the results of this work can be used to partly explain the low yield using recoil-ion trapping: First, the magnetic field strength is smaller (3 T), i.e. radial ion loss is more likely after $\beta$ decay. Second, the initial radial distribution of ions is probably larger than in the present experiment, which may increase the radial ion loss. Last, REX-TRAP is usually filled with a large number of ions (about $10^6 - 10^7$), i.e. Coulomb interaction also plays a role. Especially for the crucial injection of the ion bunch into the charge breeder REX-EBIS as, the ion distribution after $\beta$ decay including Coulomb repulsion could be too large. Nevertheless, a more detailed study of the REX-TRAP system with ab-initio simulations as shown in the present work and further measurements are required to obtain detailed information on the loss of daughter ions after in-trap decay at REX-TRAP.

## 5 Conclusion and outlook

The mass-excess values of neutron-rich manganese and iron isotopes have been determined by use of Penning trap mass spectrometry. Isomers have been identified for $^{58}$Mn and for $^{60}$Mn, where the experimental results indicate that the isomeric states were more strongly populated and their mass-excess values measured in the present work. In the case of $^{62}$Mn the longer-lived state was more strongly populated and survived the ion preparation in the ISOLTRAP setup for mass measurement. A direct assignment of the ground state was not possible. For $^{61-63}$Mn the $Q$-values were deduced from the measured mass difference with an absolute uncertainty of 4-7 keV.

The iron isotopes $^{61-63}$Fe were produced by in-trap decay in the buffer-gas-filled preparation trap of ISOLTRAP. The ion yields from ab-initio simulations agree with the values observed in the experiment, showing an efficient storage of the recoil ions with a trapping efficiency of about 50 %. The simulation showed a slight reduction of ion loss if $\gamma$ decay follows the initial $\beta$ decay to an excited level.

Although the in-trap decay method is limited to those nuclides which have both sufficient production yields and also half-lives in a time window between few tens of milliseconds and a few seconds, it has been shown to be efficient for the present investigation. This allows access to nuclides which are presently otherwise not available. With the simulation code used here, a possible experimental campaign can be planned beforehand to choose the storage parameters in order to maximize the yield of daughter nuclei.

## References

1. N. Aoi *et al.*, Phys. Rev. Lett. **102**, 012502 (2009)
2. A. Gade *et al.*, Phys. Rev. C **81**, 051304 (2010)
3. O. Sorlin *et al.*, Eur. Phys. J. A **16**, 55 (2003)
4. P. Adrich *et al.*, Phys. Rev. C **77**, 054306 (2008)
5. D. Pauwels *et al.*, Phys. Rev. C **79**, 044309 (2009)
6. W. Rother *et al.*, Phys. Rev. Lett. **106**, 022502 (2011)
7. M. Hannawald *et al.*, Phys. Rev. Lett. **82**, 1391 (1999)
8. J. Ljungvall *et al.*, Phys. Rev. C **81**, 061301 (2010)
9. K. Wimmer *et al.*, Phys. Rev. Lett. **105**, 252501 (2010)
10. C. Guénaut *et al.*, Phys. Rev. C **75**, 044303 (2007)
11. K. Blaum, Phys. Rep. **425**, 1 (2006)
12. Special issue of the International Journal of Mass Spectrometry, edited by L. Schweikhard and G. Bollen (Elsevier, Amsterdam, 2006), Vol. 251/23, pp. 85312
13. E. Kugler, Hyperfine Interact. **129**, 23 (2000)
14. M. Mukherjee *et al.*, Eur. Phys. J. A **35**, 1 (2008)
15. A. Herlert *et al.*, New J. Phys. **7**, 44 (2005)
16. S. Van Gorp *et al.*, Nucl. Instr. and Meth. A **638**, 192 (2011)
17. G. Savard *et al.*, Phys. Lett. A **158**, 247 (1991)
18. A. Herlert *et al.*, Int. J. Mass Spectrom. **251**, 131 (2006)
19. V.I. Mishin *et al.*, Nucl. Instr. and Meth. B **73**, 550 (1993)
20. M. König *et al.*, Int. J. Mass Spectrom. Ion Processes **142**, 95 (1995)
21. A.H. Wapstra, G. Audi, C. Thibault, Nucl. Phys. A **729**, 129 (2003)
22. A. Kellerbauer *et al.*, Eur. Phys. J. D **22**, 53 (2003)
23. I.F. Croall, H.H. Willis, J. Inorg. Nucl. Chem. **24**, 221 (1962)
24. U. Köster *et al.*, Nucl. Instr. and Meth. B **204**, 347 (2003)

A. Herlert et al.: Recoil-ion trapping for precision mass measurements 11

25. U. Köster, CERN-THESIS-2001-002, PhD thesis, TU München, Germany (1999)
26. C. Guénaut, priv. communication
27. C. Guénaut *et al.*, Eur. Phys. J. A **25**, s01, 35 (2005)
28. G. Audi, A.H. Wapstra, C. Thibault, Nucl. Phys. A **729**, 337 (2003)
29. ENSDF database (Evaluated Nuclear Structure Data File): http://www.nndc.bnl.gov/ensdf/
30. H.W. Ellis *et al.*, At. Data Nucl. Data Tabl. **22**, 179 (1978)
31. S.N. Liddick *et al.*, Phys. Rev. C **73**, 044322 (2006)
32. M. Oinonen *et al.*, Hyperfine Interact. **127**, 431 (2000)
33. L. Gaudefroy *et al.*, Eur. Phys. J. A **23**, 41 (2005)
34. S. Naimi *et al.*, submitted to Phys. Rev. C
35. M. Block *et al.*, Phys. Rev. Lett. **100**, 132501 (2008)
36. H. Raimbault-Hartmann *et al.*, Nucl. Instr. and Meth. B **126**, 378 (1997)
37. N. Severijns, M. Beck, O. Naviliat-Cuncic, Rev. Mod. Phys. **78**, 991 (2006)
38. O. Kofoed-Hansen, Dan. Mat. Fys. Medd. **28**, No. 9, 1 (1954)
39. A. Herlert, L. Schweikhard, Int. J. Mass Spectrom. **234**, 161 (2004)
40. E. Runte *et al.*, Nucl. Phys. A **441**, 237 (1985)
41. N. Hoteling *et al.*, Phys. Rev. C **82**, 044305 (2010)
42. H. Mach *et al.*, Acta. Phys. Pol. **40**, 477 (2009)
43. J. Van de Walle *et al.*, Eur. Phys. J. A **42**, 401 (2009)

12                          A. Herlert et al.: Recoil-ion trapping for precision mass measurements

**Table 1.** Time structure of the experimental steps in the ion traps for standard operation and for in-trap decay.

| procedure | standard operation | | in-trap decay | |
|---|---|---|---|---|
| | duration (ms) | element | duration (ms) | element |
| RFQ buncher and cooler | | | | |
| accumulation | 0.05-100 | Mn | 0.05-100 | Mn |
| cooling | 8 | Mn | 8 | Mn |
| Preparation Penning trap | | | | |
| axial cooling | 150 | Mn, Fe | 1000 | Mn, Fe |
| magnetron rf excitation | 5 | Mn, Fe | 5 | Mn, Fe |
| quadrupolar rf excitation | 100 | Mn | 100 | Fe |
| cooling of cyclotron motion | 100 | Mn | 100 | Fe |
| Precision Penning trap | | | | |
| magnetron rf excitation | 10 | Mn | 10 | Fe |
| dipolar rf excitation (cleaning) | 50 | Mn | 50 | Fe |
| quadrupolar rf excitation | 100-1200 | Mn | 100-1200 | Fe |

**Table 3.** Frequency ratios measured between $^{58m,59,60m,61-63}$Mn and $^{61-63}$Fe and the reference ion $^{39}$K$^+$ (mass of $^{39}$K $m = 39.96399848(21)$ u [28] with 1 u$= 931494.0090(71)$ keV [21] and $m_e = 548579.9110(12) \times 10^{-9}$ u). Frequency ratios of stable alkali ions as well as long-lived manganese ions $^{56,57}$Mn$^+$ relative to $^{39}$K$^+$ were measured as cross-checks. An additional systematic uncertainty of $6 \times 10^{-8}$ has been added in quadrature to the uncertainty of the frequency ratios (for details see text). In addition to the data measured in this work, frequency ratios from an earlier campaign (in 2003) are listed, for which only mass excess values have been published so far.

| ion | $r$ | $ME_{exp}$ (keV) | $ME_{lit}$ (keV) [21] |
|---|---|---|---|
| data from 2006 (as published in [34]) | | | |
| $^{58m}$Mn$^+$ | 1.4870354024(735) | -55755.4(2.7) | -55840(30) |
| $^{59}$Mn$^+$ | 1.5127070218(631) | -55525.0(2.3) | -55480(30) |
| $^{60m}$Mn$^+$ | 1.5384502463(648) | -52695.8(2.4) | -52910(90) |
| $^{61}$Mn$^+$ | 1.5641418011(653) | -51741.8(2.4) | -51560(230) |
| $^{62}$Mn$^+$ | 1.5899051939(718) | -48180.6(2.6) | -48040(220) |
| $^{63}$Mn$^+$ | 1.615606112(102) | -46886.8(3.7) | -46350(260) |
| $^{61}$Fe$^+$ | 1.5639440154(729) | -58920.2(2.7) | -58921(20) |
| $^{62}$Fe$^+$ | 1.5896104560(773) | -58877.8(2.8) | -58901(14) |
| $^{63}$Fe$^+$ | 1.615365034(155) | -55636.5(5.6) | -55550(170) |
| cross-check data from 2006 (as published in [34]) | | | |
| $^{56}$Mn$^+$ | 1.4356730300(696) | -56910.7(2.5) | -56909.7(0.7) |
| $^{57}$Mn$^+$ | 1.4613225062(714) | -57484.0(2.6) | -57486.8(1.8) |
| $^{41}$K$^+$ | 1.0512822800(609) | -35558.6(2.2) | -35559.07(0.19) |
| $^{85}$Rb$^+$ | 2.1792700552(686) | -82165.0(2.5) | -82167.331(0.011) |
| ISOLTRAP data from 2003[1] | | | |
| $^{56}$Mn$^+$ | 0.6587862217(182) | -56910.3(1.4) | -56909.7(0.7) |
| $^{57}$Mn$^+$ | 0.6705559418(275) | -57486.4(2.2) | -57486.8(1.8) |

[1]Data from [26] with reference ion $^{85}$Rb$^+$. Only mass excess published in [27]. Data included in AME2003 mass evaluation [21].

# Bibliography

Adelberger, E. G., Ortiz, C., García, A., Swanson, H. E., Beck, M., Tengblad, O., Borge, M. J. G., Martel, I., Bichsel, H., & the ISOLDE Collaboration (1999). Positron-neutrino correlation in the $0^+ \rightarrow 0^+$ decay of $^{32}$Ar. *Phys. Rev. Lett.*, 83, 1299–1302.

Aliseda, I. P., Fritioff, T., Giles, T., Jokinen, A., Lindroos, M., & Wenander, F. (2004). Design of a second generation rfq ion cooler and buncher (rfqcb) for isolde. *Nuclear Physics A*, 746, 647 – 650. Proceedings of the Sixth International Conference on Radioactive Nuclear Beams (RNB6).

Alvarez, L. W. (1937). Nuclear $k$ electron capture. *Phys. Rev.*, 52, 134–135.

Ames, F. (2002). Nipnet isolde. `https://www.kvi.nl/~trimp/web/TRAP/SLIDES/NN11/NN11.ppt`.

Ames, F., Bollen, G., Delahaye, P., Forstner, O., Huberd, G., Kester, O., Reisingera, K., & Schmidt, P. (2005). Cooling of radioactive ions with the penning trap rextrap. *Nuclear Instruments and Methods in Pysics Research A*, 538, 17–32.

Appelhans, A. & Dahl, D. (2002). Measurement of external ion injection and trapping efficiency in the ion trap mass spectrometer and comparison with a predictive model. *International Journal of Mass Spectrometry*, 216(3), 269 – 284.

Baeßler, S., Ayala Guardia, F., Borg, M., Glück, F., Heil, W., Konrad, G., Konorov, I., Muñoz Horta, R., Petzoldt, G., Rich, D., Simson, M., Sobolev, Y., Wirth, H., & Zimmer, O. (2008). First measurements with the neutron decay spectrometer a spect. *The European Physical Journal A - Hadrons and Nuclei*, 38, 17–26. 10.1140/epja/i2008-10660-0.

Barnes, J. & Put, P. (1986). A hierarchical o(n-log-n) force-calculation algorithm. *Nature*, 324, 446–449.

Beck, D., Ames, F., Beck, M., Bollen, G., Delauré, B., Schuurmans, P., Schwarz, S., Schmidt, P., Severijns, N., & Forstner, O. (2001). Space charge effects in a gas filled penning trap. *Hyperfine Interactions*, 132, 469–474.

Beck, M., Ames, F., Beck, D., Bollen, G., Delauré, B., Golovko, V. V., Kozlov, V. Y., Kraev, I. S., Lindroth, A., Phalet, T., Quint, W., Schuurmans, P., Severijns, N., Vereecke, B., & Versyck, S. (2003). Witch: a recoil spectrometer for weak interaction

and nuclear physics studies. *Nuclear Instruments and Methods in Physics Research Section A: Accelerators, Spectrometers, Detectors and Associated Equipment*, 503(3), 567 – 579.

Beck, M., Coeck, S., Kozlov, V. Y., Breitenfeld, M., Delahaye, P., Friedag, P., Herbane, M., Herlert, A., Kraev, I. S., Mader, J., Tandecki, M., Van Gorp, S., Wauters, F., Weinheimer, C., Wenander, F., & Severijns, N. (2010). First detection and energy measurement of recoil ions following beta decay in a penning trap with the witch experiment. *Eur. Phys. J. A*, 47(arXiv:1008.0207), 45. Comments: 9 pages, 6 figures (9 figure files), submitted to European Physical Journal A.

Belleman, R. G., Bédorf, J., & Zwart, S. F. P. (2008). High performance direct gravitational n-body simulations on graphics processing units II: An implementation in cuda. *New Astronomy*, 13(2), 103 – 112.

Blaum, K. (2006). High-accuracy mass spectrometry with stored ions. *Physics Reports*, 425, 1–78.

Blaum, K., Audi, G., Beck, D., Bollen, G., Herfurth, F., Kellerbauer, A., Kluge, H.-J., Sauvan, E., & Schwarz, S. (2003). Masses of $^{32}$Ar and $^{33}$Ar for fundamental tests. *Phys. Rev. Lett.*, 91, 260801.

Bollen, G., Moore, R. B., Savard, G., & Stolzenberg, H. (1990). The accuracy of heavy-ion mass measurements using time of flight-ion cyclotron resonance in a penning trap. *Journal of Applied Physics*, 68(9), 4355–4374.

Bollinger, J. J., Heinzen, D. J., Moore, F. L., Itano, W. M., Wineland, D. J., & Dubin, D. H. E. (1993). Electrostatic modes of ion-trap plasmas. *Phys. Rev. A*, 48, 525–545.

Bollinger, J. J., Mitchell, T. B., Huang, X.-P., Itano, W. M., Tan, J. N., Jelenkovic, B. M., & Wineland, D. J. (2000). Crystalline order in laser-cooled, non-neutral ion plasmas. *Physics of Plasmas*, 7(1), 7–13.

Brillouin, L. (1945). A theorem of larmor and its importance for electrons in magnetic fields. *Phys. Rev.*, 67(7-8), 260–266.

Brown & Gabrielse (1986). Geonium theory: Physics of a single electron or ion in a penning trap. *Rev. Mod. Phys.*, 58, 233 – 311.

Carrier, J., Greengard, L., & Rokhlin, V. (1988). A fast adaptible multipole algorithm for particle simulations. *SIAM J Sci Stat Comput*, 9, 669–686.

Chen, S.-P. & Comisarow, M. B. (1991). Simple physical models for coulomb-induced frequency shifts and coulomb-induced inhomogenous broadening for like and unlike ions in fourier transform ion cyclotron resonance mass spectrometry. *Rapid Communications in Mass Spectrometry*, 5(10), 450–455.

Chen, S.-P. & Comisarow, M. B. (1992). Modelling coulomb effects in fourier-transform ion cyclotron resonance mass spectrometry by charged disks and charged cylinders. *Rapid Communications in Mass Spectrometry*, 6(1), 1–3.

Chiggiato, P. & Costa-Pinto, P. (2005). Ti-zr-v non-evaporable getter films: from development to large scale production for the large hadron collider. oai:cds.cern.ch:927753. *Thin Solid Films*, 515(CERN-TS-2006-001. 2), 382–388. 13 p.

Coeck, S. (2007). *Search for non Standard Model physics in nuclear bèta decay with the WITCH experiment*. PhD thesis, K.U. Leuven.

Coeck, S., Beck, M., Delaurè, B., Golovko, V., Herbane, M., Lindroth, A., Kopecky, S., Kozlov, V., Kraev, I., Phalet, T., & Severijns, N. (2006). Microchannel plate response to high-intensity ion bunches. *Nuclear Instruments and Methods in Physics Research Section A: Accelerators, Spectrometers, Detectors and Associated Equipment*, 557(2), 516 – 522.

Coeck, S., Delauré, B., Herbane, M., Beck, M., Golovko, V., Kopecky, S., Kozlov, V., Kraev, I., Lindroth, A., Phalet, T., Beck, D., Delahaye, P., Herlert, A., Wenander, F., & Severijns, N. (2007). A pulsed drift cavity to capture 30 kev ion bunches at ground potential. *Nuclear Instruments and Methods in Physics Research Section A: Accelerators, Spectrometers, Detectors and Associated Equipment*, 572(2), 585 – 595.

Coeck, S. & et al. (2007). Ab initio simulations on the behaviour of small ion clouds in the witch penning trap system. *Nuclear Instruments and Methods in Physics Research A*, 574, 370–384.

comsol (2011). Comsol : Multiphysics modeling and simulation. `http://www.comsol.com`.

Cornille, P. (1995). The lorentz force and newton's third principle. *Canadian Journal of Physics*, 73(9-10), 619–625.

Couratin, C. (2011). $^{35}$Cl charge state distribution. private communication.

Couratin, C. (2012). First determination of the $\beta$-$\nu$ angular correlation coefficient $a$ with $^{35}$Ar at LPC trap. *to be published*.

cuda (2011). Cuda zone. `http://www.nvidia.com/object/cuda_home_new.html`.

Danielson, J. R. & Surko, C. M. (2005). Torque-balanced high-density steady states of single-component plasmas. *Phys. Rev. Lett.*, 94, 035001.

Davidson, R. C., Ed. (1974). *Theory of nonneutral plasmas*, volume 43.

De Leebeeck, V. e. a. (2011). to be published. *To be published*.

Debye, P. & Hückel, E. (1923). Zur Theorie der Elektrolyte. I. Gefrierpunktserniedrigung und verwandte Erscheinungen. *Physikalische Zeitschrift*, 24(9), 185–206.

Delauré, B. (1997). *Development of a Penning Trap based Set-up for Precision Tests of the Standard Model*. PhD thesis, Katholieke Universiteit Leuven.

Driscoll, C. F., Fine, K. S., & Malmberg, J. H. (1986). Reduction of radial losses in a pure electron plasma. *Physics of Fluids*, 29(6), 2015–2017.

Dubin, D. H. E. & O'Neil, T. M. (1999). Trapped nonneutral plasmas, liquids, and crystals (the thermal equilibrium states). *Rev. Mod. Phys.*, 71(1), 87.

Eggleston, D. L., O'Neil, T. M., & Malmberg, J. H. (1984). Collective enhancement of radial transport in a nonneutral plasma. *Phys. Rev. Lett.*, 53, 982–984.

Eliseev, S., Block, M., Chaudhuri, A., Herfurth, F., Kluge, H.-J., Martin, A., Rauth, C., & Vorobjev, G. (2007). Octupolar excitation of ions stored in a Penning trap mass spectrometer. a study performed at SHIPTRAP. *International Journal of Mass Spectrometry*, 262(1-2), 45 – 50.

Elsener, K., Acquistapace, G., Baldy, J. L., Ball, A. E., Bonnal, P., Buhler-Broglin, M., Carminati, F., Cennini, E., Ereditato, A., Falaleev, V. P., Faugeras, P. E., Ferrari, A., Fortuna, G., Foà, L., Genand, R., Grant, A. L., Henny, L., Hilaire, A., Hübner, K., Inigo-Golfin, J., Kissler, K. H., López-Hernandez, L. A., Maugain, J.-M., Mayoud, M., Migliozzi, P., Missiaen, D., Palladino, V., Papadopoulos, I. M., Pietropaolo, F., Péraire, S., Rangod, S., Revol, J. P. C., Roche, J., Sala, P. R., Sanelli, C., Stevenson, G. R., Tomat, B., Tsesmelis, E., Valbuena, R., Vincke, H. H., Weisse, E., & Wilhelmsson, M. (1998). *The CERN neutrino beam to Gran Sasso (NGS): conceptual technical design*. Geneva: CERN.

F. Glück (2011a). Axisymmetric electric field calculation with zonal harmonic expansion. *Progress In Electromagnetics Research B*, B(32), 319–350.

F. Glück (2011b). Axisymmetric magnetic field calculation with zonal harmonic expansion. *Progress In Electromagnetics Research B*, B(32), 351–388.

Fedosseev, V., Berg, L. E., Lebas, N., Launila, O. J., Lindroos, M., Losito, R., Marsh, B. A., Österdahl, F. K., Pauchard, T., Transtömer, G., & Vannesjö, J. (2008). Isolde rilis: New beams, new facilities. *Nucl. Instrum. Methods Phys. Res., B*, 266(19-20), 4378–4382.

Fermi, E. (1934). Towards the theory of $\beta$-rays. *Z. Phys.*, 88, numbers 3-4, 161–177.

Fernandes, S. (2010). *Submicro- and Nano-Structured Porous Materials for Production of High-Intensity Exotic Radioactive Ion Beams*. PhD thesis, Thèse Ecole polytechnique fédérale de Lausanne EPFL, Lausanne.

Fernandes, S., Bruetsch, R., Catherall, R., Groeschel, F., Guenther-Leopold, I., Lettry, J., Manfrin, E., Marzari, S., Noah, E., Sgobba, S., Stora, T., & Zanini, L. (2011). Microstructure evolution of nanostructured and submicrometric porous refractory ceramics induced by a continuous high-energy proton beam. *Journal of Nuclear Materials*, 416(1-2), 99 – 110. Nuclear Materials IV.

Fierz, M. (1937). Zur fermischen theorie des $\beta$-zerfalls. *Zeitschrift für Physik A Hadrons and Nuclei*, 104, 553–565. 10.1007/BF01330070.

Fléchard, X., Liénard, E., Méry, A., Rodríguez, D., Ban, G., Durand, D., Duval, F., Herbane, M., Labalme, M., Mauger, F., Naviliat-Cuncic, O., Thomas, J. C., & Velten, P. (2008). Paul trapping of radioactive $^6$He$^+$ ions and direct observation of their $\beta$ decay. *Phys. Rev. Lett.*, 101, 212504.

Fléchard, X., Velten, P., Liénard, E., Méry, A., Rodríguez, D., Ban, G., Durand, D., Mauger, F., Naviliat-Cuncic, O., & Thomas, J. C. (2011). Measurement of the $\beta$-$\nu$ correlation coefficient $a\beta\nu$ in the $\beta$ decay of trapped $^6$He$^+$ ions. *Journal of Physics G: Nuclear and Particle Physics*, 38(5), 055101.

Friedag, P. & et al. (2012). Tracking results for the electromagnetic design of the WITCH retardation spectrometer. In preparation.

Frånberg, H., Delahaye, P., Billowes, J., Blaum, K., Catherall, R., Duval, F., Gianfrancesco, O., Giles, T., Jokinen, A., Lindroos, M., Lunney, D., Mane, E., & Podadera, I. (2008). Off-line commissioning of the isolde cooler. *Nuclear Instruments and Methods in Physics Research Section B: Beam Interactions with Materials and Atoms*, 266(19-20), 4502 – 4504. Proceedings of the XVth International Conference on Electromagnetic Isotope Separators and Techniques Related to their Applications.

Gabrielse, G., Haarsma, L., & Rolston, S. L. (1989). Open-endcap penning traps for high precision experiments. *International Journal of Mass Spectrometry and Ion Processes*, 88(2-3), 319 – 332.

Gabrielse, G. & Mackintosh, F. (1984). Cylindrical penning traps with orthogonalized anharmonicity compensation. *International Journal of Mass Spectrometry and Ion Processes*, 57(1), 1 – 17.

Gaburov, E., Bédorf, J., & Zwart, S. P. (2010). Gravitational tree-code on graphics processing units: implementation in cuda. *Procedia Computer Science*, 1(1), 1119 – 1127. ICCS 2010.

Gaburov, E., Harfst, S., & Portegies Zwart, S. (2009). Sapporo: A way to turn your graphics cards into a grape-6. *New Astronomy*, 14(7), 630–637.

Gamow, G. & Teller, E. (1936). Selection rules for the $\beta$-disintegration. *Phys. Rev.*, 49(12), 895–899.

Gear, C. W. (1971). *Numerical initial value problems in ordinary differential equations*. Prentice Hall PTR.

Gioumousis, G. & Stevenson, D. (1958). Reactions of gaseous molecule ions with gaseous molecules. v. theory. *The Journal of Chemical Physics*, 29, 294–299.

Glück, F., BaeSSler, S., Byrne, J., van der Grinten, M. G. D., Hartmann, F. J., Heil, W., Konorov, I., Petzoldt, G., Sobolev, Y., & Zimmer, O. (2005). The neutron decay retardation spectrometer aSPECT: Electromagnetic design and systematic effects. *The European Physical Journal A - Hadrons and Nuclei*, 23, 135–146. 10.1140/epja/i2004-10057-1.

Gluck, F. (2012). to be published. EM field calculation.

Gorelov, A., Melconian, D., Alford, W., Ashery, D., Ball, G., et al. (2005). Scalar interaction limits from the beta-neutrino correlation of trapped radioactive atoms. *Phys.Rev.Lett.*, 94, 142501.

Gorshkov, M. V., Marshall, A. G., & Nikolaev, E. N. (1993). Analysis and elimination of systematic errors originating from coulomb mutual interaction and image charge in fourier transform ion cyclotron resonance precise mass difference measurements. *Journal of the American Society for Mass Spectrometry*, 4(11), 855 – 868.

Gottberg, A. (2011). $^{35}$ar release curve. private communication.

Greaves, R. G. & Moxom, J. M. (2008). Compression of trapped positrons in a single particle regime by a rotating electric field. *Physics of Plasmas*, 15(7), 072304.

Greaves, R. G. & Surko, C. M. (2000). Inward transport and compression of a positron plasma by a rotating electric field. *Phys. Rev. Lett.*, 85, 1883–1886.

Gustafsson, A., Herlert, A., & Wenander, F. (2011). Mass-selective operation with rextrap. *Nuclear Instruments and Methods in Physics Research Section A: Accelerators, Spectrometers, Detectors and Associated Equipment*, 626-627, 8 – 15.

Hamada, T. & Iitaka, T. (2007). The chamomile scheme: An optimized algorithm for n-body simulations on programmable graphics processing units.

Hardy, J. C. & Towner, I. S. (2005). Superallowed $0^+ \rightarrow 0^+$ nuclear $\beta$ decays: A critical survey with tests of the conserved vector current hypothesis and the standard model. *Phys. Rev. C*, 71, 055501.

Hasegawa, T., Jensen, M. J., & Bollinger, J. J. (2005). Stability of a penning trap with a quadrupole rotating electric field. *Physical Review A*, 71(2), 1–6.

Hasse, H.-U., Becker, S., Dietrich, G., Klisch, N., Kluge, H.-J., Lindinger, M., Lützenkirchen, K., Schweikhard, L., & Ziegler, J. (1994). External-ion accumulation in a penning trap with quadrupole excitation assisted buffer gas cooling. *International Journal of Mass Spectrometry and Ion Processes*, 132(3), 181 – 191.

Herczeg, P. (2001). Beta decay beyond the standard model. *Progress in Particle and Nuclear Physics*, 46(2), 413 – 457.

Herfurth, F., Blaum, K., Eliseev, S., Kester, O., Kluge, H.-J., Koszudowski, S., Kozhuharov, C., Maero, G., Neidherr, D., Quint, W., Schwarz, S., Stahl, S., & Vorobjev, G. (2006). The hitrap project at gsi: trapping and cooling of highly-charged ions in a penning trap. *Hyperfine Interactions*, 173, 93–101. 10.1007/s10751-007-9547-y.

Herfurth, F., Dilling, J., Kellerbauer, A., Bollen, G., Henry, S., Kluge, H.-J., Lamour, E., Lunney, D., Moore, R., Scheidenberger, C., Schwarz, S., Sikler, G., & Szerypo, J. (2001). A linear radiofrequency ion trap for accumulation, bunching, and emittance improvement of radioactive ion beams. *Nuclear Instruments and Methods in Physics Research Section A: Accelerators, Spectrometers, Detectors and Associated Equipment*, 469(2), 254 – 275.

Herlert, A. (2010). Isolde RFQ. private communication.

Herlert, A., Borgmann, C., Fink, D., Holm Christensen, C., Kowalska, M., & Naimi, S. (2011). Effects of space charge on the mass purification in penning traps. *Hyperfine Interactions*, 199, 211–220. 10.1007/s10751-011-0316-6.

Higgs, P. W. (1966). Spontaneous symmetry breakdown without massless bosons. *Phys. Rev.*, 145(4), 1156–1163.

Hoff, P. (1993). Production of radioactive nuclides at isolde. *Nuclear Instruments and Methods in Physics Research Section B: Beam Interactions with Materials and Atoms*, 79(1-4), 335 – 338.

Hollmann, E. M., Anderegg, F., & Driscoll, C. F. (2000). Confinement and manipulation of non-neutral plasmas using rotating wall electric fields. *Physics of Plasmas*, 7(7), 2776–2789.

Huang, X.-P., Anderegg, F., Hollmann, E. M., Driscoll, C. F., & O'Neil, T. M. (1997). Steady-state confinement of non-neutral plasmas by rotating electric fields. *Phys. Rev. Lett.*, 78, 875–878.

Iitaka, T. (2012). A novel tree code for the gpu. private communication.

Jackson, J., Treiman, S., & Wyld, H. (1957). Possible tests of time reversal invariance in beta decay. *Phys.Rev. 106*, 106, 517–521.

Johnson, C. H., Pleasonton, F., & Carlson, T. A. (1963). Precision measurement of the recoil energy spectrum from the decay of $^6$He. *Phys. Rev.*, 132, 1149–1165.

Joliot, F. & Curie, I. (1934). Artificial production of a new kind of radio-element. *Nature*, 133, 201–202.

Jørgensen, L. V., Amoretti, M., Bonomi, G., Bowe, P. D., Canali, C., Carraro, C., Cesar, C. L., Charlton, M., Doser, M., Fontana, A., Fujiwara, M. C., Funakoshi, R., Genova, P., Hangst, J. S., Hayano, R. S., Kellerbauer, A., Lagomarsino, V., Landua, R., Lodi Rizzini, E., Macrì, M., Madsen, N., Mitchard, D., Montagna, P., Rotondi, A., Testera, G., Variola, A., Venturelli, L., van der Werf, D. P., & Yamazaki, Y. (2005). New source of dense, cryogenic positron plasmas. *Phys. Rev. Lett.*, 95, 025002.

Kluge, H.-J. & Blaum, K. (2004). Trapping radioactive ions. *Nuclear Physics A*, 746, 200 – 205. Proceedings of the Sixth International Conference on Radioactive Nuclear Beams (RNB6).

König, M., G., B., Kluge, H.-J., T., O., & J., S. (1995). Quadrupole excitation of stored ion motion at the true cyclotron frequency. *International Journal of Mass Spectrometry and Ion Processes*, 142, 95–116.

Kofoed-Hansen, O. (1954). Theoretical angular correlations in allowed beta transitions. *Dan. Mat. Fys. Medd.*, 28.

Kowalska, M. (2012). GPU simulations with rubidium ions. private communication.

Kowalska, M., Naimi, S., Agramunt, J., Algora, A., Audi, G., Beck, D., Blank, B., Blaum, K., Böhm, C., Breitenfeldt, M., Estevez, E., Fraile, L. M., George, S., Herfurth, F., Herlert, A., Kellerbauer, A., Lunney, D., Minaya-Ramirez, E., Neidherr, D., Olaizola, B., Riisager, K., Rosenbusch, M., Rubio, B., Schwarz, S., Schweikhard, L., & Warring, U. (2009). Preparing a journey to the east of $^{208}$Pb with isoltrap: Isobaric purification at A = 209 and new masses for $^{211-213}$Fr and $^{211}$Ra. *Eur. Phys. J. A*, 42(3), 351–359.

Kozlov, V., Beck, M., Coeck, S., Delahaye, P., Friedag, P., Herbane, M., Herlert, A., Kraev, I., Tandecki, M., Gorp, S. V., Wauters, F., Weinheimer, C., Wenander, F., Zákoucký, D., & Severijns, N. (2008). The witch experiment: Acquiring the first recoil ion spectrum. *Nuclear Instruments and Methods in Physics Research Section B: Beam Interactions with Materials and Atoms*, 266(19-20), 4515 – 4520. Proceedings of the XVth International Conference on Electromagnetic Isotope Separators and Techniques Related to their Applications.

Kraus, C., Bornschein, B., Bornschein, L., Bonn, J., Flatt, B., et al. (2005). Final results from phase II of the Mainz neutrino mass search in tritium beta decay. *Eur.Phys.J.*, C40, 447–468.

Kugler, E. (2000). The isolde facility. *Hyperfine Interactions*, 129, 23–42. 10.1023/A:1012603025802.

Langer, L. M. & Price, H. C. (1949). Beta-spectra of forbidden transitions. *Phys. Rev.*, 76(5), 641–646.

Lee, T. D. & Yang, C. N. (1956). Question of parity conservation in weak interactions. *Phys. Rev.*, 104, 254 – 258.

Levy, R. H. (1965). Diocotron instability in a cylindrical geometry. *Physics of Fluids*, 8(7), 1288–1295.

Li, G.-Z., Guan, S., & Marshall, A. (1998). Comparison of equilibrium ion density distribution and trapping force in penning, paul, and combined ion traps. *Journal of The American Society for Mass Spectrometry*, 9, 473–481. 10.1016/S1044-0305(98)00005-1.

Liénard, E. & et al., M. H. (2005). Performance of a micro-channel plates position senstivie detector. *Nuclear Instruments and Methods in Physics Research*, A(551), 375–386.

Lobashev, V. & Spivak, P. (1985). A method for measuring the electron antineutrino rest mass. *Nuclear Instruments and Methods in Physics Research Section A: Accelerators, Spectrometers, Detectors and Associated Equipment*, 240(2), 305 – 310.

Mane, E., Billowes, J., Blaum, K., Campbell, P., Cheal, B., Delahaye, P., Flanagan, K. T., Forest, D. H., Franberg, H., Geppert, C., Giles, T., Jokinen, A., Kowalska, M., Neugart, R., Neyens, G., Noertershaeuser, W., Podadera, I., Tungate, G., Vingerhoets, P., & Yordanov, D. T. (2009). An ion cooler-buncher for high-sensitivity collinear laser spectroscopy at ISOLDE. *EUROPEAN PHYSICAL JOURNAL A*, 42(3), 503–507. 5th International Conference on Exotic Nuclei and Atomic Masses (ENAM'08), Ryn, POLAND, SEP 07-13, 2008.

Marshall, A. G. & Hendrickson, C. L. (2002). Fourier transform ion cyclotron resonance detection: principles and experimental configurations. *International Journal of Mass Spectrometry*, 215(1âĂŞ3), 59 – 75. ¡ce:title¿Detectors and the Measurement of Mass Spectra¡/ce:title¿.

Mitchell, D. W. & Smith, R. D. (1995). Cyclotron motion of two coulombically interacting ion clouds with implications to fourier-transform ion cyclotron resonance mass spectrometry. *Phys. Rev. E*, 52, 4366–4386.

Müller, B., Thümmler, T., Bonn, J., Bornschein, B., Bornschein, L., Conde, F., Flatt, B., Glück, F., Kraus, C., Otten, E., Schall, J.-P., & Weinheimer, C. (2003). Particle storage in mac-e-filters. *Nuclear Physics B - Proceedings Supplements*, 118(0), 481 –. Proceedings of the XXth International Conference on Neutrino Physics and Astrophysics.

Mukherjee, M., Beck, D., Blaum, K., Bollen, G., Dilling, J., George, S., Herfurth, F., Herlert, A., Kellerbauer, A., Kluge, H., Schwarz, S., Schweikhard, L., & Yazidjian, C. (2008a). Isoltrap: An on-line penning trap for mass spectrometry on short-lived nuclides. *The European Physical Journal A - Hadrons and Nuclei*, 35, 1–29. 10.1140/epja/i2007-10528-9.

Mukherjee, M., Beck, D., Blaum, K., Bollen, G., Dilling, J., George, S., Herfurth, F., Herlert, A., Kellerbauer, A., Kluge, H., Schwarz, S., Schweikhard, L., & Yazidjian, C. (2008b). Isoltrap: An on-line penning trap for mass spectrometry on short-lived nuclides. *The European Physical Journal A - Hadrons and Nuclei*, 35, 1–29. 10.1140/epja/i2007-10528-9.

Naimi, S., Rosenbusch, M., Audi, G., Blaum, K., Böhm, C., Borgmann, C., Breitenfeldt, M., George, S., Herfurth, F., Herlert, A., Kowalska, M., Kreim, S., Lunney, D., Minaya-Ramirez, E., Neidherr, D., Schweikhard, L., & Wang, M. (2011). Mass measurements of short-lived nuclides using the isoltrap preparation penning trap. *Hyperfine Interactions*, 199, 231–240. 10.1007/s10751-011-0318-4.

Neidherr, D., Blaum, K., Block, M., Ferrer, R., Herfurth, F., Ketelaer, J., Nagy, S., & Weber, C. (2008). Measurement and simulation of the pressure ratio between the two traps of double penning trap mass spectrometers. *Nuclear Instruments and Methods in Physics Research Section B: Beam Interactions with Materials and Atoms*, 266(19-20), 4556 – 4559. Proceedings of the XVth International Conference on Electromagnetic Isotope Separators and Techniques Related to their Applications.

Nikolaev, E. N., Heeren, R. M. A., Popov, A. M., Pozdneev, A. V., & Chingin, K. S. (2007). Realistic modeling of ion cloud motion in a fourier transform ion cyclotron resonance cell by use of a particle-in-cell approach. *Rapid communications in mass spectrometry RCM*, 21(22), 3527–3546.

Notte, J. & Fajans, J. (1994). The effect of asymmetries on non-neutral plasma confinement time. *Physics of Plasmas*, 1(5), 1123–1127.

NUDAT 2.5, N. N. D. C. (2011). National nuclear data center, brookhaven national laboratory. `http://www.nndc.bnl.gov/nudat2/index.jsp`.

Nyland, L., Harris, M., & Prins., J. F. (2007). *GPU Gems 3, Chapter 31: Fast N-body Simulation with CUDA*. Addison-Wesley.

Nyland, L., Harris, M., & Prins., J. F. (2008). *Simulations for Ion Traps Methods and Numerical Implementation*. Springer Berlin.

O'Neil, T. M. & Driscoll, C. F. (1979). Transport to thermal equilibrium of a pure electron plasma. *Physics of Fluids*, 22(2), 266–277.

Petersson, M. (2006). *A Monte Carlo method for the simulation of buffer gas cooling inside a radio frequency quadrupole*. PhD thesis, CERN.

Peurrung, A., Kouzes, R., & Barlow, S. (1996). The non-neutral plasma: an introduction to physics with relevance to cyclotron resonance mass spectrometry. *International Journal of Mass Spectrometry and Ion Processes*, 157-158(0), 39 – 83.

Peurrung, A. J. & Kouzes, R. T. (1994). Long-term coherence of the cyclotron mode in a trapped ion cloud. *Phys. Rev. E*, 49, 4362–4368.

Podadera-Aliseda, I. & Lindroos, M. (2006). *New developments on preparation of cooled and bunched Radioactive Ion beams at ISOL facilities: the ISCOOL project and the rotating wall cooling. oai:cds.cern.ch:975263*. PhD thesis, Barcelona, Polytechnic U., Barcelona. Presented on 07 Jul 2006.

Raimbault-Hartmann, H., Beck, D., Bollen, G., König, M., Kluge, H.-J., Schark, E., Stein, J., Schwarz, S., & Szerypo, J. (1997). A cylindrical penning trap for capture, mass selective cooling, and bunching of radioactive ion beams. *Nuclear Instruments and Methods in Physics Research Section B: Beam Interactions with Materials and Atoms*, 126(1-4), 378 – 382. International Conference on Electromagnetic Isotope Separators and Techniques Related to Their Applications.

Ramos, J. (2012). Nanostructured calcium oxide targets for the production of argon beams. Master's thesis, CERN.

Ramos, J., Stora, T., & Senos, A. (2011). Nanostructured calcium oxide targets for the production of argon beams.

Ravn, H., Catherall, R., Barker, J., Drumm, P., Evensen, A., Hageba, E., Hoff, P., Jonsson, O., Kugler, E., Lettry, J., Steffensen, K., & Tengblad, O. (1997). Bunched release of gases from oxide targets. *Nuclear Instruments and Methods in Physics Research Section B: Beam Interactions with Materials and Atoms*, 126(1-4), 176 – 181. International Conference on Electromagnetic Isotope Separators and Techniques Related to Their Applications.

Reich, E. S. (2010). Antimatter held for questioning. *nature*, 468(266).

Ringle, R., Bollen, G., Schury, P., Schwarz, S., & Sun, T. (2007). Octupolar excitation of ion motion in a penning trapâĂŤa study performed at lebit. *International Journal of Mass Spectrometry*, 262(1-2), 33 – 44.

Rodríguez, D., Méry, A., Ban, G., Brégeault, J., Darius, G., Durand, D., Fléchard, X., Herbane, M., Labalme, M., Liénard, E., Mauger, F., Merrer, Y., Naviliat-Cuncic, O., Thomas, J., & Vandamme, C. (2006). The lpctrap facility: A novel transparent Paul trap for high-precision experiments. *Nuclear Instruments and Methods in Physics Research Section A: Accelerators, Spectrometers, Detectors and Associated Equipment*, 565(2), 876 – 889.

Rosenbusch, M. (2009). Excitation modes for the cooling of the ion motion in penning traps. Master's thesis, Ernst-Moritz-Arndt-University.

Rubbia, C. (1984). Experimental observation of the intermediate vector bosons $W^+$, $W^-$ and $Z^0$. *Nobel lecture*.

Rustad, B. M. & Ruby, S. L. (1953). Correlation between electron and recoil nucleus in $He^6$ decay. *Phys. Rev.*, 89(4), 880–881.

Rustad, B. M. & Ruby, S. L. (1955). Gamow-teller interaction in the decay of $He^6$. *Phys. Rev.*, 97(4), 991.

Rutherford, E. (1899). Uranium radiation and the electrical conduction produced by it. *Philosophical Magazine*, 47, 109–163.

Savard, G., Becker, S., Bollen, G., Kluge, H.-J., Moore, R., Otto, T., Schweikhard, L., Stolzenberg, H., & Wiess, U. (1991). A new cooling technique for heavy ions in a penning trap. *Phys. Lett.A*, 158, 247 – 252.

Schmidt, P. (2001). *REXTRAP Ion Accumulation, Cooling, and Bunching for REX-ISOLDE*. PhD thesis, Mainz.

Schwarz, S. (2006). IonCool a versatile code to characterize gas-filled ion bunchers and coolers (not only) for nuclear physics applications. *Nuclear Instruments and Methods in Physics Research Section A: Accelerators, Spectrometers, Detectors and Associated Equipment*, 566(2), 233 – 243.

Scielzo, N. D., Freedman, S. J., Fujikawa, B. K., & Vetter, P. A. (2003). Recoil-ion charge-state distribution following the $\beta^+$ decay of $^{21}$Na. *Phys. Rev. A*, 68, 022716.

Scielzo, N. D., Freedman, S. J., Fujikawa, B. K., & Vetter, P. A. (2004). Measurement of the $\beta$-$\nu$ correlation using magneto-optically trapped $^{21}$Na. *Phys. Rev. Lett.*, 93, 102501.

Severijns, N., Beck, M., & Naviliat-Cuncic, O. (2006). Tests of the standard electroweak model in nuclear beta decay. *Rev. Mod. Phys.*, 78(3), 991.

Severijns, N. & Naviliat-Cuncic, O. (2011). Symmetry tests in nuclear beta decay. *Annual Review of Nuclear and Particle Science*, 61(1), 23–46.

Severijns, N., Tandecki, M., Phalet, T., & Towner, I. S. (2008). $\mathcal{F}t$ values of the $t = 1/2$ mirror $\beta$ transitions. *Phys. Rev. C*, 78, 055501.

Sherr, R., Muether, H. R., & White, M. G. (1949). Radioactivity of $C^{10}$ and $O^{14}$. *Phys. Rev.*, 75(2), 282–292.

Simbuca (2011). Simbuca on sourceforge. `http://sourceforge.net/projects/simbuca/`.

Spreiter, Q. & Walter, M. (1999). Classical molecular dynamics simulation with the velocity verlet algorithm at strong external magnetic fields. *Journal of Computational Physics*, 152(1), 102 – 119.

srim (2011). Srim : The stopping and range of ions in matter. `http://www.srim.org`.

Stora, T. (2010). Nanostructured calcium oxide targets for the production of argon beams. wo 2010/034364 a1. patent.

Sturm, S., Blaum, K., Breitenfeldt, M., Delahaye, P., Herlert, A., Schweikhard, L., & Wenander, F. (2009). Investigation of space-charge phenomena in gas-filled penning traps. *AIP Conference Proceedings*, 1114(1), 185–190.

Tandecki, M. (2011). *Progress at the WITCH experiment towards Weak Interaction Studies.* PhD thesis, Katholieke Universiteit Leuven.

Tandecki, M. (2012). Ionisation processes caused by penning-like traps in the mac-e filter of the witch experiment. *to be published.*

Traykov, E., Beck, M., Breitenfeldt, M., Delahaye, P., Leebeeck, V. D., Friedag, P., Herlert, A., Geeraert, N., Heirman, W., Lönne, P.-I., Mader, J., Roccia, S., Soti, G., Tandecki, M., Timmermans, M., Thiboud, J., Gorp, S. V., Wauters, F., Weinheimer, C., Zákoucký, D., & Severijns, N. (2011). A compact radio frequency quadrupole for ion bunching in the witch experiment. *Nuclear Instruments and Methods in Physics Research Section A: Accelerators, Spectrometers, Detectors and Associated Equipment*, 648(1), 1 – 14.

Van Dyck, R. S., Schwinberg, P. B., & Dehmelt, H. G. (1977). Precise measurements of axial, magnetron, cyclotron, and spin-cyclotron-beat frequencies on an isolated 1-mev electron. *Phys. Rev. Lett.*, 38, 310–314.

Van Gorp, S. (2007). Beweging van ionen in de witch penning vallen. Master's thesis, Katholieke Universiteit Leuven.

Van Gorp, S. (2012). *Search for physics beyond the standard electroweak model at the WITCH experiment.* PhD thesis, Katholieke Universiteit Leuven.

Van Gorp, S., Beck, M., Breitenfeldt, M., Leebeeck, V. D., Friedag, P., Herlert, A., Iitaka, T., Mader, J., Kozlov, V., Roccia, S., Soti, G., Tandecki, M., Traykov, E., Wauters, F., Weinheimer, C., Zákoucký, D., & Severijns, N. (2011). Simbuca, using a graphics card to simulate coulomb interactions in a penning trap. *Nuclear Instruments and Methods in Physics Research Section A: Accelerators, Spectrometers, Detectors and Associated Equipment*, 638(1), 192 – 200.

Verner, J. H. (1978). Explicit runge–kutta methods with estimates of the local truncation error. *SIAM Journal on Numerical Analysis*, 15(4), 772–790.

Vetter, P. A., Clark, R. M., Dvorak, J., Freedman, S. J., Gregorich, K. E., Jeppesen, H. B., Mittelberger, D., & Wiedeking, M. (2008). *Search for Oscillation of the Electron-Capture Decay Probability of $^{142}Pm$.* Technical Report arXiv:0807.0649. Comments: 12 pages (double-spaced), 6 figures.

Vetterling, W. T., Press, W., Teukolsky, S. A., & Flannery, B. P. (2003). *Numerical recipes in $C^{++}$: the art of scientific computing, 2nd edition.* Cambridge University Press.

Viehland, L. A. & Mason, E. A. (1995). Transport properties of gaseous ions over a wide energy range, iv. *Atomic Data and Nuclear Data Tables*, 60, 37–95.

Vogel, P. & Werner, B. (1983). Final-state interactions and time-reversal tests in nuclear $\beta$-decay. *Nuclear Physics A*, 404(2), 345 – 358.

White, W. D., Malmberg, J. H., & Driscoll, C. F. (1982). Resistive-wall destabilization of diocotron waves. *Phys. Rev. Lett.*, 49, 1822–1826.

Wiley, W. C. & McLaren, I. H. (1955). Time-of-flight mass spectrometer with improved resolution. *Review of Scientific Instruments*, 26(12), 1150–1157.

Wineland, D. & Dehmelt, H. (1975). Line shifts and widths of axial, cyclotron and g-2 resonances in tailored, stored electron (ion) cloud. *International Journal of Mass Spectrometry and Ion Physics*, 16(3), 338 – 342.

Winters, D. F. A., Vogel, M., Segal, D. M., & Thompson, R. C. (2006). Electronic detection of charged particle effects in a penning trap. *Journal of Physics B: Atomic, Molecular and Optical Physics*, 39(14), 3131.

Wolf, R., Eritt, M., Marx, G., & Schweikhard, L. (2011). A multi-reflection time-of-flight mass separator for isobaric purification of radioactive ion beams. *Hyperfine Interactions*, 199, 115–122. 10.1007/s10751-011-0306-8.

Wong, R. L. & Amster, I. J. (2007). Experimental evidence for space-charge effects between ions of the same mass-to-charge in Fourier-transform ion cyclotron resonance mass spectrometry. *International Journal of Mass Spectrometry*, 265(2-3), 99 – 105. Jean H. Futrell Honour Issue.

Wu, C., Ambler, E., Hayward, R., Hoppes, D., & Hudson, R. (1957). Experimental test of parity conservation in beta decay. *Phys. Rev.*, 105, 1413–1415.

# Curriculum vitae

## CURRICULUM VITAE – SIMON VAN GORP

PERSONAL
INFORMATION

Simon Van Gorp
Schuurhoven 165
2360 Oud-Turnhout
Belgium
tel: +32 495190068
simonvgorp@gmail.com

PERSONALITY

**Nationality** : Belgian

**Data of Birth** : August 3, 1984

**Languages**  ⋄ Dutch: *Native tongue*
⋄ English: *very fluent speaking and writing*
⋄ French: *fluent speaking and writing*
⋄ German: *notion*

**Trivia**  ⋄ Hobbies: football, snowboarding, running, travelling
⋄ Scouting: 10 years + 4 years leader
⋄ Degree as snowboard judge

EDUCATION

**University of Leuven**                                              Leuven, Belgium
*Ph.D. Nuclear Physics (in progress)*                            $2007 - 2011$
⋄ Thesis: Search for physics beyond the standard electroweak model at the WITCH experiment.
⋄ Promotor: Nathal Severijns

**University of Leuven**                                              Leuven, Belgium
*Master Physics*                                                 $2005 - 2007$
⋄ Thesis: On the movement of ions in the WITCH Penning Traps.
⋄ Promotor: Nathal Severijns
⋄ Graduated with distinction

**University of Leuven**                                              Leuven, Belgium
*Bachelor Physics*                                               $2004 - 2005$

**University of Antwerp**                                             Antwerp, Belgium
*Bachelor Computer Science*                                      $2002 - 2004$

**Secondary school, Sint-Pietersinstituut**                          Turnhout, Belgium
*Degree in Mathematics and Sciences*                             *1996 - 2002*

PUBLICATIONS

1) **S. Van Gorp**, *First determination of the bèta-neutrino angular correlation factor, a, on $^{35}Ar$ with the WITCH-setup*. To be published.

2) A. Herlert, **S. Van Gorp**, D. Beck, K. Blaum, M. Breitenfeldt, B.R. Cakirli, S. George, U. Hager, F. Herfurth, A. Kellerbauer, H.-J. Kluge, D. Lunney, R. Savreux, S. Schwarz, L. Schweikhard, C. Yazidjian, *Precision mass measurements of neutron-rich iron isotopes after in-trap decay*. To be published.

3) **S. Van Gorp**, M. Beck, M. Breitenfeldt, V. De Leebeeck, P. Friedag, A. Herlert, T. Iitaka, J. Mader, V. Kozlov, S. Roccia, G. Soti, M. Tandecki, E. Traykov, F. Wauters, Ch. Weinheimer, D. Zákoucký and N. Severijns, *Simbuca, using a graphics card to simulate Coulomb interactions in a penning trap*. Nucl. Inst. and Meth. A. **638**, $192 - 200$ (2011).

4) **S. Van Gorp** *IS433: A Penning Trap simulation program for the WITCH experiment that utilizes a Graphics Card to calculate Coulomb interactions*. isolde Spring Newsletter, $5 - 6$ (2011).

5) E. Traykov, M. Beck, M. Breitenfeldt, P. Delahaye, V. De Leebeeck, P. Friedag, A. Herlert, N. Geeraert, W. Heirman, P.-I. Lonne, J. Mader, S. Roccia, G. Soti, M. Tandecki, M. Timmermans, J. Thiboud, **S. Van Gorp**, F. Wauters, C. Weinheimer, D. Zákoucký and N. Severijns, *A compact radio frequency quadrupole for ion bunching in the WITCH experiment*. Nucl. Inst. and Meth. A **648**, 1–14 (2011).

6) V. Golovko, F. Wauters, S. Cottenier, M. Breitenfeldt, V. De Leebeeck, S. Roccia, G. Soti, M. Tandecki, E. Traykov, **S. Van Gorp**, D. Zákoucký and N. Severijns1, *Hyperfine field and hyperfine anomalies of copper impurities in iron.* Phys. Rev. C **84** (2011).

7) M. Tandecki, D. Beck, M. Beck, H. Brand, M. Breitenfeldt, V. De Leebeeck, P. Friedag, A. Herlert, V. Kozlov, J. Mader, S. Roccia, G. Soti, E. Traykov, **S. Van Gorp**, F. Wauters, Ch. Weinheimer, D. Zákoucký and N. Severijns. *Computer controls for the WITCH experiment.* Nucl. Inst. and Meth. **629**, 396 − 405 (2011).

8) F. Wauters, I. Kraev, D. Zákoucký, M Beck, M. Breitenfeldt, V. De Leebeeck, V. Golovko, V. Kozlov, T. Phalet, S. Roccia, G. Soti, M. Tandecki, I. Towner, E. Traykov, **S. Van Gorp** and N. Severijns, *Precision measurements of the $^{60}Co$ β-asymmetry parameter in search for tensor currents in weak interactions.* Phys. Rev C. **82**, 14 (2010).

9) N. Severijns, A. Belyaev, A. Erzinkyan, P. Eversheim, V. Filimonov, V. Golovko, H. Gurevich, P. Herzog, I. Kraev, A. Lukhanin, V. Noga, V. Parfenova, T. Phalet, A. Rusakov, M. Tandecki, Y. Toporov, C. Tramm, E. Traykov, **S. Van Gorp**, V. Vyachin, F. Wauters, D. Zákoucký and E. Zotov, *Hyperfine field of einsteinium in iron and nuclear magnetic moment of $^{254}Es$.* Phys. Rev. C. **79**, 6 (2009).

10) F. Wauters, I. Kraev, D. Zákoucký, M. Beck, V.V. Golovko, V.Yu. Kozlov, T. Phalet, M. Tandecki, E. Traykov, **S. Van Gorp** and N. Severijns, *A GEANT4 Monte-Carlo simulation code for precision (bèta) spectroscopy.* Nucl. Inst. and Meth. A. **609**, 156 − 164 (2009).

11) F. Wauters, V. Leebeeck, I. Kraev, E. Traykov, **S. Van Gorp**, N. Severijns and D. Zákoucký, *β asymmetry parameter in the decay of $^{114}In$.* Phys. Rev. C. **80** (2009).

12) F. Wauters, I.S. Kraev, M. Tandecki, E. Traykov, **S. Van Gorp**, D. Zákoucký and N. Severijns, *Performance of silicon PIN photodiodes at low temperatures and in high magnetic fields.* Nucl. Inst. and Meth. A **604**, 563–467 (2009).

13) V.Yu. Kozlov, M. Beck, S. Coeck, P. Delahaye, P. Friedag, M. Herbane, A. Herlert, I.S. Kraev, M. Tandecki, **S. Van Gorp**, F. Wauters, Ch. Weinheimer, F. Wenander, D. Zákoucký and N. Severijns, *The WITCH experiment: Acquiring the first recoil ion spectrum.* Nucl. Inst. and Meth. B. **266**, 4515 − 4520 (2008).

PARTICIPATION IN WORKSHOPS AND CONFERENCES

**Low-energy fundamental-interactions physics at ISOL@MYRRHA**    Mol, Belgium
*oral - First determination of the a correlation with the WITCH experiment*    *October 3, 2011*

**Advances in Radioactive Isotope Science (ARIS)**    Leuven, Belgium
*poster - Simbuca: A Penning Trap simulation program.*    *June 1, 2011*

**Ecole Joliot-Curie**    Lacanau, France
*oral - Weak Interactions group Leuven*    *October 1, 2010*

**International Nuclear Physics Conference (INPC)**    Vancouver, Canada
*poster - WITCH: status and perspectives*    *June 5, 2010*

**Trapped and charged particles (TCP)**    Saariselkä, Finland
*oral - Using a graphics card to simulate space charge effects + Simbuca*    *April 14, 2010*

**ISOLDE workshop**    CERN, Switserland
*oral - The WITCH experiment: status and perspectives*    *November 11, 2008*

**ENAM conference**    Ryn, Poland
*poster - Measurement of the recoil energy of ions escaping a Penning Trap*    *September 9, 2008*

**Fantom school on the Early Universe**    Münster, Germany
*oral - The use of radiofrequent fields at WITCH*    *April 14, 2008*

**Brix workshop**    Mol, Belgium
*oral - WITCH: status and perspectives*    *March 9, 2008*

**Detectors** : Positions sensitive MCPs, silicon Pin diodes, Germanium detectors

**Cryogenics** : Experience with cryostats with nitrogen and helium cryoliquids, and with superconducting magnets.

**Ultra High Vacuüm** : Performed an upgrade of the WITCH experiment from $10^{-7}$ mbar to $10^{-10}$ mbar. Experience with UHV materials, pumps and coatings.

**HV** : Experience with High Voltage and fast (microseconds) switching of HV.

**Ion beam manipulation** : Experience with ion sources, beam tuning and operation of Penning ion traps.

**Simulations** : Developed a Penning Trap simulation package, Simbuca. It is the first application that calculates the Coulomb interaction between ions on a graphics card instead of on a conventional CPU. Because of this approach, simulations that would have taken 3 years are now performed within 3 days. Various other experiments are now also using Simbuca to help understanding the ion motion in a Penning Trap.

**Markup Languages** : HTML, CSS, LaTeX

**Programming Languages** : C$^{++}$, Java, PHP, linux bash

**Specialized physics and mathamatical Software** : Comsol, SIMION, SRIM, Root, Maple, MATLAB, AutoCAD